A Numerical Investigation of the Flow Around Rectangular Cylinders

by

Nathan Steggel

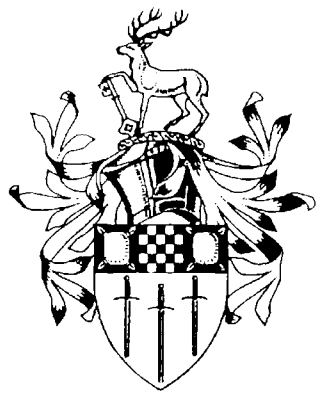

School of Mechanical and Materials Engineering
The University of Surrey
Guildford GU2 5XH
United Kingdom

Thesis submitted for the degree of
Doctor of Philosophy

March 1998

Abstract

The viscous flow around rectangles defined by afterbody length, B, and cross-stream dimension, A, is investigated through a hybrid discrete vortex method. For uniform flow conditions the effects of varying the side ratio, B/A, the angle of incidence, α, and the Reynolds number, Re, are all considered. Pulsating flow results are reported for rectangular cylinders with B/A values of 0.62, 1.0, 2.0 and 3.0, a B/A=1.0 cylinder inclined at 45° and a circular cylinder.

At a fixed Reynolds number, Re=200, the variation of drag coefficient with side ratio shows C_D increasing with decreasing B/A. This contrasts with the known result at higher Reynolds number, $10^4 \leq Re \leq 10^5$, for which a maximum drag occurs close to B/A=0.6. A peak is observed in both the Strouhal number and lift coefficient close to B/A=0.30. This is explained by the afterbody suppression of the shear layer interaction. In the case of the square cylinder, results are presented for the variation of drag coefficient and Strouhal number with Reynolds number, $50 \leq Re \leq 5\times10^3$. Good agreement with experiment is shown although for $Re \geq 500$ the calculated Strouhal number is dual valued.

The 'lock-in' characteristics under pulsating flow are shown to be highly dependent on body geometry. All the cylinders are shown to exhibit an asymmetric resonant mode within which the shedding frequency is controlled at half the forcing frequency and the mean forces increase. Several different shedding patterns are predicted across this asymmetric synchronisation range. A 'quasi-symmetric' mode is also observed for some cylinders characterised by near wake symmetry and a substantial reduction in mean forces. A pseudo-phase lag is defined which relates a moment of the lift cycle to a moment of the forcing oscillation. This is shown to change across the synchronisation range of each cylinder considered and the change is found to be greater at lower forcing amplitude.

Acknowledgements

Those who have helped me during the course of my PhD studies are too numerous to mention in full so I will restrict myself to the star players in this equation.

Much as I love the Bognor Regis Unemployment Benefit Office I am truly thankful for being saved from the monotony of dishing out UB40's by Dr Nicole Rockliff and Professor Ian Castro. Dr Rockliff gave me strong encouragement throughout and her prompt reading of the thesis drafts was particularly appreciated. At one stage my nerve packed in - shoulder nerve that is - and I remain grateful to Professor Castro for aiding me with the completion of the BBAAIII paper whilst I was in severe pain. I should also like to thank Professor Mike Graham and the research staff at Imperial College from whom I received some excellent advice during the early stages.

Extra special thanks are due to Dad, for meticulously proof reading the thesis, Mum, for keeping Dad sane, and Ange, for keeping me sane.

Other key players, in order of appearance, are Duv - the man who gave us the silver egg-cup, Dr Gough the current World Record Holder for thesis length, temporally and spatially, Ms 'Grade-One' Azapagic, Slobs, who enlightened me on the finer aspects of fractal footysophy, and saxman Stephane, on joue au petinque?

Finally I must mention the staff and students of EnFlo, particularly Matt, for putting up with me in the lab over the past year.

Notation

Roman:

A	Cylinder diameter.
B	Cylinder length
C_D	Drag coefficient.
C_L	Lift coefficient.
C_P	Pressure coefficient.
d	Maximum cross-stream dimension
f_e	Forcing frequency.
f_S	Shedding frequency.
f_0	Natural shedding frequency (Uniform flow).
F_X,F_Y	Drag, lift components of force.
g_{ij}	Metric tensor.
J	Jacobian of transformation.
K	Keulegan-Carpenter number.
NV	Number of vortices.
NX	Size of mesh in ξ direction.
MY	Size of mesh in η direction.
p	Fluid pressure.
P	Total pressure.
Re	Reynolds number.
St	Strouhal frequency.
t	Time.
u,v	Components of velocity in physical plane.
U_0	Upstream flow velocity.
U_A	Velocity amplitude of upstream flow pulsations.
U_S	Velocity at separation point.
$W(z)$	Complex potential.
x_e	Cylinder displacement amplitude.
x,y	Co-ordinates in physical plane.
$z(x,y)$	Complex co-ordinate in physical plane.

Greek:

α	Angle of incidence.
Γ	Circulation.
μ	Kinematic viscosity.
ν	Fluid viscosity.
ρ	Fluid density.
σ	Cut-off strength of vortices.
τ	Period of forcing oscillation.
ω	Vorticity.
$\Omega(\xi,\eta)$	Complex co-ordinate in computational plane.
ξ,η	Co-ordinates in computational plane.
ψ	Stream function.
ϕ	Velocity potential.

Subscripts:

i,j	Value at (i,j)th mesh point.
k	Value of kth discrete vortex.

Contents

List of Figures

Chapter 2

Chapter 3

Chapter 4

Chapter 5

Chapter 6

Chapter 1

Introduction

1.1 Motivation

Flows past cylindrical obstacles, such as the circular and rectangular cylinders examined in this study, may be considered to lie within the general research area of bluff body aerodynamics and a vast amount of literature has been devoted to this field. The practical impetus for such research ranges from evaluation of the aerodynamic loading exerted on aerofoils to the simulation of wind-induced oscillations experienced by large structures.

The flow past a streamlined body, such as an aerofoil at low incidence, remains attached over the majority of the body surface and only separates towards the aerofoil trailing edge. This contrasts with the flow around a bluff obstacle for which separation occurs over a large portion of the surface area and where the wake is usually characterised by regions of high vorticity. Morton (1984) has described how the generation of vorticity results from the tangential motion of a boundary relative to a fluid and from the pressure gradients acting along that boundary. Viscous diffusion and convection then work to spread the vorticity into the fluid interior.

For uniform flow past two-dimensional bodies, the creation, diffusion and subsequent convection of vorticity results in the formation of large-scale vortices shed periodically into the wake region. As these vortices are shed alternately from opposite faces of the body they exert an oscillatory force on the obstacle normal to the freestream. Since the vortical regions of the flow are associated with low pressure values the base pressure, or pressure at the rear of the obstacle, will be low inducing a high value of drag. A more detailed description of the physical processes behind vortex shedding is contained within Chapter 2.

Buildings, bridges and ocean pipelines are all examples of bluff obstacles which, when exposed to strong winds or heavy seas, might be susceptible to structural damage. When an oscillatory, upstream flow component is present further complications may result. At certain oscillatory amplitudes and frequencies resonance can occur between the shedding frequency and upstream flow frequency. As a result the stresses exerted on the obstacle may be further increased or other undesirable side effects might be induced. An example of this is in the application of vortex flowmeters to the measurement of flowrate. These meters measure volumetric flowrate proportional to shedding frequency but for pulsating or pumping flows the shedding frequency can resonate, or 'lock-in', with the pulsation frequency resulting in inaccurate measurements.

Engineers are therefore interested in being able to predict what kinds of stresses are likely to occur, under what circumstances, and how the design can be adapted in order to minimise the possibility of structural failure. It is thus the job of the fluid dynamicist to assist in the design process by building numerical or laboratory models to simulate the complex fluid-structure interactions which take place. Fluid dynamicists are also interested in these flows from a more fundamental point of view as even the flows about the most simple geometries are not yet fully understood. They wish to gain a greater understanding of phenomena such as flow separation, reattachment and transition to turbulence, and to understand how the frequency and strength of vortex shedding varies with Reynolds number, body geometry, freestream turbulence and other defining parameters of the flow.

1.2 Methods for the simulation of bluff body flows

In the laboratory, wind tunnel or water tank experiments can be devised to study the flow characteristics. Loadings can be estimated from pressure tappings on the body surface or load bearings. Velocity measurements in the wake region are usually made by Hot-Wire Anemometry (HWA) or Laser Doppler Anemometry (LDA). Dominant frequencies in the wake can then be extracted by looking at the power spectrum of velocity samples although this is more difficult with LDA techniques since the sampling rate is low and non-uniform. Flow visualisation by introduction of smoke or dye, upstream of the body, is frequently used in experimental analysis. The graphical output cannot give much quantitative description but useful qualitative observations of the wake formation processes and phenomena such as separation can be extracted.

Laboratory experiments are costly, time-consuming and involve factors such as wall effects and probe intrusion. It is thus inevitable in the age of the computer that numerical techniques are being widely used to simulate bluff body flows. The Navier-Stokes equations (1.1) are a set of non-linear partial differential equations derived from the principle of conservation of linear momentum [see for example Acheson (1990)]. These are given below together with the continuity condition (1.2) for an incompressible fluid:

$$\frac{\partial \boldsymbol{u}}{\partial t} + (\boldsymbol{u} \cdot \nabla)\boldsymbol{u} = -\frac{1}{\rho}\nabla p + \nu \nabla^2 \boldsymbol{u} + \boldsymbol{g}, \tag{1.1}$$

$$\nabla \cdot \boldsymbol{u} = 0. \tag{1.2}$$

In the above $\boldsymbol{u}$ is the velocity vector and p the fluid pressure. $\boldsymbol{g}$ is the gravitational acceleration and the kinematic viscosity is defined as $\nu=\mu/\rho$, ρ being the fluid density and μ the viscosity of the fluid. These equations cannot be solved exactly but a variety of numerical schemes have been developed which model the equations of motion in order to obtain approximate solutions. These schemes are now widely used for research and development within both academia and industry in the form of CFD (computational fluid dynamics) codes. The major advantage in using CFD as a tool for solving the Navier-Stokes equations is that detailed analysis of the flow can be obtained since values for all calculated parameters are deduced throughout the computational domain at each time step.

An important non-dimensional parameter is the Reynolds number Re which represents the ratio of inertial to viscous terms. For bluff body flows Re is normally defined as

$$Re = \frac{U_0 d}{\nu}, \tag{1.3}$$

where d is the maximum cross-stream diameter of the bluff body under consideration and U_0 the freestream velocity. Roughly speaking as Re increases the scales of fluid motion present in the flow reduce in size. To obtain adequate solutions the numerical schemes must resolve or model the smallest scales of motion and therefore the computational power required to solve the problem increases with increasing Reynolds number.

Most numerical schemes are mesh-based in nature. Direct numerical simulations (DNS) ensure that the grid is refined enough to include the smallest scales of motion in the calculations. At present DNS calculations are restricted by computational power to low Reynolds number flows below $Re=10^3$. Most bluff body flow applications occur in the range $10^4<Re<10^5$. Higher Reynolds numbers ($Re>10^3$) can be modelled by adding a suitable scheme to the simulation, usually called a *turbulence model*, which parameterises the smaller scales of motion.

An irrotational flow is defined as a flow for which no vorticity is present. Mathematically, irrotational flows past arbitrary objects can be simply represented by what are known as potential solutions. The flow around bluff obstacles can in general be characterised by concentrated areas of vorticity contained within largely irrotational motion. This property is fundamental to the discrete vortex method (DVM) which models the irrotational part of the flowfield as a potential solution and introduces many discrete packets of vorticity, or vortex particles, to simulate the wake and boundary layer region. By solving the vorticity transport equation (or using the Biot-Savart Law) the transport and interaction of these vortical regions can be effectively simulated. In contrast direct numerical simulations of the flowfield approximate the equations of fluid motion by mesh-based finite-difference or finite-volume relations which solve for pressure and velocity over the entire flowfield at each time step. Unless the mesh is exceptionally small the finest scale fluid motions will not be adequately simulated. Thus the discrete vortex method is advantageous in concentrating computational effort on the complex wake and boundary layer region and in its ability to simulate the smallest scale fluid motions by many vortex particles.

Many typical bluff structures can be approximated as long cylinders, and for simulation purposes two-dimensional cylindrical cross-sections are often used. In numerical simulations the effects of spanwise or three-dimensional fluctuations in the flow are often ignored and a two-dimensional model is devised which treats each plane of flow as identical. This has the advantage of mathematical simplicity and saves valuable CPU time. Although a 2-D representation of the flowfield will not be exact, good approximations of the aerodynamic loadings can be obtained and the dominant features of the flow will still be apparent. Of course in the laboratory the simulation can never be fully two-dimensional but there are other benefits to pursuing 2-D simulations. A

two-dimensional solution may often be considered as the limiting solution to a more complex 3-D problem. In addition flow visualisations have played an important role in the study of fluid dynamic processes and their interpretation is greatly eased by the use of a 2-D configuration.

1.3 Scope of the present study

The primary objective of the present study is the numerical investigation of flows about rectangular cylinders. In particular the 'lock-in' characteristics under pulsating flow conditions past these obstacles are examined. Other studies have been initiated to determine the effects of pulsating flow on the vortex shedding behind triangular and T-shaped geometries. The initial stimulus for this research stems from a series of laboratory experiments conducted by Al-Asmi and Castro (1992) on the effects of pulsating flow past typical vortex shedding flowmeter geometries. They studied the effects of shape and blockage ratio on 'lock-in' characteristics over a range of oscillation amplitudes and frequencies at a typical Reynolds number of Re=1.5×10^4.

However the main topic of this thesis concerns the flows past rectangular cylinders. An outline of the physical appearance of vortex shedding is given at the beginning of Chapter 2 followed by an overview of relevant bluff body aerodynamics literature. A review of the rectangular cylinder literature is preceded by a section on circular cylinders. The added complications involved when there is an upstream oscillatory flow component present or when the body itself is undergoing vibration are discussed in section 2.4. Chapter 2 concludes with a summary of the main findings for flows past rectangular cylinders and identifies those areas which require further research.

As with most computational methods the discrete vortex method started out as a simple model but rapidly developed into a diverse multitude of models as the numerous researchers constructed their own theoretical schemes, interchanging ideas and discarding or incorporating methods according to the needs of their particular simulation. Essentially vortex methods originated as inviscid Lagrangian models which neglected the diffusion of vorticity. To reduce computational expense hybrid Eulerian-Lagrangian schemes were developed. These solve the velocity field on a mesh before interpolating back to individual vortices for convection purposes. According to Morton (1984) the decay of vorticity can only take place within the fluid interior and results from the cross-diffusion of vorticity of opposite signs. Viscous diffusion of vorticity has usually been incorporated by splitting the vorticity transport equation into diffusion and convection parts. The development of these theoretical concepts is outlined in Chapter 3 in conjunction with a review of DVM literature. Chorin (1973) and Clements (1973) were amongst the first to model bluff body flows using discrete vortex methods but many have followed in their footsteps since. Papers which study the uniform flow past circular and sharp-edged bodies have been reviewed along with some papers which examine oscillatory flow past bluff bodies. A more concise review can be found in Sarpkaya (1994).

A hybrid vortex-in-cell method with a finite difference scheme to solve the viscous diffusion equation was chosen for all simulations in this study. This method was first developed by Graham (1988) although a similar

hybrid scheme was independently developed by Chang and Chern (1990). Subsequent applications include the work of Meneghini (1994) who used the discrete vortex method to simulate cross-flow oscillations past circular cylinders at Re=200. Meneghini's results clearly showed the 'lock-in' characteristics for oscillation frequencies f_e close to the natural shedding frequency f_0 and the 'lock-in' boundary was determined. A version of Meneghini's code was obtained in the initial stages of this research. The modifications made to the DVM code chosen for this study took up a considerable part of the research time. A description of the code together with those modifications made are given in Chapter 4.

A major part of the code development included the derivation and implementation of a surface pressure calculation scheme. To calculate force coefficients the DVM has previously either used the Blasius theorem, which relates the force on the body to the rate of change of momentum in the fluid travelling across the body, or related the gradient of vorticity normal to the body to the surface pressure gradient. As vortices leave the computational domain, results from the Blasius theorem become excessively noisy and for sharp edged bodies the vorticity gradient is noisy near corners, resulting in erroneous surface pressure calculation. A new method of finding the surface pressure was therefore required here. Manipulation of the momentum equations in a generalised co-ordinate format leads to an integral expression for the surface pressure which is applicable for any co-ordinate transformation. Evaluating the surface pressure by this integral method is more accurate for sharp-edged bodies and the derived pressure integral expression should therefore provide a good basis for estimating surface pressures around other shapes in future studies.

Uniform flows past rectangular cylinders are discussed in Chapter 5. Results were obtained for the effects of variation of side ratio, angle of incidence and Reynolds number. These effects are discussed in relation to changes in the mean measured parameters such as force coefficients and vortex shedding frequency as well by observations from flow visualisations of the vortex particles.

In-line oscillatory flow results past a series of circular and rectangular cylinders at Re=200 are presented in Chapter 6. The lock-in regimes for a range of oscillation amplitudes and frequencies are discussed and simulated flow visualisation is presented for the different modes of shedding. Under both uniform and oscillatory flow conditions comparison is made with existing numerical and experimental data. Finally conclusions and suggestions for future work directions are discussed in Chapter 7.

Chapter 2

Bluff Body Aerodynamics

A large quantity of literature exists in the field of bluff body aerodynamics. Some recent reviews of the general topic include the papers by Oertel (1990), Roshko (1993) and Laurence and Mattei (1993). A review of oscillatory flow topics has been conducted by Bearman (1984). It is fair to state that flows past circular cylinders have received the most attention in the literature and this is particularly true for flows of an oscillatory nature. In this Chapter the literature review will concentrate on papers which examine the flow past rectangular cylinders. However some papers on the flow past circular cylinders are included since many analogies can be drawn. Some introductory material will first be given to explain why vortex shedding is a dominant feature of such flows.

2.1 Background Theory

To begin, some simple definitions must be made and the potential solution for flow past a circular cylinder will be presented. This will be of use later on when the discrete vortex method theory is described since it may be used to simulate the irrotational regions of flow. In a Cartesian (x,y) co-ordinate system, the velocity vector in two dimensions is defined as $\boldsymbol{u}=(u,v)$. The introduction of a stream function ψ is mathematically beneficial, as will be shown later on, but ψ exists only for two-dimensional and incompressible flows. Velocity can be expressed in terms of the spatial gradients of the stream function as written in (2.1):

$$u = \frac{\partial \psi}{\partial y}, v = -\frac{\partial \psi}{\partial x}. \tag{2.1}$$

Streamlines are lines of constant ψ and for a steady flow are equivalent to the paths which fluid particles will follow. Vorticity, ω, is a measure of the local angular velocity or spin of a fluid element. Mathematically it is defined as the curl of velocity,

$$\omega = \nabla \times \boldsymbol{u}. \tag{2.2a}$$

In two dimensions the vorticity becomes a scalar quantity,

$$\omega = \frac{\partial v}{\partial x} - \frac{\partial u}{\partial y}. \tag{2.2b}$$

Poisson's equation for the stream function follows directly from the definitions of stream function and vorticity, (2.1) and (2.2), and is

$$\omega = -\nabla^2 \psi. \tag{2.3}$$

When there is no vorticity present, i.e. $\nabla \times \boldsymbol{u} = 0$, the flow is termed irrotational. For an irrotational flow a velocity potential ϕ can be introduced such that

$$\boldsymbol{u} = \nabla \phi \qquad \text{i.e. } u = \frac{\partial \phi}{\partial x}, v = \frac{\partial \phi}{\partial y} \tag{2.4}$$

If the flow is two-dimensional, incompressible and irrotational then the velocity field can be represented by both (2.1) and (2.4) and a complex potential function W can be defined as

$$W(z) = W(x + iy) = \phi + i\psi \tag{2.5}$$

Scalar quantities such as ψ, ϕ and W remain invariant under a conformal transformation of the body geometry. This means that if we are able to determine the complex potential in one plane of geometry, say the z-plane, and there exists a transformation to another plane of geometry, z', then the complex potential at points in z will remain the same at the corresponding points in z' under the conformal transformation.

The complex potential for the flow about a circular cylinder of radius a is well documented (see for example Acheson (1990)) and is given as

$$W(z) = U_0 (z + a^2 / z). \tag{2.6}$$

From (2.5), with a conversion to polar co-ordinates, the stream function can be written as

$$\psi = U_0 (r - a^2 / r) \sin\theta. \tag{2.7}$$

From (2.7) the solution of the velocity field in irrotational flow can be obtained. Furthermore substitution of the surface values of velocity into Bernoulli's equation yields C_P, the surface pressure coefficient:

$$C_p = \frac{p - p_\infty}{q_\infty} = 1 - 4\sin^2\theta . \tag{2.8}$$

This result, derived in most elementary texts on fluid dynamics, e.g. Kuethe and Chow (1986), shows that the surface pressure attains a maximum value at the forward and rear stagnation points. Over the rear portion of the body the flow travels from a region of low pressure to a pressure maximum; the importance of this adverse pressure gradient will be seen in the following section.

2.1.1 Boundary layer and flow separation

In reality viscous effects are important. The fluid viscosity causes the flow to stick to solid surfaces and at the interface a no-slip condition exists such that the fluid velocity there is zero. Outwards from the boundary is a thin layer known as the boundary layer in which the velocity gradient is very high. The velocity rises from zero on the body to approximately the mean flow speed within a short distance. Separation can be described by considering the impulsive start of the fluid motion from rest. At the instant that the fluid motion is started the flow contains no circulation, i.e. the motion is irrotational and can be described by the potential flow solution. Potential flow theory predicts an adverse pressure gradient on the rear surface of the cylinder. It is possible to show that the fluid within the boundary layer is slowed in regions where $\partial p/\partial s>0$ (s being the direction along the body surface). A mathematical argument for this statement is given in Kuethe and Chow (1986, p326). If this adverse pressure gradient is sufficiently intense then the direction of flow will be reversed forcing the fluid to separate. Generally we say that separation tends to occur where there is an adverse pressure gradient or the fluid flows from a low pressure region to a high one.

Initially the irrotational flow solution shows this point to be the rear stagnation point but as the flow progresses this point moves quickly towards the front of the cylinder reaching a steady separation angle of around 80°. For a symmetrical bluff object, such as a circular cylinder, this separation process will initially be symmetrical with two separation bubbles forming a symmetrical vortex pair as shown in Figure 2.1.

2.1.2 Onset of vortex shedding

In the case of the flow about a bluff symmetrical body we can consider the flow to start from rest and assume the initial motion to be irrotational. As vorticity diffuses out from the body surface the boundary layer thickens until a short time later the flow separates. This will occur almost instantaneously at the leading edge corners for a sharp-edged obstacle, but for an obstacle of continuous curvature, such as a circular cylinder, the separation will begin at the rear stagnation point before moving forward until a stationary position is reached. Meanwhile the vorticity diffuses out from the body surface and two thin vortex layers form symmetrically and curl up on themselves. As more vorticity is shed from the surface this vortex pair grows in strength and size, extending itself further downstream as seen in Figure 2.1.

For small Reynolds numbers, up to about Re=50, this arrangement is stable and the vortex pair grows until reaching some steady point at which time there is a balance between the vorticity being added to the vortex pair from the shear layer and the vorticity diffusing out from the vortex pair into the main body of fluid. As the Reynolds number is increased beyond Re=50 this stability cannot be upheld. An asymmetry develops and one vortex rolls up over the other and is shed into the wake as a starting vortex. Vortices of opposite sign are then shed alternately into the wake resulting in the Karman vortex street pattern shown in Figure 2.2. It should be noted that even at lower Re any asymmetrical disturbance may trigger an instability in the vortex pair arrangement.

The frequency of vortex shedding is regular and is denoted f_s in the literature although under uniform flow conditions this frequency is sometimes called the natural shedding frequency f_0. The Strouhal number is defined as the non-dimensional frequency of vortex shedding under uniform flow conditions and is given by

$$St = \frac{f_0 d}{U_0}. \tag{2.9}$$

Varying the Reynolds number may alter the Strouhal number significantly and these effects are discussed for both circular and rectangular cylinders in Sections 2.3.1 and 2.4.1 respectively.

2.2 Flows past circular cylinders

The flow about a circular cylinder is by far the most studied of all flows about bluff bodies due to its importance in engineering and the ease with which mathematical and laboratory models can be implemented. A concise review of flows about circular cylinders is given by Williamson (1996a). An overview is presented here since many of the findings have analogous results in the flows past bluff obstacles of other geometries.

2.2.1 Effect of Reynolds number

The plot of base pressure coefficient, Figure 2.3, clearly demonstrates that the nature of the flow is highly dependent on Reynolds number. Strouhal number vs. Reynolds number is plotted in Figure 2.4 for Re<450. The discontinuities in the Strouhal number and base pressure curves are attributable to the appearance and growth of instabilities in the flow which may alter the flow pattern. Various regimes have been identified and the different instabilities associated with the transition between these regimes are now receiving much attention. Williamson (1996a) has taken results from researchers who have been careful with the set-up of the experiment since upstream turbulence levels, cylinder roughness, aspect ratio and end conditions can all have a significant effect on the exact location of these transitions. Recently stability analysis has become an area of research used to identify the flow instabilities and how they are responsible for changing the shedding patterns. A small disturbance can grow either locally at its point of generation, in which case it is termed *absolutely unstable*, or

can be convected downstream growing in time but leaving the point of generation undisturbed in which case it is referred to as a *convective instability*. Von Karman was the first to interpret the vortex street as an intrinsic property of the wake structure and analysed the stability of vortex streets as early as 1912. The growth rates of these instabilities are very small which is why an obstacle wake may stretch for a considerable distance downstream. Equivalently the high levels of vorticity associated with the wake region may persist long after an obstacle has passed through that location. In the case of aircraft it is important to ensure suitable time periods elapse between aircraft landings on account of this phenomenon.

The steady laminar regime, $Re<49$, consists of a symmetric vortex pair whose length grows with increasing Reynolds number. As described earlier the steady regime cannot be sustained with increasing Re since the vortex pair cannot grow indefinitely. An instability develops at approximately $Re=49$. This primary wake instability, known as a Hopf bifurcation, is amplified with increasing Re and induces periodic two-dimensional vortex shedding which can be sustained up to a Reynolds number of around 200 provided care is taken in the experiment to ensure that the end conditions induce parallel shedding. Three-dimensional instabilities develop beyond $Re=200$; these give a discontinuity in the curve as local vortex dislocations form along the span of the cylinder. Henderson and Barkley (1996) used a stability analysis technique to try and determine where these three-dimensional instabilities develop. A direct numerical simulation of the 2-D flow was solved and stored before a stability analysis was carried out by applying an infinitesimal 3-D disturbance to the 2-D solution. Henderson and Barkley found a critical value of $Re_c=187.5$ and an instability wavelength of 4 cylinder diameters which agrees well with the experimental observations of Williamson (1996b). This secondary instability has been termed 'mode A' by Williamson and is known to be hysteretic (see Figure 2.4) since if the Reynolds number is gradually decreased the instability can be sustained down to $Re=170$. Observations of the base pressure plot, Figure 2.3, show that the base pressure reaches a local peak value at the end of regime BC and this looks similar to the peak which would have been reached had the straight line region of AB been extended. From the Strouhal number curve a second discontinuity can be seen at $Re=240$. This is associated with a further instability, known as 'mode B', of a wavelength similar to the bluff dimension. The 'mode A' and 'B' instabilities are clearly captured in Figure 2.5. As the Reynolds number increases 'mode B' shedding gradually becomes more dominant but there appears to be a range of Reynolds number for which both modes are present.

Thereafter in region CD (Figure 2.3) there is a sudden and sustained decrease in base suction up to $Re=10^3$, associated with an increase in the vortex formation length. Williamson accounts for this decrease by stating that the small scale 3-D structures become increasingly disordered in this regime; however current research is unable to provide a satisfactory explanation for the exact mechanism. Regime DE covers a wide range of Reynolds number, $Re=10^3$ to $Re=2\times10^5$, and most practical applications of bluff body flows would fall within this range. The base pressure gradually rises across the Re range, although on a less steep curve than in the AB regime, and as expected this is associated with a decrease in the formation length. This regime is known as the shear layer transition regime since the turbulent transition point in the shear layer moves upstream as Re is increased.

In regime EG the boundary layer becomes turbulent and this is associated with a reattachment of the separation bubble and a secondary separation at approximately 140 degrees. As a result the wake width is now very much reduced and hence the base suction drops considerably.

2.3 Flows past rectangular cylinders

Structures which may be of rectangular cross section include buildings, bridges, vortex flowmeters and design features such as beams and fences. A basic understanding of the aerodynamics past such objects is necessary since we wish to understand the loadings to which they will be exposed and how susceptible they are to aeroelastic instability.

The defining flow and body geometry parameters for 2-D uniform flow past rectangular cylinders are shown in Figure 2.6. Parameters which vary the geometry of the problem are the afterbody length or side ratio B/A and the angle of attack α. The Reynolds number Re and Strouhal number St are usually non-dimensionalised according to d, the maximum cross-stream dimension, as in equations (1.3) and (2.9). However some researchers have used the rectangle width A to non-dimensionalise, in which case

$$Re_A = \frac{U_0 A}{\nu}, \qquad St_A = \frac{f_0 A}{U_0}. \tag{2.10}$$

Drag, D, and lift, L, act parallel and normal respectively to the free stream and their respective coefficients are defined as

$$C_D = \frac{2D}{\rho U_0^{\,2} d}, \qquad C_L = \frac{2L}{\rho U_0^{\,2} d}. \tag{2.11}$$

In contrast with the flow past smooth obstacles, for sharp-edged objects the separation will occur almost instantaneously at the corner point since the pressure gradient will be so large there. However if the body is symmetrical and cylindrical then the vortex pair will still grow in the wake until, as described earlier, the balance of vorticity diffusion cannot be maintained and the Karman vortex street results. If the rectangle is placed at an angle of attack then asymmetry is observed immediately and we expect the vortex street to appear much sooner after an impulsive start. The vortices in this case will no longer be of equal magnitude and hence the mean lift will be non-zero.

Much work has already been done in an attempt to describe the effect of changing side ratio, angle of attack and Reynolds number on the two-dimensional flow past rectangular cylinders and in particular how the strength and

frequency of vortex shedding vary. A summary of the main findings accumulated from past research follows and this has been split into laboratory and numerical data.

2.3.1 Laboratory measurements on the effect of *B/A* and *Re* variation

Bearman and Trueman (1972) were amongst the first to investigate the effect of varying the side ratio. Their study consisted of laboratory experiments conducted over a Reynolds number range $Re=2\times10^4$ to $Re=7\times10^4$, with side ratios varying in the range $0.2\leq B/A\leq1.2$. The high drag which occurs at a side ratio of $B/A=0.6$ had been a surprise result at the time of its discovery. Prior to that it had been thought that all bluff bodies had a roughly uniform drag coefficient since C_D had been found to be close to 2.0 for both a flat plate placed normal to the stream and for a square sectioned cylinder. Bearman and Trueman's (1972) experiments were thus an attempt to shed some further light on the origin of this high drag and of the interaction taking place between the separated flow and the afterbody surface downstream of separation.

Figure 2.7 shows drag and base pressure plotted against side ratio. The most striking feature is the sharp drag peak which occurs at $B/A=0.62$ with $C_D=2.94$. By introducing a splitter plate at the base Bearman and Trueman were able to demonstrate that the high drag could be controlled. The wake splitter plate increases the size of the separated region behind the body, delaying the interaction between the two shear layers until much further downstream, and hence vortex formation takes place much further from the body base. Since a vortex represents a low pressure region, the further the vortices form from the rear of the body the higher the base pressure and hence the lower the drag. An examination of surface pressure distributions for 3 different afterbody lengths showed the base pressure distribution to be fairly uniform for cases where $B/A=1.0$ and 0.2 but for $B/A=0.6$ the base pressure is markedly lower towards the centre of the base which suggests that the vortices from upper and lower surfaces have their formation centres along the base centre line. The major conclusion from this work is that for a flat plate placed normal to the oncoming stream the vortices are forming quite far from the body but as we increase the afterbody length this distance decreases, resulting in lower base pressure and higher drag. However this cannot continue indefinitely and we reach a critical depth, at which time the separating layers begin to interact with the downstream corner and vortices start to form further from the body again.

Laneville and Yong (1983) offered a slightly different perspective on the same problem, concentrating on flow visualisation of the vortex shedding. They used an oil film visualisation technique to obtain time-averaged flow patterns and as a result were able to identify various geometrical parameters of the flow such as length of separation bubble, distance between centres of vortices, and distance of vortex centre from trailing edge. Their qualitative findings could then be compared with the quantitative results of Bearman and Trueman (1972). Figure 2.8 outlines what the general time-averaged flow pattern looks like. Vortices are shed asymmetrically into the wake but the time averaged flow pattern is symmetrical and two new parameters are defined, v_c the distance between vortex centres, and v_p the distance of a vortex centre from the body base. The variation of these parameters with side ratio, as found by Laneville and Yong, is given in Figure 2.9 and plates of the averaged flow visualisation in Figure 2.10 give a clearer indication of how the vortex positions vary. At low and high

side ratio the distance between vortex centres is quite large but for intermediate side ratio the vortex centres are almost indistinguishable. The authors note that for $0.3<B/A<0.8$ there is a serious variation in the drag with the drag maximum occurring at around 0.6. As expected the lowest base pressure corresponds to the point where vortices are forming tightly behind the trailing edge giving high base suction in that region. The front face pressure distribution remains almost identical over this range while the base pressure shows a large variation with afterbody length. The smaller v_p is, the closer vortices are forming to the rear of the body and the lower the base pressure. With smaller v_c the vortices are forming very close together and hence the base pressure distribution will no longer be linear on the rear surface. A physical description of the processes behind the drag variation has been attempted by the authors. For $B/A<0.5$ the side wall is too short to allow for any interaction between the afterbody and the separating flow. However as the afterbody length increases the separation bubble grows and begins to exert a downwash effect on the vortex formation. This forces the vortices to form nearer to the body, pulling them in behind the body and closer together. Beyond $B/A=0.625$ the separation bubble is roughly 60% of the side length and as it is now further from the trailing edge its influence on the vortex formation diminishes and the vortices are free to again form further apart from the wake centre line and further back from the rear surface. It is suggested that intermittent reattachment may occur for $1.0<B/A<3.0$ but beyond 3.0 reattachment is fully established with vorticity shed periodically from the separation bubble.

Ohya (1994) conducted base pressure measurements for rectangular cylinders with side ratios $B/A=0.4$, 0.5 and 0.6 in an attempt to demonstrate that a discontinuity in the wake pattern close to the 'golden ratio' could explain the peak in the drag curve. Two different wake patterns were found as clearly indicated in Figure 2.11. At $B/A=0.4$ the vortices form far from the body and thus base pressure is high and drag low. At $B/A=0.6$ the vortices form close to the body and along the wake centreline corresponding to low base pressure and thus high drag. At $B/A=0.5$ there is a discontinuity in the flow structure with vortex shedding intermittently changing between these two modes. This jumping of modes is an important result but it is peculiar that neither Bearman and Trueman (1972) nor Laneville and Yong (1983) have reported this in their earlier works. Indeed both of these earlier papers suggest a smooth and continuous variation in drag coefficient and wake pattern with no mention of any discontinuity. Laneville and Yong in particular were interested in the wake visualisation paying close attention to the vortex formation positions and would surely have discussed this intermittency had it been present in their experiments. No clear description of the reason behind the appearance of this critical flow pattern is given by Ohya other than it 'appears to be caused by an interaction between the separated shear layers and the body downstream of separation' which mimics almost word for word what Bearman had said twenty two years earlier.

Reynolds number effects of flows past rectangular cylinders have received attention in a series of papers. In the earliest study, by Okajima (1982), a comprehensive experimental investigation was undertaken to determine the vortex shedding frequencies of rectangular cylinders with side ratios $B/A=1.0$, 2.0, 3.0 and 4.0 over the range $70<Re<2\times10^4$. Okajima's preliminary statement reads, 'In the case of a sharp edged body, like a rectangular cylinder, separation is fixed at the leading edge and the aerodynamic characteristics are said to be relatively

insensitive to Reynolds number.' However, 'at extremely low *Re*, the separation takes place at the trailing edge, due to immediate reattachment of the flow at the leading edge. As *Re* increases, steady reattachment becomes impossible and the leading edge separation develops. Furthermore transition to turbulent flow occurs as the Reynolds number is increased.' Hence Okajima reports that for a certain range of *Re* the Strouhal number is likely to be highly dependant on *Re*. A water tank was used to conduct experiments where $Re<300$ and a wind tunnel for higher *Re*. In each set of experiments a hot-wire probe measured velocity fluctuations and hence the shedding frequencies.

The measurements from various investigations on the *Re* dependence of rectangular cylinders has been compiled by Norberg (1993). The compilation includes laboratory investigations by Okajima (1982), Igarishi (1985) and Norberg (1993) in addition to the numerical studies of Davis and Moore (1982), Franke *et al* (1990), Okajima *et al* (1990) and Ohya *et al* (1990). Figure 2.12 has been reproduced from his paper and indicates the *Re* dependence of the $B/A=1.0$, 2.0 and 3.0 cylinders. Quite different Reynolds number dependent characteristics are observed in each case.

Figure 2.12(a), $B/A=1.0$: The Strouhal number curve is continuous and roughly constant for $Re>1000$ but shows some variation below this value with an experimental peak of 0.14 for $120<Re<250$. Those values found from numerical simulations are generally found to be higher than the laboratory values.

Figure 2.12(b), $B/A=2.0$: The Strouhal number increases linearly up to $Re=400$ but then a discontinuity arises where there are two apparent values. For $Re>600$ the Strouhal number again increases but above a Reynolds number of 2000 there is considerable scatter in the results.

Figure 2.12(c), $B/A=3.0$: Initially *St* increases linearly up to $Re=600$. This is followed by a discontinuous region, $600<Re<5000$, within which 3 different frequencies can be seen; a large amount of scatter is present in this region as the results were dependent not just on Reynolds number but on actual model size since this affected the end conditions. This suggests that three-dimensional motions become dominant within this *Re* range and that these are highly dependant on the model end conditions. Above $Re=5000$ the Strouhal number remains roughly constant at $St=0.16$.

In general it is noticed that the scatter in the results appears to increase with higher side ratio; this is perhaps because the vortex shedding from longer bodies is more susceptible to the experimental set-up.

Okajima's (1982) research includes some hot-wire measurements of the mean and turbulent components of velocity across the wake for the $B/A=2.0$ and 3.0 cylinders at several different Reynolds numbers. These results give an indication of the variation in wake width and vortex formation position with Reynolds number. For the $B/A=2.0$ cylinder the wake is narrow at $Re=300$ and widens with increasing *Re*. At low Reynolds number there is reattachment along the side surfaces with separation again from the trailing edge and hence the vortices form

further downstream. At higher Reynolds number the flow becomes fully separated from the leading edge without reattachment to the side surface. Clearly one can conclude from this work that discontinuities in the Strouhal number curve occur at values of *Re* which are strongly dependant on the value of *B/A*. For the square cylinder no such discontinuity, or critical *Re*, has been observed. For the *B/A*=2.0 cylinder the critical *Re* is shown to be around 500; it is about 1000 for the *B/A*=3.0 cylinder. However this effect does not occur for the *B/A*=4.0 cylinder since the flow remains reattached to both upper and lower surfaces throughout the *Re* range. Okajima notes that the freestream turbulence level of 0.5% may have had a significant impact on the detachment and reattachment of the flow. This implies that a change to the value of freestream turbulence may incur a significant alteration to the way in which the Strouhal number depends on *Re*.

In summary, for *Re* below the critical region the flow detaches from the leading edge and reattaches on either the upper or lower surface during a period of vortex shedding, but for *Re* above this critical value the flow becomes fully detached from the cylinder. However at *B/A*=1.0 the afterbody length is too short for reattachment and at *B/A*=4.0 the afterbody is long enough to ensure the separated flow is always reattached regardless of the Reynolds number.

An experimental investigation of the flow past rectangles of greater side ratio has been performed by Nakamura *et al* (1991). Measurements were made for side ratios $3<B/A<16$. Four main regimes have been identified by the authors at Reynolds numbers in the range, $1.5\times10^4 \leq Re \leq 3.1\times10^4$:

(1) $B/A < 3.2$: The flow is fully separated from the leading edge and shear layer interaction takes place without reattachment.

(2) $3.2 < B/A < 7.6$: The shear layers reattach periodically and a regular vortex street is formed in the wake.

(3) $7.6 < B/A < 16$: The separation bubble is always fully attached. Its length varies periodically and, at its maximum, the bubble divides in a random manner shedding vortices into the wake but no regular street is apparent.

(4) $B/A > 16$: The plate is long enough for a turbulent shear layer to develop and a regular vortex street results from the interaction of the two turbulent shear layers. The limiting case of a flat plate parallel to the flow is of fundamental interest to fluid dynamics but remains outside the scope of the present study.

However at lower Reynolds numbers, $1000<Re<3000$, regular vortex shedding is found throughout the range of side ratios as can be seen from Figure 2.13. If the Strouhal number based on afterbody length is determined, stepwise increases can be observed at side ratios *B/A*=6, 9 and 12. Each mode of shedding corresponds to a number of vortices forming along the side of the body. Near the jumps between the modes both frequencies can

be observed as illustrated in Figures 2.14(a),(b) for a B/A=8.0 cylinder. Three vortices form along the side of the rectangle in (a) and two vortices form along the side in (b).

2.3.2 Numerical simulations on the effect of *B/A* and *Re* variation

Numerical models, quite understandably, have a much shorter history and have been confined mainly to two-dimensional laminar situations. Davis and Moore (1982) were the first to model the flow past rectangles with a two-dimensional direct numerical simulation at Reynolds numbers between 100 and 2800, and with side ratios B/A=0.6, 1.0 and 1.7. Their studies were conducted at low Re in order to minimise the effects of turbulence. Some experimental runs were also made for comparison although only the Strouhal frequencies were estimated. In a subsequent paper, Davis *et al* (1983), they follow on from their previous work by including the effects of adding an outer boundary to the flow. Since wind tunnel experiments must invariably be conducted within confining walls it makes sense to include the effects of blockage within the numerical simulation as a test of their influence. The Reynolds number varies from 100 to 1850 and blockage ratios of 0.25 and 0.17 are studied at the same side ratios as before. The presence of a confining boundary was found to increase both the drag and Strouhal number. What is striking about the results is that they did not make further calculations of the flow for values of B/A less than 0.6. They were aware of the critical drag found by experiment at higher Reynolds number but did not model this numerically. The authors have noted that even though the model is rather crude and certainly unable to examine small scale motions in turbulent regions it has still been able to give a fair indication of the drag and Strouhal number in comparison to the experiment. These early numerical results are rather limited in scope but problems which still hinder current simulations can be identified. A two-dimensional model will not be able to simulate the effects of any three-dimensional instabilities on the flow. This is apparent in the calculated values of Strouhal number which are consistently higher than experiment for Re>500. In the experiment the addition of blockage tended to increase Strouhal number with increasing blockage. Since blockage is known to enhance a two-dimensional flow profile this further verifies what has previously been stated, i.e. that Strouhal number should be expected to be overestimated in a two-dimensional simulation at Reynolds numbers for which three-dimensional instabilities are inherent in real flows.

A high Reynolds number, $Re=2\times10^4$, simulation of the effects of afterbody length has been conducted by Nagano *et al* (1982) with a discrete vortex method. In this study the side ratio is varied in the range $0.5<B/A<2.0$ and a drag maximum was found which has not been observed in any other numerical results. The peak was not nearly as sharp as that determined experimentally and the Strouhal number was consistently higher across the range. The high Strouhal numbers can again be attributed to the two-dimensional nature of the simulation. In two-dimensional space spanwise vortex stretching cannot occur, so all the vorticity is convected in the downstream direction; this leads to more rapid vortex development and hence a higher Strouhal number results. This is readily observed when confining walls are introduced as they tend to increase the two-dimensional nature of the problem. However this does not account for the drag peak being so undistinguished. It is possible that the numerical method removed too much vorticity for the lower side ratio cases as the drag

coefficient is clearly much lower than that found experimentally, i.e. the circulation reduction scheme needed some adjustment according to side ratio.

Franke *et al* (1990) have calculated numerically the laminar vortex shedding flow past a square cylinder for $Re \leq 300$ with a 2-D direct numerical simulation. Their work is geared towards the creation of a fully three-dimensional turbulent code capable of modelling more practically applicable situations. They state that the accuracy of the numerical results will depend strongly on the near-wall grid resolution. They also started their simulations with a gradual increase of free-stream velocity up to the final value as impulsive starts were found to generate long time disturbances which damped out only slowly. They further suggest that fully periodic vortex shedding is reached faster if the fluid is slowly accelerated from rest. In comparing these results with other numerical and experimental data, namely the Strouhal numbers obtained by Davis and Moore(1982) and Okajima(1982), the authors point out that a large discrepancy in the data exists, perhaps because of the treatment of the sharp edges which can influence the vortex shedding. They also find that for $Re<150$ the separation occurs on the rear corners and that up to this Re, the vortex size decreases with increasing Reynolds number and thus there is a reduction in C_D. However beyond Re=150 the opposite effect occurs. At Re=250 and Re=300 additional frequencies are reported in the drag coefficient spectrum, although for the square cylinder this has not been reported experimentally.

In an extension to his earlier laboratory based work, Okajima (1990) has examined numerically the flows about cylinders of side ratio in the range $0.6 \leq B/A \leq 8.0$. A finite difference method was used for low Reynolds number simulation, $150 \leq Re \leq 800$, and a discrete vortex method was chosen to model a high Reynolds number flow, although the exact Re is not given since the method is inviscid, i.e. it does not incorporate a viscous diffusion scheme. Comparison is made with results from a series of laboratory experiments in which base pressure (see Figure 2.15) and Strouhal number were measured for bodies of different side ratio over a large Re range, but it is not stated how these were performed.

At low Reynolds numbers the aim was to identify for each cylinder a critical Re range for which the Strouhal number jumped due to some interaction between shear layers and trailing edge taking place. Below this Re value, which varies for different B/A, Okajima states that the flow can generally be said to separate from the leading edge of the cylinder and reattach on both upper and lower surfaces, with the Karman vortex street observed in the wake. However one must assume that there exists a range of Re over which the flow is intermittently separating and reattaching. Beyond the critical Re the flow remains fully detached for $B/A<2.5$. This implies that, since the trailing edge no longer interacts in any significant manner with the separating shear layer, the Strouhal number should remain approximately constant above the critical Reynolds number and indeed this appears to be the case. Reattachment occurs for rectangles with side ratios greater than 2.5 even at higher Reynolds number. There were not really enough runs performed to give a proper comparison with the earlier experimental results, Okajima (1982). The discontinuity in the St vs. Re curve for the B/A=2.0 cylinder did appear to be predicted by the simulation, which leads to the assumption that the instabilities responsible for this

mechanism are two-dimensional in nature; i.e. the shear layer interaction with the trailing edge. No attempt was made to model flows at $B/A<0.6$ although the researchers were fully aware of the high Re critical drag phenomena. Base pressure variation with Reynolds number is also investigated in Okajima (1990) and the results are graphed in Figure 2.15 for the $B/A=1.0$ and $B/A=2.0$ cylinders. In each case the base pressure shows a very large variance with Reynolds number particularly in the $Re<1000$ region. The scatter in results is large but some of the trends appear to be analogous to those exhibited in the plot of base pressure variation for a circular cylinder, Figure 2.3. A local maximum in base suction is observed in the Reynolds number range $1500<Re<2000$ for the $B/A=1.0$ and $B/A=2.0$ cylinders. It was also shown that the base suction maximum occurs at around $Re\approx400$ for the $B/A=6.0$ and $B/A=8.0$ cylinders. In each case the base suction then falls but the Reynolds number for minimum drag varies widely from $Re\approx800$ when $B/A=8.0$ to $Re\approx10^4$ when $B/A=2.0$. For the circular cylinder case a local maximum was reported at $Re=260$ and a minimum at approximately $Re\approx10^3$, but whether the mechanisms responsible for these extrema are similar remains to be investigated.

The high Re DVM runs give good agreement with experimental results for the drag coefficient vs. B/A. The drag increases with decreasing side ratio down to $B/A=0.6$ as expected but no simulations were performed for lower values of B/A; this again is surprising as it would appear to be a natural progression to attempt to recreate the experimentally-determined golden ratio value. Vortex formation appears stronger and tighter (i.e. close to rear surface) for the 0.6 ratio but the lower side ratio cases are required to make significant comment on the vortex shedding and formation lengths.

Two papers attempt a numerical examination of the work by Nakamura *et al* (1991) with the side ratio in the range $3<B/A<10$ and $Re\leq1000$. A study of vortex shedding from flat plates with square leading and trailing edges at $Re=1000$ has been undertaken by Ohya *et al* (1992). A direct finite-difference analysis of the Navier-Stokes equations is used and although there is no turbulence model included in the simulation the jump in Strouhal number is still well observed at $B/A=6.0$ although the agreement with experiment is less satisfactory at higher values of B/A. A transitional mode is found at $B/A=8.0$ with two distinct shedding frequencies. Nakayama *et al* (1993), in a closely related study, then reduced the Reynolds number to $Re=200$ and 400. At $Re=200$ the Strouhal number shows a linear variation with B/A, whereas for $Re=400$ the Strouhal number increases stepwise with B/A in a similar manner to the experimental results for $Re=1000$. This implies that the impinging shear layer instability appears between $Re=200$ and 400. The impinging shear layer instability has been described as where the separating shear layer from the leading edge becomes unstable in the presence of a sharp trailing edge corner.

2.3.3 Effect of angle of attack

If the simulation is an attempt to model the flows about rectangular structures exposed to a true engineering environment then we would not expect the flow always to be aligned normal to the structure in question. Changing the angle of incidence is similar to changing the afterbody shape. The interaction between the separating shear layers may be delayed as the cross-stream dimension is increased and a reattachment bubble may

form on the windward edge with secondary separation from the trailing corner. It is thus important to identify how the incidence effects the vortex formation and induced forces.

Kniseley (1990) reviewed the findings on Strouhal numbers of rectangular cylinders at incidence and performed some experiments of his own on cylinders with B/A ranging from 0.04 to 2.0 and with angles of attack from 0 to 90 degrees. A series of water tank and wind tunnel studies were conducted and Figure 2.16 shows Kniseley's findings for Strouhal number, drag and lift. The Reynolds number varies with angle of attack and from cylinder to cylinder between 0.46×10^4 and 3.10×10^4, since it is defined according to the maximum cross-stream dimension. Three side ratios are shown, B/A=0.25, 0.5 and 1.0 but since the angle of attack is extended to 90 degrees in the two former cases these can also represent B/A=4.0 and 2.0 with the angle of incidence reversed. In each case the initial increase in angle of attack is associated with a sharp increase in Strouhal number and significant decrease in drag and lift coefficient. At some angle of incidence (approximately 13° for B/A=1.0 and approximately 20° for B/A=0.25 and B/A=0.5) the Strouhal numbers level off for each side ratio at around St=0.18-0.19. The lift coefficient continues to decrease, but at a lower rate, for B/A=0.25, increases a little before levelling off in the B/A=0.5 case and increases rapidly to C_L=0 in the range $30°\leq\alpha\leq45°$ for the square cylinder. Since the B/A=1.0 cylinder is symmetric at α=45° we expect the lift coefficient to be zero at this incidence but it is perhaps surprising that the lift remains near zero over such a range of angles. This can however be explained by consideration of the difference in the afterbody shape between α=0° and α=45°. At α=0° only a small change in the angle of attack is required before the afterbody will start to interact with the separated shear layer. In contrast at α=45° a larger change is necessary. It can also be noted that at high incidence in the B/A=0.5 case which is equivalent to low incidence for B/A=2.0 there is a dual shedding frequency which is due to intermittent reattachment as described earlier.

Zaki *et al* (1994) conducted some numerical and laboratory experiments on square cylinders over a range of Reynolds numbers and angles of attack. The numerical results are fairly limited and deal only with the Strouhal number of a square cylinder up to Re=250. The laboratory experiments were conducted in a gravity-fed water-tunnel and the experimental set-up allowed a low level (0.2%) of freestream turbulence to be maintained. Velocity measurements in the wake were made by hot-film anemometry and hence the Strouhal frequencies could be extracted. Figure 2.17 outlines the different flow patterns expected around a square cylinder as the angle of attack is varied. According to Zaki the flow becomes attached along one side close to $\alpha\approx10°$. The separation bubble then shrinks with increasing incidence. Zaki's results for three different Reynolds numbers (Re=1790, 2450 and 6140) are given in Figure 2.18. A similar trend to Kniseley's (1990) results for the square cylinder is observed with an initial increase in St followed by a shallower decrease and then a levelling off of St. The magnitude of the Strouhal number is somewhat different and this is caused in part because Kniseley's Strouhal number is based on the maximum cross-stream dimension. But at lower Re Zaki's experimental results are questionable. A comparison with Figure 2.12(a) raises serious doubt as to how Zaki's measurements could have generated such low St values. $St\approx0.12$ is the lowest value generally observed in this Re range. Zaki himself makes no comment on this large discrepancy in results but there must be some reason for the low values of St.

An explanation might perhaps be derived from the model aspect ratio, end effects, or the experimental (measurement) technique itself since a gravity-fed water tank is not commonly used.

An experimental study was undertaken by Norberg (1993) with B/A=1.0, 1.62, 2.5 and 3.0. Measurements were carried out in a wind tunnel with free-stream turbulence less than 0.06% over $5\times10^3 \leq Re \leq 1.3\times10^4$. The Strouhal frequency, lift and drag were shown to vary with angle of attack in a similar manner to that described previously in the analysis of Kniseley's results.

A recent series of numerical simulations has been made by Sohankar *et al* (1996) for low Reynolds number laminar flows. They implemented a DNS code to model the flow and the variation of the main parameters is given in Figure 2.19. Some fundamental differences can be detected between these results and those found at higher *Re* described above. At low angles of incidence the Strouhal number behaves in a similar manner to that observed at higher Reynolds number. *St* rises sharply until the reattachment point and then falls rapidly. In the studies at higher *Re* there was a plateau for middle incidences, $20° < \alpha < 70°$, where the Strouhal number changed little but here the Strouhal frequency begins to rise again after an initial drop. The reasons for such contrasting behaviour remain unclear although one should not expect a change in the incidence angle to affect the flow characteristics in a similar manner at different Reynolds numbers.

2.3.4 Free-stream turbulence

Real atmospheric flows past buildings, bridges and other external structures will not have a fully uniform upstream flowfield. The upstream flow will contain a certain amount of free-stream turbulence and this approaching turbulence can have a direct effect on the flow past bluff obstacles. Classically it is known that for flows past smooth bodies, such as circular cylinders and spheres, the effects of upstream turbulence are to cause an early onset of the boundary layer transition to turbulence. This delays separation and decreases the wake width; hence base pressure increases and drag falls. This arrangement is more complex for flows past blunt obstacles and the type of turbulence as well as the bluff geometry will have a direct bearing on how the flow is affected. Free-stream turbulence is normally characterised by two parameters, an integral length scale, L_X, and an intensity u'/U_0 where u' is the root mean square (rms) value of the free-stream velocity fluctuations. Although no study of the effects of upstream turbulence is to be made in this report it is interesting to note the dependency of certain flow features in particular with regards to turbulence length scale. Instabilities which develop in the bluff body wake with increasing *Re* are known to be of different scale and may have similar effects on the flow as those due to upstream turbulence.

Gartshore (1984) studied the effect of upstream turbulence on fluctuating lift and base pressure values of rectangular cylinders. It had been thought at the time that turbulence scale was rather unimportant and that only the turbulence intensity was contributory to altering the flow. The results showed that small intensity turbulence could increase the loadings for rectangles with B/A<0.6, i.e. side ratio below the critical geometry, but decreased the loadings on longer rectangles. As the turbulence intensity is increased a threshold is reached

beyond which the aerodynamic forces no longer decrease for longer rectangles but for shorter rectangles the forces start to decrease back towards the zero turbulence value. The author points out the need for further studies to identify the effects of turbulence scale on the flow and, in a similar paper, Nakamura and Ohya (1984) have tackled this issue. They have performed detailed experiments on the effects of both scale and intensity but perhaps the easiest way in which to visualise the results is to see their plot of base pressure vs. side ratio, Figure 2.20. In smooth flow there is a drag peak at around B/A=0.62 but this peak and its intensity are decreased in small scale turbulence. It would be most useful to extend this graph to a series of curves so that we can identify further the effects of scale. It should be noted that, as has already been described, other factors such as Reynolds number, tunnel blockage and cylinder aspect ratio can affect the flow. Hence care must be taken when comparing different studies since they may represent quite different problems and this can often be the reason why different authors present contradictory results. The results are summarised between small scale and large scale effects. Small-scale turbulence leads to enhanced roll-up and stronger vortex shedding for short cylinders, but for longer cylinders the trailing edge interaction with the shear layer is enhanced, which results in weaker vortex shedding and hence higher base pressure. Large-scale turbulence weakens the vortex shedding behind cylinders of any dimension as it reduces the spanwise correlation; i.e. the fluid is freed to move along the span of the bluff obstacle and hence base pressure rises.

In a more recent paper Nakamura (1993) has reviewed the main findings of freestream turbulence effects on bluff body flows. Figure 2.21 shows how turbulence scale has a different effect according to side ratio. On the right hand side of the figure the limiting values in smooth (low turbulence) flow are shown. The author describes the general bluff body flow as being composed of 'two basic flow modules'. Firstly the boundary layer separation and reattachment and secondly the Karman street formation. Reattachment will not occur for short bodies but there can still be interaction between the trailing edge geometry and the separating shear layer. Two length scales are proposed as being most relevant to the flow, the thickness of the separated shear layer and the distance between the shear layers or body size, although this author would consider the wake size as a more appropriate scale since the previous two in no way account for the afterbody geometry. Nakamura states that if one of the basic flow modules is affected by some upstream disturbance then the bluff body flow may be significantly altered. For rectangular cylinders the findings are identical to the previous paper but Nakamura has described small scale turbulence as being of the scale of the shear layer and large scale as the scale of the body width. This is a difficult conclusion to draw from the graphs presented by Nakamura. Certainly the base pressure appears to be maximal when $L_X/A \approx 2.0\text{-}3.0$ for all cylinders and a minimum is attained at $L_X/A \approx 0.5$ for the B/A=0.4 cylinder, but these do not really tie in with a shear layer scale of 0.1 and a body scale of 1.0. It would, therefore, seem that some other scales might be more appropriate.

Wolochuk *et al* (1994, 1996) discuss the effects of turbulence in a study to test how the accuracy of vortex-shedding flowmeters might be effected. For an accurate flowmeter the Strouhal number must remain constant over a range of Reynolds number and must give a good signal-to-noise ratio such that the reading is strong. Their work was concerned with looking at the Strouhal number dependency rather than lift and drag as in

previous research. Figure 2.22 shows that a 15% decrease in Strouhal number was achieved for a 2.5% level of turbulence intensity (Tu) but then the Strouhal number gradually rose again as Tu was increased further. The authors were unable to create Tu<2.5% in their tunnel so it remains unclear as to whether the Strouhal number suddenly drops or gradually drops to some minimum value with Tu<2.5%. The turbulence length scale had a more consistent effect, Figure 2.23. As the length scale was increased from 0.25 the Strouhal number dropped by as much as 25% at L_x/A=3.0 before rising again at larger length scales. This is consistent with the results of Nakamura who also found maximum disturbance to the flow at around L_x/A=3.0. Although a mixture of triangular and rectangular geometries were used it is not thought that this would greatly affect the trend of the results. The variation with Reynolds number was also examined as the flowmeter must remain accurate over a wide range. The Strouhal number remains roughly constant with Reynolds number for each turbulence length scale chosen. This contrasts with the work of Norberg (1986) who did similar studies on the flows past circular cylinders and found quite a variation in Reynolds number, probably because, as described earlier, for separation from a smooth surface the separation point can move and thus an early onset of turbulent transition in the boundary layer and wake weakens the vortex shedding and the loadings fall. In conclusion for a vortex-shedding flowmeter to be adapted for use in unsteady flows the flowmeter would need to be calibrated under turbulent conditions and the length scale of turbulence should be maintained at a constant value. The integral length scale could be controlled upstream of the bluff obstacle by some kind of mesh or shroud, generating the required turbulence. Alternatively the obstacle could be scaled much smaller than the length of the turbulence present in the application.

2.4 Oscillatory flows

The problems associated with flow-induced vibration and other oscillatory flow phenomena represent an area of major interest within engineering. It is thus not surprising that a large body of literature exists in this field. Reviews of oscillatory flow topics can be found in Sarpkaya (1979a) and Bearman (1984). Research has concentrated mainly on oscillatory flow past circular cylinders, an area which has been briefly reviewed by Griffin and Hall (1995), and on cross-flow oscillations. Recently however more attention has been focused on in-line oscillations and other body geometries. The following review will deal with research carried out since Bearman's (1984) review in which various problems were identified as requiring further research and clarification. These include the phase mechanism between the induced forces and the oscillatory component and the role of the afterbody shape.

2.4.1 Introduction and definitions

The addition of an oscillatory flow component to the flow past a bluff body can have dramatic consequences. Offshore structures are subject to the imposed oscillatory conditions of the wave and tidal motion. It is thus important that these structures are designed such that their natural frequencies lie outside the range of any wave

frequencies. A recent application in this area is discussed by Borthwick and Herbert (1990) who have studied the wave response of offshore structures susceptible to damage and failure from resonant vibrations.

Similarly buildings and bridges may be subject to large wind imposed forces. If these forces are large enough a structural oscillation may be induced. Bluff aircraft components attached to the fuselage will also generate periodic turbulence. When the natural vibration frequency of these components is similar undesirable oscillations may be induced which can lead to structural fatigue. A further area of importance is that of vortex shedding flowmeters which are susceptible to upstream disturbances. These instruments are based on bluff obstacles which generate periodic vortex shedding. By detecting the shedding frequency the flowrate can be deduced. However if the upstream disturbances are sufficiently intense and periodic they may alter the shedding frequency and hence the accuracy of the flowmeter.

The addition of an upstream oscillatory flow component will be considered in these studies. The uniform component of the upstream velocity is U_0 and the amplitude of the oscillatory component is U_A. Thus an in-line oscillation is expressed as

$$\boldsymbol{u} = (U_0 + U_A \sin 2\pi f_e t)\hat{\boldsymbol{e}}_x, \tag{2.12a}$$

and a cross-flow oscillation as

$$\boldsymbol{u} = U_0\hat{\boldsymbol{e}}_x + U_A \sin 2\pi f_e t\hat{\boldsymbol{e}}_y, \tag{2.12b}$$

where f_e is the forcing frequency of the imposed oscillation, and $\hat{\boldsymbol{e}}_x$ and $\hat{\boldsymbol{e}}_y$ represent the unit vectors in the x and y directions respectively. A cylinder displacement amplitude y_e or x_e defined by

$$y_e \text{ or } x_e = \frac{U_A}{2\pi f_e} \tag{2.13}$$

is more commonly used than a flow oscillatory amplitude since most studies of this nature are primarily related to flow-induced structural vibration problems. y_e is used to define cross-stream cylinder displacement and x_e to define in-line cylinder displacement.

As will be described later in this section and in Chapter 6, for a range of oscillation frequencies and oscillatory amplitudes resonance or 'lock-in' is expected for both these oscillatory motions. The 'lock-in' regime is defined as the range of oscillatory frequencies and amplitudes for which the vortex shedding frequency f_s is directly controlled by the forcing frequency f_e. Broadly speaking in the case of cross-flow oscillations we expect 'lock-in' to occur for values of f_e close to the natural shedding frequency f_0, while for in-line oscillations 'lock-in' is expected when f_e is roughly double f_0. Figures 2.24 and 2.25 illustrate the difference between the 'lock-in' ranges

typically observed for both kinds of oscillation. Figure 2.24 is a reproduction of a plot by Griffin and Hall (1995) of the 'lock-in' boundaries found for cross-flow oscillations over a range of Reynolds numbers. 'Lock-in' is found to occur for $0.55<f_e/f_0<1.25$ provided the oscillation amplitude is sufficient, but the 'lock-in' range is self-limiting in magnitude; i.e. an upper boundary for 'lock-in' is also shown. It should also be noted that 'lock-in' occurs predominantly at frequencies less than the Strouhal frequency, $f_e/f_0<1.0$. Barbi *et al* (1986) have accumulated the results from several studies and have plotted the 'lock-in' range for in-line oscillations past circular cylinders. In this instance 'lock-in' occurs over a wide range, $1.2<f_e/f_0<2.6$, again provided the amplitude of oscillation exceeds a critical value. It is clear from these figures that resonant modes can be sustained over a wide range of Reynolds number and forcing frequency. Even outside the ranges of synchronisation however the oscillatory effects may still be capable of influencing the flow.

Under uniform flow conditions a pair of oppositely-signed vortices (positive vorticity being defined in an anticlockwise sense) are shed into the wake during each period of vortex shedding. As these vortices are shed asymmetrically and are of equal magnitude they exert an oscillatory lift force on the cylinder with a zero mean value. The difference between the 'lock-in' of in-line and cross-flow oscillations can be explained by considering how the flow velocity varies with time in each case. When the oscillatory component of velocity is normal to the stream, it is consistent that inside the 'lock-in' regime a pair of vortices can be shed into the wake with the same frequency as the forcing frequency and that these vortices will be of equal magnitude and oppositely signed as before. This may occur since the magnitude of the normal flow component oscillates at double the oscillatory frequency.

For an in-line oscillation however the magnitude of the streamwise velocity oscillates with the same frequency as the imposed oscillation. This means that if 'lock-in' were to occur at $f_s=f_e$ for an in-line oscillation then the vortex shedding would have to be symmetric to ensure a mean lift force of zero. Alternatively asymmetric 'lock-in' can occur at $f_s=0.5f_e$ such that vortices of equal magnitude are shed into the wake. This explained in more detail in Chapter 6 (section 6.8).

2.4.2 Cross-stream oscillations

A bluff obstacle exposed to an oncoming stream is subject to vortex shedding and an oscillatory force is induced normal to the free stream. The body may start to vibrate periodically and furthermore these vibrations may interact with the Karman vortex street. If resonance occurs between the structure and the vortex shedding the forces will be further increased. It is thus important to be able to model this scenario. In the laboratory cylinders are forced to vibrate with different frequencies and in computer simulations this is represented by the addition of an oscillatory component to the freestream fluid.

A comprehensive laboratory study of the flow structure from an oscillating cylinder is documented in two parts by Ongoren and Rockwell (1988a and 1988b). Cylinders of circular, square and triangular cross-section were forced to vibrate in directions normal and transverse to the oncoming stream at Reynolds numbers between 584

and 1300. A sudden change in the near-wake dynamics was known to occur as the forcing frequency increased across the synchronisation range. Their study was therefore motivated by a desire to understand this phenomenon and how the vortex formation length is effected.

Figure 2.26, which shows oscillatory flow past a circular cylinder, illustrates this phenomenon quite clearly. Each picture is taken at the same phase angle, the moment of maximum negative displacement of the cylinder. As f_e/f_0 is increased from 0.85 to 1.0 the vortex formation length shortens but the phase of the formation position is maintained. A shortening of the formation length would normally indicate an increased drag but this was not measured. At f_e/f_0=1.05 there is an indication that the vortex shedding is switching to the upper surface and by f_e/f_0=1.17 this phase switch is completed. It is also apparent that the wake is straight after the phase switch and no longer appears at an angle of inclination to the base region. This suggests that the lift oscillations may have a lower amplitude after the phase shift. Ongoren and Rockwell showed a similar phase shift through the synchronisation range for a triangular cylinder although the switch takes place in the opposite sense to the phase switch outlined for the circular cylinder. For the triangular cylinder there was no change in the wake inclination angle since the separation points are fixed on a blunt obstacle. In Figure 2.27 the flow past a square cross-sectioned cylinder is shown. An examination reveals that there is no phase switching for this body geometry but there is a substantial shortening of the vortex formation length and the optimum vortex street definition occurs at f_e/f_0=1.35 and not for values closer to f_e/f_0=1.0 as might be expected.

Williamson and Roshko (1988) conducted a series of experiments in a towing tank with $300<Re<1000$. Figure 2.28, reproduced from their study, details the synchronisation patterns found near the fundamental 'lock-in' region. Three different patterns emerge. Mode ***2S***, found in the fundamental 'lock-in' range where the familiar Karman vortex street is observed, mode ***2P***, in which two pairs of oppositely-signed vortices are shed into the wake in each cycle, and an asymmetric mode ***P+S*** in which a single vortex is shed from one side of the cylinder and a pair from the other side in each cycle. The authors report that for $Re<300$ the ***2P*** pattern is replaced by ***P+S*** mode shedding. Two curves are seen, labelled I and II, which represent discontinuities in the phase of the lift force on the body. II is for increasing frequency and I for decreasing frequency. This shows that there is a hysteretic phenomenon occurring here. The phase shift was found to link in with the switch in shedding mode.

An encouraging numerical study of the high Reynolds number turbulent flow past a square cylinder forced to oscillate normal to the freestream is presented by Launder and Kato (1993). They used a k-ε model to simulate turbulence effects. Their preliminary results are encouraging in that they predict the phase switch across the 'lock-in' range (Figure 2.29(a)) and show the lift to be greater within this regime (Figure 2.29(b)). However few quantitative results are presented and the lift time histories shown in their paper appear far too regular for a turbulent flow. One would expect that the turbulent wake which develops downstream would manifest itself as noise in the drag and lift time histories.

Low Reynolds number computations have been performed by Okajima and Kitajima (1993). Their initial numerical study consists of a two-dimensional direct numerical simulation of the oscillatory flow past circular and rectangular cylinders at $Re=10^3$, with the oscillatory amplitude set at 14% of the body diameter. The results are graphed in Figures 2.30. The Strouhal numbers under uniform flow conditions are not given but there is a definite 'lock-in' range for the circular cylinder, $0.2< St_e <0.25$. For the rectangular cylinders however the flow remains locked-in once the frequency is greater than some lower limit. These limiting values are St_e =0.06, St_e =0.07 and St_e =0.1 for cylinders with B/A=1.0, B/A=2.0 and B/A=3.0 respectively. It is peculiar that no upper limit on the frequency for resonance of the rectangular cylinders was found in this study. For the circular cylinder the lift force is higher within the synchronised regime but for the rectangular cylinders the lift force initially rises as the 'lock-in' region is first entered but then falls before rising sharply throughout the rest of the calculations made.

In a continuation of the above study Okajima (1995) has extended the computations to three dimensions since 3-D instabilities are known to develop beyond the laminar shedding regime. He also presented some experimental results for cross-flow oscillations past square cylinders at Re=1000. Figure 2.31 presents results from the 2-D, 3-D and experimental simulations. Only a few 3-D cases were considered since the code is computationally expensive. The experimental results verify the existence of a large 'lock-in' boundary and show that the 2-D simulation predicts 'lock-in' for smaller frequencies than expected. This is improved by the 3-D simulation although the calculated lift forces are still far higher than the experimental results. The agreement of both simulations is better within the 'lock-in' regime and this is probably because the flow tends to exhibit more two-dimensional behaviour under resonance.

Meneghini and Bearman (1993) have simulated the cross-flow oscillations past circular cylinders at low Reynolds number, Re=200, by a hybrid discrete vortex method. Their 'lock-in' chart is shown in Figure 2.32 and indicates a 'lock-in' range of $0.75<f_e/f_0<1.05$ provided the amplitude of oscillation is sufficient. More significantly they were able to predict the $P+S$ shedding mode visualised in Figure 2.33, previously described by Williamson and Roshko (1988), under high amplitude oscillatory motion. The nature of the vortex method is such that graphical output of the wake structure can be readily obtained in the simulation, an advantage which highlights its potential to examine the wake structures of other geometries.

A direct numerical simulation of 2-D laminar flows, Re=200, past transversely oscillating cylinders is described by Copeland and Cheng (1995). Figures 2.34(a) and (b) show how lift and drag vary as the frequency changes throughout the synchronisation regime. The oscillation amplitude is fixed at 10% of the cylinder diameter and resonance occurs for $0.7<f_e/f_0<1.1$ which is a larger range than observed by Meneghini and Bearman who found resonance over the range $0.9<f_e/f_0<1.05$ at the same amplitude. Near f_e/f_0=1.0 there are seen to be two solutions for the lift and drag. These two solutions correspond to two slightly different modes of shedding [see Figures 2.34(c) and (d)] although both would be categorised as $2S$ modes since two oppositely signed vortices are shed in each cycle. The phenomenon is hysteretic since as the frequency is gradually increased the force curves follow

the upper segment associated with type (i) shedding before jumping down to the lower curve associated with type (ii) shedding but if the frequency is then gradually decreased the lower curve is followed and type (ii) shedding can be maintained down to a lower frequency. This hysteresis effect is known as a saddle node bifurcation.

2.4.3 In-line oscillations

Structural oscillatory motions induced in line with the free stream are not as common as cross stream oscillations. This is essentially because the oscillatory component of the forces induced by vortex shedding is considerably greater in the cross-stream direction. Hence studies of in-line oscillatory nature are more important in the context of an imposed upstream unsteadiness to the flow.

The results from a number of laboratory based studies for the in-line pulsating flow past circular cylinders have been plotted by Barbi *et al*, (1986), see Figure 2.25. The plot demonstrates that, provided a sufficient amplitude of oscillation is surpassed, 'lock-in' can be induced over a frequency range $1.2<f_e/f_0<2.6$ for in-line oscillations. However Barbi has found evidence for 'lock-in' at Re=40000 with f_e/f_0=1.0 provided $x_e/D>0.4$ and this is attributed to a higher Reynolds number increasing the size of the 'lock-in' boundary.

In a continuation of their cross-flow oscillation study Ongoren and Rockwell (1988b) have analysed the mode competition which can occur between antisymmetric and symmetric shedding modes in pulsating flows. A circular cylinder was subjected to forced oscillations at an angle α with respect to the free stream. When α=0° the oscillations are in-line. The flow is synchronised into antisymmetric shedding for $f_e/f_0\approx2.0$ and to a symmetric shedding pattern for $f_e/f_0\approx3.0$. Outside these synchronisation regimes there was found to exist competition between the two modes. Figure 2.36 demonstrates how the mode competition varies across the range of forcing frequencies examined. N_A and N_S are the numbers of antisymmetrical and symmetrical shedding cycles measured over a long period such that when the ratio $N_A/(N_A+N_S)$=1.0 shedding is purely antisymmetric and when the ratio equates to zero the shedding is of symmetric type. For pulsations at α=0° one may observe that antisymmetric synchronised shedding dominates at f_e/f_0=2.0 but for greater values the shedding mode becomes predominantly symmetric and is fully synchronised at f_e/f_0=3.0. For $f_e/f_0\approx1.0$ there is intermittency between the two. The competition between these two modes is further highlighted by examination of Figure 2.35 which shows flow visualisation of the different modes at various forcing frequencies. At f_e/f_0=3.0 only the symmetric mode is found. It would certainly be interesting to compare this mode competition with results from obstacles of differing geometry and perhaps identify how afterbody geometry and obstacles with fixed separation points may alter the mode competition or perhaps suppress it completely.

An experimental study of the effects of in-line, periodic flow oscillations on vortex shedding from sharp-edged bodies has been made by Al-Asmi and Castro (1992). Their work was primarily concerned with how the 'lock-in' range was dependant on body geometry and in particular those geometries which are frequently used in vortex shedding flowmeters. A good vortex flowmeter should generate strong periodic vortex shedding over as wide a

flowrate as possible and it is important that Reynolds number effects are minimised by keeping the separation points fixed i.e. choosing a sharp-edged obstacle. Thus the afterbody geometry is perhaps the most important single factor affecting performance. Five geometries were studied systematically over a range of forcing frequencies and amplitudes. Figure 2.37 shows the minimum displacement amplitude required to induce 'lock-in' as a function of forcing frequency. At x_e/d=0.05 the triangular and T-shaped obstacles exhibited 'lock-in' over $1.5<f_e/f_0<2.1$, compared with $1.9<f_e/f_0<2.3$ for the rectangular cylinder; the flat plate had an even smaller range of $1.9<f_e/f_0<2.05$. At higher displacement amplitudes the range of 'lock-in' increases and for the flat plate and T-shaped bodies a symmetrical shedding mode could be induced when $x_e/d>0.07$. This was observed by a paraffin smoke visualisation technique. However this mode always appeared in competition with the antisymmetric mode. The greater susceptibility to resonance of the triangular and T-shaped geometries is perhaps surprising since vortex flowmeters commonly employ these shapes as they produce strong and regular shedding under uniform conditions. Some further investigations were made showing that an increased blockage ratio tended to widen the size of the 'lock-in' boundaries.

The numerical study of Okajima and Kitajima (1993) described earlier also examined oscillations of an in-line nature at $Re=10^3$. Their results are plotted in Figure 2.38. In the circular cylinder case, 'lock-in' with f_e/f_s=2.0 is observed for $0.3<St_e<0.45$. A natural shedding frequency of f_0=0.227 is given by the authors and thus their 'lock-in' boundary corresponds to $1.3<f_e/f_0<2.0$. For the rectangular cylinders 'lock-in' of two distinct kinds is observed. In one f_e/f_s=2.0 and in the other f_e/f_s=1.0. The lift force is reduced for both types of resonance and is near zero over certain ranges for the B/A=2.0 and 3.0 cylinders which is indicative of symmetric shedding. There is even some indication that there may be symmetric shedding for the B/A=1.0 cylinder at high oscillatory frequencies, St_e >0.4. Although no experimental data exists against which to compare these results, Okajima (1995) showed for the cross-flow case that 2-D calculations do not agree well with experiment at $Re=10^3$ and it would be expected that a 3-D calculation would also be required to gain reasonable accuracy for in-line oscillations at this Reynolds number.

A more appropriate Reynolds number, Re=200, for 2-D calculations was chosen by Minewitsch *et al* (1994) in their study of square cylinders forced to oscillate in-line. Figure 2.39 reproduced from their paper shows that 'lock-in' was attainable over the range $1.6<f_e/f_0<2.4$ above a threshold oscillation amplitude. This is compared with the 'lock-in' boundary of Griffin and Ramberg (1976) for a circular cylinder. A strong similarity between the two boundaries is seen for $f_e/f_0<2.0$ but above 2.0 the circular cylinder appears more susceptible to 'lock-in'. Figure 2.40 gives a clear indication of how the 'lock-in' response varies for a series of fixed oscillatory amplitudes. The frequency range for synchronisation initially increases as the forcing amplitude increases. However the authors reported that there appears to exist an amplitude limit to 'lock-in', similar to that demonstrated in Figure 2.24 for cross-flow oscillations, above which there is competition between symmetric and antisymmetric modes. However the boundaries of this region remain undefined at present. Minewitsch *et al* suggested that symmetric shedding is induced where the minimum Reynolds number at the point of maximum negative displacement of the cylinder, can attain a value less than 50 since, under uniform flow conditions,

asymmetry only arises beyond this *Re*. If this could be verified then symmetric regimes would be expected for similar frequencies and amplitudes of other cylinders but analysis of Okajima and Kitajima's (1993) results for several different cylinders shows that the onset of symmetric modes is highly dependant on body geometry and was not observed at all for the circular cylinder. Another mechanism is more likely to be responsible. A possible suggestion is that the phase of shedding may change in a similar way to the phase change in cross-flow oscillations noted by Ongoren and Rockwell (1988a). Analysis of the vortex shedding process under in-line oscillatory flows may provide greater insight into the symmetric mode and how it relates to the phase change phenomenon.

Further works examine the effects of oscillating bluff obstacles at an angle of attack to the freestream. Xi-yun *et al* (1994) presented a numerical study closely associated with the work of Ongoren and Rockwell (1988b). Their direct numerical simulation modelled the flow past circular cylinders at $Re=10^3$. As already discussed this is perhaps a little high for 2-D DNS simulations but they did manage to obtain evidence of competition between symmetric and antisymmetric shedding modes at certain frequencies and amplitudes. Utsunomiya *et al* (1995) made an experimental study of the yaw angle effects on vortex-induced oscillations of rectangular cylinders. Most wind tunnel tests of bridge aerodynamics are carried out with the wind normal to the bridge since it is considered that this scenario should give the most stringent test of the bridge stability. However since the natural wind is not always aligned normal to the bridge it was felt necessary to perform some experiments with a yaw angle. The findings showed that a strong wind-induced response could still be maintained at a yaw angle as high as 70°.

2.5 Summary of geometrical and upstream effects in flows past rectangular cylinders

2.5.1 Afterbody length and Reynolds number

At high *Re* a critical side ratio, $B/A=0.62$, exists at which vortices form close behind the body and the base pressure is minimum (Figure 2.7). The shedding pattern is thought to be discontinuous (Figure 2.11) at slightly lower values of side ratio. It is not known how this critical side ratio depends on Reynolds number and in particular how the base pressure varies under laminar flow conditions. For bodies longer than $B/A=2.0$ there exists a critical Reynolds number for which the separating shear layer intermittently reattaches and this is associated with dual Strouhal frequencies (Figure 2.12). The square cylinder has too short an afterbody for reattachment at any *Re*.

2.5.2 Angle of attack

Varying the angle of attack acts in a similar manner to extending the afterbody. At small angles of attack, $\alpha<10°$, and for short bodies, $B/A<2.0$, the Strouhal number increases and both the lift and drag decrease. A

reattachment angle is reached, dependant on B/A, beyond which Strouhal number and drag coefficient remain fairly constant but lift begins to rise (Figure 2.16). In the laminar Re range recent calculations suggest a somewhat different variation (see Figure 2.19) but this remains to be clarified.

2.5.3 Freestream turbulence

Small scale turbulence decreases the base pressure of short rectangles, $B/A<0.5$, but increases the base pressure on longer rectangles, as shown on Figure 2.21, hence shifting the critical side ratio phenomenon. Large scale turbulence appears to increase the base pressure for all rectangles. The effects of turbulence intensity are not as dramatic although the Strouhal number drops by as much as 15% for low intensity turbulence before making a slight recovery at higher intensities (see Figure 2.22).

2.5.4 Cross-stream oscillations

Primary 'lock-in' is found near $f_c/f_0=1.0$ and for some geometries a phase shift in the vortex shedding has been found across the synchronisation range. At higher oscillation amplitudes new shedding modes, $\boldsymbol{P+S}$ or $\boldsymbol{2P}$, can be excited (see Figures 2.28 and 2.33). The induced forces are greater within the 'lock-in' range. 2-D simulations are unsuited to flows at $Re>10^3$, although they give better agreement within the 'lock-in' range since the flow exhibits greater 2-D behaviour under resonant conditions. The degree to which phase shift is discontinuous and the effect of cylinder base geometry on the near wake structure requires clarification.

2.5.5 In-line oscillations

Primary 'lock-in' occurs near $f_c/f_0=2.0$. Symmetric shedding modes are possible over certain ranges of frequency and amplitude. Outside the primary 'lock-in' range there is competition between the symmetric and antisymmetric shedding (see Figures 2.35 and 2.36). The effect of the afterbody on the appearance of these symmetric modes needs to be identified. There may also exist a similar phase switching as found for cross-flow oscillations.

2.6 Aims of the present study

Several key aims of the present study can now be identified. A numerical study of the flows about rectangles will be undertaken. The calculations will be two-dimensional and so the Reynolds number should be restricted to $Re<500$. For uniform flow conditions the effects of side ratio, angle of attack and, to a lesser extent, the Reynolds number on the flow characteristics and mean measured parameters should be investigated. In particular the side ratio for which a drag maximum is found should be determined and compared with the known high Reynolds number result. In-line oscillations will be simulated past a selection of cylinders. The variation of the lock-in characteristics with side ratio should be determined. The relationship between the phase of the lift and drag to the phase of the oscillatory flow component will also be investigated.

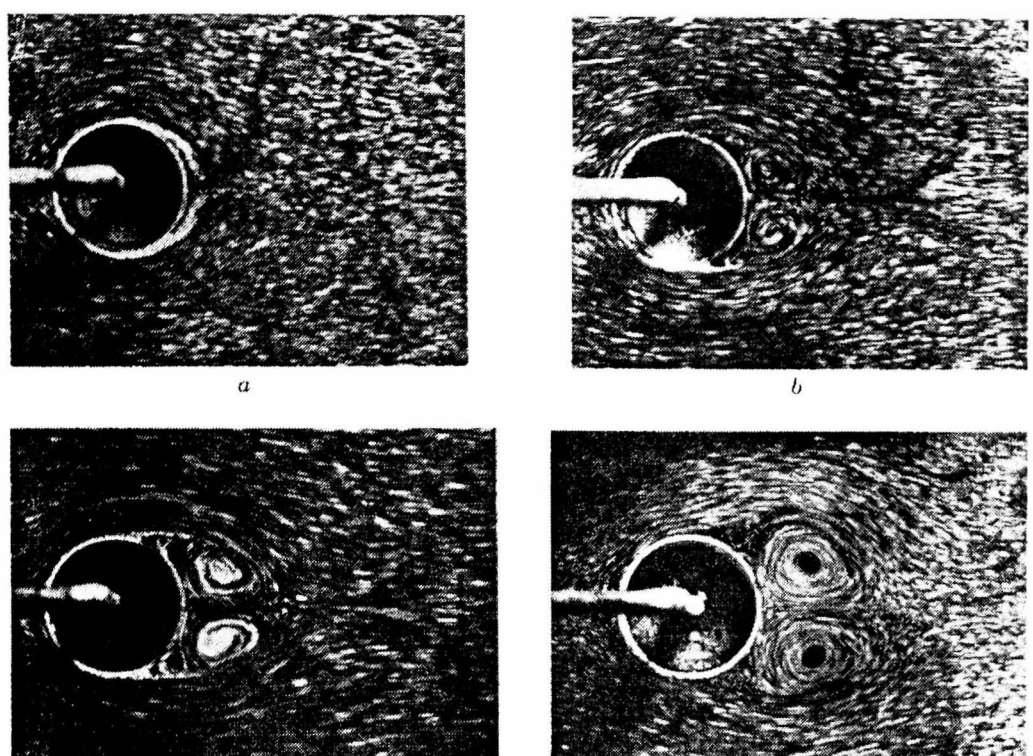

Figure 2.1 Growth of vortex pair after impulsive start of flow, from Goldstein (1965).

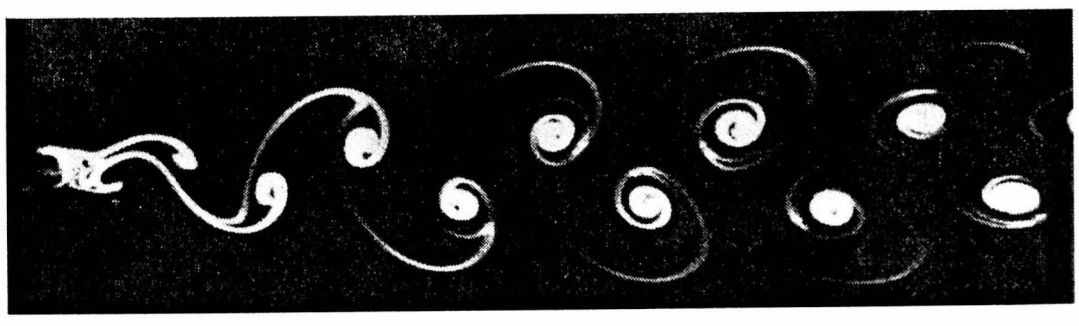

Figure 2.2 Flow visualisation of Karman vortex street behind a circular cylinder at Re=105, Van Dyke (1982).

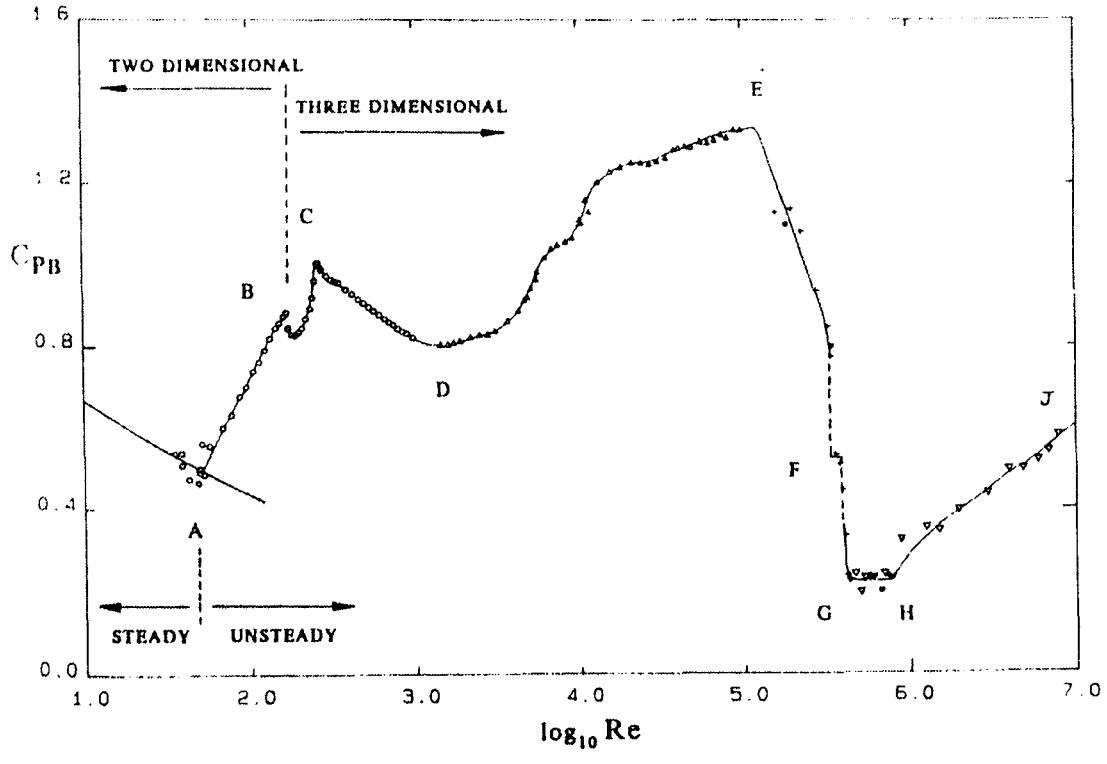

Figure 2.3 Effect of Reynolds number on base pressure coefficient for a circular cylinder, from Williamson (1996a).

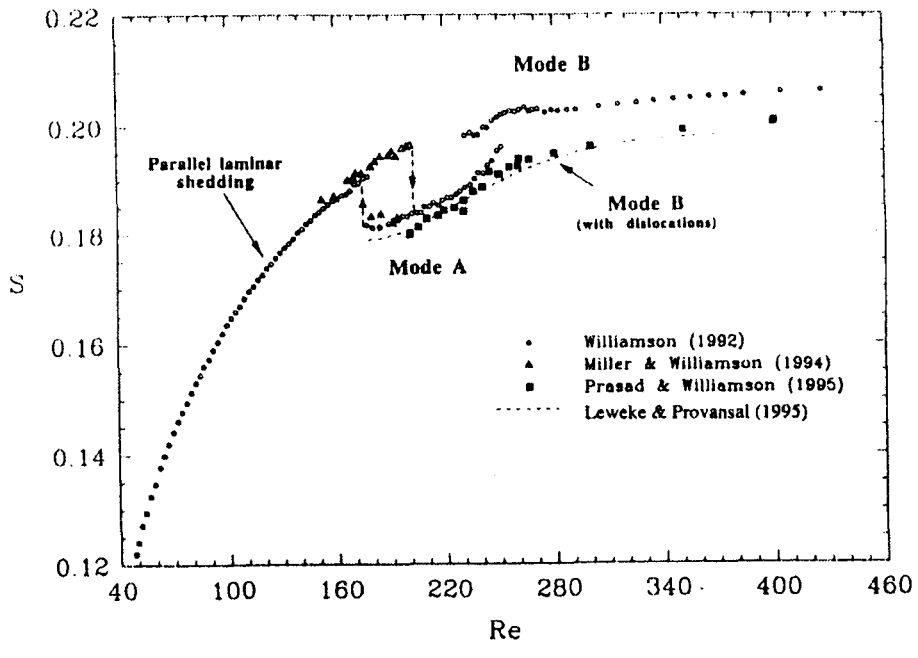

Figure 2.4 Effect of Reynolds number on Strouhal number for a circular cylinder, from Williamson (1996a).

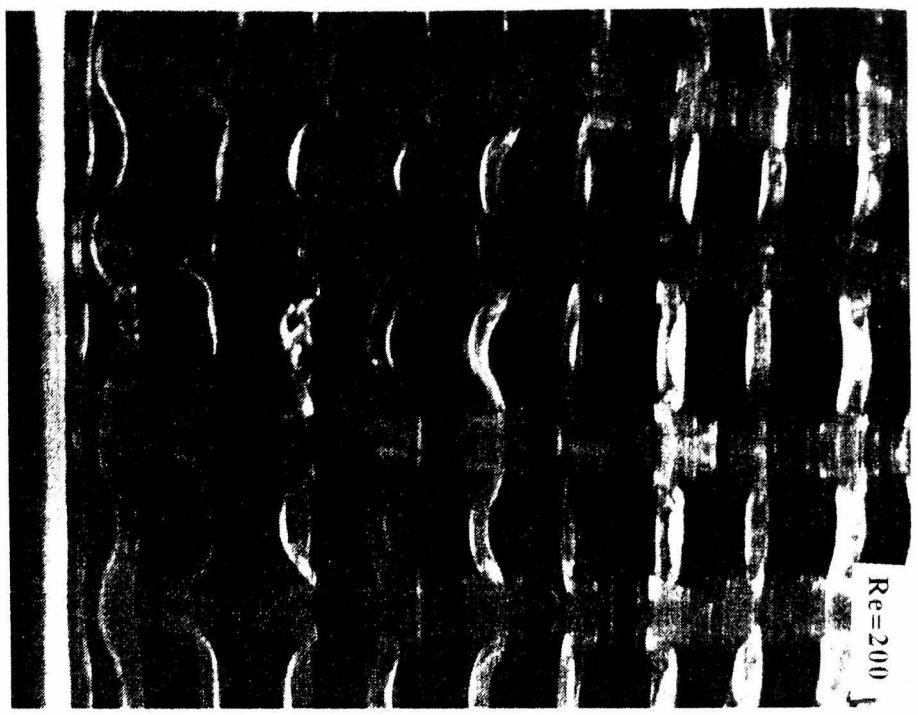

(a) Mode A instabilities, wavelength ≈ 4 body diameters.

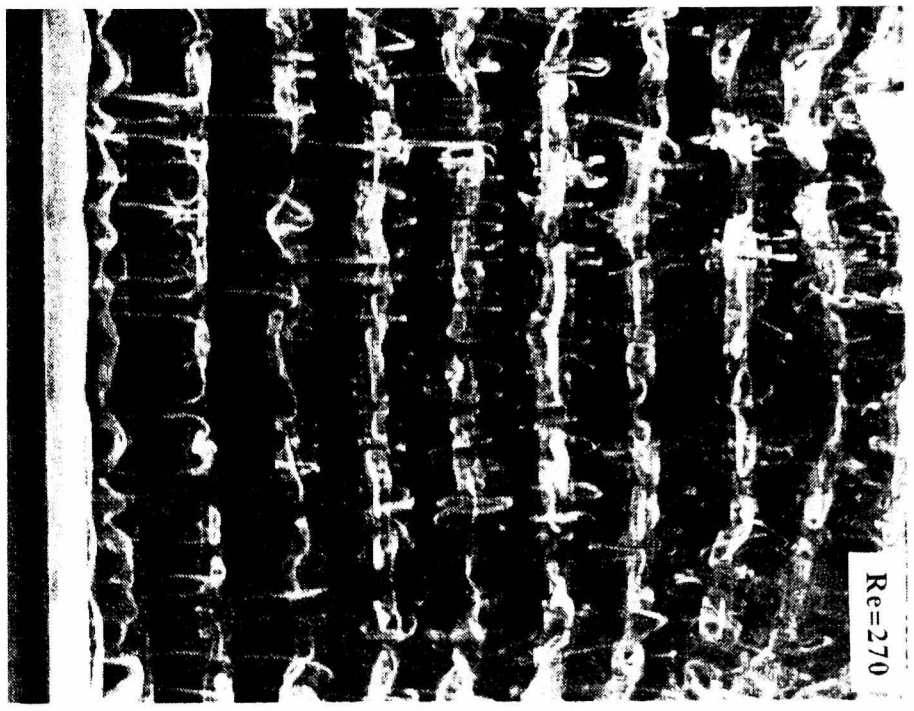

(b) Mode B instabilities, wavelength ≈ 1 body diameter.

Figure 2.5 Development of spanwise instabilities, from Williamson (1996b).

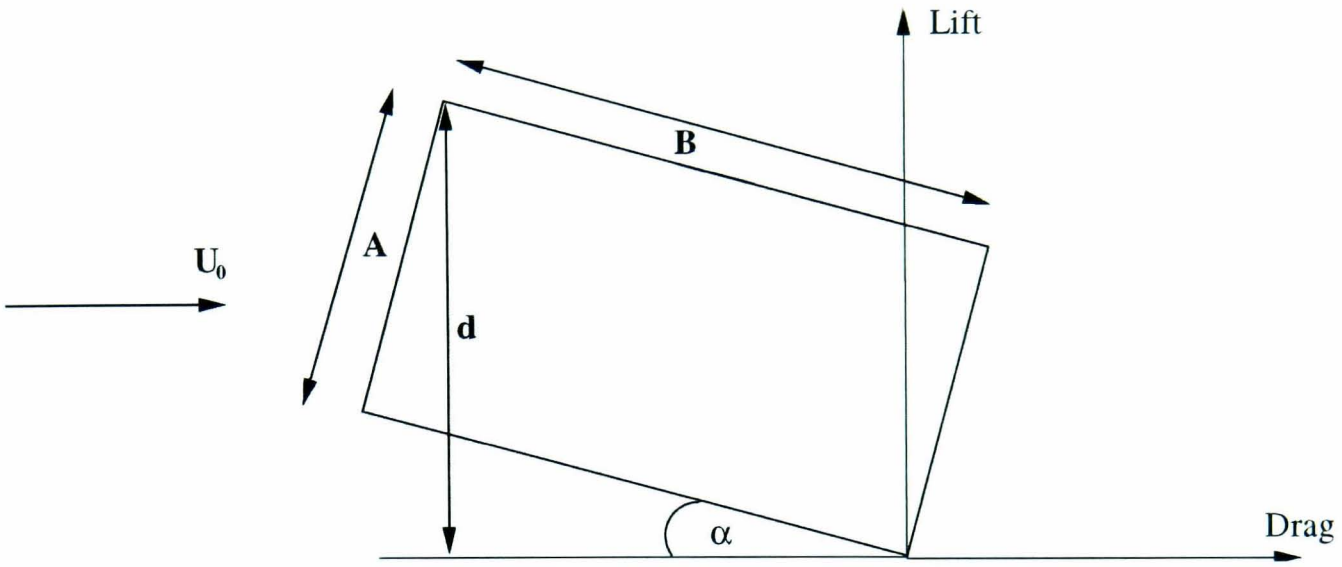

Figure 2.6 Generalised geometry for flow past rectangular cylinders

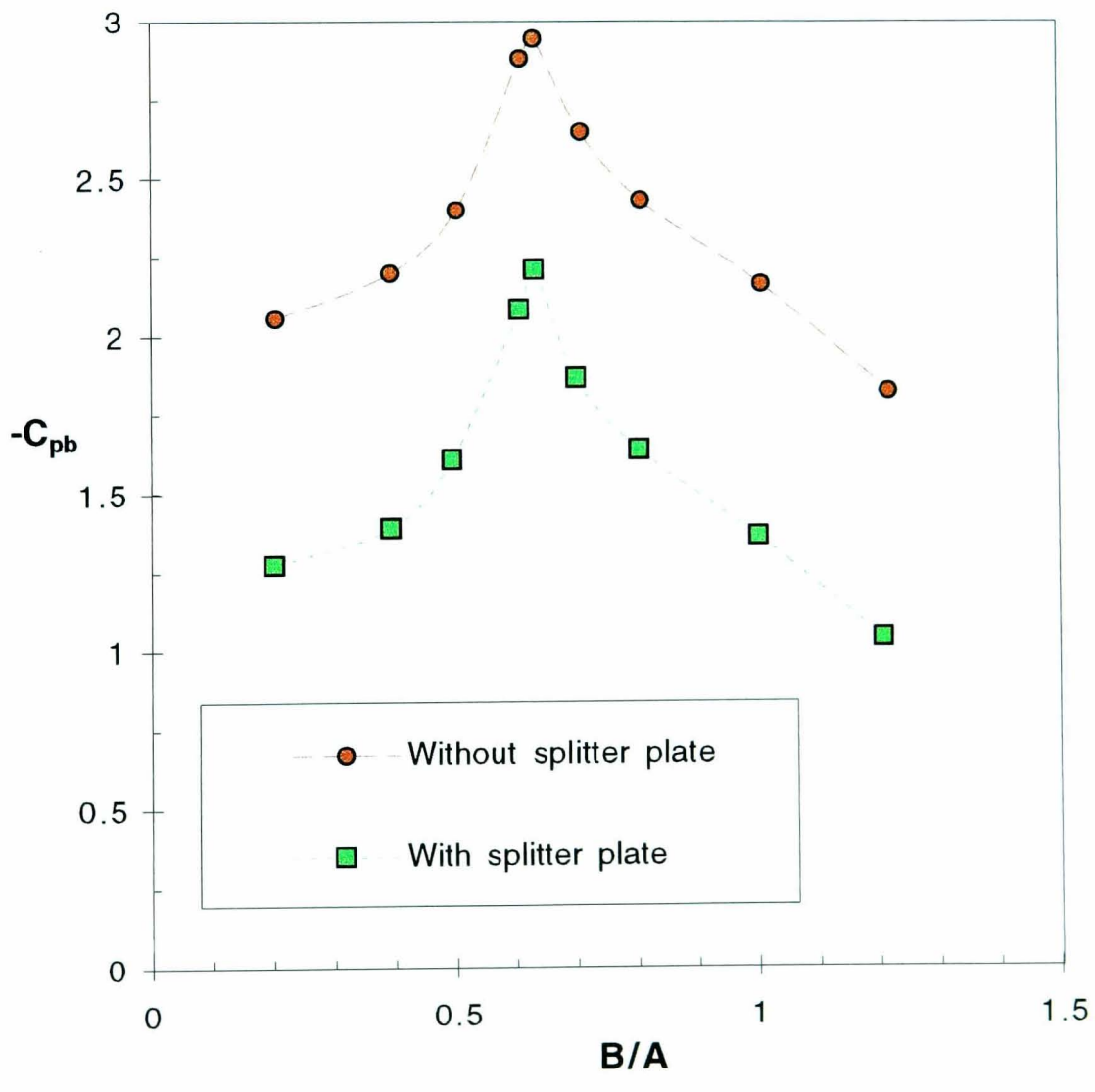

Figure 2.7 Base pressure coefficient vs. side ratio for rectangular cylinders (Re=2-7×10^4), from Bearman and Trueman (1972)

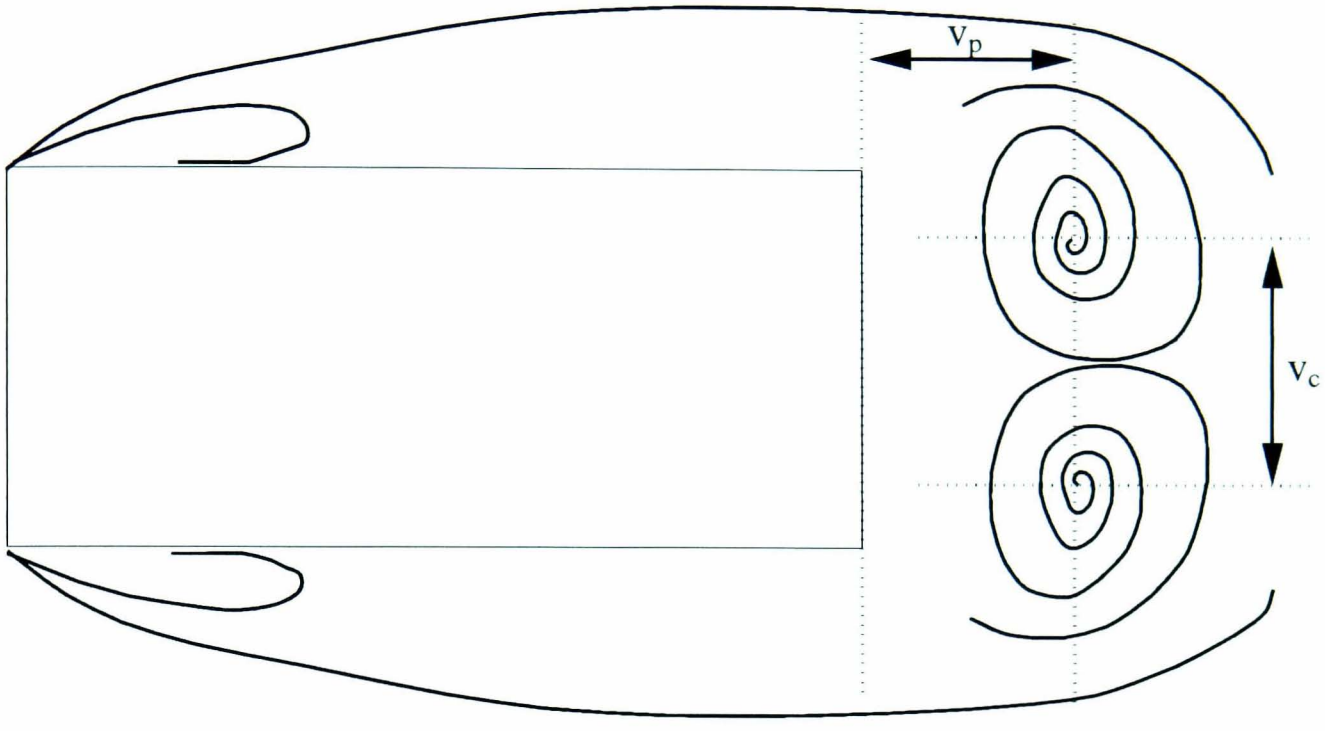

Figure 2.8 Schematic of time averaged flow pattern around rectangular cylinder

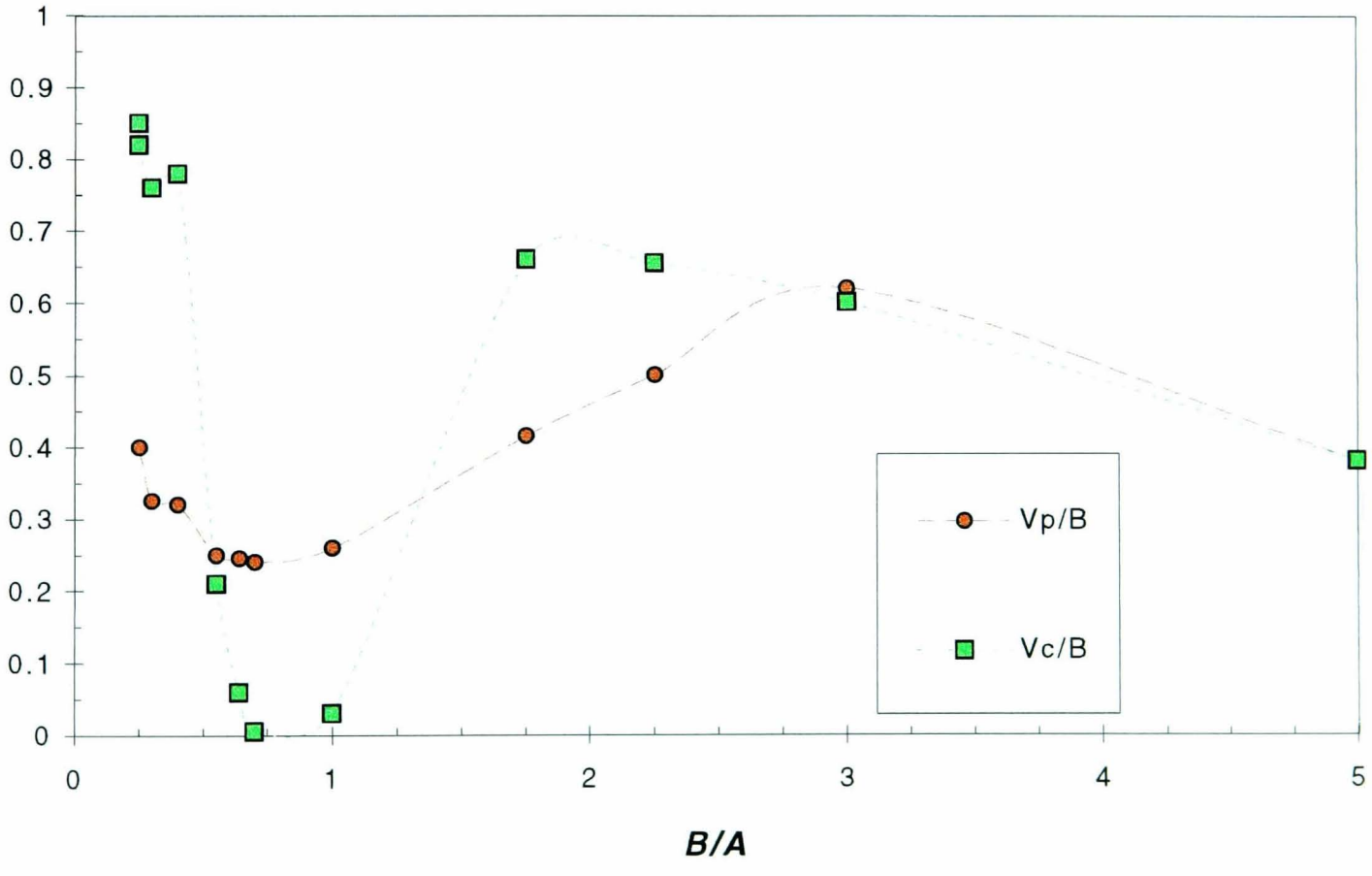

Figure 2.9 Variation of vortex formation positions with side ratio, from Laneville and Yong (1982)

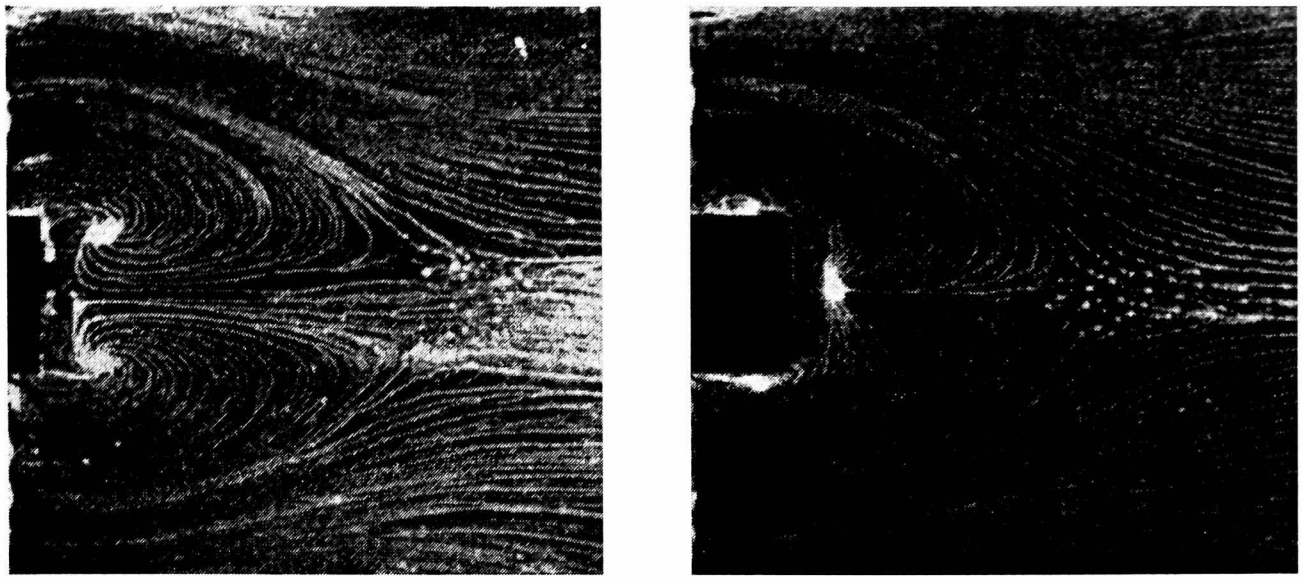

(a) B/A=0.25

(b) B/A=0.64

(c) B/A=1.75

Figure 2.10 Time-averaged flow visualisation behind rectangular cylinders, from Laneville and Yong (1982)

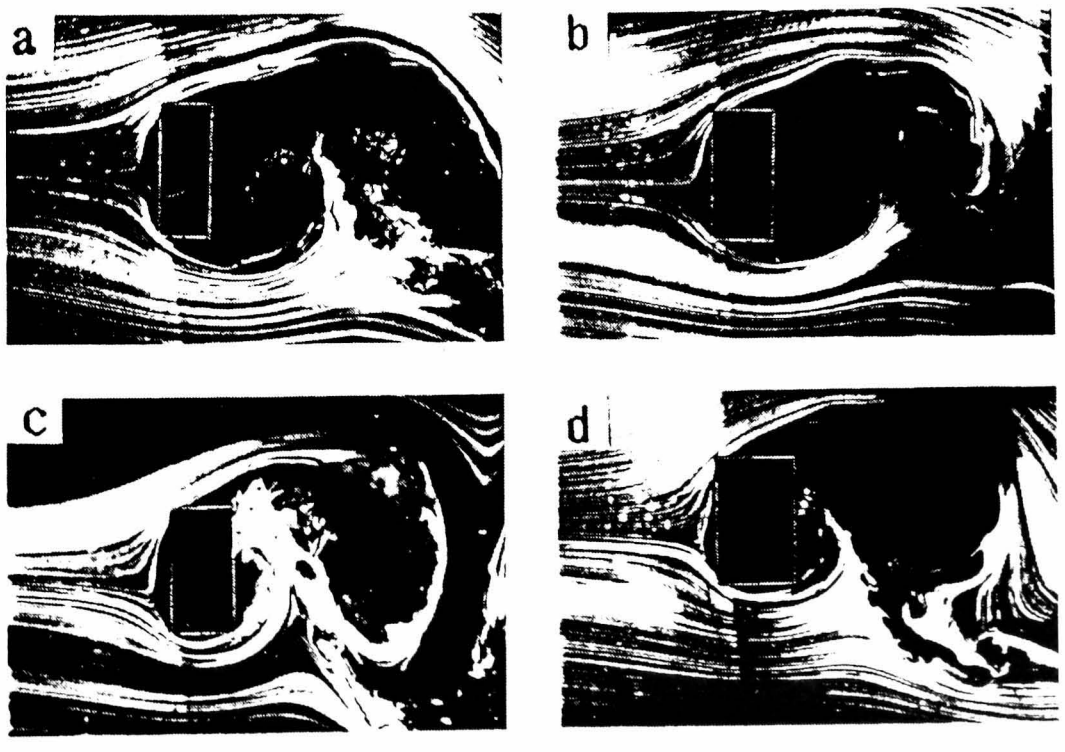

Figure 2.11 Discontinuity in shedding mode from Ohya (1994)
(a)B/A=0.4; (b),(c) B/A=0.5; (d)B/A=0.62

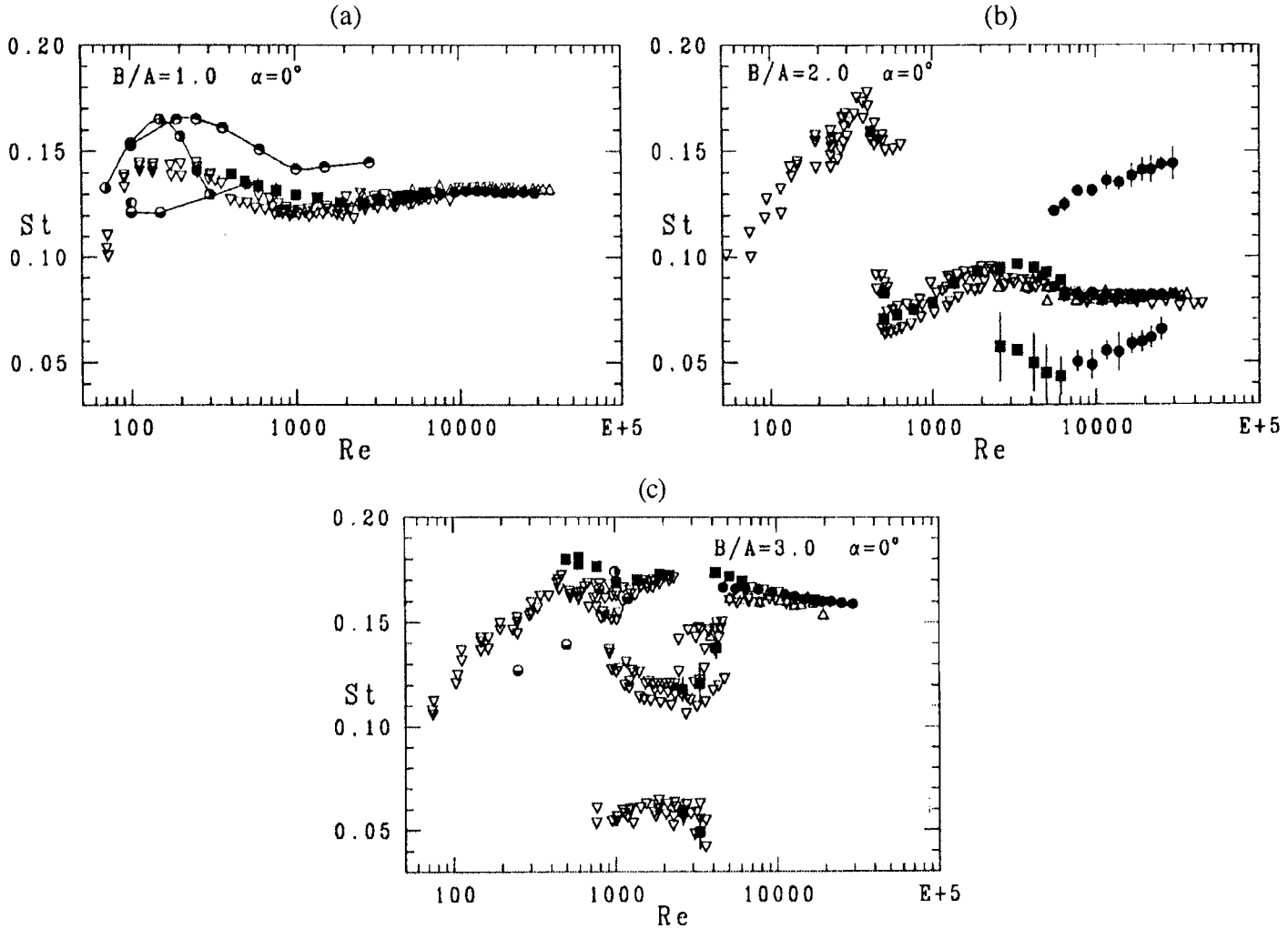

Figure 2.12 Strouhal number vs. Reynolds number for rectangular cylinders.
—◊— Davis and Moore (1982); ▽ Okajima (1982); △ Igarishi (1985); —◊— Franke *et al* (1990);
—◊— Okajima *et al* (1990); ◗ Ohya *et al* (1990); ●, ■ Norberg (1993);
(a) *B/A*=1.0, (b) *B/A*=2.0, (c) *B/A*=2.5, (d) *B/A*=3.0, from Norberg (1993).

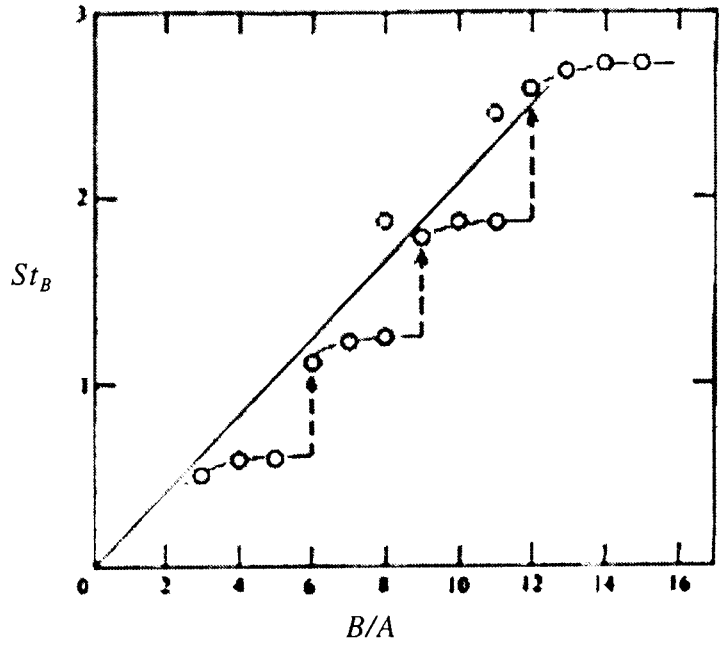

Figure 2.13 Strouhal number based on afterbody length vs. side ratio, Re=(1-3)×10^3,
from Nakamura *et al* (1991)

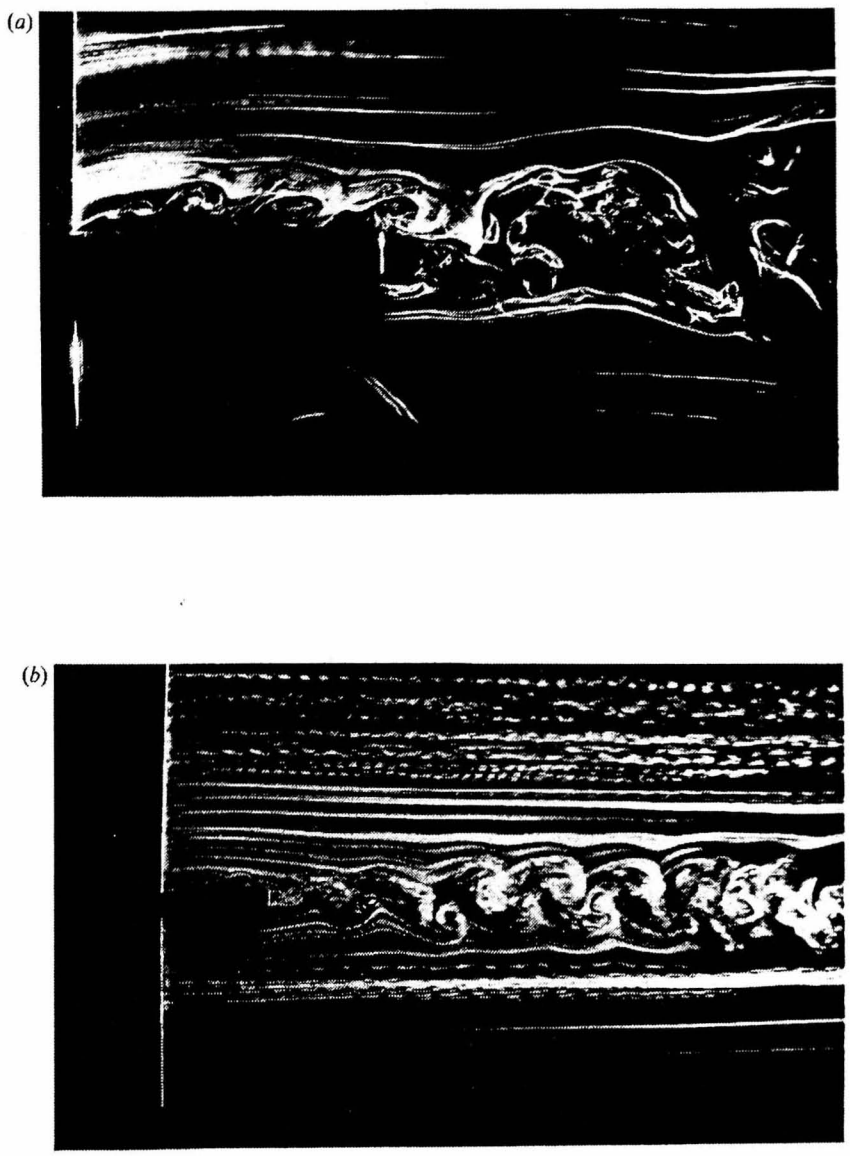

Figure 2.14 Flow visualisation at B/A=8.0, Re=10^3 from Nakamura et al (1991)

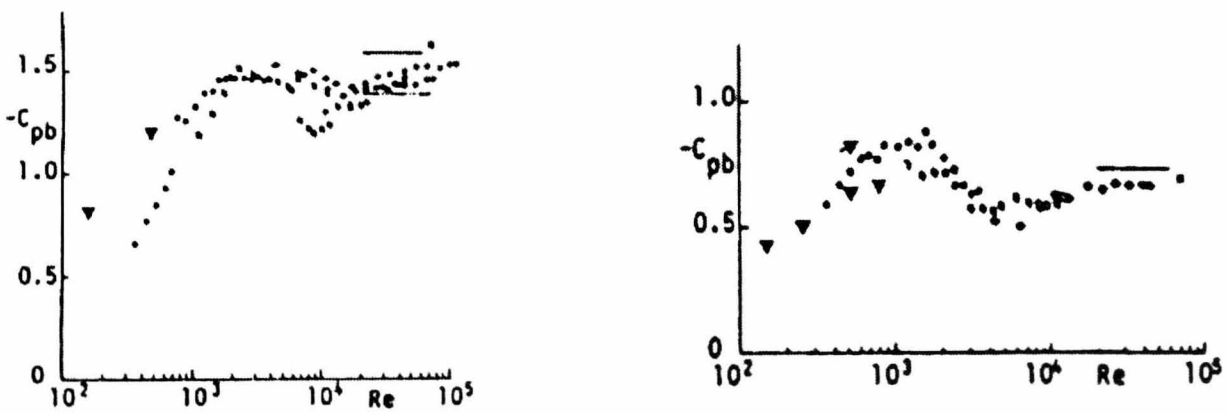

(a) B/A=1.0 (b) B/A=2.0

Figure 2.15 Base pressure coefficient vs. Reynolds number, from Okajima (1990);
▼ - numerical results, ● - measured results

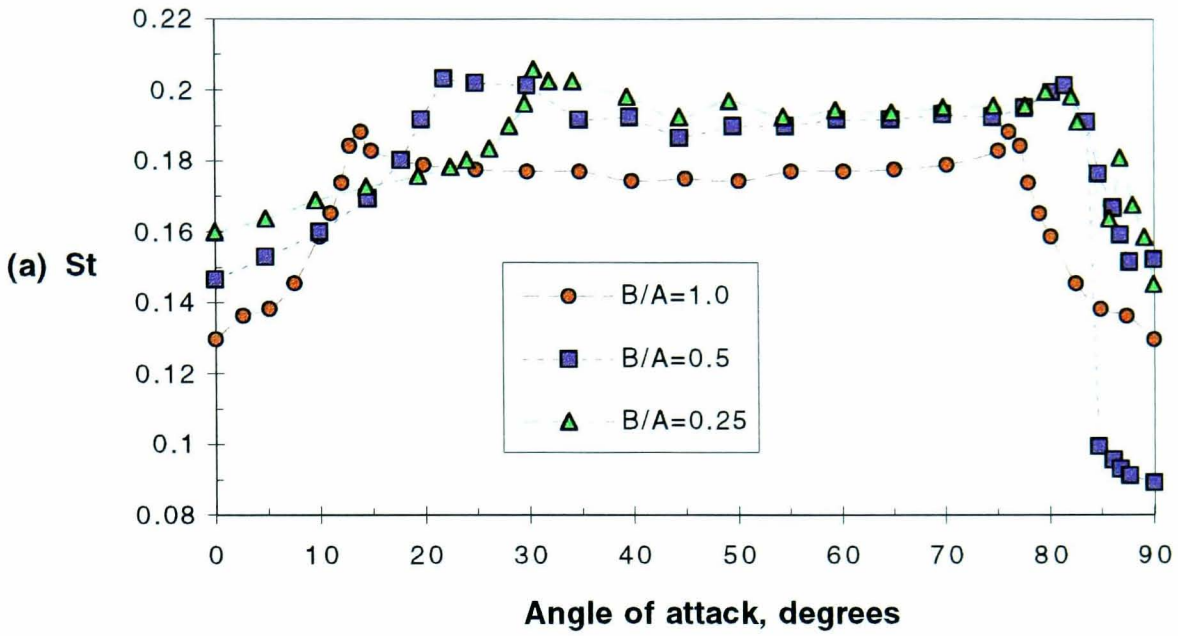

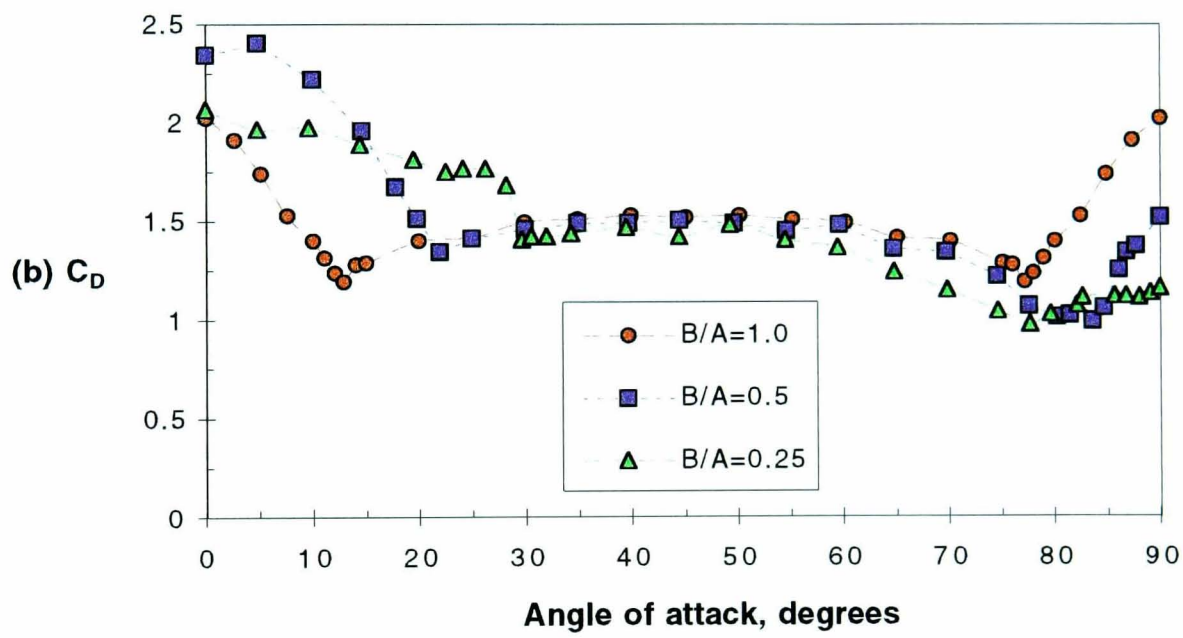

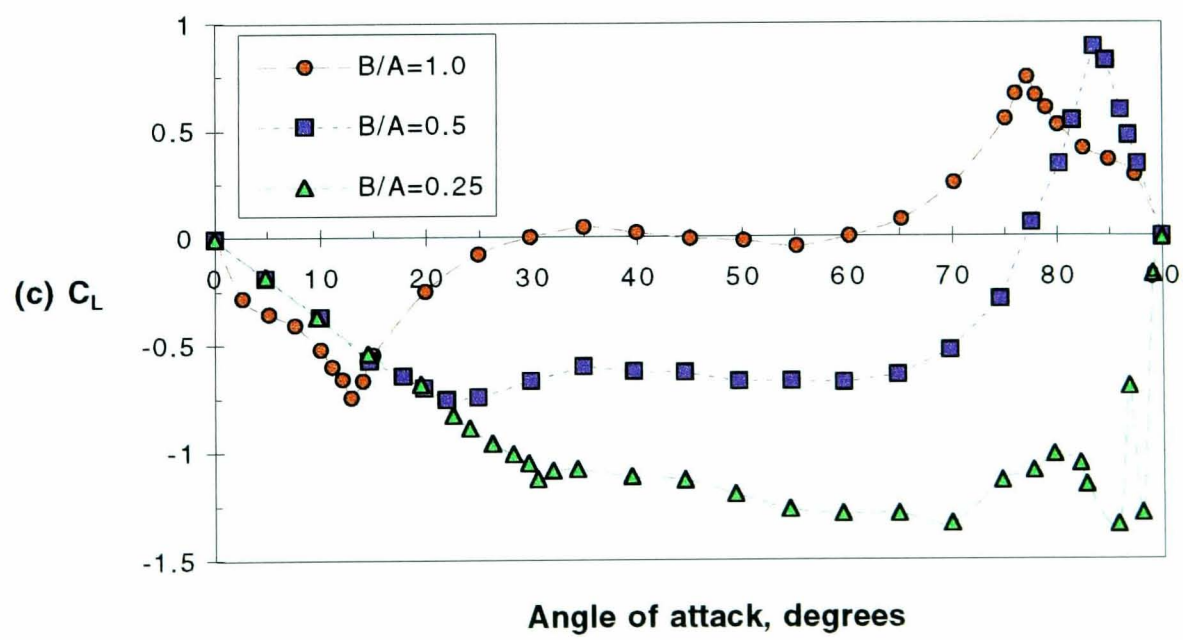

Figure 2.16 Strouhal number, drag coefficient, lift coefficient vs. angle of attack; B/A=0.25, 0.5, 1.0; Re=(2-7)×10^4; from Knisely (1990).

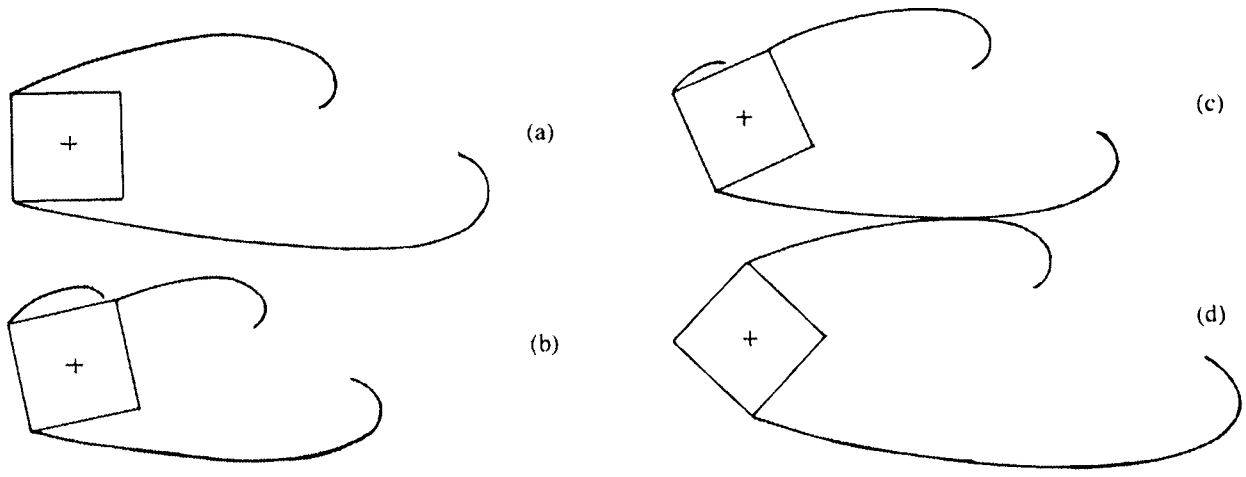

Figure 2.17 Schematic of flow pattern past square cylinder at incidence
(a) α=0° (b) α=10° (c) α=22.5° (d) α=45° from Zaki *et al* (1994).

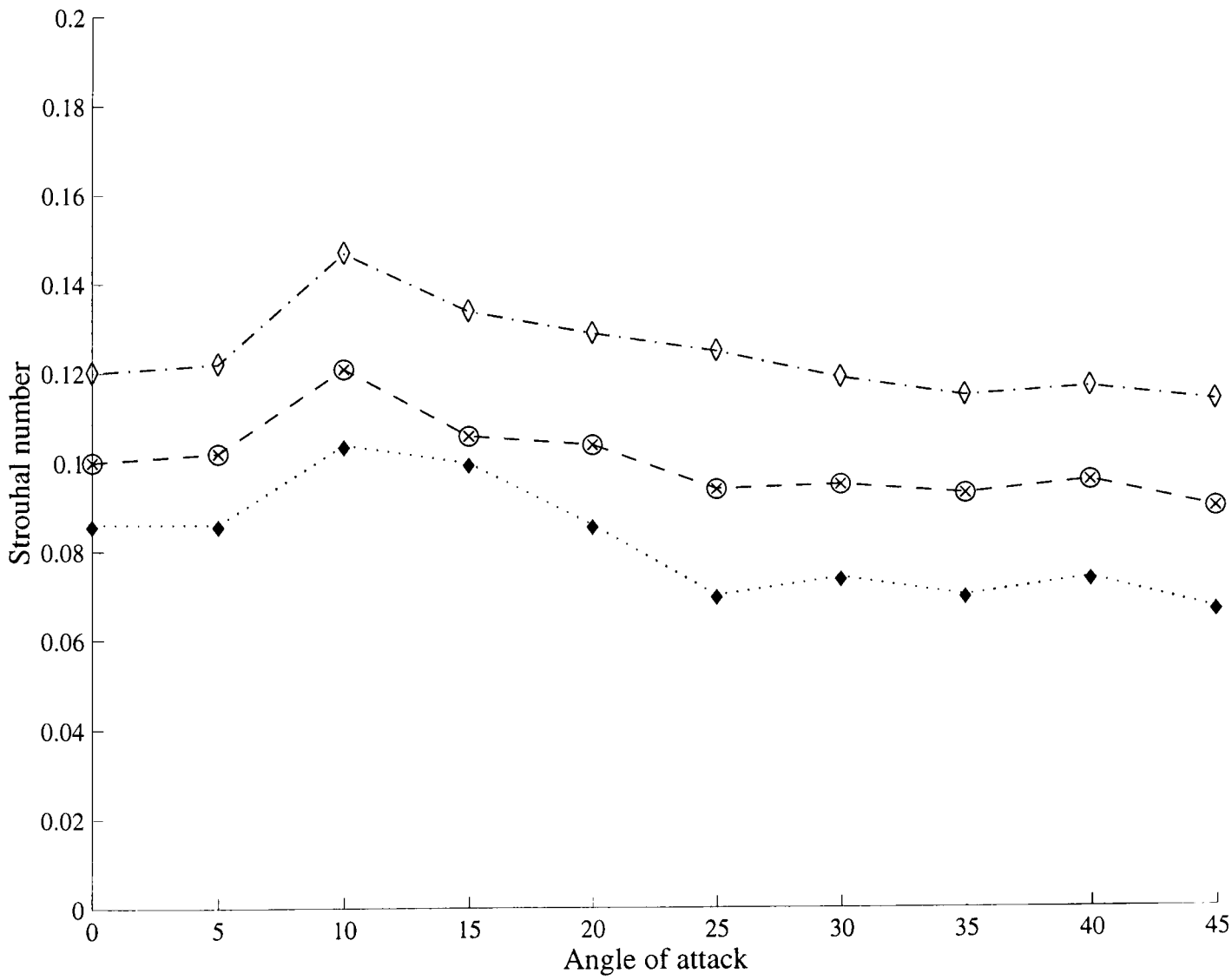

Figure 2.18 Strouhal number vs. angle of incidence for *B/A*=1.0 cylinder
♦ *Re*=1790, ⊗ *Re*=2450, ◊ *Re*=6140 from Zaki *et al* (1994).

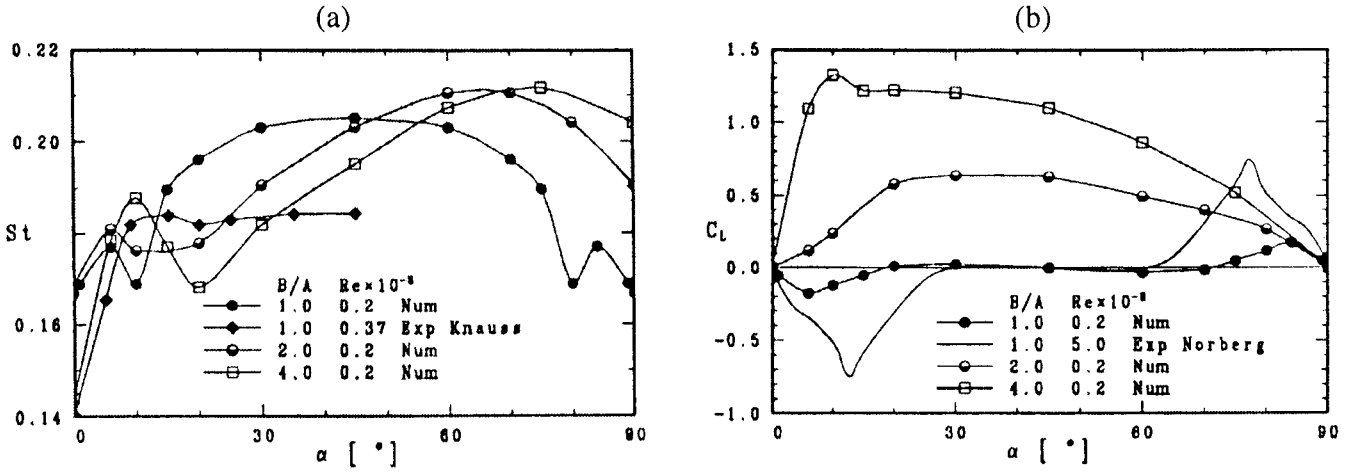

Figure 2.19 Effect of angle of attack on mean measured parameters from Sohankar *et al* (1996).
(a) Strouhal number, (b) Lift coefficient, (c) Pressure drag coefficient, (d) RMS. lift vs. angle of attack.

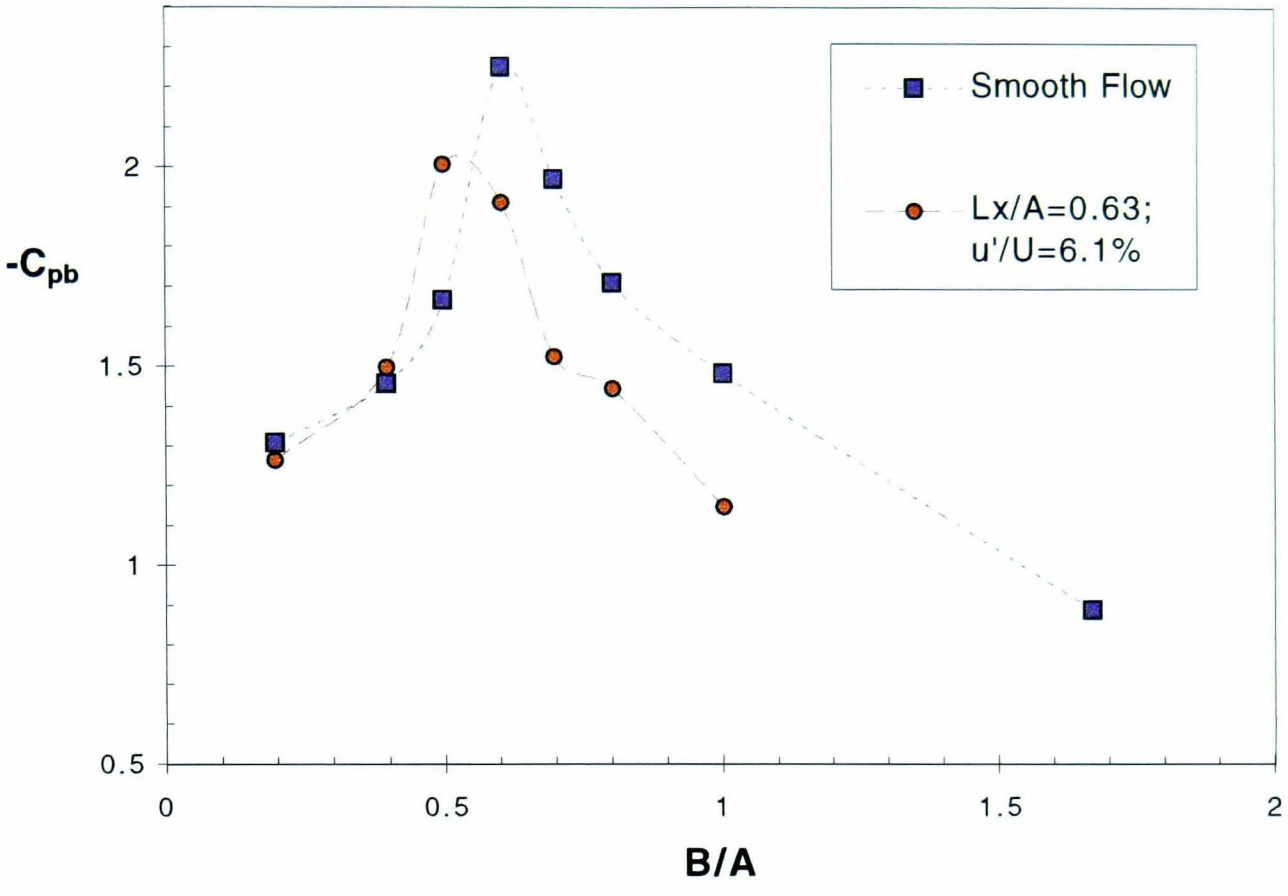

Figure 2.20 Effect of turbulence on critical depth from Nakamura and Ohya (1984)

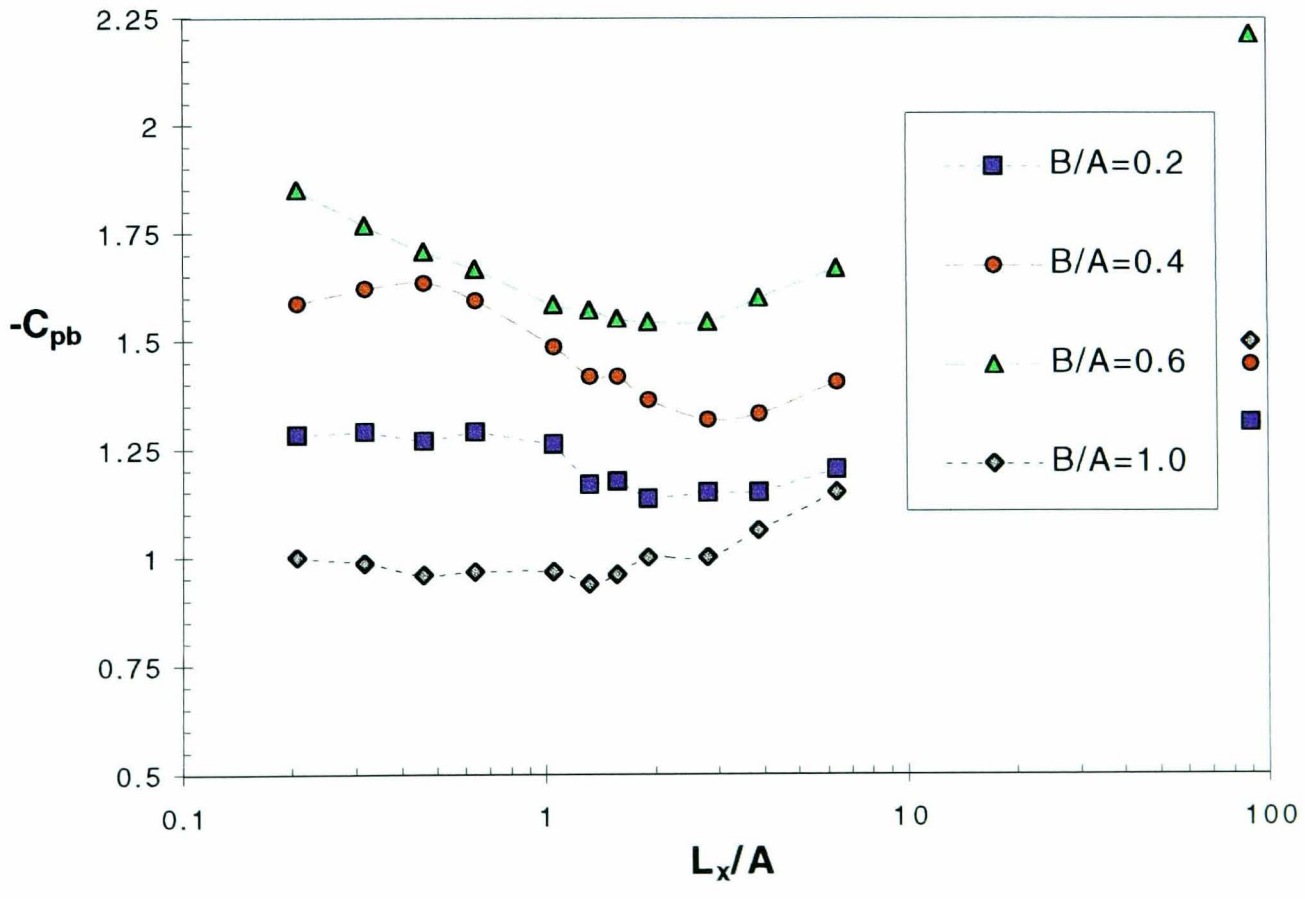

Figure 2.21 Effect of turbulence scale on base pressure coefficient
for rectangular cylinders from Nakamura (1993)

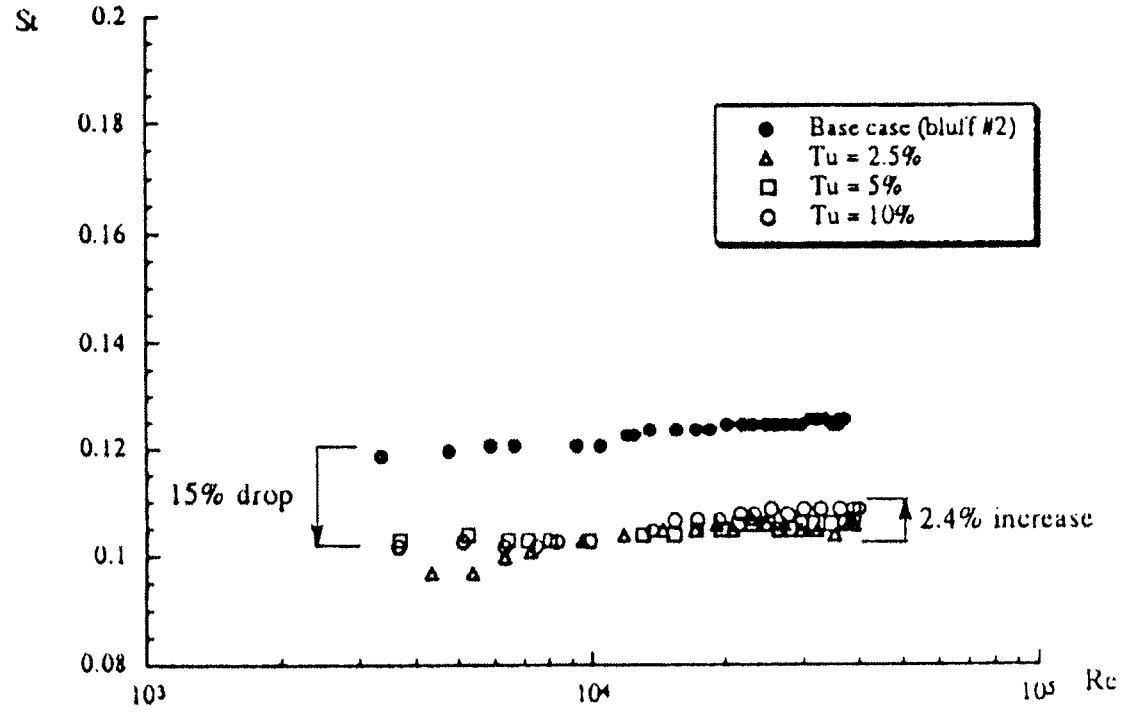

Figure 2.22 Effect of turbulence intensity on Strouhal number, from Wolochuk *et al* (1996)

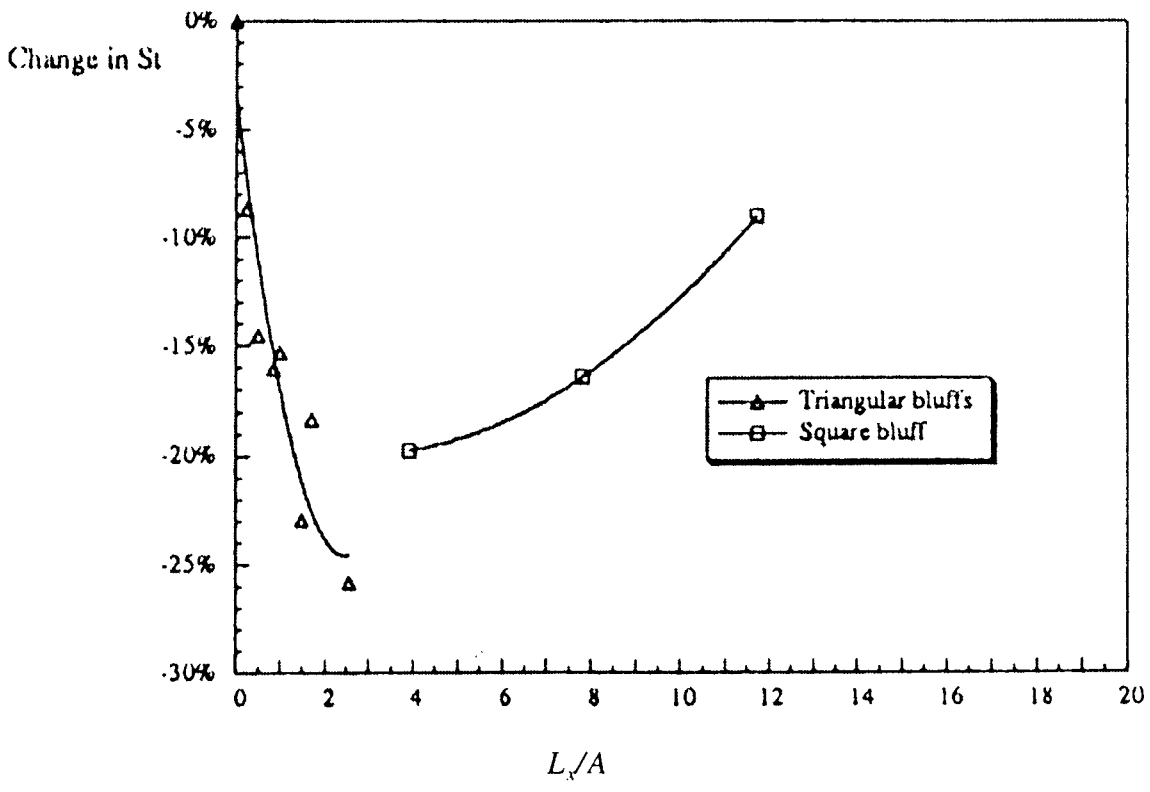

Figure 2.23 Percentage decrease in Strouhal number with turbulence length scale, from Wolochuk *et al* (1996)

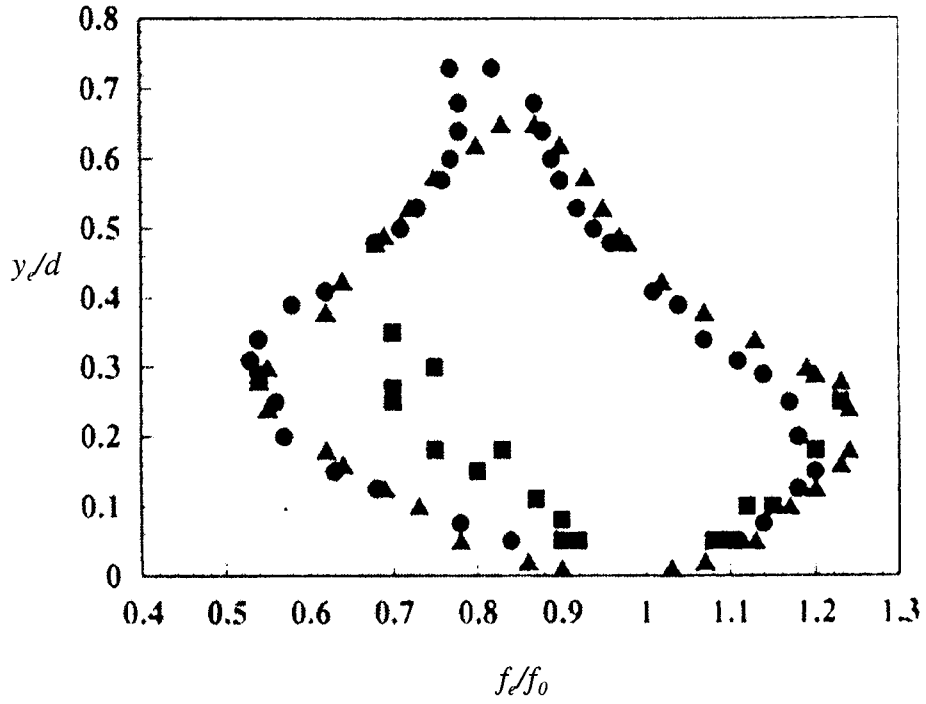

Figure 2.24 'Lock-in' boundary for cross flow oscillations from Griffin and Hall (1995)
■ - Re=100 to 300; ● - Re=1500; ▲ - Re=1650.

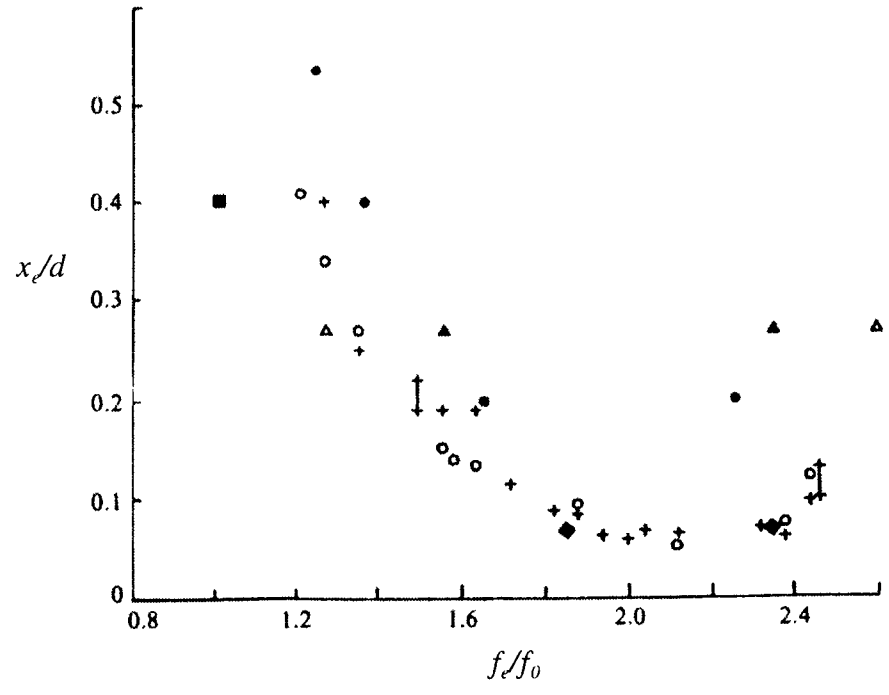

Figure 2.25 Minimum amplitude for 'lock-in' of in-line oscillations, from Barbi *et al* (1986).
▲ - Re=80; ● - Re=100; ○, ✦ - Re=190; ◆ - Re=3000; △ - Re=4000; ■ - Re=40000.

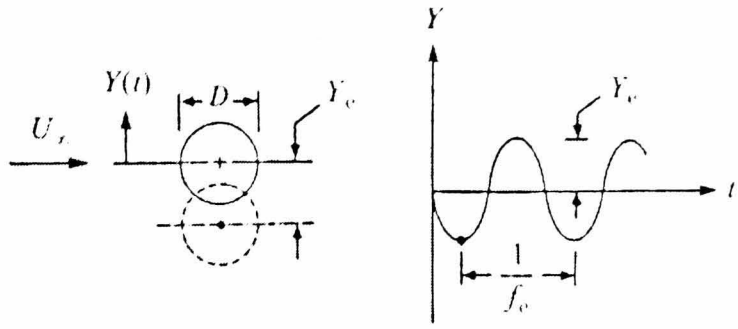

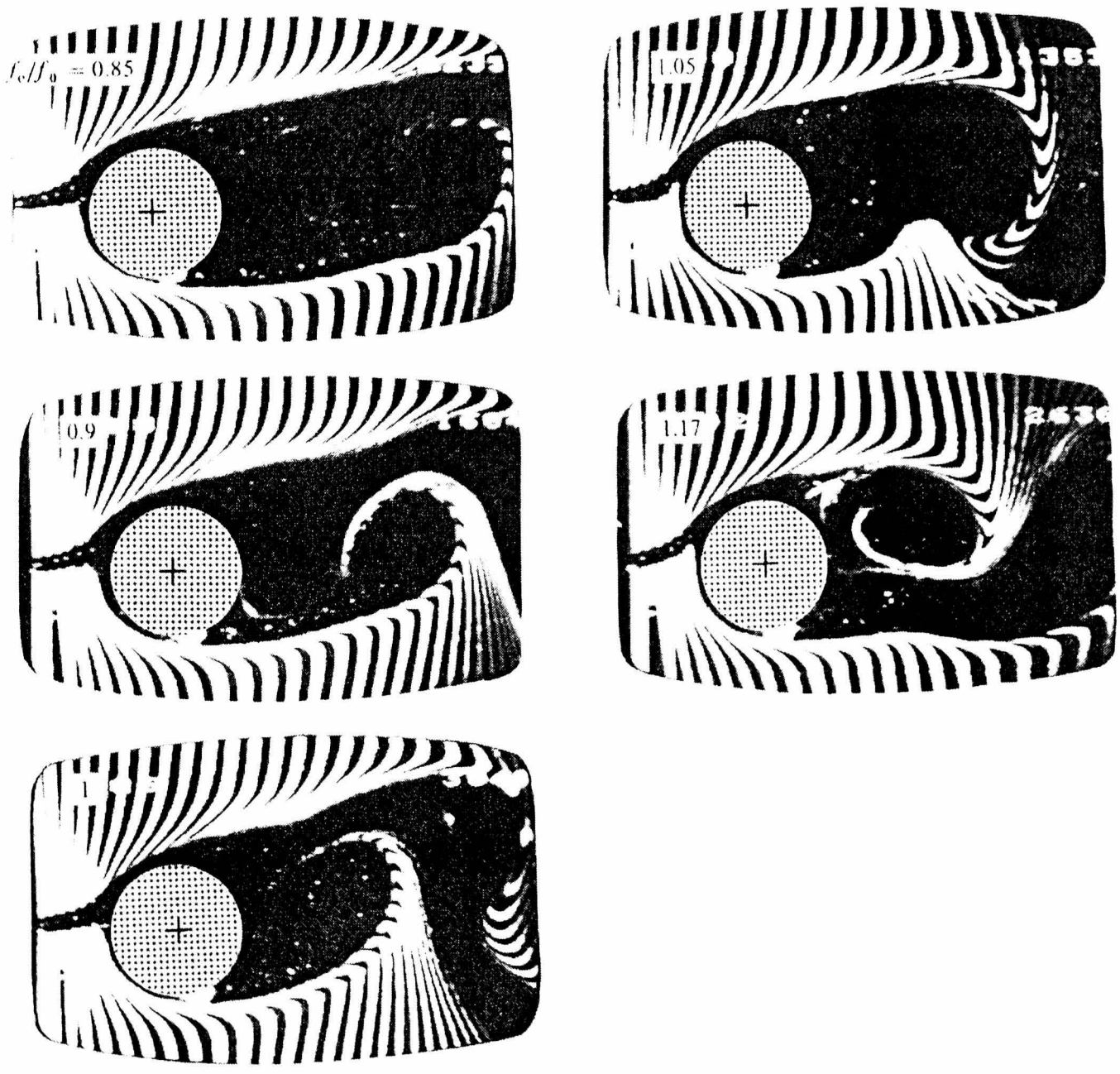

Figure 2.26 Effect of the ratio f/f_0 on the near wake structure of a circular cylinder. All images are taken at the moment of maximum negative displacement of the cylinder, from Ongoren and Rockwell (1988a).

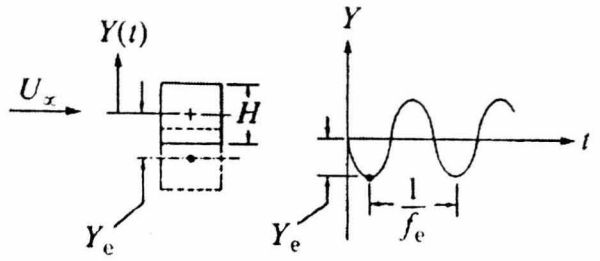

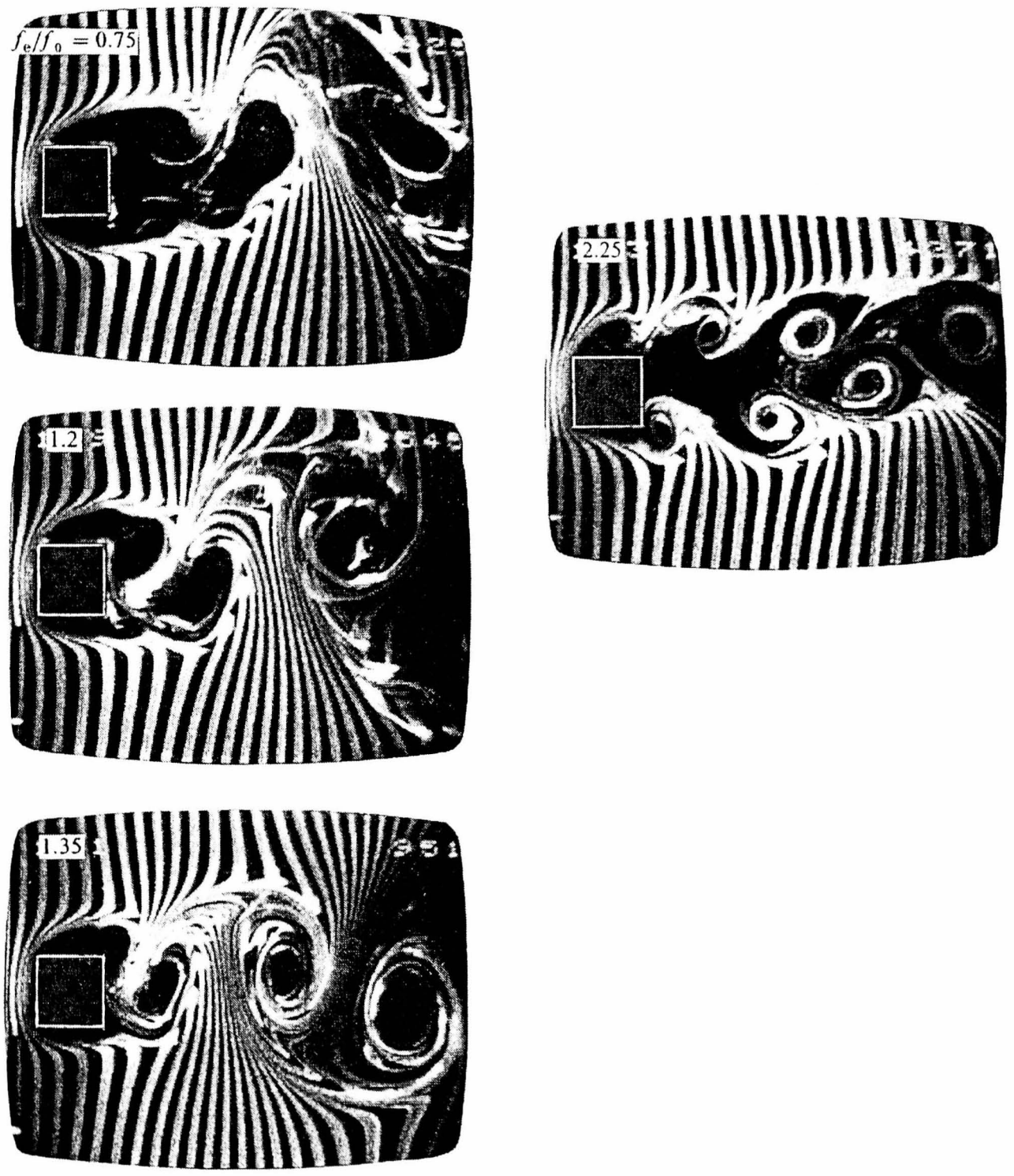

Figure 2.27 Effect of the ratio f_e/f_0 on the near wake structure of a square cylinder. All images are taken at the moment of maximum negative displacement of the cylinder, from Ongoren and Rockwell (1988a).

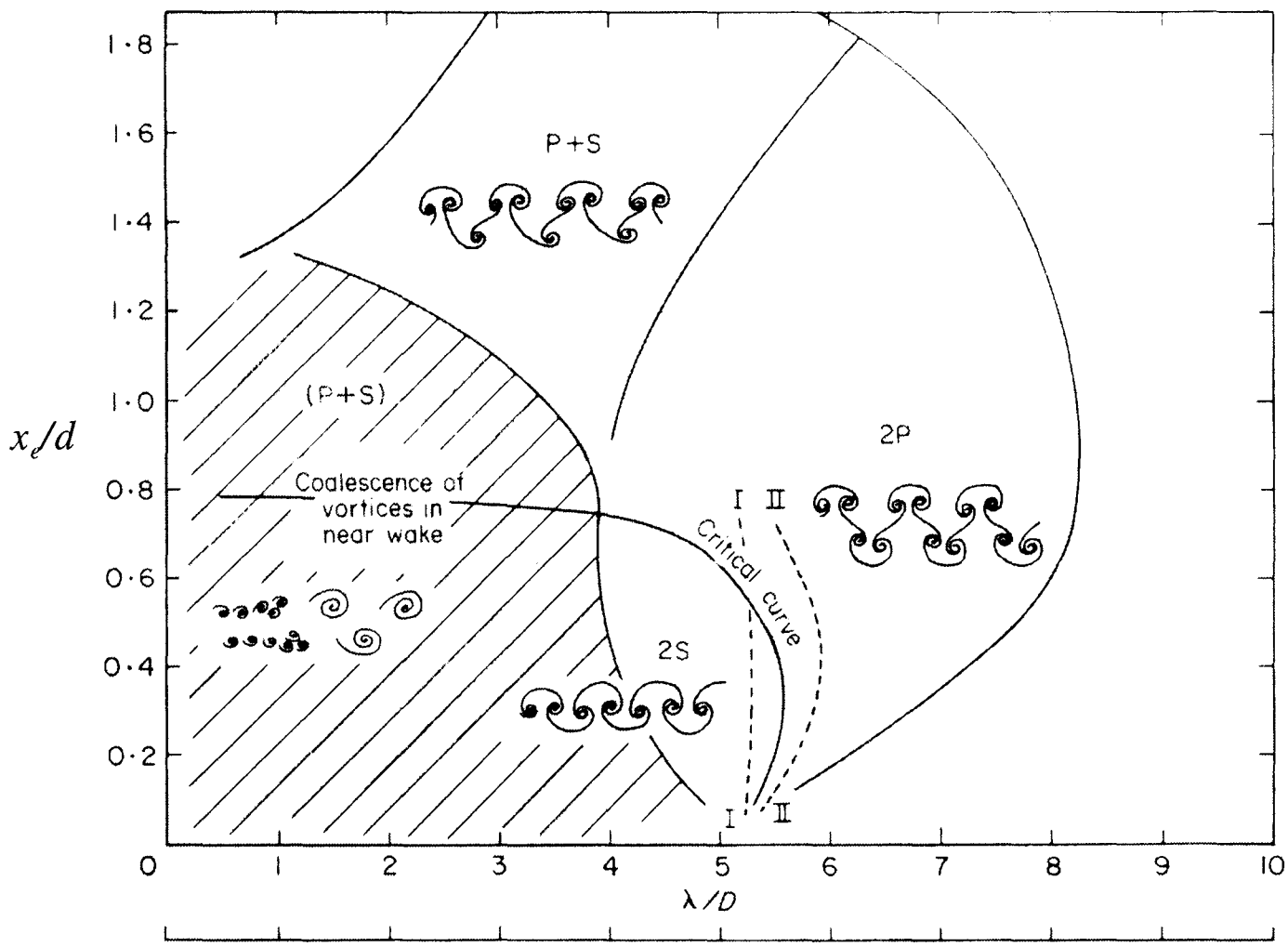

Figure 2.28 Map of vortex patterns near fundamental 'lock-in' region, from Williamson and Roshko (1988)

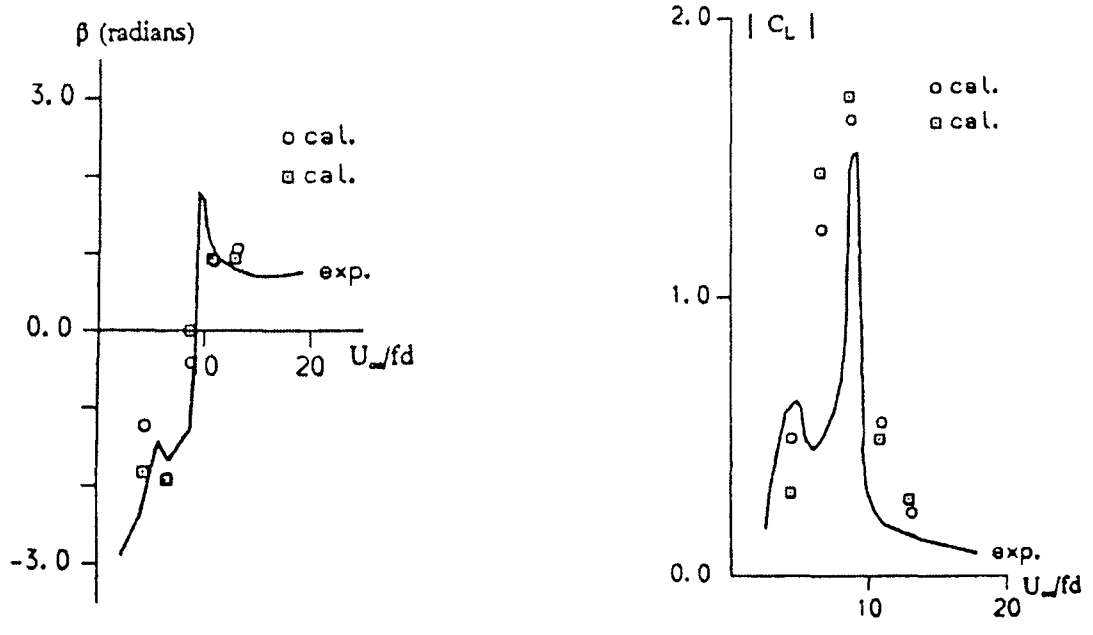

(a) Phase angle vs. reduced velocity

(b) Rms. lift vs. reduced velocity

Figure 2.29 Effect of reduced velocity on phase angle and rms lift; Flow-induced oscillations in turbulent flow around square cylinder (*Re*=22000); From Launder and Kato (1993).

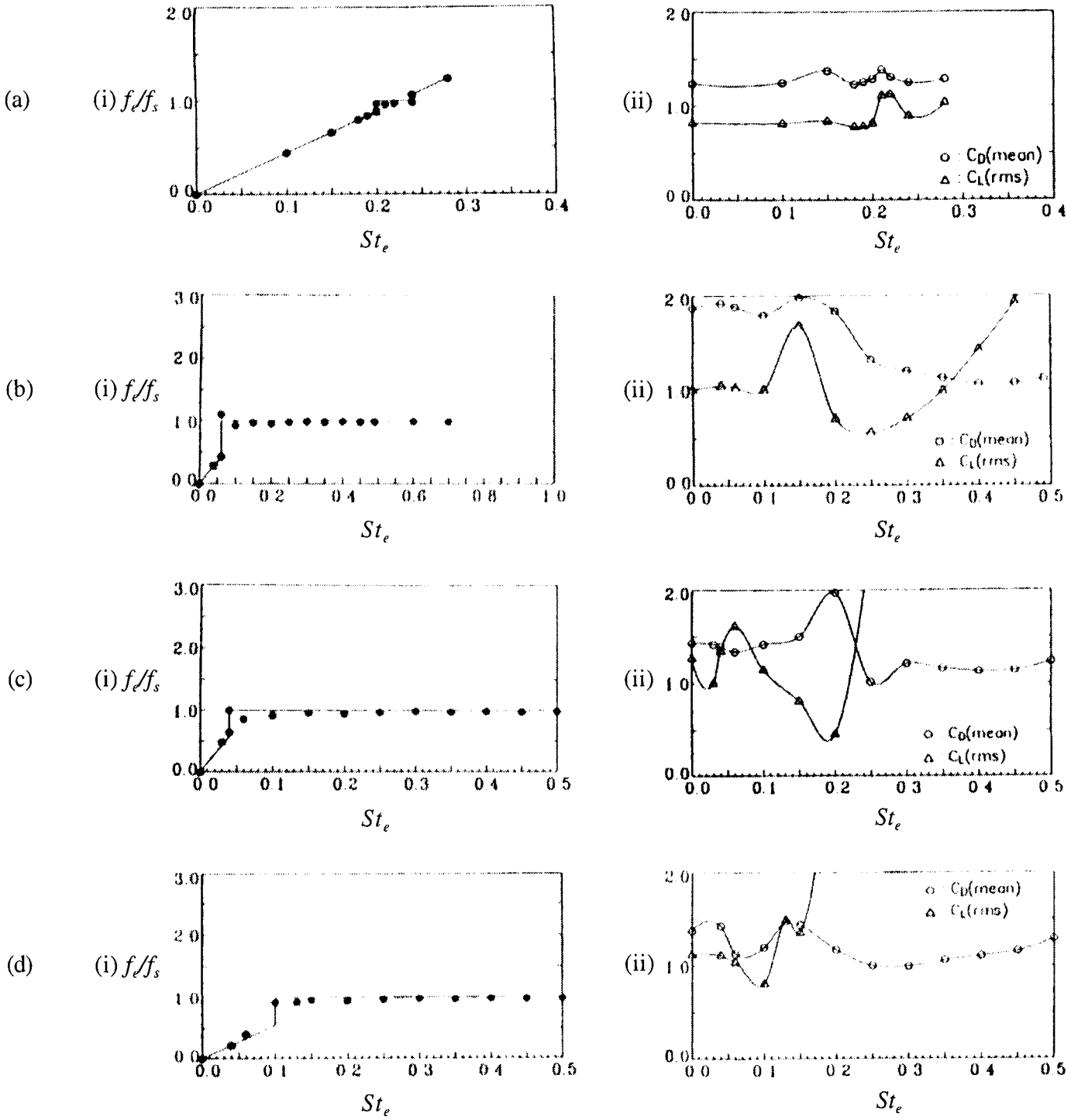

Figure 2.30 f_e/f_s, C_D, $C_{L(rms)}$ vs. St_e for cross flow oscillations; Re=10^3, from Okajima and Kitajima (1993)
(a) Circular cylinder, (b) B/A=1.0 cylinder, (c) B/A=2.0 cylinder, (d) B/A=3.0 cylinder.

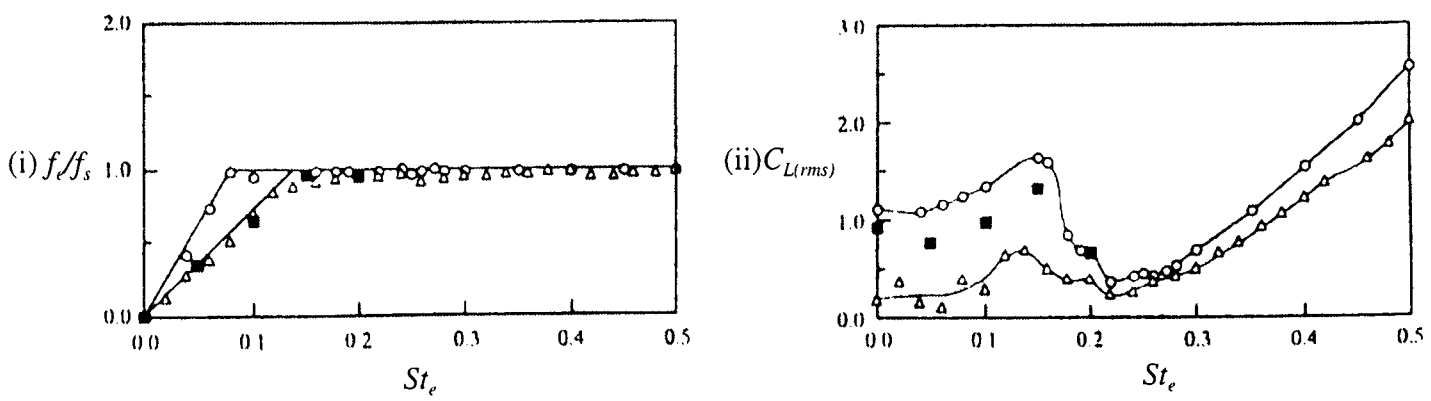

Figure 2.31 f_e/f_s, $C_{L(rms)}$ vs. St_e for B/A=1.0 cylinder at Re=10^3, from Okajima (1995).
■ 3-D calculations, —○— 2-D calculations, —△— laboratory measurements.

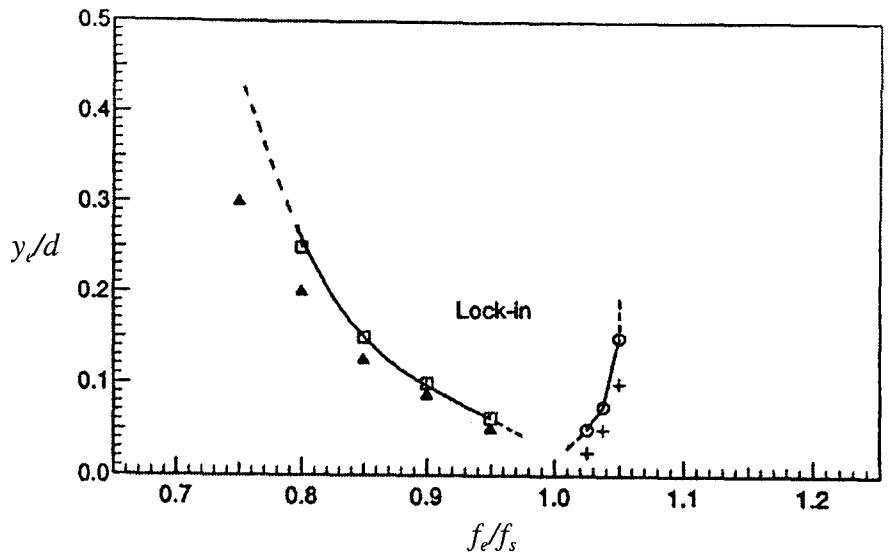

Figure 2.32 'Lock-in' boundary for cross flow oscillations from Meneghini and Bearman (1993). ⊕, lock-in $f_e/f_s<1$; ⊕ lock-in $f_e/f_s>1$; ▲ no lock-in $f_e/f_s<1$; + no lock-in $f_e/f_s>1$.

Figure 2.33 *P+S* mode of shedding as predicted by Meneghini and Bearman (1993)

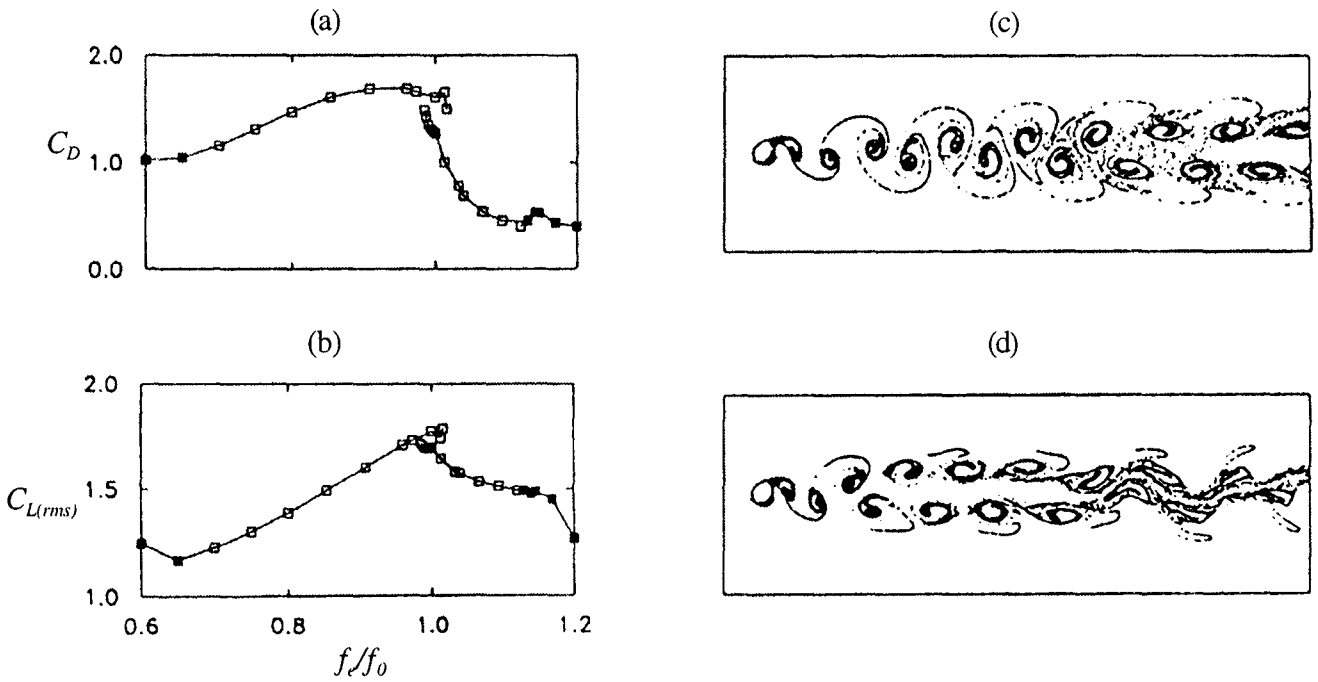

Figure 2.34 (a) C_D, (b) $C_{L(rms)}$ vs. f_e/f_0 for circular cylinder at Re=200 from Copeland and Cheng (1995). (c), (d) Streaklines showing distinct vortex patterns from Copeland and Cheng (1995).

Figure 2.35 Comparison of asymmetrical and symmetrical shedding modes for a circular cylinder All images taken at the moment corresponding to maximum upstream cylinder displacement, from Ongoren and Rockwell (1988b).

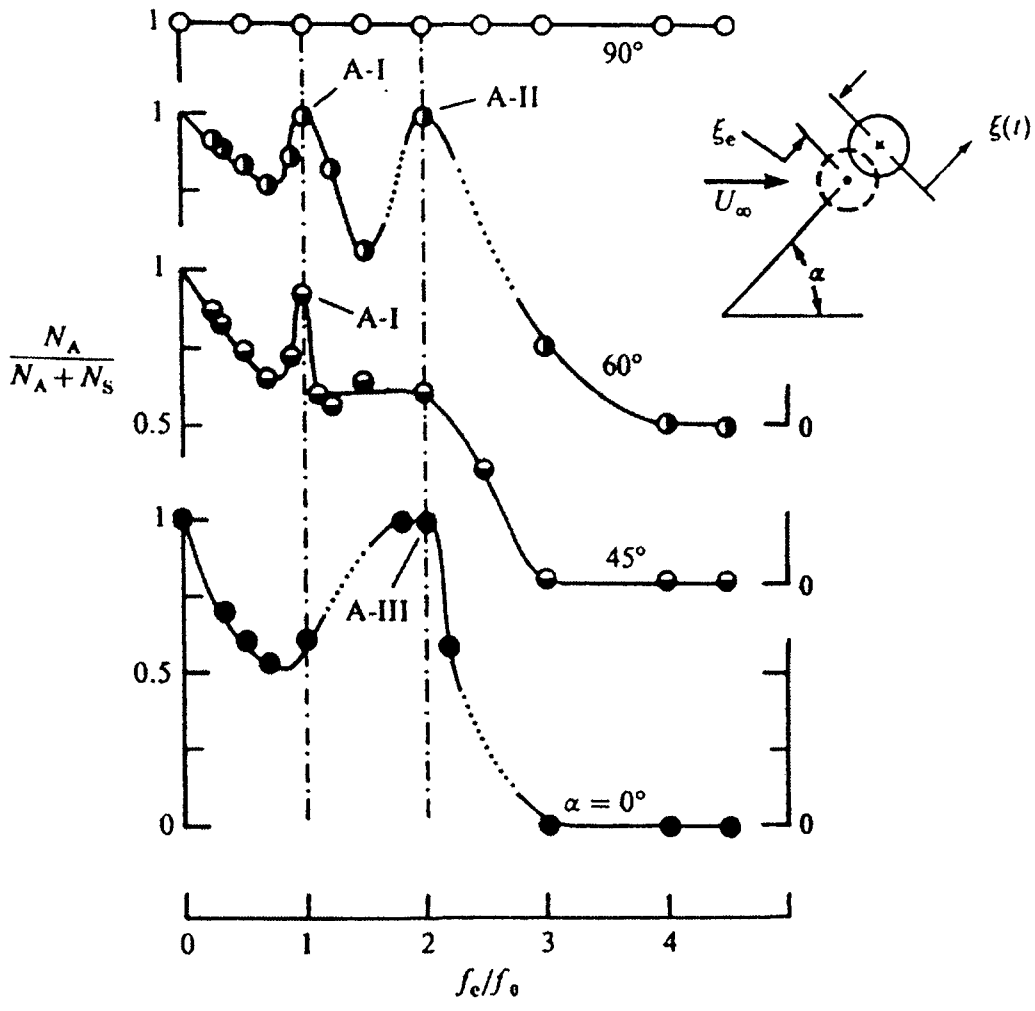

Figure 2.36 Predominance of asymmetric shedding mode vs. f_e/f_0. Cylinder forced to oscillate at an inclination, from Ongoren and Rockwell (1988b)

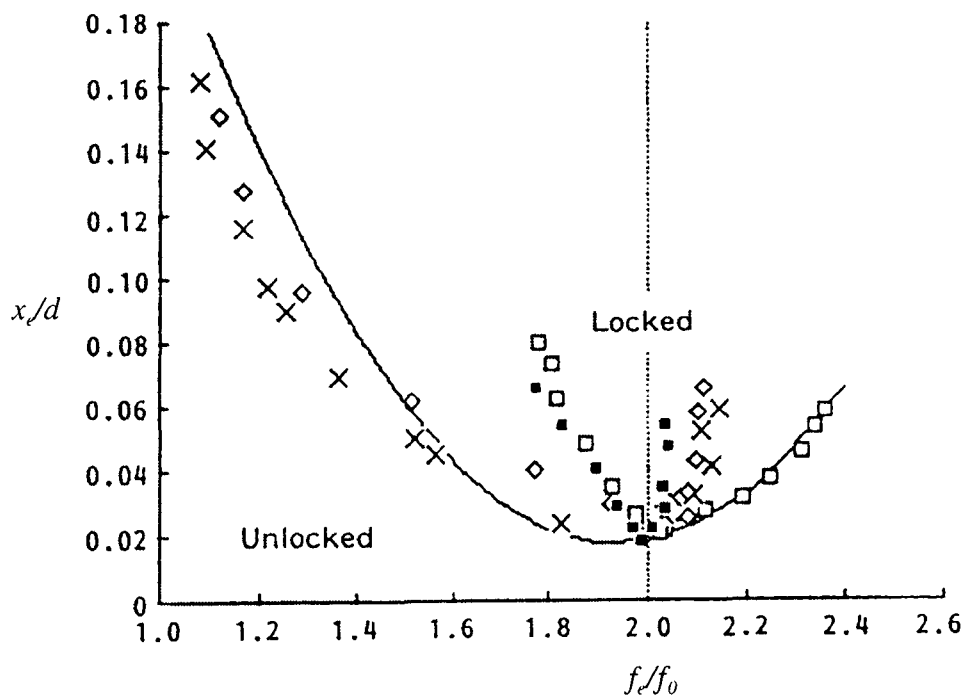

Figure 2.37 'Lock-in' boundaries from Al-Asmi and Castro (1992)
-- circular cylinder; ■ flat plate; ◊ T-shape; × triangular; □ rectangular, B/A=0.67.

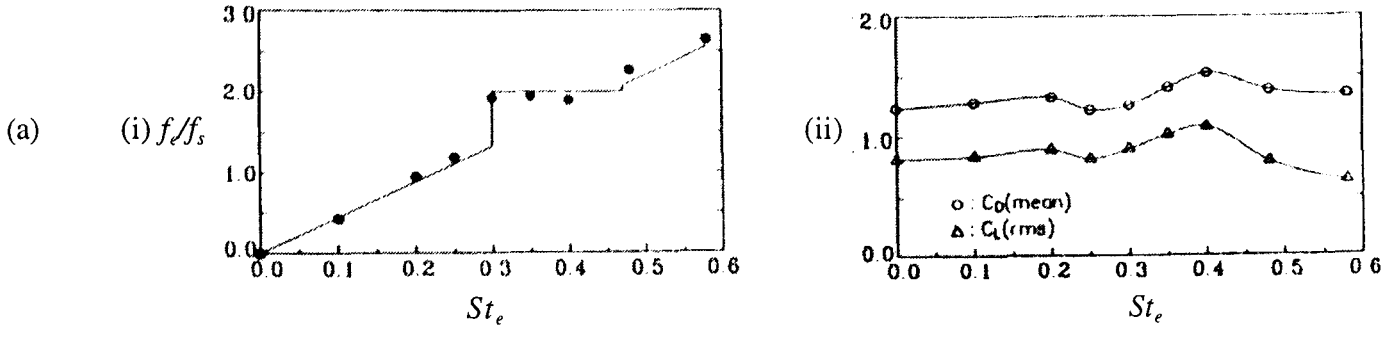

2.38 f_e/f_s, C_D, $C_{L(rms)}$ vs. St_e for in-line oscillations; Re=10^3, from Okajima and Kitajima (1993)
(a) Circular cylinder, (b) B/A=1.0 cylinder, (c) B/A=2.0 cylinder, (d) B/A=3.0 cylinder.

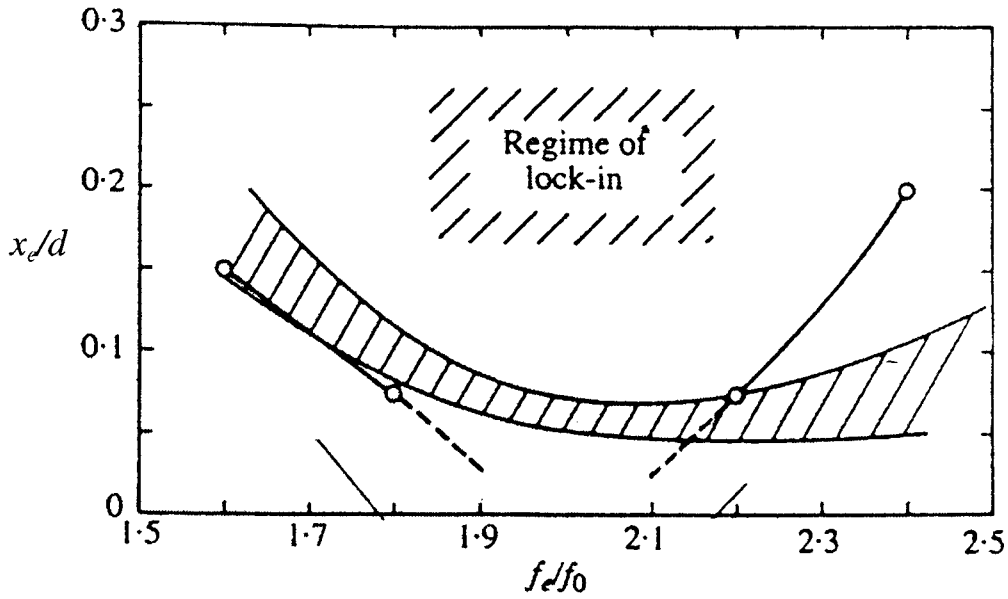

Figure 2.39 'Lock-in' boundary for in-line oscillations past square cylinder from Minewitsch *et al* (1994); Shaded area is 'lock-in' boundary for circular cylinder found by Griffin and Ramberg (1976).

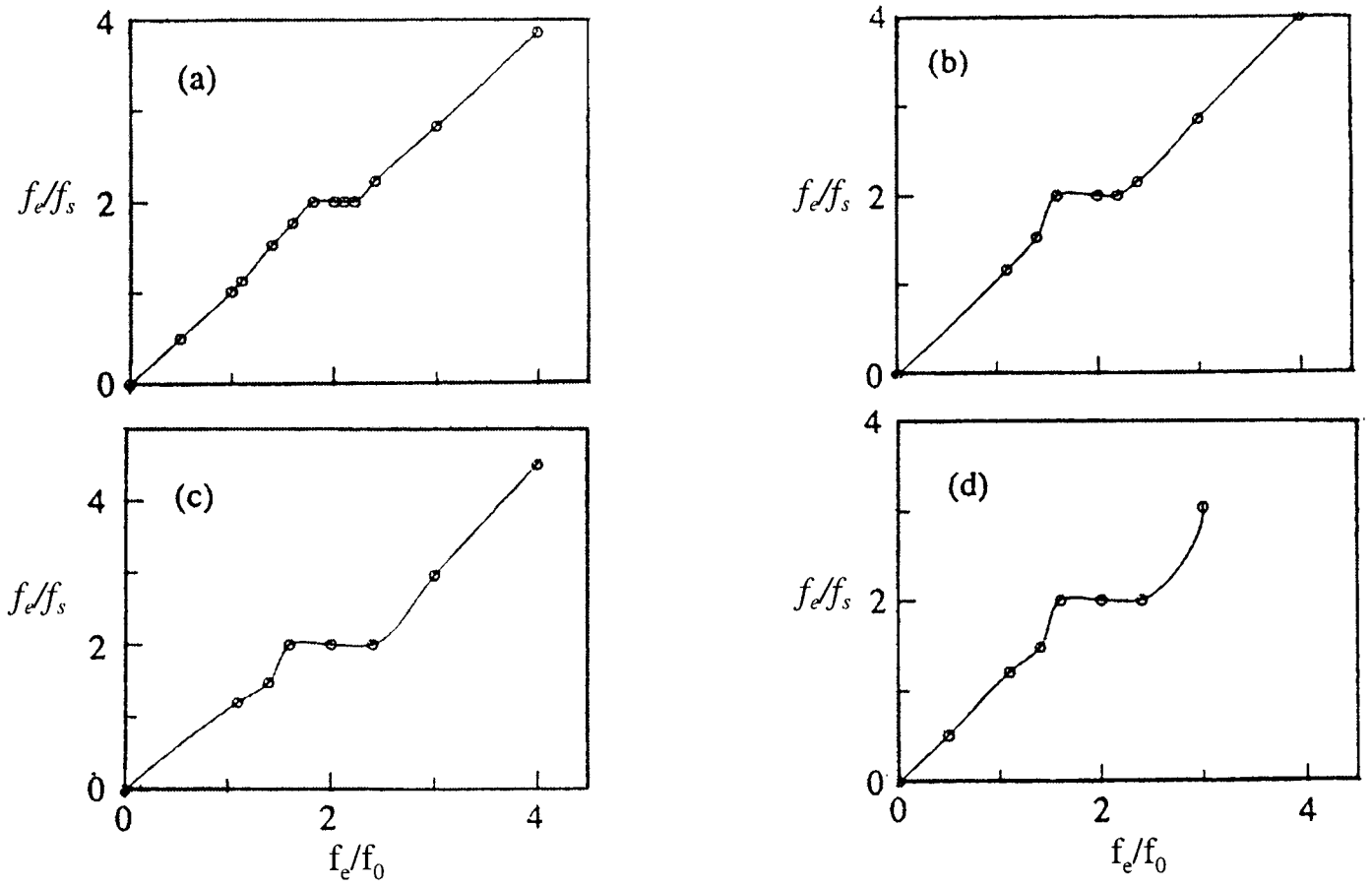

Figure 2.40 Effect of forcing frequency on shedding frequency from Minewitsch *et al* (1994)
(a) x_e/d=0.125; (b) x_e/d=0.175; (c) x_e/d=0.225; (d) x_e/d=0.275.

Chapter 3

Theoretical Basis and Applications of Discrete Vortex Methods

Vortex methods have received considerable research attention over the past twenty five years and detailed reviews of the topic can be found in Leonard (1980), Sarpkaya (1994) and Lewis (1995). Their basis stems from the assertion that many flows exhibit largely irrotational motion with regions of high vorticity limited to small parts of the flow. This is particularly relevant to bluff body flows for which the wake and boundary layer regions contain high levels of circulation but the main body of fluid is nearly irrotational. These vortex methods were originally developed to simulate high Reynolds number flows past bluff bodies as direct numerical methods were inappropriate for such calculations. More recently hybrid vortex methods have been developed which incorporate viscosity and model low *Re* bluff body flows. The various schemes which are commonly used in vortex methods are introduced in the following sections before an analysis of their application to two-dimensional bluff body flows is given. Finally a short discussion of a few three-dimensional vortex method calculations is included.

3.1 Definitions

3.1.1 Circulation

Circulation is a property closely associated with vorticity. If the fluid velocity along a line element $\boldsymbol{dl}$ joining the points A and B is given by $\boldsymbol{u}$, then the circulation is defined as

$$\Gamma_{AB} = \int_A^B \boldsymbol{u}.\boldsymbol{dl}\,; \tag{3.1}$$

by use of Stokes' theorem the circulation of a closed curve C enclosing surface S can be related to vorticity by

$$\Gamma_C = \int_C \boldsymbol{u}.dl = \int_S \nabla \times \boldsymbol{u}.dS = \int_S \omega.dS\,. \tag{3.2}$$

3.1.2 Biot-Savart Law

The Biot-Savart law, as documented in Kuethe and Chow (1986), relates the velocity $\boldsymbol{u}$ induced at a point $\boldsymbol{r}$ in space to the net circulation strength Γ of a line element $\boldsymbol{dl}$:

$$\boldsymbol{u} = \frac{\Gamma \boldsymbol{dl} \times \boldsymbol{r}}{4\pi r^3}. \tag{3.3}$$

Biot and Savart originally deduced this law to determine the magnetic field intensity (corresponding to $\boldsymbol{u}$) induced by an electric current (corresponding to Γ). For an infinite line vortex in three dimensions, the equation simplifies to the familiar form,

$$u_\theta = \frac{\Gamma}{2\pi h}, \tag{3.4}$$

where h is the perpendicular distance to the line element. A two-dimensional simulation considers each plane of flow identical, with point vortices replacing line vortices.

3.2 Lagrangian vortex scheme

In its simplest form the vortex method consists of many point vortices, or 'vortex particles', released into an otherwise irrotational and inviscid flowfield. At any spatial co-ordinate the velocity is obtained by a summation of the velocities induced by each discrete vortex together with the irrotational velocity u_ϕ, so that

$$\boldsymbol{u}(\boldsymbol{r}, t) = \boldsymbol{u}_\phi(\boldsymbol{r}, t) + \sum_{k=1}^{NV} \frac{\Gamma_k}{2\pi|\boldsymbol{r} - \boldsymbol{r}_k|} \qquad (\boldsymbol{r} \neq \boldsymbol{r}_k) \tag{3.5}$$

where the flow is made up of NV vortex particles, of strength Γ_k at position $\boldsymbol{r}_k$. From (3.5) particle velocities are obtained and the particles can then be convected to their new positions ready for the next time step.

Introduction of these particles is at flow separation points, easily determined for sharp edged obstacles, and determined from experimental results for circular cylinders or smooth bodies. Γ_k, the circulation of each vortex element, is kept constant throughout the computation and, in the simplest models, is the same for each vortex element. Clements (1973) obtained the relationship

$$\frac{\partial \Gamma}{\partial t} = \frac{1}{2} U_S^2 \tag{3.6a}$$

by differentiation of equation (3.1) with respect to time and subsequent integration with respect to velocity. U_S represents the velocity at the edge of the boundary layer near to the separation point and thus (3.6) yields the rate

of change of circulation at the edge of the boundary layer. Since vorticity is created at the body surface, the simplest vortex models introduce particles of strength

$$\Gamma = 0.5U_S^2 \Delta t \tag{3.6b}$$

at each time step, at the separation points.

At a solid-fluid interface the condition of no flow through the body boundary must be maintained. By placing image vortices at suitable points within the body's interior the normal component of velocity induced on the body surface can be equated to zero. A conformal transformation takes all calculations into a computational plane in which image vortex positions and the irrotational potential flowfield are more easily determined. In a real flow viscous effects are important within the boundary layer region and imply the existence of a no-slip condition along the interface. However using image vortices does not satisfy the no-slip condition along the boundary; i.e. that the tangential component of velocity must also be zero. For this reason most vortex methods introduce vortices at the edge of the boundary layer and any vortices which subsequently creep too close to the body surface are reflected away from the body boundary.

This fully Lagrangian method has several advantages over Eulerian grid-based schemes. There is no outer boundary and so no external boundary conditions need to be satisfied. The computations deal almost exclusively with the regions of flow dominated by vorticity and so no additional calculations are made in the irrotational flow regions. Since there is no mesh, and provided a sufficient number of vortices are introduced, even the smallest scale phenomena are represented in the simulation.

With all the advantages of a fully Lagrangian method there are some shortcomings which must be accounted for. Each discrete vortex represents a singularity in the flow, i.e. the velocities induced near vortex positions are very large, and vortices that approach each other too closely will incur unrealistically large velocities and tend to orbit each other in a manner not associated with any physical phenomenon. The effects of viscous diffusion have been entirely neglected, and although the model is suitable for high Reynolds number flows of negligible viscosity, it is desirable that the model should be capable of examining a range of Re and in particular simulate the effects of viscous diffusion on the flow. Any model which realistically simulates the complex wake characteristics inherent in most bluff body flows requires the use of a large number of vortices ($NV \approx O(100,000)$) which in turn implies that $O(NV^2)$ computations are necessary at each time step. Evidently this is unsatisfactory as even the most advanced computers will not be sufficient for long time runs. Finally, the introduction of vorticity is rather arbitrary. Vorticity generation results from the tangential acceleration of a boundary relative to a fluid and from the pressure gradients acting along that boundary which implies its creation all round the fluid-solid interface and not just at the separation points. Most of these problems can be resolved while adhering to the Lagrangian nature of the model and a description of the various methods used follows.

3.2.1 Vortex Blobs

The use of point vortices implies that flow singularities will be present in the model. As suggested by Chorin (1973), the local vortex motion will then be poorly represented and to overcome this some researchers have introduced vortex blobs of finite radius. Most commonly used is the Rankine vortex; the velocity induced by such a vortex of radius r_0 and at distance r from its centre is given by

$$u_\theta = \frac{\Gamma r}{2\pi r_0^2} \quad for\ r < r_0, \tag{3.7a}$$

$$u_\theta = \frac{\Gamma}{2\pi r} \quad for\ r > r_0. \tag{3.7b}$$

Solving the Navier-Stokes equations for a single vortex in an unbounded incompressible domain yields the velocity induced by a Lamb (or Gaussian) vortex, the core size of which grows in proportion to ν, the fluid viscosity, and t, the time since the vortex was created;

$$\mathbf{u}_\theta(\mathbf{r}, t) = \frac{\Gamma(1 - e^{-\mathbf{r}^2/4\nu t})}{2\pi\mathbf{r}}. \tag{3.7c}$$

This Gaussian element is also commonly used in vortex methods. However although (3.7c) represents an exact solution for a single vortex, the velocity field induced by a distribution of Lamb vortices is not a solution of the Navier-Stokes equations. This introduces serious doubt as to the ability of Gaussian vortex distributions to simulate complex flows.

Some researchers have introduced circulation reduction schemes in an attempt to account for the three-dimensional effects which a fully two-dimensional model is clearly incapable of predicting. Γ, the vortex strength, is reduced at each time step according to some arbitrary experimentally-determined scheme and this is assumed to account for the vortex stretching which takes place normal to the flow direction for a truly three-dimensional flow. However this author believes that two-dimensional simulations should be restricted to the simulation of flows which exhibit strongly two-dimensional behaviour.

3.2.2 Amalgamation schemes

The motivation for frequently-used vortex merging or amalgamation schemes stems from two main problems. Firstly, if the Biot-Savart Law is being used to calculate velocities it is important to limit the number of vortices in the flow and keep computational effort to a minimum. The second problem is encountered where vortices in close proximity induce large velocities in each other. Morton (1984) states that the decay of vorticity can only take place within the fluid interior and results from the cross-diffusion of vorticity of opposite signs. Since it is known that some natural merging and cancelling of vorticity will occur in real flows when two vortical regions interact, it is logical that the same might be allowed to occur within the simulation.

In general, once a cloud of vortex particles is deemed to have passed sufficiently downstream, or once several vortex particles have approached within a certain distance of each other, j vortices of strengths $\Gamma_1,\Gamma_2,....\Gamma_j$ will be merged into a single equivalent vortex, of strength $\Sigma\Gamma_j$, positioned at the centre of vorticity, z, where,

$$z = \frac{\sum \Gamma_j z_j}{\sum \Gamma_j}. \tag{3.8}$$

As vortices progress further downstream their influence on the upstream flow will diminish considerably and thus 'sufficiently downstream' is defined as the point beyond which the vortex cloud can be approximated by a single vortex without affecting the upstream flow. In some simulations the vortices may even be removed from calculations altogether.

3.3 Viscous diffusion

Viscosity is fundamental to the diffusion of vorticity within a fluid. This concept can be readily appreciated by manipulation of the Navier-Stokes equations to obtain the vorticity transport equation,

$$\frac{\partial \omega}{\partial t} = -\boldsymbol{u} \cdot \nabla \omega + (\omega \cdot \nabla \boldsymbol{u}) + \nu \nabla^2 \omega. \tag{3.9}$$

The left-hand side of equation (3.9) represents the rate of change of vorticity. On the right the first term equates to the change in vorticity due to convection. It should be noted that in three dimensions line vortices are shed into the flow. The two-dimensional approximation assumes every plane of flow to be identical with point vortices replacing line vortices. The term in brackets represents rate of deformation of vortex lines and therefore does not exist for a two-dimensional model. The final term gives the rate of change of vorticity due to viscous diffusion.

In two-dimensional models it is considered convenient to split (3.9) into a convection and a diffusion equation and any model that accounts for the viscous diffusion of vorticity must incorporate (3.10b) into the simulation.

$$\left.\frac{\partial \omega}{\partial t}\right|_c = -\boldsymbol{u} \cdot \nabla \omega, \tag{3.10a}$$

$$\left.\frac{\partial \omega}{\partial t}\right|_d = \nu \nabla^2 \omega. \tag{3.10b}$$

3.4 Vortex-In-Cell (VIC) Method

Using the Biot-Savart Law to compute velocities can become prohibitively expensive since a simulation may contain as many as 100,000 vortices. On the other hand grid-based Navier-Stokes solvers cannot simulate the small-scale details with sufficient accuracy. As a result a method which combines an Eulerian mesh with Lagrangian vortex convection was developed. Christiansen (1973) was the first to use this scheme in relation to the interaction of vortex elements. In essence the Vortex-In-Cell method uses an Eulerian reference mesh on which to solve Poisson's equation ($\omega = -\nabla^2\psi$) introduced in Section 2.2 before the convection of vortices is simulated in a purely Lagrangian manner. A distribution of NV vortices of strength Γ_k is assumed. An area weighting scheme (see Figure 3.1) is then used to distribute vorticity from each point vortex to the surrounding mesh points:

$$\omega_{(m)} = \frac{\Gamma_k a_{(m)}}{a^2} \qquad (m=1,2,3,4) \tag{3.11a}$$

This yields the values of vorticity at the mesh points. By solving Poisson's equation the stream function values on the mesh points can be found. Equations (3.11b) and (3.11c) then give mesh point flow velocities which are re-interpolated onto the vortices before they are convected.

$$u_{i,j} = \frac{1}{J_{i,j}} \frac{\partial \psi_{i,j}}{\partial \eta}, \tag{3.11b}$$

$$v_{i,j} = -\frac{1}{J_{i,j}} \frac{\partial \psi_{i,j}}{\partial \xi} \tag{3.11c}$$

Diffusion can be incorporated into the method either by random walk or by forming a finite difference diffusion equation from (3.10b), as in Graham (1988). The random walk tries to represent diffusion in a statistical manner which is a rather indirect method of solving (3.10b). The change in vorticity at the mesh points is computed before being distributed to nearby vortices. If no vortices exist in the surrounding mesh, a new vortex is created at the grid point.

3.5 Calculation of force coefficients

The Blasius theorem has been the most commonly used method for evaluating forces in vortex methods as it directly relates body forces to the vorticity field. However for the flow around circular cylinders the gradient of vorticity method has also been successfully implemented.

3.5.1 Generalised Blasius theorem

The Blasius theorem can be derived from Bernoulli's equation (see Acheson (1990)); for a steady flow with complex potential $W(z)$, the components of force on the body are

$$F_X - iF_Y = \frac{1}{2} i\rho \oint_C \left(\frac{dW}{dz}\right)^2 dz. \tag{3.12}$$

Wu and Sankar (1980) have formulated what is called a generalised Blasius theorem, applicable to non-steady flows,

$$\boldsymbol{F} = F_X + iF_Y = \rho \frac{d}{dt} \int_R z \otimes \omega dx dy, \tag{3.13}$$

and it is straightforward to apply (3.13) within the DVM as will be seen in Chapter 4.

3.5.2 Gradient of vorticity method

A relationship for the change in pressure along a body surface can be deduced by applying boundary conditions to the momentum equation at the surface. The momentum equation in the x-direction is

$$\frac{\partial u}{\partial t} + u\frac{\partial u}{\partial x} + v\frac{\partial u}{\partial y} = -\frac{1}{\rho}\frac{\partial p}{\partial x} + \nu\left(\frac{\partial^2 u}{\partial x^2} + \frac{\partial^2 u}{\partial y^2}\right). \tag{3.14}$$

If we assume there exists a boundary at y=0 and apply the no-slip condition at the body surface, i.e. u,v=0 along y=0, we obtain:

$$\left.\frac{\partial p}{\partial x}\right|_{y=0} = \mu \left.\frac{\partial^2 u}{\partial y^2}\right|_{y=0} \tag{3.15}$$

Vorticity is defined as $\omega = \partial v/\partial x - \partial u/\partial y$ which is equivalent to $\omega = -\partial u/\partial y$ at the body surface and hence we derive

$$\frac{\partial p}{\partial x} = -\mu \frac{\partial \omega}{\partial y} \tag{3.16}$$

which relates the surface pressure gradient to the gradient of vorticity normal to the body surface.

3.6 Applications

Vortex methods have been applied to many flow situations and a comprehensive description of these would be too large to include here. Sarpkaya (1994) presents a fuller account but the following review is confined to two-dimensional simulations about bluff cylinders and a few three-dimensional computations.

3.6.1 Flows around circular cylinders

Gerrard (1967) was the first to apply the DVM to flow around circular shaped bodies. His work was an attempt to simulate high sub-critical Reynolds number flow past cylinders and ignored the effects of viscosity and turbulence. Individual vortices were shed at each time step from points slightly downstream of experimentally chosen separation points. The vortex strengths were determined from the velocity calculated at the introduction points and they were convected under action of the flow past the body and of the induced velocity from other vortex particles. His results for lift and drag were rather crude but highlighted the problems future research would encounter such as the computational expense incurred by a fully Lagrangian model, the singularities present in the flow when point vortices are used and the need to include some form of diffusion model in the simulation.

The time-splitting approach, which treated convection and diffusion separately, incorporating a random walk to simulate viscous diffusion, was first applied by Chorin (1973). His work looked at flow over a Reynolds number range, $10^2 \leq Re \leq 10^5$, but instead of point vortices, vortex blobs were used which ensured there were no singularities present in the flow. Because of the singularity associated with a point vortex, the convection of point vortices has a problem associated with the particles separation becoming too small leading to unrealistically high velocities. To overcome this vortex blobs consisting of evenly distributed vorticity over a small area are introduced, ensuring that for neighbouring blobs the flow remains bounded whilst distant blobs affect each other like point vortices. The vorticity transport equation is split into convection and diffusion parts, as in equations (3.9), with blob velocities induced from the vorticity field and diffusion represented by adding a random walk to the vortices' motion. The solution of (3.9b) can be statistically simulated by two independent sets of Gaussian random variables, each having zero mean and standard deviation defined by $\sigma=\sqrt{(2\Delta t/Re)}$. A full explanation can be found in Sarpkaya (1994). Each random variable represents the spatial displacement of a vortex element in one dimension, hence two variables are required. One may argue that the simulation of diffusion by a random walk method gives a good overall representation of the amount of viscous diffusion present in the flowfield. However locally it is not solving the diffusion equation explicitly.

Forces were evaluated by the gradient of vorticity method. Drag coefficient results showed C_D decreasing with Re roughly in line with experimental results but the drag crisis, shown in region EG of Figure 2.3, occurred too early. According to Chorin this was due to 'excess noise in the numerical calculations analogous to the early onset of turbulent flow in a noisy wind tunnel'. However beyond this region at $Re=10^5$, $C_D=0.27$ which agrees well with experimental data.

It must be emphasised that most DVM simulations have been trying to reproduce two-dimensional flow when any real flow will exhibit some three-dimensional phenomena. In an attempt to make some modifications for

three-dimensional effects Sarpkaya and Schoaff (1979) introduced a circulation reduction scheme which reduced the strength of each vortex by an amount proportional to its strength.

Smith and Stansby (1988) developed a model based on the Vortex-In-Cell method for convection and Chorin's (1973) random walks for viscous diffusion. Runs were carried out in the range of Reynolds numbers 2.5×10^2 to 10^5 and compared with two analytical time-series solutions for short times. Longer run times were compared with Eulerian finite-difference solutions and with some flow visualisation experiments. Vortices were introduced at the cylinder surface to satisfy the no-slip condition and agreement with other methods proved good provided enough vortices were created at each time step. As the Reynolds number was increased more vortices were required. The authors suggested that convergence with fewer vortices might be achieved by using vortex blobs incorporated into a suitably-defined Vortex-In-Cell algorithm.

Ogami and Akamutso (1991) were the first to use the diffusion velocity approach for viscous flow simulation. From the vorticity transport equation (3.9) they derived the following equation,

$$\frac{\partial\omega}{\partial t}+\frac{\partial}{\partial x}\left[\left(u-\frac{\nu}{\omega}\frac{\partial\omega}{\partial x}\right)\omega\right]+\frac{\partial}{\partial y}\left[\left(v-\frac{\nu}{\omega}\frac{\partial\omega}{\partial y}\right)\omega\right]=0, \tag{3.17a}$$

where the convection velocities u and v are found from Biot-Savart summation and diffusion velocities u_d and v_d are defined as

$$u_d=-\frac{\nu}{\omega}\frac{\partial\omega}{\partial x}, \tag{3.17b}$$

$$v_d=-\frac{\nu}{\omega}\frac{\partial\omega}{\partial y}. \tag{3.17c}$$

Gaussian vortex cores were employed to simulate flows at Re=40 and 1200. The results compared favourably with DNS calculations and showed an improvement on a random vortex method, particularly at low Re. The main problem with this approach is the computational expense incurred in evaluating convection and diffusion velocities. According to Sarpkaya (1994) the diffusion velocities, based on a Gaussian vorticity distribution, do not satisfy the equation of continuity which implies that the theoretical foundations of this model are also inappropriate.

A novel method has been introduced by Clarke and Tutty (1994) in an attempt to reduce computational cost without resorting to the Vortex-In-Cell method. They have formulated a "zonal decomposition algorithm" for the Biot-Savart velocity summation. The effects of vortices sufficiently distant from the calculation point are clumped into single equivalent vortices while nearby vortices are treated in the normal fashion. Viscous effects are included using a combination of the random walk and diffusion velocity techniques and body representation is via a panel method. Although runs up to Re=3000 produced satisfactory results, some doubt exists as to how effective this method is at reducing computational cost.

3.6.2 Flows around sharp edged bodies

For sharp-edged bodies an accurate form of body representation is required to ensure the boundary condition at the surface is satisfied. Problems can arise at corners, with mathematical singularities yielding physically inaccurate flow properties. One advantage of sharp-edged bodies is that the separation point is fixed whereas the circular cylinder requires careful determination of separation points for introduction of discrete vortices.

Ham (1968) applied the discrete vortex method to the aerodynamic loading of a two-dimensional aerofoil during dynamic stall. Beyond the stall angle of attack separation takes place over a large percentage of the wing section surface area and thus at high incidence a bluff body flow simulation using the DVM is appropriate. Clements (1973) modelled the flow behind a semi-infinite square-based cross section. An appropriate Schwartz-Christoffel transformation projects the exterior region of the body onto the upper half plane with the body boundary represented by the real axis. Vortex velocities are found from addition of the free-stream potential flow and the velocities induced by all the other vortices. Image vortices of opposite sign but equal strength are required to satisfy the surface boundary condition. Vortices were introduced at the corners or separation points but to avoid flow singularities their velocities were determined a short distance away at the edge of the shear layer. The strength of these shed vortices was determined from the relationship $\Gamma=(U_s^2/2)$. An amalgamation scheme was used to limit the computational expense required. Clusters of vortices that had passed a suitable distance downstream were replaced by a single equivalent vortex. Good predictions for the Strouhal number, the form of vortex shedding and some of the mean flow velocities were obtained but no force coefficients were calculated.

A similar study was conducted for flow over inclined flat plates by Sarpkaya (1975). The Joukowski transformation is used to represent the body surface as a circle in the computational plane. The model did not account for viscous diffusion in any way but included amalgamation of vortices and removal of those particles which approached the body boundary too closely. Normal force coefficients were somewhat larger than those obtained experimentally, probably because the effects of viscous diffusion were neglected, but the Strouhal number was predicted satisfactorily.

An investigation into the flow around rectangular prisms was carried out by Nagano *et al* (1982). Gaussian vortices (3.7b) were adopted in a Lagrangian scheme. The core growth of Gaussian vortices implies some viscous diffusion is present but to account for the experimentally-measured loss of vorticity a circulation reduction scheme was introduced. Figure 3.2(a) shows the reduction in circulation strength measured experimentally in the wake. In the simulation this circulation reduction is approximated by imposing a decay of the individual vortex strengths as a function of time (see Figure 3.2(b)). Vortex clusters that have travelled sufficiently far downstream are amalgamated according to equation (3.8). Forces were obtained from the generalised Blasius theorem and showed good comparison with experiment.

In each of the studies by Ham, Clements, Sarpkaya and Nagano, vorticity is created by the introduction of vortex particles at the separation points at each time step. This arbitrary introduction of vorticity at the separation points is insufficient, since vorticity can clearly be created at all points along the fluid-solid interface. A more realistic scheme is therefore required which creates vorticity along the entire body boundary.

A random vortex method was used by Summers et al (1985) to compute the wind-induced loadings on buildings. The boundary layer around the obstacle was modelled by sheets of vorticity sufficiently distributed to ensure the no-slip boundary condition was satisfied. Discrete vortex elements were created at the edge of this shear-layer and subsequently convected. Any vortices returning to the shear layer were amalgamated with other sheets of vorticity or became sheets themselves.

Dolan et al (1990) used the hybrid vortex-in-cell method to simulate the vortex streets formed around a triangular vortex obstacle in a bounded flow. According to Dolan the presence of an outer boundary appears to force the flow to exhibit strongly two-dimensional vortex shedding, making a 2D vortex method a suitable model for simulation. An expanding mesh was applied to the near-body region and this was combined with a regular mesh for the outer region (see Figure 3.3). This was necessary since the conformal transformation applied to the body geometry could not accommodate the pipe boundaries. Some previous experimental work had been performed and the values of Strouhal number and mean drag coefficient were in good agreement with these. Figure 3.4 shows flow visualisation from this simulation.

3.6.3 Oscillatory flow applications

Many bluff body flows of real engineering importance have an oscillatory component in the upstream flow, such as pumped flow past vortex-shedding flowmeters or the combined wave and current motion past offshore structures. For a certain range of frequencies and amplitudes the wake characteristics can be seriously altered. In particular the vortex shedding frequency can "lock onto" or resonate with the oscillatory flow frequency. Some bridges have been known to collapse in heavy gales when the vortex shedding has locked onto the frequency of the bridges' wind-induced oscillations. Other applications include the flow past vortex shedding flowmeters where flowrate is measured proportional to shedding frequency. If the vortex shedding frequency is altered by some upstream disturbance then an erroneous measurement will be indicated.

An interesting application to oscillatory flow was carried out by Longuet-Higgins (1981) in an attempt to calculate the drag coefficients over steep sand ripples. He used the basic Lagrangian form of the vortex method together with a series of conformal transformations (see Figure 3.5) to represent the flowfield on the interior of a circular cylinder. The model neglected viscous diffusion but included a simple amalgamation scheme to combine clusters of vortices which had moved a sufficient distance from the boundary into a single equivalent vortex. Calculated drag coefficients compared well with both laboratory and field experimental results.

Smith and Stansby (1991) used Chorin's (1973) random vortex method, combined with a conformal transformation for body representation and a VIC algorithm for computing velocities efficiently, to study the oscillatory flow around variously-shaped cylindrical bodies. Their research was concerned with the oscillatory motion of cylinders within fluids and in particular how hydrodynamic damping works to reduce the amplitude of motion. This was simulated by assuming the fluid to be oscillating with a velocity amplitude U_A and the cylinder motionless. As such it is no longer appropriate to define the flow by the Reynolds number, and an alternative non-dimensional parameter, the Keulegan-Carpenter number $K=U_A t/d$ (where t is the period of oscillation and d the cylinder diameter) is used. Drag coefficients were averaged over half cycles of the flow and a

comparison with experimental results showed reasonable agreement. The authors' discussion concentrated on flow visualisation of the vortex structures present and how these structures are affected by changing the Keulegan-Carpenter number. Their flow visualisation remained symmetric for $K<2.0$ but above this value the vortical structures became increasingly asymmetric, in contrast with the laboratory visualisation for which symmetry persisted until a value of $K=4.0$. This may in part have been due to the fact that diffusion was modelled by the random walk method, introducing asymmetrical disturbances into the simulation.

With a similar model Yeung and Vaidhyanathan (1993) studied forced and vortex-induced oscillations of a circular cylinder, the oscillations being normal to the free stream flow. The random vortex method was used in conjunction with a boundary integral method. To increase computational efficiency a VIC scheme was incorporated into the velocity calculation, the grid being composed of a fine inner mesh (128×128) and a coarse outer mesh (256×256). The size of the outer mesh was enlarged at each time step so that particles, once created, could not be removed from the calculation. Results for uniform flow, forced cylinder oscillations and vortex-induced oscillations were given for Reynolds numbers of 1000-3000. The lock-in phenomenon was reproduced for a range of amplitudes and frequencies of oscillation but the authors considered their quantitative results to be unrealistic (when compared with laboratory experiments) as no circulation reduction scheme was present in the model. However this lack of agreement is to be expected at the Reynolds numbers chosen for this simulation. 3D instabilities become increasingly important as the Reynolds number is increased and it is highly questionable that a circulation reduction scheme could have effectively accounted for the appearance of these instabilities.

A hybrid vortex-in-cell method, with the diffusion equation (3.10b) solved on a finite difference mesh, has been implemented very effectively by Meneghini and Bearman (1993). The simulations were only conducted at low Re but showed the lock-in boundary for transverse oscillatory flow and demonstrated a new mode of vortex shedding (see Figure 2.33). Figure 2.32 shows the lock-in boundary with f the forcing frequency, f_s the natural shedding frequency, y_e the amplitude of cylinder oscillation and d the cylinder diameter. Mean force coefficients compared well with experimental results. The main drawback of this method is the introduction of a finite difference mesh which needs to be very fine to model the shear layer accurately.

3.6.4 Three-dimensional applications

Vortex methods which attempt three-dimensional simulations are far rarer in the literature and have only recently been applied to bluff body applications. Extra difficulties arise from the increased computer power required to calculate such flows and from the need to include the vortex stretching term in the vorticity transport equation (3.9), which can be neglected in two dimensions. Since it is known that spanwise instabilities develop in circular cylinder wakes above $Re\approx180$ it is reasonable to suggest that similar phenomena will occur for other cylinder wakes and thus two-dimensional models will be insufficient for such simulations.

Leonard (1985) has reviewed the computations by 3-D vortex methods concentrating on wing tip vortex interaction and the interaction of ring vortices in an unbounded medium. Couet *et al* (1981) calculated the time evolution of two vortex rings using a vortex-in-cell scheme with vortex filaments. Bluff body applications are

even less common but a few studies have been made recently. Kiya (1992) simulated the flow past a circular disk using vortex blobs and a fully Lagrangian scheme based on the Biot-Savart law for the convection of blobs. A spiral wake structure was observed which showed that the model was capable of capturing a three-dimensional wake. However no comparison was made with any existing measurements such as wake velocities or disk drag and so it is difficult to gauge how the simulation relates to a physical flow at the present stage.

A 'fast' vortex method is described by Chua and Quackenbush (1993) who have attempted to speed up the velocity calculations by imposing a grid of cubic boxes onto the computational area and clustering the vortex elements within each box together. The velocity field is then calculated from a twofold summation of near-field and far-field components. At a given point the velocity induced by the near field consists of a Biot-Savart summation of those vortices within the same box and those within adjoining boxes. Vortices more than one box length away are considered as far-field; their influence is evaluated at the centre of the box and a Taylor series expansion estimates the velocity at particular points within the box. A direct Biot-Savart summation requires a run time proportional to NV^2. This contrasts with the 'fast' vortex method for which a run time proportional to $NV^{1.63}$ is necessary. The propagation of an isolated vortex ring is computed both by direct Biot-Savart summation and by the fast vortex method and there is a negligible difference in results. This method will probably prove useful for high Reynolds number inviscid simulations but would be inappropriate for application at low *Re* unless a non-mesh based viscous diffusion scheme could be incorporated into the model.

Doorly and Liu (1994) describe a Particle-In-Cell viscous vortex method which computes the impingement of a vortex ring on a wall. The vortex rings are approximated by many overlapping vortex blobs. Vortex blobs were originally introduced in order to avoid the singularities present when point vortices are employed. However by implementing a particle-in-cell scheme these flow singularities are excluded from the calculations and it is not clear what further benefits can be derived from using vortex blobs within a PIC method. The method shows promise for the simulation of developing instabilities within boundary layer flows and a comparison with the laboratory visualisation for a vortex ring rebounding off a wall shows reasonable agreement over a short time but detailed comparisons of any measurable quantities were not made.

Computations of the flow past circular cylinders has been undertaken by Graham and Arkell (1994) in an extension of the two-dimensional hybrid vortex method developed by Graham (1988) and described earlier. The simulation employs an unstructured tetrahedral mesh set-up (see Figure 3.6) with a fine near-body resolution and coarse outer mesh. Using a tetrahedral mesh ensures that the vortex-in-cell scheme remains efficient, as there are only four nodes within each cell, but requires a finite element method for the solution of the vorticity-velocity formulation. Initially the code was tested on a circular cylinder of height half the diameter. A symmetry condition was imposed at either end of the cylinder and this, combined with restricting the cylinder's height, ensured that the flow remained two-dimensional. As previously discussed in Chapter 2 three-dimensional spanwise instabilities are known to occur at wavelengths similar to the cylinder diameter, A or at $4A$. The authors found good agreement for this test case with the 2-D results but did not try modelling the behaviour of longer cylinders, although this would certainly be an interesting area for further research as numerical simulations have not, as yet, modelled the appearance of such spanwise instabilities. The flow past a mildly

tapered circular cylinder was also examined and vortex dislocations were found to appear towards the end with smaller diameter as a result of the discontinuity in shedding frequencies between the two ends (see Figure 3.7).

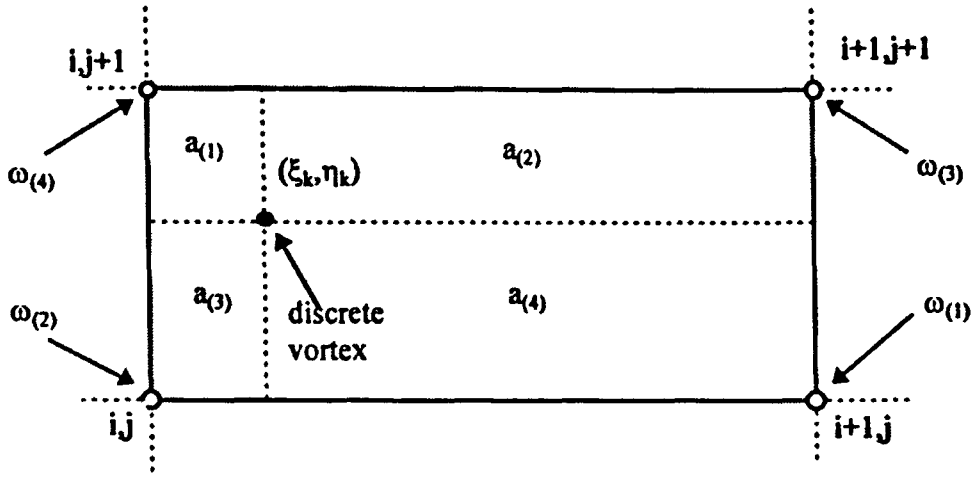

Figure 3.1 Area weighting scheme to distribute vorticity

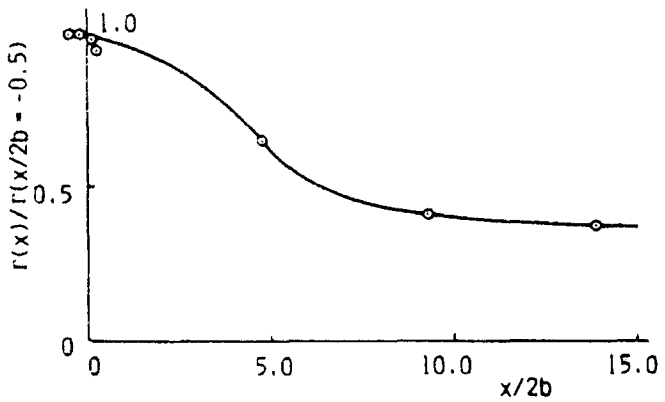

(a) Loss in vorticity obtained experimentally for square prism at Re=2.5×10^4
x/2b represents the distance travelled downstream.

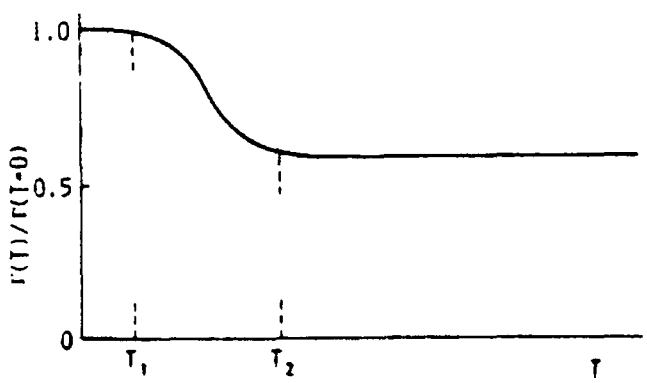

(b) Loss in vorticity approximated by numerical model, T is time since creation of vortex element.

Figure 3.2 Experimental observation and numerical approximation of vorticity loss from Nagano *et al* (1982).

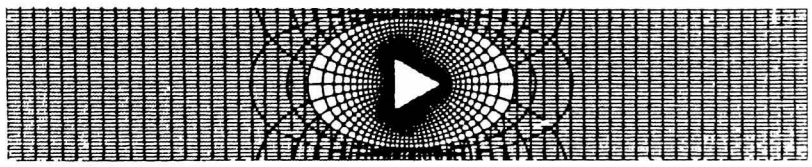

Figure 3.3 Double mesh for triangular body in duct (Dolan *et al*, 1990)

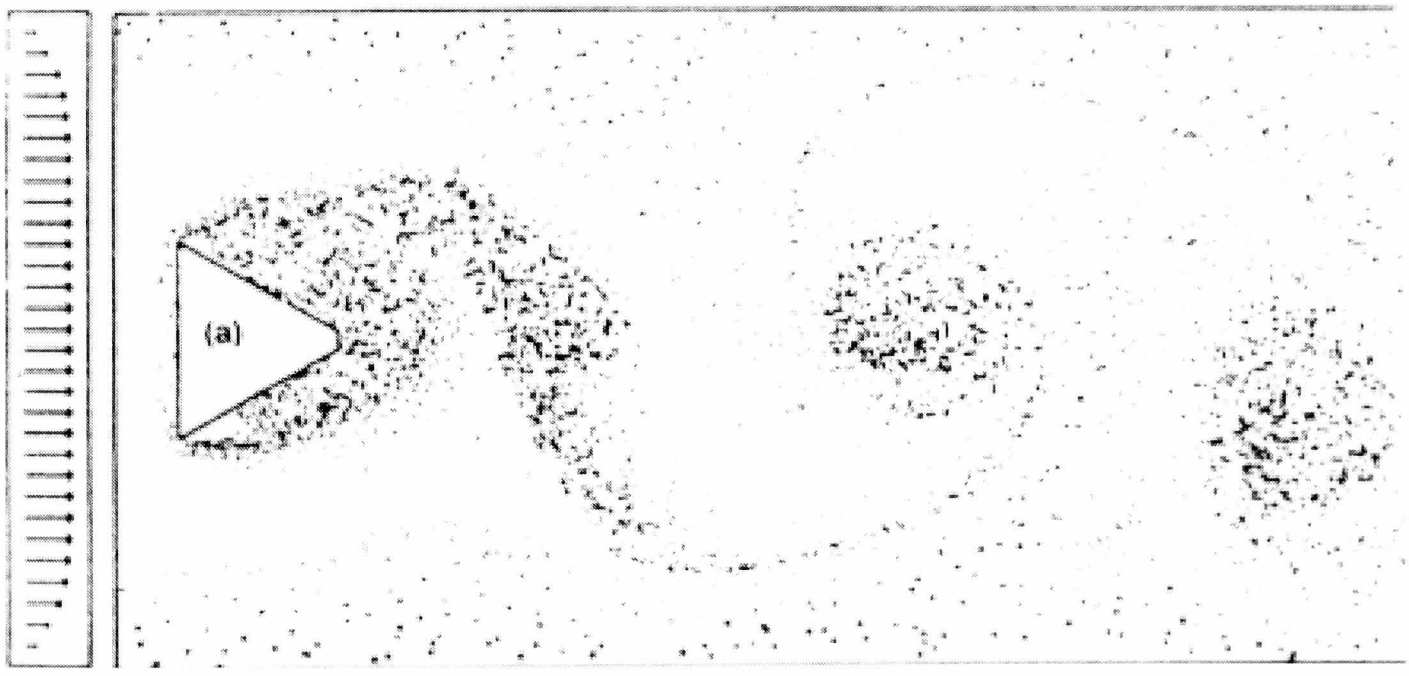

Figure 3.4 Vortex street for symmetric velocity profile (Dolan *et al*, 1990)

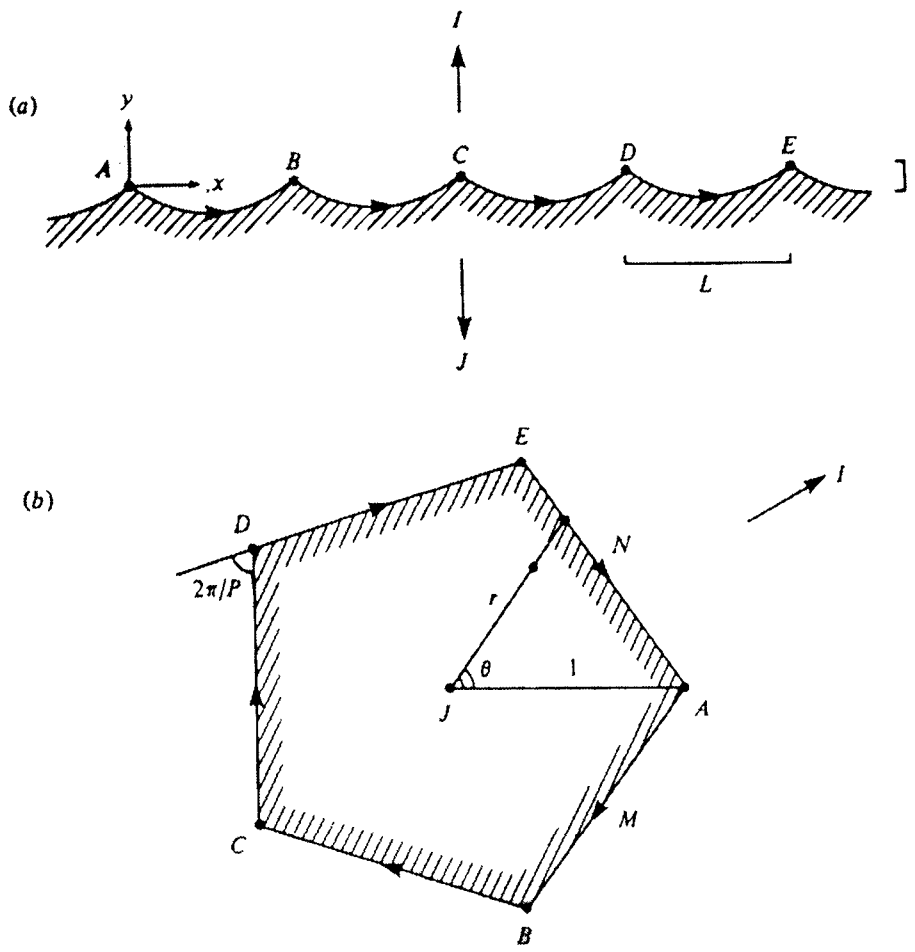

Figure 3.5 Conformal transformation takes flow from (a) physical plane (ripple profile) to (b) exterior of a polygon and from there to the interior of a circle (computational plane), Longuet-Higgins (1981).

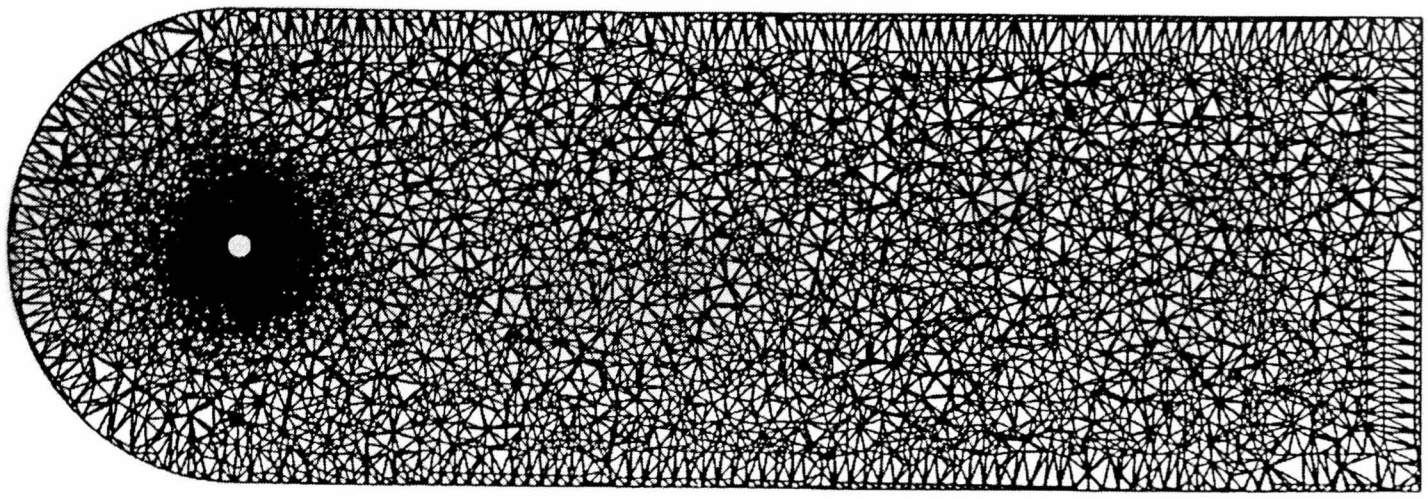

(a)

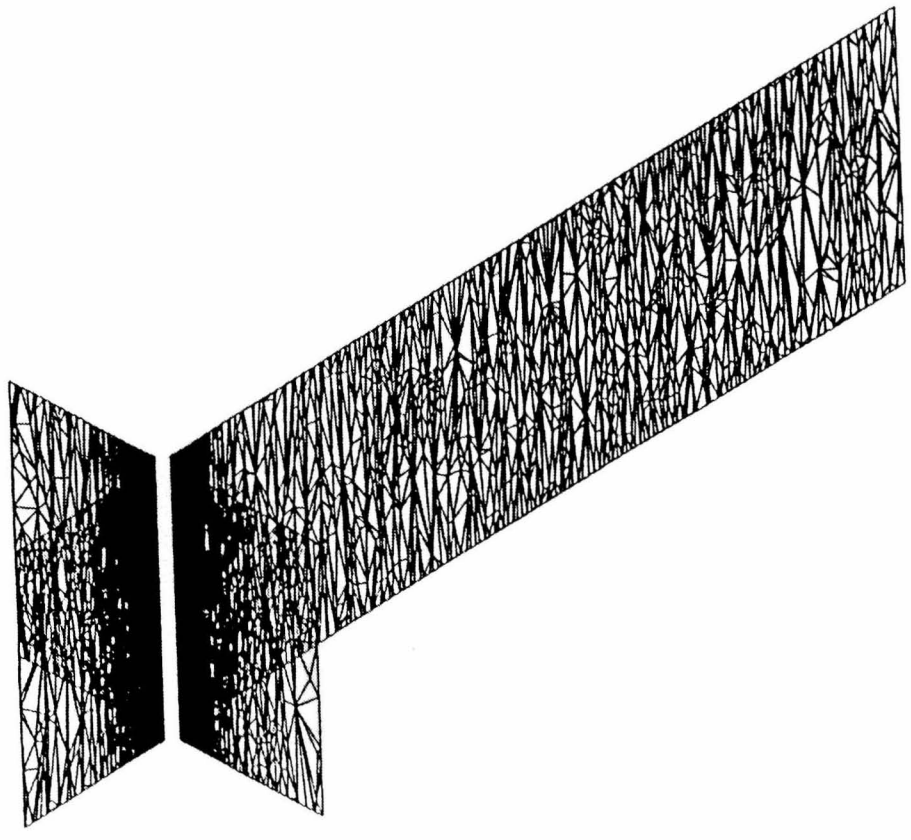

(b)

Figure 3.6 Unstructured tetrahedral mesh employed by Graham and Arkell (1994)
(a) x-y slice, (b) x-z and y-z slices.

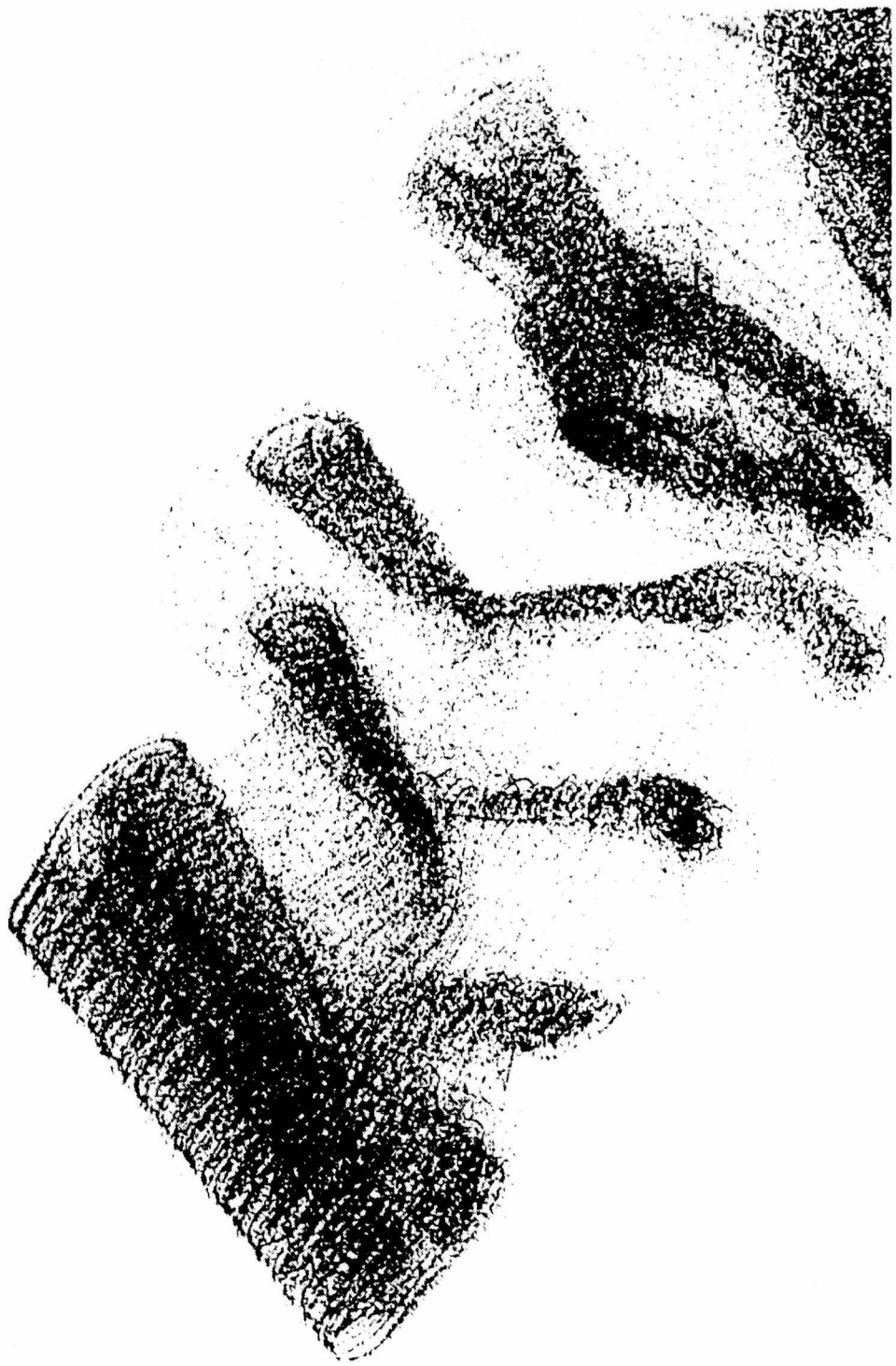

Figure 3.7 Vortex dislocation in shedding past tapered cylinder from Graham and Arkell (1994)

Chapter 4

The Hybrid Discrete Vortex Method

The code used in this study was first developed at Imperial College (Graham, 1988). Subsequent applications of the code included those by Dolan *et al* (1990) who simulated the vortex streets formed around a triangular shaped body and Meneghini and Bearman (1993) who predicted the lock-in boundary for a circular cylinder subjected to cross-flow oscillations. The research described here commenced with the intention of studying flows about shapes typically used by vortex-shedding flowmeters; i.e. rectangular, triangular and T-shaped.

Major alterations were required to the conformal transformation, grid set-up and method of calculating forces. The Schwarz-Christoffel transformation was applied to allow the simulation of flows past any rectangle. The grid was set up in such a way that the user has direct control over the placing of the inner and outer mesh positions. Previously the Blasius theorem or gradient of vorticity method have been used to calculate forces but the presence of sharp edges necessitated a new method in this study. A formulation for the generalised momentum equations was derived which yielded an integral relationship for the change in pressure along the surface.

A description of the theory is given which closely follows that of Meneghini (1994). Certain corrections have been made due to the confusion which existed in the relations between circulation and vorticity in his study. An outline and flowchart give a clearer indication of how the simulation follows the theory. The chapter concludes with a summary of those modifications made during the course of the current research.

4.1 Equations in transformed plane

All calculations take place in a transformed co-ordinate frame; therefore the Navier-Stokes equations must be formulated in a manner valid for an arbitrary co-ordinate transformation $x = f(\xi, \eta)$, $y = g(\xi, \eta)$. Vorticity and velocity in the transformed plane are defined as follows:

$$\tilde{\omega} = \frac{1}{J}\left(\frac{\partial(J\dot{\eta})}{\partial\xi} - \frac{\partial(J\dot{\xi})}{\partial\eta}\right), \tag{4.1a}$$

$$\tilde{u} = (\dot{\xi}, \dot{\eta}). \tag{4.1b}$$

Tildes have been used to represent variables in the transformed plane. J is the Jacobian or mapping derivative of the transformation, given by

$$J = \begin{vmatrix} \frac{\partial x}{\partial \xi} & \frac{\partial x}{\partial \eta} \\ \frac{\partial y}{\partial \xi} & \frac{\partial y}{\partial \eta} \end{vmatrix}. \tag{4.1c}$$

4.1.1 Vorticity transport equation

The vorticity transport equation was introduced in Chapter 3(see equation 3.9). For a general co-ordinate transformation and for a two-dimensional application it can be written

$$\frac{\partial \tilde{\omega}}{\partial t} = \frac{\nu}{J} \nabla^2 \tilde{\omega} - \tilde{u}.\nabla \tilde{\omega}, \tag{4.2}$$

The derivation of (4.2) can be found in Meneghini (1994). An operator splitting technique is then used to split the temporal change of vorticity into convection and diffusion parts:-

$$\left[\frac{\partial \tilde{\omega}}{\partial t}\right]_{convection} = -\tilde{u} \cdot \nabla \tilde{\omega}, \tag{4.3a}$$

$$\left[\frac{\partial \tilde{\omega}}{\partial t}\right]_{diffusion} = \frac{\nu}{J} \nabla^2 \tilde{\omega}. \tag{4.3b}$$

Viscous diffusion is incorporated by a finite difference approximation of (4.3b) and this is outlined in Section 4.6. A stream function is introduced to determine convection velocities as described below.

4.1.2 Poisson's equation

The velocities in the transformed plane, $\dot{\xi}$ *and* $\dot{\eta}$, are defined in terms of the stream function ψ by

$$\dot{\xi} = \frac{1}{J} \frac{\partial \psi}{\partial \eta}, \qquad \dot{\eta} = -\frac{1}{J} \frac{\partial \psi}{\partial \xi}. \tag{4.4}$$

Combining (4.4) with the definition of vorticity (4.1a) leads to Poisson's equation relating the vorticity in the transformed plane to the stream function:

$$\frac{\partial^2 \psi}{\partial \xi^2} + \frac{\partial^2 \psi}{\partial \eta^2} = -J\tilde{\omega}. \tag{4.5}$$

Convection of vorticity is simulated in a mixed Eulerian-Lagrangian manner. Vorticity, the stream function and velocities are first calculated on a finite difference mesh before being interpolated onto individual vortex particles ready for advection to new positions. An outline of the code follows before a more detailed description of individual components is given.

4.2 Outline of code

Figure 4.1 presents a flowchart outline for the running of the DVM code. As can be seen two versions exist. Poisson's equation relating the stream function and vorticity is solved on the mesh using Fast Fourier Transform (FFT) techniques. In the versions of the code written by Graham (1988) and Meneghini (1994) the stream function is solved twice within each time step.

4.2.1 Initial set-up

Initially user defined variables must be declared such that the conformal transformation and grid can be set up. The transformation works in such a way that the maximum cross-stream dimension d is found within the code and not set by the user. Instead the Reynolds number is user-defined and the upstream flow velocity U_o is calculated to give the required Re:

$$U_0 = \frac{Re.\nu}{d}. \tag{4.6}$$

In addition the time step Δt, vortex cut-off strength σ, number of grid points (NX, MY) and total number of time steps must be defined. At present the code is equipped to model circular and rectangular geometries. Once the conformal transformation and mapping derivatives have been calculated the simulation begins with iterations as described below and outlined in Figure 4.1.

4.2.2 First time step

At the beginning of the first time step the flow is assumed to be inviscid and thus there are no vortex particles present in the flow. In step (**C1**) since the vorticity is zero, only the potential solution yields a contribution to the stream function, $\psi_{i,j}$. (**D**) then solves the finite difference diffusion equation on the mesh before (**F**) creates

new vortices at mesh points where $\Delta\Gamma_{i,j}$ is above the threshold value σ. Mesh velocities are directly related to the stream function and hence vortices are convected in (**H**).

4.2.3 Subsequent time steps

At the beginning of each subsequent time step a distribution of NV vortices will exist which are interpolated onto the mesh, step (**B**), to find the mesh values of circulation, $\Gamma_{i,j}$. Since there is now a vorticity field the stream function in (**C1**) is found as a summation of the potential value and the solution to Poisson's equation. The finite difference diffusion equation is solved in (**D**), and step (**E**) is now necessary to distribute the change in vorticity to nearby vortices. In step (**F**) new vortices are created at mesh points (i,j) where there are no neighbouring vortices and $\Delta\Gamma_{i,j} > \sigma$. Those with a strength less than σ are removed from the calculation in (**G**). After convection (**H**) the force coefficients can be evaluated if required. However (**I**) does not alter the convection or diffusion of vorticity in any way and thus it is not necessary to compute these at every time step.

Graham's original code included an extra step (**C2**) in which the stream function was re-calculated after the diffusion step (**D**). After updating the mesh values of vorticity an FFT is again performed to re-compute stream function values before calculating the convection velocities. Performing FFT's is an expensive operation and thus an argument exists for simply solving Poisson's equation once, in each time step, making considerable savings in time. This could also be thought of as simulating diffusion and convection simultaneously, which is what occurs physically, therefore providing a more accurate representation of the fluid flow. The two versions were compared for uniform flow cases during the initial stages of this project and the findings are reviewed in section 4.10.

4.3 (Step A) Conformal transformation and grid set-up

The choice of mesh is very important in our simulation. Generation of vorticity occurs at the body surface and it is desirable that our model more accurately follows the fluid motion in the boundary layer region close to the body surface. A conformal transformation is used which takes the body surface in the physical plane onto a line segment, $0 \le \xi \le 2\pi$, in the computational plane. The region of interest, in this transformed (ξ,η) plane, is a bounded rectangle (see Figure 4.2) with the ξ axis representing the body surface. Provided a suitable transformation, of the form $x = f(\xi,\eta)$, $y = g(\xi,\eta)$, can be found the flow about any obstacle can be modelled. Constraints on the solution of Poisson's equation require the mesh to be uniformly spaced and periodic in one direction, although it can be variable in the other. The transformation simplifies the imposition of boundary conditions and allows a rectangular mesh to be set up which is periodic in the ξ-direction. The mesh spacing must therefore be uniform in the ξ-direction but may vary in the η-direction such that the near body region is more finely resolved.

4.3.1 Schwarz-Christoffel formulation

The Schwarz-Christoffel formulae can be found in many standard textbooks on conformal mapping and complex analysis; e.g. Nehari (1952) and Phillips (1957). The formulae give mappings between the regions exterior and interior of polygons to the regions exterior and interior of circles. Since we can also map from circles onto half planes or strips a whole series of transformations exist which are useful in the fields of fluid dynamics and electrostatics. The following expression, taken from Bieberbach (1953, p117), maps the region exterior to the unit circle, $|t| \geq 1$, onto the exterior of a polygon with exterior angles $\alpha_k \pi$:

$$\frac{dz}{dt} = C_{ct} \frac{(t-a_1)^{\alpha_1}(t-a_2)^{\alpha_2}.....(t-a_n)^{\alpha_n}}{t^2}, \tag{4.7a}$$

where the constant C_{ct} is a complex correction factor which adjusts the polygon size and orientation. The constants a_k and α_k must satisfy the following conditions:

$$\sum \alpha_k = 2, \tag{4.7b}$$

$$\sum a_k \alpha_k = 0, \tag{4.7c}$$

$$|a_k| = 1. \tag{4.7d}$$

The last condition signifies that the a_k are points on the unit circle; they correspond to the polygon's vertices under the mapping.

For this study a transformation was required which could take the exterior of a rectangle onto a semi-infinite strip in the computational plane. This meant that an expression had to be derived which combined the transformation (4.7a) with one between the unit circle and the required rectangular strip. A full derivation is provided in Appendix A and the final transformation is

$$\frac{dz}{d\Omega} = \sqrt{2}\sqrt{cos(2(\Omega - \Omega_0)) - (\beta^2 - \gamma^2)}, \tag{4.8}$$

where the constant C_{ct} has been assumed equal to unity. This means that the code user has no control over the rectangle size. Since the Reynolds number and fluid viscosity are user-defined the upstream velocity is calculated, within the code, to give the required Re. Flows at incidence were simulated by changing the velocity direction rather than altering the body geometry. From (4.8) it is possible to explain how the computational grid was set-up.

4.3.2 Grid set-up

The grid must be uniform and periodic in the ξ-direction in order that FFT methods may be used to solve Poisson's equation. In the η-direction it is desirable that the mesh spacing varies as in the boundary layer and near wake region good resolution is necessary but far from the body less resolution is required. Meneghini (1994) tested two different η expansions in his calculations. A quadratic expansion was found to be better than an exponentially-varying mesh as the outer cell sizes did not grow as rapidly. Initially their quadratic mesh expansion was applied for this transformation but it was found to be too inflexible in that the outer extent of the grid and more importantly the inner cell spacing could not be controlled in a satisfactory manner. As a result a grid set-up was developed which gives the code user more control. Two user-defined variables are introduced, M_{in} and M_{out}, which define the distances to the first grid line out from the body and to the outer boundary in relation to the rectangle diameter. A summary of the way in which the mesh is set-up follows:-

(i) Find surface mesh points and rectangle dimensions

Initially the surface mesh points $(x_{k,1},y_{k,1})$ are found by integrating along η=0 from ξ=0 to ξ_k,

$$x_{k,1}+iy_{k,1}=\int_{\xi=0}^{\xi_k}\left.\frac{dz}{d\Omega}\right|_{\eta=0}d\xi=\int_{0}^{\xi_k}\sqrt{2(cos(2(\xi_k-\pi))-2\beta^2+1)}d\xi, \tag{4.9a}$$

where

$$\xi_k=\frac{2\pi k}{NX} \tag{4.9b}$$

This integral (4.9a) is approximated by a rectangular rule summation over small increments $\Delta\xi$/1000. We need only calculate the mesh points up to k=NX/4 since the rectangle and grid are symmetric about the x and y axes. The rectangle length B and diameter A are then given by,

$$B=2y_{nx/4,1}, \qquad A=2x_{nx/4,1}. \tag{4.9c}$$

(ii) Calculate η_2 and η_{MY}

η_2 and η_{MY} are the η values at the first mesh point out from the body and at the outermost mesh point in the computational plane and must be found before the constants which define the quadratic mesh variation (see below) can be calculated. M_{in} and M_{out} are user defined variables to control these positions in the physical plane. M_{out} is the number of body diameters from the body surface to the mesh outer boundary and M_{in} is the number of body diameters to the first mesh point out from the body. The distance to the first mesh point from the body surface varies in the physical plane, being smallest at the corners and largest at the mid-points of the sides. For this reason M_{in} is defined at the mid-point of the upper side surface. Then the boundary layer region can be

resolved adequately by a suitable choice of M_{in}. The integration is taken along $\xi=\pi/2$ from $\eta=0$. η_2 and η_{MY} are found as the required limits of the integrals;

$$iM_{in}A = \int_0^{\eta_2} \sqrt{2(cos(2(i\eta - \frac{\pi}{2})) - 2\beta^2 + 1)}\, d\eta; \tag{4.10a}$$

$$iM_{out}A = \int_0^{\eta_{MY}} \sqrt{2(cos(2(i\eta - \frac{\pi}{2})) - 2\beta^2 + 1)}\, d\eta. \tag{4.10b}$$

As in (4.9a) these integrals were approximated by a rectangular rule summation over many small intervals of $\Delta\eta$. Typically M_{in}=0.025 and M_{out}=100 and the effect of varying these parameters has been examined in the next Chapter.

(iii) Solution of quadratic grid variation

As previously mentioned Meneghini (1994) tested an exponential and a quadratic expansion of his mesh, deciding that the exponential expansion was too fast, i.e. grid sizes became too large too quickly so that the outer region was not suitably resolved. Therefore for this study a quadratic expansion of the form

$$\eta_j = k_1 j^2 + k_2 j + k_3 \tag{4.11a}$$

was chosen. At the body surface j=1 and η_1=0. Thus k_3 follows immediately as k_3=-k_1-k_2. η_2 and η_{MY} correspond to the mesh points at j=2, j=MY and thus simultaneous equations can be written to find k_1 and k_2:

$$\eta_2 = 3k_1 + k_2, \tag{4.11b}$$

$$\eta_{MY} = (MY^2 - 1)k_1 + (MY - 1)k_2. \tag{4.11c}$$

Hence the constants k_1 and k_2 are

$$k_1 = \frac{[\eta_{MY} - \eta_2(MY - 1)]}{(MY - 1)(MY - 2)}, \tag{4.11d}$$

and

$$k_2 = \eta_2 - 3k_1. \tag{4.11e}$$

Once these constants have been determined, equation (4.11a) is used to calculate the mesh point values of η for all j between j=2 and j=MY-1.

(iv) Perform conformal transformation on quarter plane

After calculating the η_j from (4.11a) the rest of the mesh co-ordinates in the physical plane $(x_{i,j},y_{i,j})$ can be computed:

$$\begin{aligned} x_{k,j}+iy_{k,j} &= x_{k,1}+iy_{k,1}+\int_{\eta=0}^{\eta_j}\left.\frac{dz}{d\Omega}\right|_{\xi_k} d\eta \\ &= x_{k,1}+iy_{k,1}+\int_{0}^{\eta_j}\sqrt{2(cos(2(\xi_k-\pi+i\eta))-2\beta^2+1)}d\eta \end{aligned} \tag{4.12}$$

These need only be calculated for k=1 to $NX/4$ since the grid is symmetric. A double reflection is then used, purely for convenience, as it saves time in the set-up part of the simulation.

(v) Calculate Jacobian at each mesh point

The physical plane mesh co-ordinates $(x_{i,j},y_{i,j})$ are only needed when graphical output of the vortex positions is required and play no part in the simulation evolution. The Jacobian of the transformation is required throughout the calculations as can be seen from the representation of the equations in an arbitrary co-ordinate system detailed in Section 4.1. For a transformation given by

$$z = f(\Omega) = \int_0^{\Omega} g(\Omega')d\Omega', \tag{4.13a}$$

the Jacobian can be expressed as

$$J = |f'(\Omega)|^2 = |g(\Omega)|^2. \tag{4.13b}$$

Hence for the rectangular geometry transformation the Jacobian is given simply by

$$J = 2\left|cos\,2(\Omega-\Omega_0)-\beta^2+\gamma^2\right|, \tag{4.13c}$$

or at the mesh co-ordinates,

$$J_{k,j} = 2\left|cos\,2(\xi_k+i\eta_j-\pi)-\beta^2+\gamma^2\right|. \tag{4.13d}$$

For the transformation of sharp edged obstacles J is zero at the vertex points which implies a singularity in the flowfield. It is therefore necessary to apply special attention to the value of J in this region. Some kind of smoothing is necessary, equivalent to a slight smoothing of the corner itself, in order to remove the resulting singularities from the simulation. Graham (1994) wrote a DVM code to simulate the flows past square (B/A=1.0) cylinders in which the Jacobian value at the vertex points was set to the value at the first mesh point

out: $J_{vp,1}=J_{vp,2}$ where vp has been used to indicate vertex position. However a more general scheme was required for this study since for rectangles of longer and shorter side ratio the Jacobian becomes very small at several grid points in the near corner region. A limiting value J_{lim} is chosen. At grid points for which $J_{k,j}<J_{lim}$ an ad-hoc smoothing scheme is applied to update values of $J_{k,j}$:

$$J_{k,j} = J_{lim} + \frac{3(J_{k,j+1} - J_{lim})}{4} \tag{4.13e}$$

The scheme starts at grid points a few cells away from the body surface before moving in to the body grid points in order to achieve a smooth variation in the Jacobian. J_{lim} was set to be 0.01, for all calculations, which is comparable to the minimum Jacobian value used in Graham's code. The effect of altering J_{lim} or the Jacobian smoothing scheme was not extensively tested in this study. However Scolan and Faltinsen (1994) have used a Vortex-In-Cell Method to study the flow around cylinders with sharp edges. In their study the mapping derivative was artificially smoothed at and near the corners. It was shown that this artificial treatment of the Jacobian values did not strongly influence the mean measured parameters and mainly affected the skin friction drag.

4.4 (Step B) Interpolation of vortices onto mesh

At the beginning of each time step the flow consists of a distribution of NV vortex particles each defined by spatial location (ξ_p, η_p) and individual vortex strength, Γ_p. Circulation is related to the net vorticity over a region of the flow (see equation 3.1) and on the mesh can be expressed as,

$$\Gamma_{i,j} = J_{i,j} \frac{\Delta\xi(\eta_{j+1} - \eta_{j-1})}{2} \tilde{\omega}_{i,j} \tag{4.14a}$$

The vorticity from each particle is distributed to the surrounding mesh points using the VIC scheme outlined in Section 3.4. Equation (3.11a) gives the distribution of vorticity in the physical plane. An expression for the circulation applicable to both physical and computational planes is:

$$\Gamma_{(m)} = \Gamma_p \frac{a_{(m)}}{a} \tag{4.14b}$$

4.5 (Step C) Solution of Poisson's equation

Since the code makes calculations in terms of circulation we can use (4.14a) to rewrite Poisson's equation introduced in Section 4.1.2:

$$\left(\frac{\partial^2\psi}{\partial\xi^2}+\frac{\partial^2\psi}{\partial\eta^2}\right)\Bigg|_{i,j}=\frac{-2\Gamma_{i,j}}{\Delta\xi(\eta_{j+1}-\eta_{j-1})}. \tag{4.15}$$

A finite difference representation of (4.15) would yield a set of linear equations coupled in the ξ and η directions. However by first taking the Fourier Transform (FT), and making use of certain transform properties, it is possible to obtain a set of equations which are uncoupled in the ξ-direction and can be solved by Gaussian elimination. It is the uniform spacing and periodicity of the mesh in one direction which enables the FT method to uncouple the equations. The ξ direction must be chosen for uniform spacing since the grid is periodic in ξ. In any case a variable spacing is favoured in the η direction such that the code concentrates effort on the boundary layer and near-wake regions.

The Fourier Transform solution technique is more comprehensively detailed in Appendix B. Essentially with $\Gamma_{i,j}$ known at each mesh point a Discrete Fourier Transform of equation (4.15), taken in the ξ-direction, yields a set of linear tridiagonal equations at each value of k:

$$a_{kj}\Psi_{k,j+1}+b_{kj}\Psi_{k,j}+c_{kj}\Psi_{k,j-1}=d_{kj} \tag{4.16}$$

Gaussian elimination reveals values of $\Psi_{i,j}$, the Discrete Fourier Transform of the stream function on the mesh. Taking inverse transforms then yields the stream function as required. The process is significantly speeded up by applying a Fast Fourier Transform algorithm which restricts the number of cells in the ξ direction to be a power of two.

Boundary conditions are necessary for ψ with the no slip condition implying ψ is constant on the body surface and ψ=0 is taken for convenience. At the outer boundary ψ is given by the potential flow solution, ψ_{pot}, which has been described in Appendix C. From (C8), with C_{cf}=1 and $\xi_0=\pi$, the irrotational potential flow solution on the mesh is expressed:-

$$\psi_{pot}\Big|_{(i,j)}=-2U\sin(\xi_i-\pi)\sinh\eta_j \tag{4.17}$$

In theory the outer boundary condition on ψ should be supplemented to take into account the effect of each individual vortex particle. Meneghini (1994) satisfied this condition by applying a Biot-Savart summation at the outer boundary. Biot-Savart summations are computationally expensive operations and since the outer boundary is positioned around 130 body diameters downstream it was anticipated that the additional Biot-Savart term could

be ignored without adversely affecting the simulations. Preliminary investigations showed no significant difference in the results obtained in the case of square and circular cylinders and thus the results presented in Chapters 5 and 6 do not include the Biot-Savart summation. It has since been suggested that for rectangles of smaller *B/A* ratio the boundary condition may have more influence and that imposing a symmetry condition on the outer boundary in effect fixes the position of the upstream stagnation point.

Some further simulations have thus been carried out in both uniform and pulsating flow, results from which are documented in Appendix H. The results indicate that although the inclusion of the Biot-Savart contribution does have some effect this effect is only significant when considering $C_{L(rms)}$ and rectangles with $B/A<1.0$. Under in-line oscillatory flow conditions the differences are less significant although there is clearly a consistent increase. Further comment is made in Appendix H.

4.6 (Step D) Calculation of finite difference diffusion equation

The diffusion equation (4.3b) is solved using a finite difference mesh with suitable boundary conditions for vorticity on the body surface and outer mesh boundary. A finite difference diffusion equation expressed in terms of circulation has been derived;

$$(1-\alpha\nu\Delta t\Theta^2_{(\eta)})\Delta\Gamma^{(t)}_{(i,j)} = \nu\Delta t(\Theta^2_{(\xi)}+\Theta^2_{(\eta)})\Gamma^{(t)}_{(i,j)}, \tag{4.18a}$$

where

$$\Delta\Gamma^{(t)}_{(i,j)} = \Gamma^{(t+\Delta t)}_{(i,j)} - \Gamma^{(t)}_{(i,j)} \tag{4.18b}$$

and $\Theta^2_{(\eta)}$ and $\Theta^2_{(\xi)}$ are finite difference operators. The finite difference representation is explicit in the ξ direction and uses the parameter α to control the degree of implicitness in the η direction. A full derivation of equation (4.18a) is given in Appendices D and E together with definitions for the finite difference operators.

Some boundary conditions on vorticity and circulation must be defined in order to solve equation (4.18a). Vorticity at the body surface is defined by

$$J_{(i,1)}\tilde{\omega}_{(i,1)} = -\frac{2\psi_{(i,2)}}{\eta_2^2}, \tag{4.19a}$$

which is a first order approximation of the solution to (4.5) at the boundary. In terms of circulation this can be written:

$$\Gamma_{(i,1)} = -\frac{\psi_{(i,2)}\Delta\xi}{\eta_2}. \tag{4.19b}$$

At the outer boundary $\Delta\Gamma_{(i,MY)}=0$ is assumed for the simulation, which is a reasonable assumption to make since diffusion effects will be negligible far away from the body. The system (4.18) represents a set of tridiagonal equations which are solved by Gaussian elimination to yield values of $\Delta\Gamma_{(i,j)}$, the change in circulation at each mesh point. These changes are then re-interpolated onto the existing point vortices in a reverse VIC scheme or a new vortex is created at each mesh point with no neighbouring vortices.

4.7 (Step E) Distribution of change in circulation to nearby vortices and vortex creation

The changes in circulation must then be re-interpolated onto the existing vortices in such a way that total circulation is conserved,

$$\Gamma_p^{(t+\Delta t)} = \Gamma_p^{(t)} + \sum_{m=1}^{4} \frac{\Delta\Gamma_{(m)} a_{(m)}}{a_t}, \tag{4.20}$$

where a_t is defined as the sum of $a_{(m)}$ values associated with all those vortices which neighbour grid point (m). This ensures that circulation is conserved where there is more than one neighbouring vortex. If no vortex neighbours the grid point then, provided $\Delta\Gamma_{i,j} > \sigma$, the cut-off strength, a new vortex is created there.

4.8 (Step F) Convection of vortex particles

Each individual vortex must be convected to new positions ready for the next time step. With $\psi_{i,j}$ known, equations (4.4) give the velocities at the grid points. An interpolation is carried out to give the velocities at the vortex positions:

$$\dot{\xi}_k = \sum_{m=1}^{4} \dot{\xi}_{(m)} \frac{a_{(m)}}{a}, \tag{4.21a}$$

$$\dot{\eta}_k = \sum_{m=1}^{4} \dot{\eta}_{(m)} \frac{a_{(m)}}{a}. \tag{4.21b}$$

First order approximations

$$\xi_k^{(t+\Delta t)} = \xi_k^t + \dot{\xi}_k^t \Delta t\ , \tag{4.22a}$$

$$\eta_k^{(t+\Delta t)} = \eta_k^t + \dot{\eta}_k^t \Delta t\ . \tag{4.22b}$$

are then used to convect vortices to their new positions.

4.9 (Step G) Calculation of force coefficients

4.9.1 Blasius theorem

The Blasius theorem (3.12), see for example Clements (1973), has been a popular choice for calculating force coefficients in previous DVM simulations. It is simple to implement and does not require the pressure field to be calculated since it directly relates the body force to the vorticity field. Simple manipulation is required to expand (3.13) into components of drag and lift expressed as a summation of mesh circulation values $\Gamma_{i,j}$:

$$Drag = F_X = -\frac{\rho}{\Delta t}\sum_{i=1}^{NX}\sum_{j=1}^{MY} y_{i,j}(\Gamma_{i,j}^{t} - \Gamma_{i,j}^{t-\Delta t}), \tag{4.23a}$$

$$Lift = F_Y = \frac{\rho}{\Delta t}\sum_{i=1}^{NX}\sum_{j=1}^{MY} x_{i,j}(\Gamma_{i,j}^{t} - \Gamma_{i,j}^{t-\Delta t}). \tag{4.23b}$$

Calculating the forces from equations (4.23) works well in traditional fully Lagrangian DVM codes in which there is no outer boundary and vortices are not removed from the calculation but the hybrid method employed here necessitates a mesh outer boundary and as vortices leave the computational region inaccuracies rapidly build up until the results are meaningless. A more versatile method is required for estimating the surface pressure around sharp edged bodies and to be applicable to any body geometry requires an examination of the Navier-Stokes equations in a generalised co-ordinate format.

4.9.2 Line integral method

Voke and Collins (1984) have used tensor analysis to derive a generalised form of the momentum equations which is applicable to any co-ordinate transformation. For an incompressible, constant viscosity flow these reduce to

$$\partial_t u^i = -g^{ij}\partial_j P + 2u^j\omega_j^i - 2\nu J^{-1}\partial_j(J\omega^{ij}) \tag{4.24}$$

This result, in combination with the relationships between the covariant and contravariant velocity, vorticity and metric tensors, has been used to obtain expressions which can be used in the hybrid DVM code to calculate the pressure gradients throughout the mesh. A complete account of this derivation can be found in Appendix F. Careful handling is necessary as vorticity is defined differently from the definitions used by Voke and Collins. Taking i=1 as the ξ direction and i=2 as the η direction two equations for the spatial variation in pressure have been derived:

$$-\frac{\partial P}{\partial \xi} = J\frac{\partial \dot{\xi}}{\partial t} - J\dot{\eta}\tilde{\omega} + \nu\frac{\partial \tilde{\omega}}{\partial \eta}, \tag{4.25a}$$

$$-\frac{\partial P}{\partial \eta} = J\frac{\partial \dot{\eta}}{\partial t} + J\dot{\xi}\tilde{\omega} - \nu\frac{\partial \tilde{\omega}}{\partial \xi}. \tag{4.25b}$$

Since P is a scalar quantity, it is invariant under co-ordinate transformations and therefore the expressions (4.25) can be applied to calculate the pressure field at required time intervals within the simulation. For smooth bodies the surface pressure can be satisfactorily calculated by applying the no-slip boundary condition, i.e. $\dot{\xi}, \dot{\eta} = 0$ on the body surface. Equation (4.25a) then reduces to the well known form

$$-\frac{\partial P}{\partial \xi} = \nu \frac{\partial \tilde{\omega}}{\partial \eta}, \tag{4.26}$$

which relates the gradient of vorticity normal to the body surface to the surface pressure gradient. Chorin (1973) and Meneghini (1994) both applied this method to their evaluation of the forces experienced by circular cylinders but for sharp-edged bodies this is not sufficient as the vorticity gradient becomes noisy near corners resulting in large errors.

As a result a novel method has been developed in which the surface pressure gradient is found by first integrating (4.25) out from the surface along a line of constant ξ, then integrating along a line of constant η, before finally integrating back in to the surface along another line of constant ξ. The summation of these integrals then gives the surface pressure gradient:-

$$\Delta P_i = P_i - P_{NX} = -\int_{(NX,1)}^{(NX,j)} \frac{\partial P}{\partial \eta} d\eta - \int_{(NX,j)}^{(i,j)} \frac{\partial P}{\partial \xi} d\xi - \int_{(i,j)}^{(i,1)} \frac{\partial P}{\partial \eta} d\eta \tag{4.27}$$

The choice of j is arbitrary since the expression (4.27) remains valid for any j. In this study a value of j=MY-3 was chosen. It is probable that when vortices leave the computational domain errors are introduced into the calculations of vorticity and velocity nearby although these effects will diminish with distance from the outer boundary. This suggests that a lower value of j could have been chosen but the effects of varying j were not rigorously examined in the present study.

Once the surface pressure distribution is known, pressure components of lift and drag coefficients can be found by integrating the pressures around the surface. P_{NX} is the pressure at the upstream stagnation point, which is assumed fixed. However since lift and drag are determined by the pressure difference between faces it is not necessary to give this a specific value. The skin friction contribution is found from the definition of shear stress at the wall,

$$\tau_{i,1} = -\mu \omega_{i,1}. \tag{4.28}$$

4.10 Summary of code alterations

A conformal transformation has been implemented which in theory should allow the calculation of flows about any rectangular geometry. The grid has been set up in such a way that the user has direct control over the placing of the first mesh out from the body and of the outer boundary mesh. Typical grid systems are shown in Figures 4.2 and 4.3 for several rectangles. The grid lines are seen to congregate near the corners, particularly when the rectangle is either very short or long, e.g. Figure 4.3(a).

A description of the theory has been given which closely follows Meneghini's work (1994). However corrections have been made due to the confusion which existed in the relationship between circulation and vorticity. The finite difference diffusion scheme was adjusted to allow for the variation of the Jacobian in the ξ-direction, which occurs for non-circular geometries.

In the version of the code which was initially inherited Poisson's equation was solved twice at each time step so that the stream function was recalculated immediately after the diffusion step but before convection. It was argued that this was not necessary since by only solving Poisson's equation once each timestep convection and diffusion are being modelled simultaneously. This is particularly relevant since the boundary condition on wall vorticity uses the value of stream function found in the first solution. In Figure 4.4 force time histories are plotted for versions which use both one and two FFT's per cycle. Table 4.1 summarises the mean values found in each case. It is clear from the figures and mean values that the differences between the two sets of results are negligible. Since the version which solves Poisson's equation once per timestep is considerably less computationally expensive it has been used for all the remaining data presented in this thesis.

	C_D	$C_{L(rms.)}$	St
1FFT	1.15	0.39	0.190
2FFT	1.15	0.38	0.190

Table 4.1(a) *Re*=200, Circular cylinder.

	C_D	$C_{L(rms.)}$	St
1FFT	1.44	0.25	0.157
2FFT	1.44	0.24	0.157

Table 4.1(b) *Re*=170, Square cylinder.

The outer boundary condition on the stream function has been simplified somewhat. In the original version a Biot-Savart summation was used to calculate the outer mesh values of ψ but in this instance the stream function has been set to the potential flow solution at the outer boundary. Some further simulations were conducted to directly assess the influence of neglecting the Biot-Savart contribution. These results are tabulated in Appendix H and indicate that the mean forces are consistently underestimated without the correct boundary condition but that this effect was only significant on rectangles of small *B/A* and under uniform flow conditions. There was no evidence that the boundary condition affected the movement of the upstream stagnation position.

The previous methods for calculating the force coefficients were found to be ineffective for sharp-edged obstacles and so a new technique was developed based on a form of the momentum equations generalised for any conformal transformation. A comparison between the Biot-Savart law, gradient of vorticity method and integral scheme is provided in Figure 4.5 for circular cylinders. Table 4.2 contains the mean values found using each method. The Blasius solution initially settles down into a clearly periodic force curve but once vortices begin to leave the computational domain both lift and drag oscillate in a noisy and unphysical manner. The gradient of vorticity method fares considerably better but, as previously stated, this method cannot be applied to sharp-edged obstacles since we cannot define a surface gradient at the corners. However the integral technique shows some improvement with the drag curve now oscillating with a regular amplitude.

Stansby and Slaouti (1993) simulated vortex shedding past circular cylinders by a random vortex method and used two schemes to calculate the mean forces, a Blasius type scheme and a scheme which calculated the surface pressure from the rate of change of circulation. They found closer agreement between the two schemes than is shown in the present calculations. The reasons for the greater discrepancy in the present calculations remain unclear although the Blasius scheme used in Stansby and Slaouti's simulations differs from Wu and Sankar's (1980) generalised Blasius theorem formulated for non-steady flows which has been applied in this study.

In Figure 4.4 the integral method was used to calculate force coefficients and periodic lift curves of steady amplitude were obtained for the flow about the square cylinder. Thus the integral method appears to be a promising technique and this is further borne out by the results obtained in Chapters 5 and 6 which on the whole compare well with existing numerical and experimental data.

	C_D	$C_{L(rms.)}$	St
Blasius	1.25	0.51	0.190
Gradient of vorticity	1.14	0.35	0.190
Integral	1.15	0.39	0.190

Table 4.2 *Re*=200, Circular cylinder;
Comparison of force calculation methods.

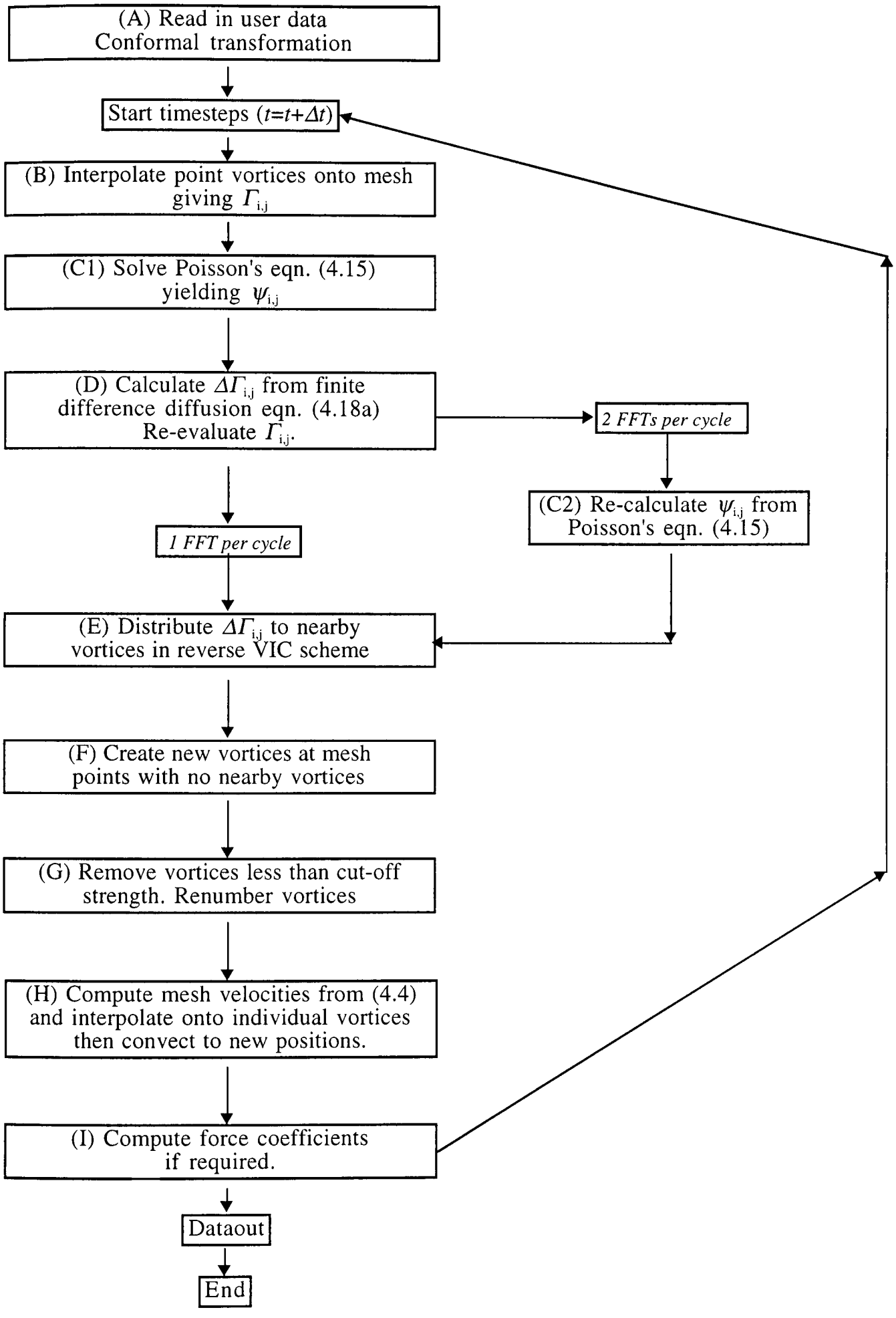

Figure 4.1 Flowchart of Hybrid DVM code

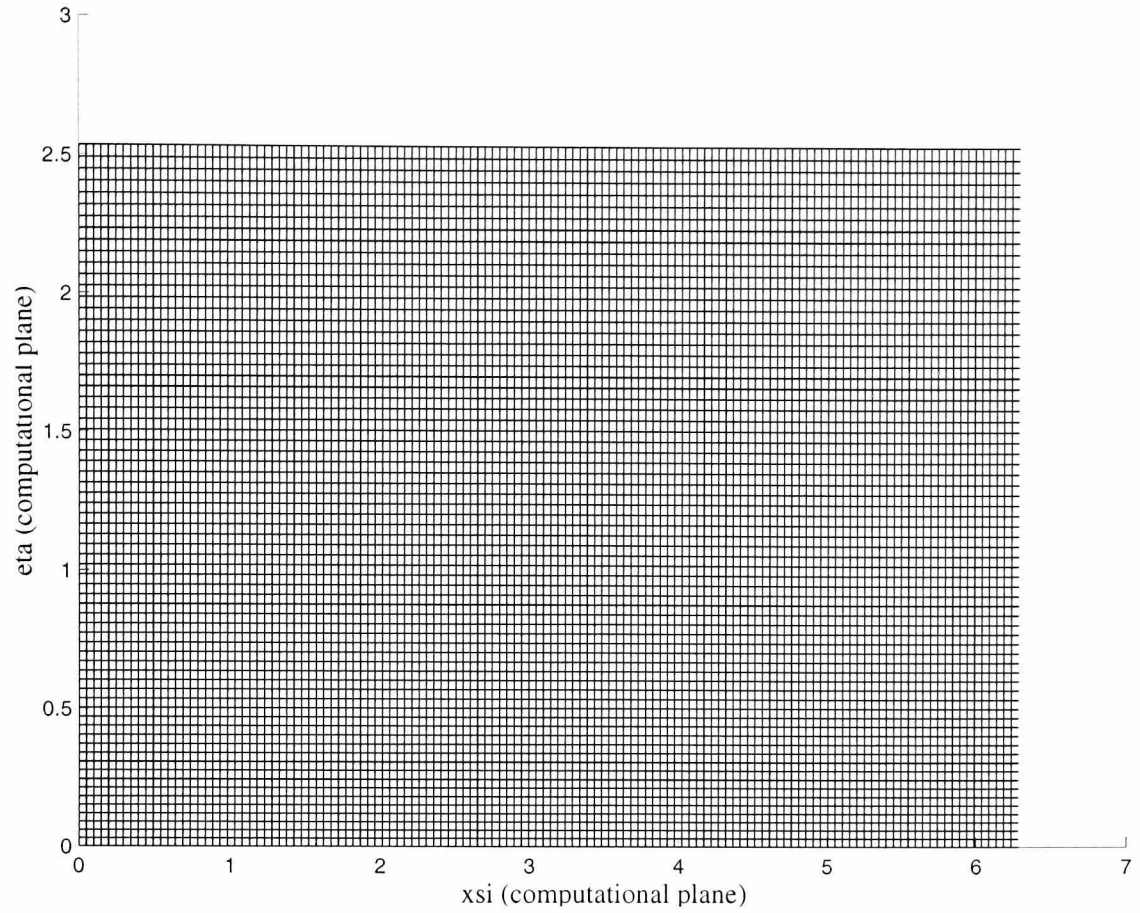

(a)

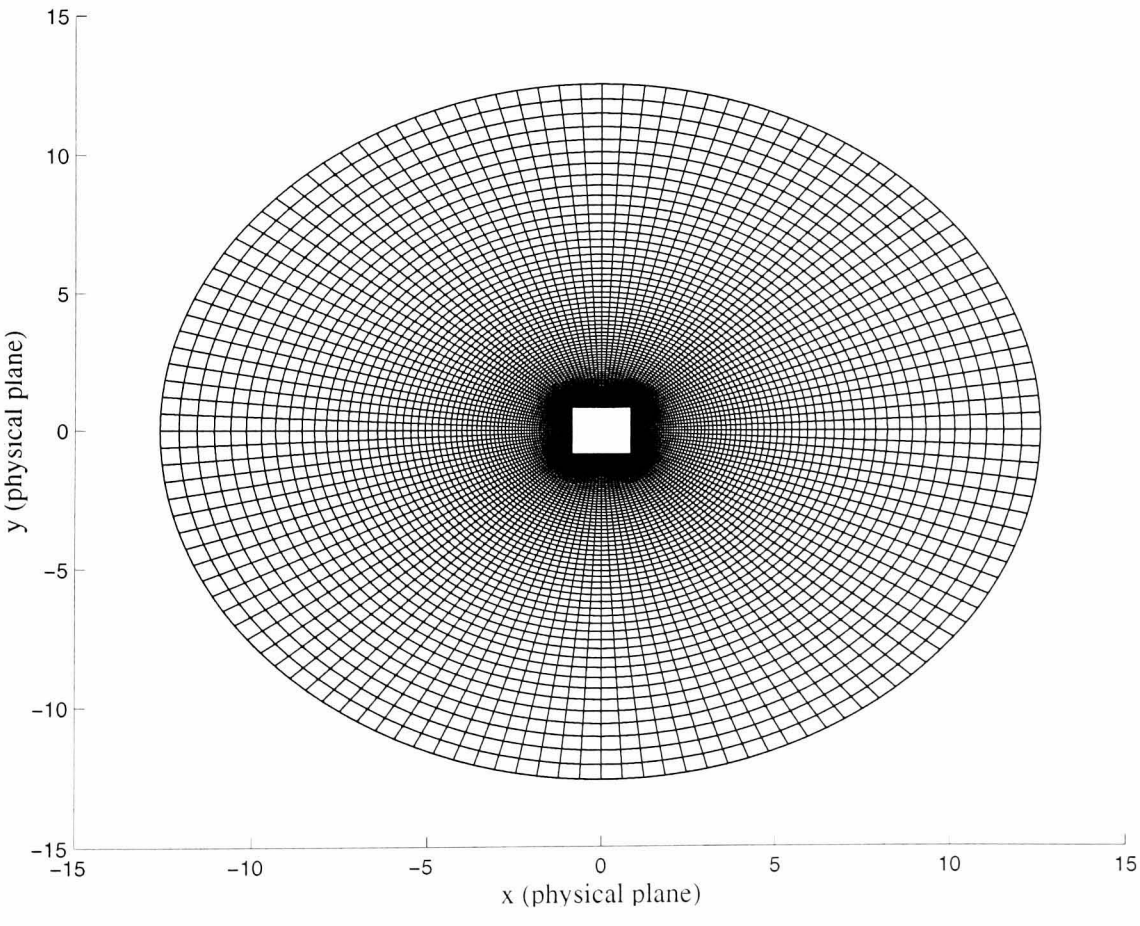

(b)

Figure 4.2 Mesh in computational and physical plane.
B/A=1.0, $NX*MY$=128*128, M_{in}=0.025, M_{out}=130.
(a) Comp. plane, grid shown to 70 cells out, (b) Phys. plane, grid shown to 70 cells out

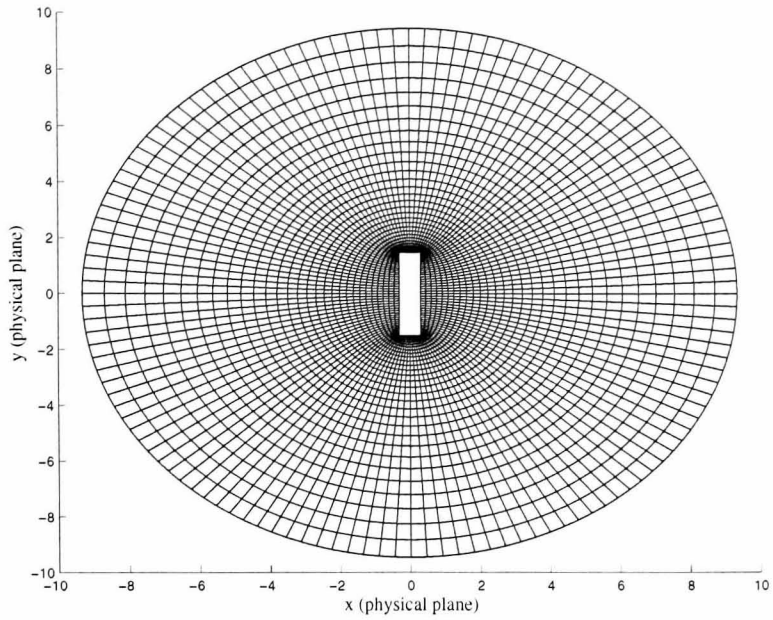

(a)

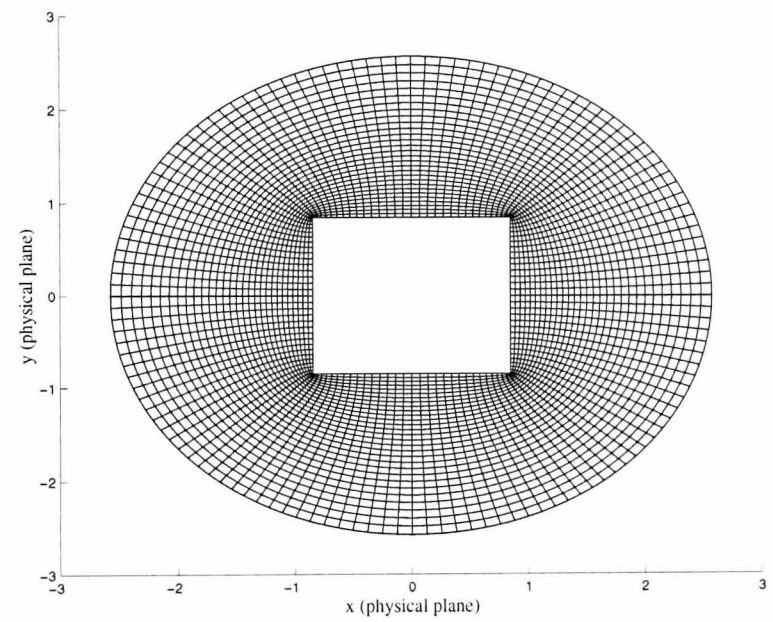

(b)

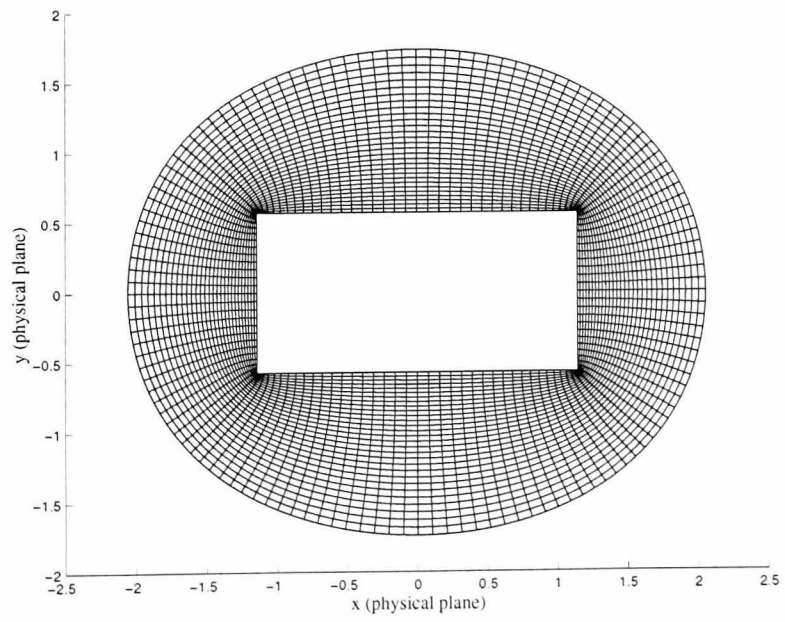

(c)

Figure 4.3 Near surface mesh in physical plane.
Grids shown to 30 cells out, $NX*MY$=128*128, M_{in}=0.025, M_{out}=130.
(a) B/A=0.2, (b) B/A=1.0, (c) B/A=2.0

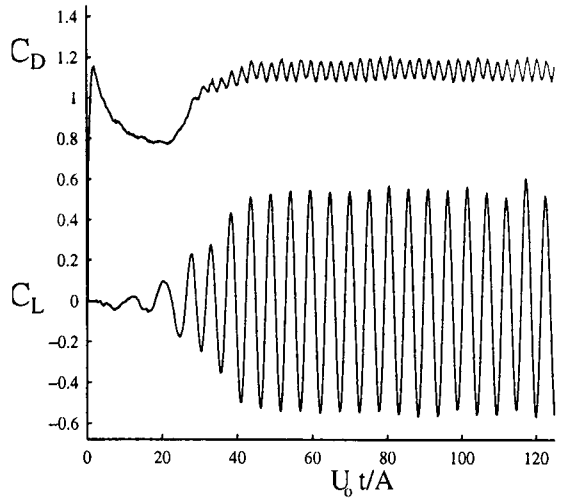

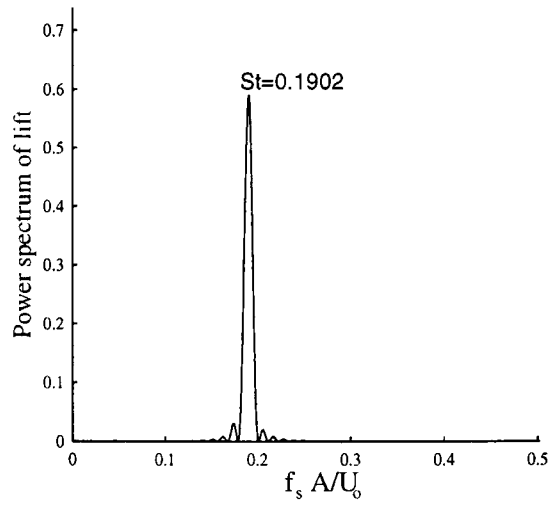

(a)

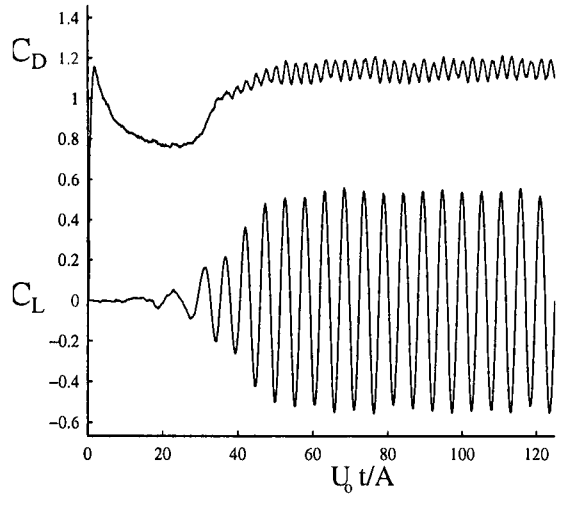

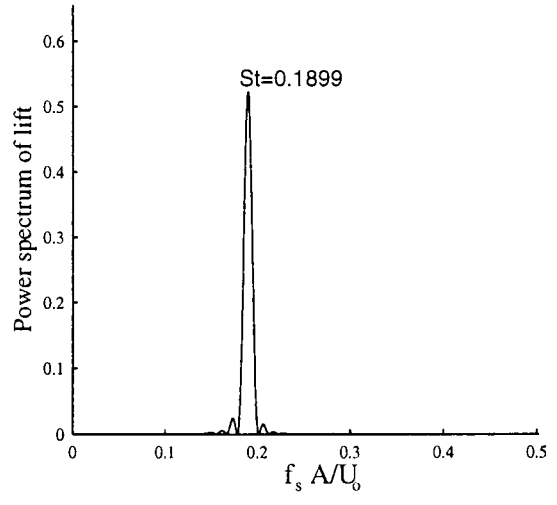

(b)

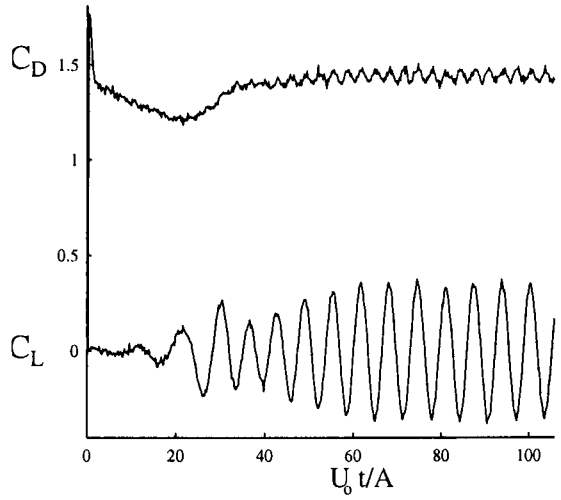

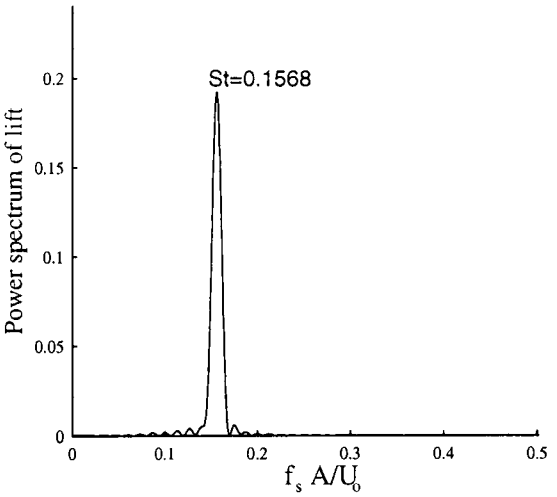

(c)

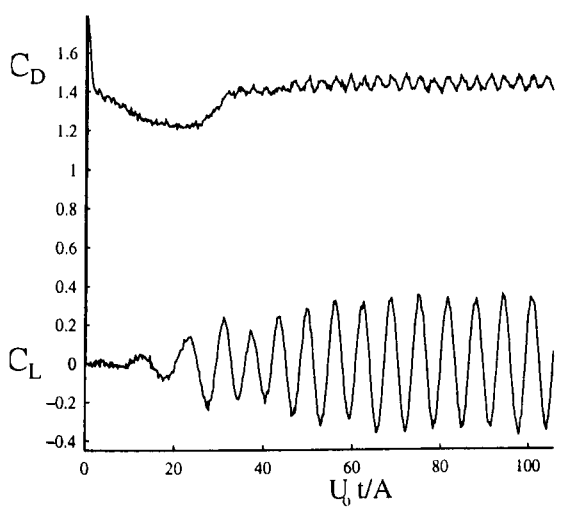

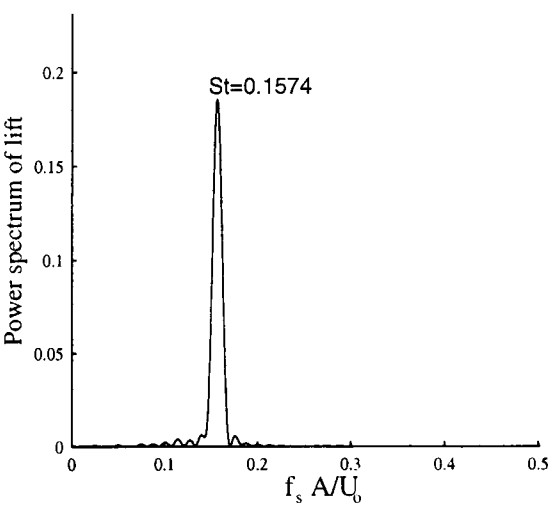

(d)

Figure 4.4 Effect of changing code to 1 FFT per time step on force time histories.

Circular cylinder, *Re*=200, (a) 1 FFT per Δt, (b) 2 FFT per Δt.
Rectangular cylinder *Re*=170, (c) 1 FFT per Δt, (d) 2 FFT per Δt.

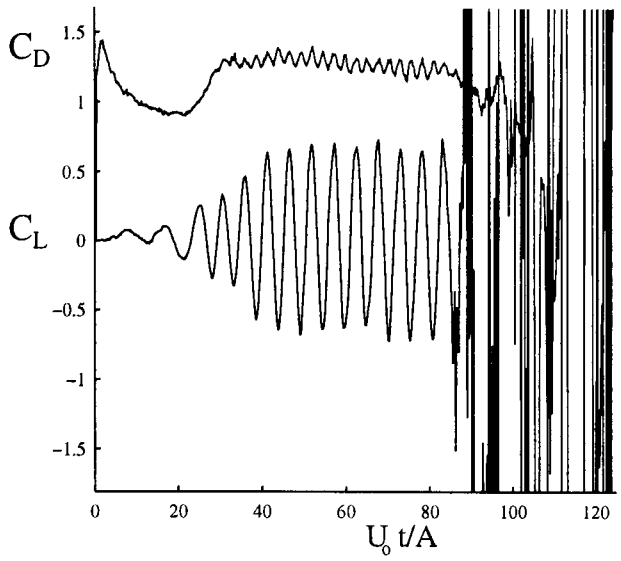

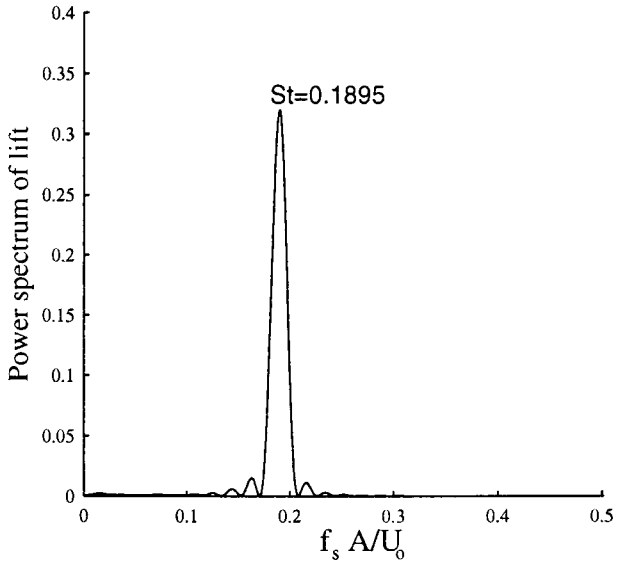

(a)

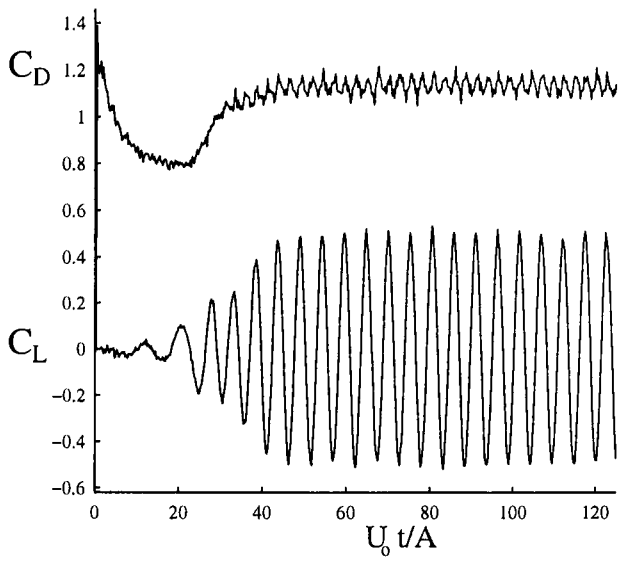

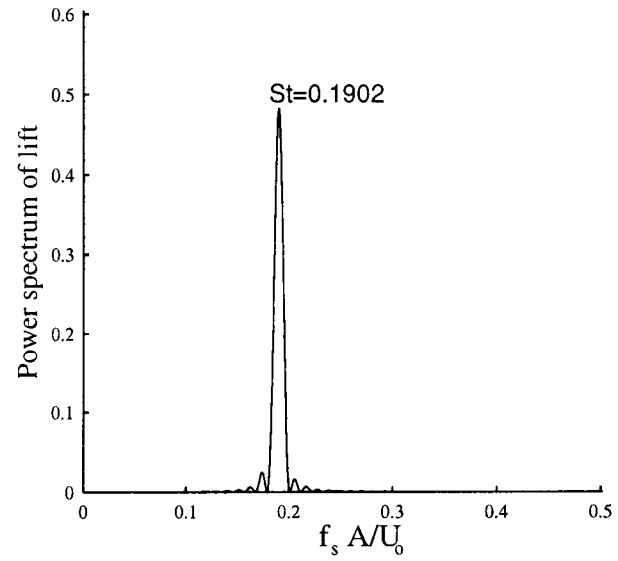

(b)

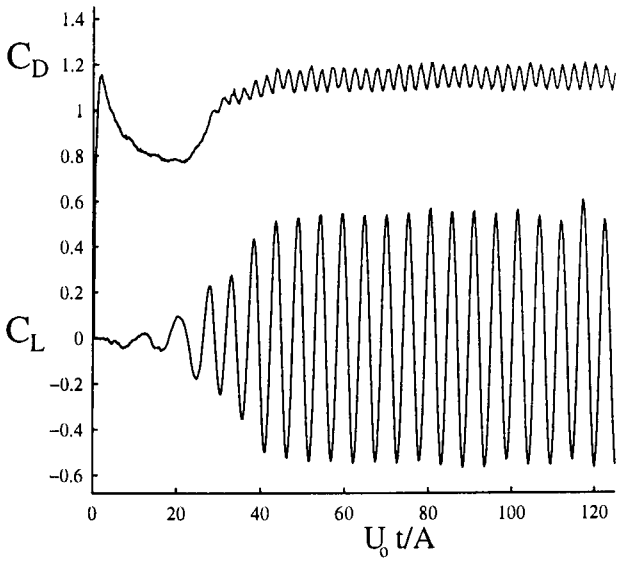

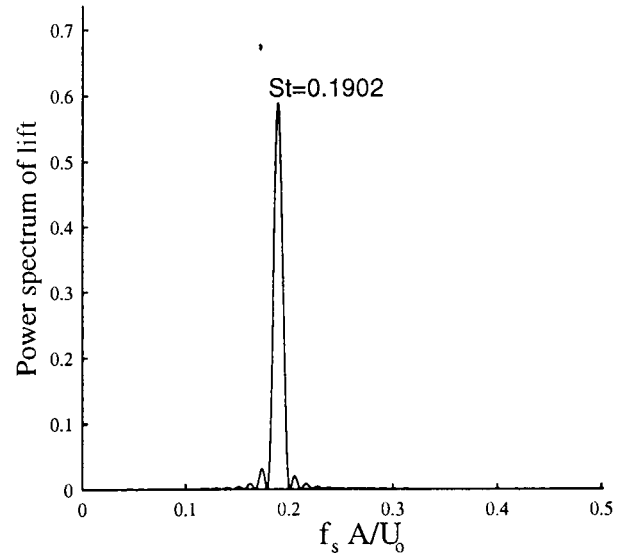

(c)

Figure 4.5 Comparison between force calculation methods
Flow about circular cylinder, *Re*=200.
(a) Blasius, (b) Gradient of vorticity, (c) Integral method

Chapter 5

Simulation of Uniform Flow Past Rectangular Cylinders

At the outset of this project it was not intended that a major study of the uniform flows about bluff bodies would be conducted. The uniform flow simulations were to be used as a tool for checking that the code was fully operational, i.e. that new developments and additions to the code such as the pressure calculation method and the mesh set-up were functioning in the required manner. Finding the free stream value of the Strouhal number under uniform conditions would also be necessary for each bluff geometry under which pulsating flow would be simulated. However once an initial assessment had been conducted of the existing literature, *viz.* Chapter 2, it became apparent that although the circular cylinder has been widely studied (recently Williamson (1996a) has published a fairly comprehensive review of flows past circular cylinders) there exist large gaps in the knowledge of flows past other bluff cylinders. Most laboratory experiments have been conducted in the high Re regime. Direct numerical simulations have been restricted to flows below $Re<1000$ which are classified here as low Reynolds number flows. Only a few numerical calculations of low Re flow around rectangular cylinders existed when this work first started. Therefore the variation of side ratio B/A and Reynolds number below $Re<1000$ have been studied here to gain further insight into the fundamental aspects which occur, such as the trailing edge interaction with the separated shear layer, which at higher Re is thought to be significant in the critical drag phenomenon which occurs close to $B/A=0.62$. However before these findings can be discussed the description of input parameters and output available from the code must be explained.

5.1 Code parameters

A full description of the three input files, *sqdata1*, *sqdata2* and *sqdata3* required to run the code is given in Appendix G. The user is concerned with setting up the flow geometry, the mesh and what data is required as output. Output files are *sqdata4*, *coords*, *prforce*, *sfpres* and *fort.30*, ..., *fort.30+n*. Since the user defines the flow geometry in terms of Reynolds number *sqdata4* outputs dimensional values for the obstacle diameter and flow velocity. *coords* contains the mesh co-ordinates in both the physical and the computational planes and the

corresponding values of Jacobian. Pressure and skin friction forces are output to *prforce*. The vortex positions are built up within *fort.30*, ..., *fort.30+N*, each of the files containing data on the vortex positions and strengths at a distinct timestep. A flow visualisation video can then be created consisting of the N output frames or frames can be chosen to coincide with the phase of the lift force, i.e. the phase of vortex shedding. *sfpres* contains values of the surface pressure distribution at instants corresponding to the *fort.*** files so that the combined surface pressure distribution and near-wake flow visualisation can be analysed simultaneously.

5.2 Effect of input parameters on simulation results

The following quantities directly affect the performance of the simulation: MY, NX - Number of grid points in η and ξ directions respectively; M_{out}, M_{in}, - Relative distance (with respect to cylinder diameter in physical plane) of outermost grid line and innermost grid line from cylinder; J_{lim} - Limiting value on Jacobian of transformation; σ_{min} - Vortex cut-off strength; Δt - Timestep.

A converged simulation may be defined as the limiting case beyond which any further refinements to these parameters makes no apparent change to the observed results. However this is rather a simplification of the true scenario as it assumes that the solution will continuously improve with finer spatial and temporal resolution and that the available computing facilities can cope with the extra resolution. In the code all the calculations which directly affect the outcome of the simulation are made 'double precision'.

When we come to do the pulsating flow analysis we will see that each geometry requires of the order of 50 runs to build up the 'lock-in' picture. It is therefore important to ensure that the runtime of the simulation does not become excessive in the search for greater simulation convergence. We wish for the code to run as quickly as possible whilst giving results which are converged to a reasonable confidence level.

It is important to appreciate that these results are not expected to give a definitive answer for flow parameters such as drag and Strouhal number but rather they complement and add to existing data. The existing experimental and numerical data fall within a variation range of 20% or more. The effect of varying the input parameters was rigorously examined for the B/A=1.0 cylinder and only partially examined for other cylinders. In each case the Reynolds number is set at Re=200 and the upstream flow is uniform. It was then assumed that, from a knowledge of the simulation performance around these geometries, suitable input parameters could be chosen for similar bluff geometries.

Meneghini (1994) previously examined the effect of using different mesh sizes, $MY \times NX$, in flows around circular cylinders. The Fast Fourier Transform algorithm requires that 2^n grid points must be used in the ξ-direction but the number used in the η-direction is arbitrary. Meneghini found 128×128 to be optimum. It was

found that increasing the mesh refinement further merely added to the computational expense without providing any significant improvement in the output quality. Therefore in this study a 128×128 mesh has been used for all simulations.

In setting a value for M_{out} the main aspect to take into consideration is that the far wake is known to have an influence on upstream developments. Since the effects of vortices leaving the computational domain are neglected it is important that the boundary is placed a reasonable distance downstream such that these effects are diminished. On the other hand if the boundary is placed too far out then the code will not be able to cope with the large numbers of vortices which are carried downstream and will also lose spatial resolution of the near wake. M_{out} should therefore be chosen to be as small as possible without causing any adverse effects on the flow.

The actual minimum vortex strength Γ_{min} permitted within the code is related to the user defined value σ_{min} by

$$\Gamma_{min} = U_0 \Delta t \Delta\xi_{min} \sigma_{min}. \tag{5.1}$$

It is desirable that Γ_{min} should be as small as possible in order that all the vorticity created at the body surface and diffused throughout the flowfield is represented within the simulation. However, making this quantity too small results in the creation of a large number of point vortices, increasing computational expense. One might argue that by imposing a cut-off limit we are in some way copying the circulation reduction schemes incorporated into higher Reynolds number DVMs. In these methods vorticity has sometimes been reduced in an attempt to account for some of the 3-D vortex stretching which would occur in a real flow, but at low Re 3-D instabilities are not as important, although they are observed for Re>170 in the case of the circular cylinder. Williamson (1996b) has described the initial appearance of 3-D instabilities in the form of oblique shedding from circular cylinders but it is debatable whether or not this is possible from a sharp-edged cylinder since the separation point will be steady along the span. This may mean that the flow about sharp-edged cylinders remains 2-D until higher Re is reached. In this study the cut-off limit is imposed only to limit computational expense and is not an attempt to account for any 3-D phenomena which may be present in the flow.

The time step Δt, inner mesh position M_{in} and minimum Jacobian value J_{min} can be considered together since there is a restriction on the time step in the diffusion solver which is dependent on the minimum cell size:

$$\Delta t \leq \frac{1}{2\nu(\Delta x^{-2} + \Delta y^{-2})}. \tag{5.2a}$$

This result can be derived by a stability analysis of the vorticity transport equation. Roache (1976) presents a complete account of the one-dimensional diffusion instability problem. However since all calculations for this

simulation take place in a computational plane the co-ordinate transformed version of the time constraint is required; this is

$$\Delta t \leq \frac{J}{2\nu(\Delta\xi^{-2} + \Delta\eta^{-2})}. \tag{5.2b}$$

This constraint has been used as a guide when choosing the time step to be used in the calculations but each obstacle geometry needs to be considered separately since the mesh geometry will vary considerably between cases. Equation (5.2b) demonstrates that the time step required for stability decreases as the mesh size and Jacobian value decrease. Since $\Delta\xi$ is constant for all rectangles the constraint will be most restrictive where $\Delta\eta$ and J are smallest, say $(\Delta\eta_{min}, J_{min})$. $\Delta\eta_{min}$ is a function of the transformation and M_{in}. The transformation has a singularity at sharp corners such that the value of Jacobian is zero which would thus place an impossible limit on this time constraint. A limit on the minimum value of the Jacobian is imposed, J_{lim}, such that the time constraint becomes meaningful. The scheme for the convection of vorticity would also break down at the corner if no limit was introduced. Graham (1994) in his code to examine the flow around square cylinders merely forced the value of the Jacobian at the corner mesh point on the body to be equal to the value at the first mesh point out. In this simulation the Jacobian has been smoothly varied in the vicinity of the corner as described in Chapter 4. This is equivalent, physically, to a slight smoothing of the corner geometry and it would be expected that with lower values of J_{lim}, the corner should appear sharper and thus more vorticity should be created.

The variations in the results with changes in the input parameters M_{out}, σ_{min}, M_{in} and Δt are investigated below. These variations were tested extensively for the B/A=1.0 case and less rigorously for a few other geometries. Convergence was determined according to the variation in the main measured parameters, C_D, St and $C_{L(rms)}$, since these properties can often be compared with previous research. The effect on any qualitative analysis of the flow such as wake width, vortex formation position and recirculation was not investigated.

5.2.1 Effect of input parameters: B/A=1.0 cylinder

Changing the downstream extent of the simulation by altering M_{out} has perhaps the most easily identifiable effect on the results. Table 5.1 summarises the effect on the mean flow parameters and Figure 5.1 graphs some force time histories. We can see that the main influence of M_{out} can be observed in the lift time history. As the downstream extent of the simulation is reduced there is a jump in the lift curve which is magnified for smaller M_{out}. This corresponds to the point at which vortices begin to leave the computational domain and clearly NV, the number of vortices present at the end of the calculation, reduces substantially as M_{out} decreases. The near invariance of the Strouhal number suggests that the far stream effects are largely unimportant at the body surface as vortices are still shed regularly and at the same frequency. The drag is also almost invariant with the change in M_{out}.

M_{out}	C_D	$C_{L(rms)}$	St	NV
160	1.46	0.40	0.153	140146
130	1.46	0.42	0.152	138681
100	1.47	0.37	0.153	114798
70	1.47	0.49	0.154	84793
50	1.47	0.62	0.155	62091

Invariant parameters: M_{in}=0.025, Δt=0.005, σ_{min}=0.00075, J_{lim}=0.01

Table 5.1 Effect of outer boundary position on calculated parameters: B/A=1.0 cylinder

Reducing the cut-off strength below σ_{min}=0.005 has little effect on the measured parameters as can be seen from Table 5.2. C_D and St vary insignificantly while the number of vortices and $C_{L(rms)}$ increase. An M_{out} of 130 and σ_{min} of 0.00075 were chosen for all further calculations although it may have been possible to use a higher value of cut-off strength. The smaller value was chosen since reducing it did not involve a large increase in run time and also to ensure that the simulation included as much of the vorticity diffused from the surface as possible.

σ_{min}	C_D	$C_{L(rms)}$	St	NV
0.00500	1.46	0.376	0.154	79977
0.00100	1.46	0.395	0.153	101859
0.00075	1.46	0.397	0.153	109681
0.00025	1.46	0.399	0.152	119071

Invariant parameters: M_{in}=0.025, M_{out}=130, Δt=0.005, J_{lim}=0.01

Table 5.2 Effect of cut-off strength on calculated parameters: B/A=1.0 cylinder

Since the minimum time step satisfying the diffusion criterion is linked to the position of the first mesh point out from the body it is appropriate to consider the effect of Δt and M_{in} together. Meneghini (1994) also used a quadratic mesh expansion but it was not clear how the parameters were used to effect the mesh co-ordinates. As the geometry was circular the conformal transformation produced a radial mesh with the first mesh point being equidistant from the surface all around the body. Meneghini used values in the range $0.009<M_{in}<0.015$ but for a circular geometry this set the distance to the first grid point all around the body surface. With the conformal transformation necessary for the rectangular geometry the mesh in the physical plane will be nearer to the body at the corner points than at the mid-span. Typically with M_{in} set to 0.03, for the B/A=1.0 cylinder, the corner grid is at a distance of $0.005A$ and since we apply the constraint in the transformed plane it is the value of Jacobian at this point, J_{min}, which controls the time step constraint as defined in equation (5.2b).

Table 5.3 shows how $\Delta\eta_1$ and J_{min} vary with M_{in} and give corresponding values for the time step limit according to equation (5.2b). The values indicate that by increasing M_{in} a higher timestep can be used within the simulation whilst ensuring that the solution remains stable. The three values of M_{in} below have each been tested over a range of time steps to establish if the stability criterion on Δt is suitable.

M_{in}	$\Delta\eta_1$	J_{min}	$\Delta t \leq$
0.022	0.0264	0.082	0.0022
0.030	0.0359	0.11	0.0046
0.050	0.0598	0.18	0.0130

Table 5.3 Variation of diffusion time constraint with M_{in}, J_{lim}=0.01: B/A=1.0 cylinder

M_{in}	Δt	C_D	$C_{L(rms)}$	St	NV
0.05	0.0050	1.44	0.328	0.158	67124
0.05	0.0025	1.44	0.329	0.159	75124
0.05	0.0010	1.45	0.327	0.160	84927
0.03	0.0050	1.46	0.385	0.154	90637
0.03	0.0025	1.45	0.363	0.159	97170
0.03	0.0010	1.45	0.340	0.160	105405
0.022	0.0050	1.47	0.395	0.153	104433
0.022	0.0025	1.47	0.370	0.158	110850
0.022	0.0010	1.46	0.360	0.159	120710

Table 5.4 Effect of inner mesh position and timestep on calculated parameters: B/A=1.0 cylinder

Stable solutions were obtained for all the runs summarised in Table 5.4. As M_{in} is decreased the force coefficients become higher, more notably in the case of the lift, and more vortices are created within the simulation. This follows since with smaller grid spacing near the body surface the diffusion and creation of vorticity can be spread over more points. Drag and Strouhal number are consistent to within ±5%, C_D=1.45±0.02, St=0.156±0.004, and r.m.s. lift to within ±10%, $C_{L(rms)}$=0.36±0.04, for the range of Δt and M_{in} considered. Viewing the above results it may be considered that the stability time constraint of equation (5.2b) is a little stringent as stable solutions have been simulated with the timestep set above the constraint but this is not surprising since the corner grids represent only a small, albeit important, part of the simulation and the constraint will be comfortably enforced in the vast majority of the simulation domain.

In arguing for choice of time step and M_{in} this author would state that it is not just the importance of convergence of flow parameters which is important. The production of a smooth force time history and clearly periodic vortex street are also of importance. A value of M_{in}=0.025 and Δt=0.005 were chosen for future B/A=1.0 cylinder runs since this gives a stable solution and the main measured parameters fall close to the mean of the values in Table 5.4. At M_{in}=0.05 the convergence level is similarly high and far fewer vortices are created within the simulation which would have been beneficial from a time consideration. However it was considered more important to keep the near-wall resolution as fine as possible. Ideally a lower timestep should be used but this would hinder the use of the code in performing many pulsating flow cases later on. It should also be appreciated that in the recent DNS calculations of Sohankar *et al* (1996) although C_D was not found to be particularly susceptible to the grid set-up, $C_{L(rms)}$ and St varied considerably.

5.2.2 Effect of input parameters: Diamond cylinder

A B/A=1.0 cylinder inclined to the flow at α=45°, or diamond cylinder, was also tested for convergence as the time step was decreased. Mesh geometry parameters were chosen as for the B/A=1.0 cylinder at zero incidence. It was felt that this case might represent a more demanding convergence test than the cylinder at zero incidence since the corner separation will be more severe. However Table 5.6 shows the measured quantities to vary little as Δt is decreased below 0.01 and encouragingly the results fall within a smaller percentage range than the zero incidence cylinder convergence tests.

Δt	C_D	$C_{L(rms)}$	St	C_{Ds}
0.01	1.93	0.69	0.201	0.23
0.005	1.95	0.69	0.202	0.23
0.001	1.93	0.68	0.201	0.23
0.0005	1.92	0.69	0.203	0.23

Invariant parameters: M_{in}=0.025, M_{out}=130, J_{lim}=0.01

Table 5.5 Effect of timestep on mean flow parameters for diamond cylinder.

5.2.3 Chosen parameters

The parameters chosen for simulations in this study are listed in Appendix G, Table G.2. Some points should be noted. For rectangles of smaller side ratio, σ_{min} was increased in order to limit the number of vortices which became very large. The distance to the first grid line from the rectangle surface varies around the body surface and is largest at the mid-points of the longer sides. This has to be taken into account when setting M_{in} on rectangles with small or large B/A. Hence M_{in} is increased as B/A increases. The final column of Table G.2 shows the total non-dimensional time of each simulation and also gives an indication of how many body diameters downstream the vorticity created during the initial stages of the calculations will travel.

5.3 Effect of side ratio (B/A)

Earlier in Chapter 2 a description was given of the effects of varying the side ratio for turbulent flows, $Re>10^4$. Bearman and Trueman (1972) and others have shown that there appears to exist a critical side ratio at which the base pressure and drag attain a maximum value (see Figure 2.7). Ohya (1994) showed that there was a discontinuity in the flow pattern close to B/A=0.5 with two distinct shedding modes occurring intermittently. The two shedding modes are associated with different values of base pressure since in one mode the vortices are forming further downstream. However other researchers, notably Laneville and Yong (1983), have not witnessed this intermittency; perhaps because time-averaged values were measured and no examination was made of the fluctuating values. The precise mechanism for the 'golden ratio' phenomenon is still uncertain although it is clearly a result of interaction between the separating shear layer and the trailing edge. It should be noted that full reattachment, within the turbulent Reynolds number region, does not occur until $B/A\approx2.5$. At lower Reynolds number a critical drag has not been observed. In laboratory experiments it is difficult to measure the drag at low Reynolds number, particularly for short bodies, since the cross-stream dimension A must be quite small to allow for flow at low Reynolds number. There should not be extra difficulty in simulating numerically the flows about shorter rectangles but this is an area where results are scarce and the majority of numerical studies which do exist have not attempted to simulated flows with $B/A<0.6$, e.g. Davis and Moore (1982) and Okajima *et al* (1993). An inviscid discrete vortex method for prediction of high Reynolds number flow used by Okajima (1990) did show a peak in the drag close to B/A=0.6 although the peak was not as sharp as that found experimentally. Generally though the numerical simulation of cylinders with $B/A<0.6$ has been avoided. The work of Nakamura (1993), in which upstream turbulence is shown to decrease the critical ratio, suggests that the 'golden ratio' effect may well be Reynolds-number dependant, particularly within the laminar regime, since the interaction between the separating shear layer and trailing edge may differ from that observed at higher Reynolds number. Thus a study of the effect of varying B/A at low Reynolds numbers is presented here. A similar but totally independent study was conducted at the same time in Sweden and results from both studies were presented at the same conference [Sohankar *et al* (1996) and Steggel and Rockliff (1997)] so that a blind comparison could be made between the two sets of data.

For this investigation simulations were undertaken with the side ratio varying between $0.02<B/A<8.0$. Results of drag, Strouhal number, r.m.s. lift and skin friction drag are graphed in Figure 5.2. No evidence can be seen from Figure 5.2(a) for any drag maximum occurring, even at much lower side ratios than the critical value of B/A=0.62 reported at higher Re. Some typical force time histories which span the range of side ratios studied are shown in Figure 5.3. This dataset is more comprehensive than that presented in Steggel and Rockliff (1997) which was restricted to $0.4<B/A<2.5$. The earlier limitations arose since at that stage M_{in} could not be set within the code and became exceptionally small for B/A outside this range. This in turn led to a requirement for prohibitively small time steps. No laboratory measurements of drag variation with side ratio exist at this Re, although Okajima (1995) has determined C_D for the B/A=1.0 cylinder. The only authors who had previously tested the variation in drag with side ratio were Davis and Moore (1982) and Okajima *et al* (1993) but neither of

these investigations examined flows below B/A=0.6. These older numerical results all predict slightly higher values of drag than those found in this study. Encouragingly a strong correlation is found with the recent calculations of Sohankar *et al* (1996). Their work encompassed a direct numerical simulation of flows for $0.25<B/A<4.0$ and their drag coefficients are in remarkable agreement across the whole range of side ratios. Since similar results have been obtained using a different method (DNS) and a rectangular mesh, it is presumed that the method and mesh employed in this study are sufficient over the range of side ratios studied.

The Strouhal number results shown in Figure 5.2(b) have a great deal more scatter. Above B/A=1.0 the numerical calculations give consistent values of $0.15<St<0.17$. The present calculations are around 10% higher than those measured in the laboratory and typically all the numerical results are around 10-20% higher than experiment. It is thought that this is due to the two-dimensional nature of the simulations which cannot account for any spanwise movements. These will decrease the rate of vortex formation since not so much fluid need be entrained in the streamwise direction. Below B/A=1.0 no experimental data exists but the present results, and those of Sohankar *et al* (1996), indicate an increase in Strouhal number as B/A decreases with a maximum value of $St\approx0.20$ occurring close to B/A=0.3. At still lower side ratios the Strouhal number falls back to a value similar to that found for the B/A=1.0 cylinder and clearly this reduction in Strouhal number is uncorrelated with the drag curve.

A similar trend is observed in the r.m.s. lift curve (see Figure 5.2(c)) with a maximum of 0.7 occurring close to B/A=0.3. Interestingly Sohankar *et al* also predict a dip in the lift curve although their Strouhal number still appears to be rising at B/A=0.25. Unfortunately there are no laboratory measurements with which the numerical data can be compared. There is still quite a degree of uncertainty attached to the numerically obtained values of $C_{L(rms)}$. It was greatly influenced by factors such as the downstream extent of the mesh, the near-wall resolution and the simulation time step. Indeed Sohankar *et al* provided similar findings predicting $C_{L(rms)}$ in the range 0.15-0.4 for the B/A=1.0 cylinder. Their most resolved mesh gave a value of 0.3 which is closer to the value obtained here. The variation in drag and Strouhal number was only a few percent in comparison so clearly it is more difficult to predict the surface pressure variation along the side walls, probably because the variation in time of the side wall surface pressure is far greater than that along the base wall and the upwind face will have a surface pressure which hardly varies at all with time. A greater understanding of the mechanism behind the peaks observed in the St and $C_{L(rms)}$ curves may be possible by closer inspection of the time variation in surface pressure distributions and by flow visualisation of the near-wake development.

The skin friction drag C_{Ds} is plotted against side ratio in Figure 5.2(d). A rough estimate of the degree of recirculation along the side surfaces should be possible since a negative C_{Ds} implies a large amount of reversed flow. C_{Ds} is positive for small side ratios and becomes negative at $B/A\approx0.33$. At B/A=8.0 it is positive again. No other calculations were performed for $B/A>4.0$ so the side ratio at which skin friction becomes positive

again was not found. The side ratio at which C_{Ds} becomes negative corresponds to the observed peaks in the lift and Strouhal number curves.

Force time histories for rectangles with $0.02<B/A<8.0$ are presented in Figure 5.3. A peculiarity arises for $B/A=0.02$, which corresponds almost to a flat plate normal to the stream. There appear to exist two solutions as the drag alternates between a high and low value. This jump in the drag curve suggests an intermittency in the shedding mode although no observations of the vortex wake have been made. It is not clear if the mechanism responsible for this intermittency is similar to that found by Ohya(1994) (see Figure 2.11) for a $B/A=0.5$ cylinder at $Re=6700$; further investigations would be necessary to clarify this point. For $0.1<B/A<2.0$ the force histories give reasonable periodicity and indicate smooth vortex shedding but a change occurs in the start-up of vortex shedding between $B/A=0.2$ and 0.5. At $B/A=0.1$ and 0.2 after the initial onset of vortex shedding the drag oscillates around a higher value than its long term mean. In contrast for $B/A\geq0.5$ the drag oscillates about its average value immediately after the initial settling phase. At $B/A=4.0$ there is a large amount of noise in the force time history and, although this has been dampened somewhat at $B/A=8.0$, it indicates that either the vortex shedding is not regular or there are some instabilities along the side walls perhaps involving intermittent flow reattachment.

In summary no maximum in the drag was found as observed at higher Reynolds number but the results were in broad agreement with those of Sohankar *et al* (1996) and appear to predict that the drag increases continuously with decreasing side ratio. An interesting question arises as to what would be the drag coefficient and Strouhal number for a flat plate placed normal to the flow at a low Reynolds number. This limiting case could provide a definitive answer as to whether the drag continues to increase with reduced side ratio. Either the 'critical drag' is a consequence of turbulent flow conditions or three-dimensional instabilities are responsible. The latter case can perhaps be ruled out since the 2-D vortex simulation of Okajima (1990) predicted a drag maximum at higher Reynolds number although the peak was greatly reduced from the experimentally determined values. An explanation for the peak in the lift and Strouhal number close to B/A=0.3 is given from the near wake flow visualisation analysis, Section 5.6.

5.4 Effect of Reynolds number

Reynolds number effects for bluff body flows have been summarised in Chapter 2. Williamson (1996a) has made an extensive review of circular cylinders but only a few results exist for Re dependence of rectangular cylinders. Okajima (1995) has recently determined the drag over a wide range of Re for the $B/A=1.0$ cylinder and data combined from several investigations on the Strouhal number variance for rectangles with $1.0<B/A<3.0$ have been published by Norberg (1993) (see Figure 2.12). Numerical computations have been limited to a few studies mainly at low Re.

No convergence tests were carried out as to the effects of altering code parameters at Reynolds numbers other than 200 and when varying the simulation Reynolds number, all code input parameters were kept constant other than the time step. For $Re>200$ Δt was decreased proportionally such that the flow would travel the same distance between time steps but the mesh was unaltered from the $Re=200$ case. However this negates the possibility of phenomena occurring in smaller spatial scales and at lower time scales as Re is increased. For $Re<200$ Δt was kept constant and the run time extended so that the flow had time to develop. This was necessary since the diffusion constraint on the time step does not alter with Reynolds number.

Indeed the Reynolds number dependence would probably not have been tested at all had not Okajima's (1995) laboratory data become available during the study since it was not anticipated that the DVM simulations would provide meaningful information of the flow above $Re=500$. Results have been summarised in two subsections below. Firstly the findings relating to the $B/A=1.0$ cylinder are considered and then the combined effects of Reynolds number and B/A ratio are briefly examined.

5.4.1 Effect of *Re* variation on $B/A=1.0$ cylinder

Figure 5.4 plots drag coefficient, Strouhal number, r.m.s lift and skin drag vs. Re respectively for the square ($B/A=1.0$) cylinder. On the drag plot the previous numerical results of Davis and Moore (1982) and Franke *et al* (1990) are plotted along with Okajima's (1995) laboratory measurements for completeness. The results of Sohankar *et al* (1996) are also included. Sohankar *et al* simulated the flow over $50<Re<300$ and the agreement with DVM is strong in this range. Above $Re=150$ there is remarkable agreement with the measurements of Okajima. The DVM calculations closely follow the drag slope up to $Re=900$ at which point the drag peaks at around $C_D=2.1$-2.2, before falling back to a local minimum at $Re=2\times10^3$ with $C_D\approx1.7$. Surprisingly the recovery in drag beyond $Re=2\times10^3$ is also well predicted up to $Re=5\times10^3$, although at $Re=10^4$ the DVM gave a very low drag and the separation point had moved, giving a narrow wake analogous to a fully developed turbulent wake found for high Re flows past a circular cylinder. It was not anticipated that the DVM could make very sensible predictions of drag above $Re=500$ since three-dimensional effects and the growth of instabilities become increasingly important. Between $800<Re<2000$ the DVM calculations are slightly scattered in comparison to Okajima's data but certainly the prediction of a peak and dip followed by a subsequent rise suggest that the mechanisms responsible for these phenomena are 2-D in nature. A comparison with Figure 2.3 reveals some large similarities between the C_D vs. Re curves of the circular and square cylinders. Williamson (1996a) attributed the drag decline of region CD (see Figure 2.3) for the circular cylinder to an elongation of the vortex formation length caused by increasing disorder of developing small scale 3-D structures. Region CD, $200<Re<1200$ for the circular cylinder, corresponds directly to the range $900<Re<2\times10^3$ for the square cylinder and one assumes that the same mechanisms must be responsible for the drag variations of each curve. It would therefore be reasonable to suggest that small scale 3-D structures cannot be responsible for the fall in drag since a 2-D simulation was able to predict their presence and even estimate the Reynolds number at which they occur in agreement with the measurements of Okajima.

Figure 5.4(b) plots St vs. Re. The agreement with experiment is most satisfactory for $Re<500$, although the measurements of Okajima (1982) and Norberg (1993, 1996) certainly show more scatter in this range. Vortex shedding was predicted for Reynolds numbers as low as $Re=50$ by the DVM but no attempt was made to simulate the flow below this Reynolds number since calculations would be hindered by the need to perform lengthy runs before the shedding process develops. At this low Re the Strouhal number of $St=0.1$ agrees well with the laboratory data of Norberg who witnessed shedding down to $Re=47$. Both the measured values of Norberg and the present numerical calculations increase linearly up to $Re=150$. Above $Re=150$ the laboratory measurements indicate a gradual decline in St before it levels off at a Strouhal frequency of approximately 0.13 for $Re>10^3$. The DVM calculations are in close agreement with Norberg's data up to $Re=500$ but at higher Re the laboratory measurements and DVM calculations are quite different. Two dominant frequencies are observed in the range $600<Re<1500$ and for $Re>2000$ a single dominant frequency exists but the Strouhal number is considerably higher, $0.22<St<0.24$ than the experimentally determined values. It might be conjectured that the shedding process becomes increasingly controlled by three-dimensional and turbulent instabilities which are not accounted for in the DVM simulation.

The r.m.s lift and skin drag plotted in Figures 5.4(c) and 5.4(d) respectively are not quite as informative since no comparison with experiment can be made. Below Reynolds numbers sufficient to induce vortex shedding the lift coefficient must be zero since the wake consists of a symmetric vortex pair. Above $Re=50$ $C_{L(rms)}$ increases with Reynolds number reaching a peak near $Re=850$, similar to that found in the drag curve, before falling to a local minimum at $Re=2000$ and then slowly recovering again. Below $Re=200$ there exists a reasonable agreement with the previous numerical data of Davis and Moore (1982), Franke *et al* (1990) and Sohankar *et al* (1996). Skin friction is found to be negative for $150<Re<1000$ suggesting a substantial region of reversed flow along the side walls at these Reynolds numbers.

The force time histories of Figure 5.5 confirm the points made about the Strouhal curve. Emergence of vortex shedding is found at $Re=50$ although the curve has some irregularities present. Thereafter for $Re<500$ strongly periodic vortex shedding is found with $0.13<St<0.16$. For $500<Re<2000$ two frequencies are found in the spectral analysis of the lift curve. Above $Re=2000$ the strongly periodic vortex shedding returns but at a Strouhal number far exceeding the experimentally determined values.

A summary of the main findings from the DVM calculations of Reynolds number dependence for the $B/A=1.0$ cylinder follows. Vortex shedding was simulated for Reynolds numbers in the range $50<Re<10^4$. Norberg (1993) detected a Strouhal frequency at $Re=47$. Initially the flow remains attached to the side surfaces, implying positive skin friction drag, and separates from the trailing edge. With increasing Reynolds number the vortices form further from the base, resulting in decreased drag but the lift and Strouhal number both increase. Skin friction decreases as regions of recirculation begin to emerge along the side surfaces. At about $Re=150$ St is at a maximum, C_D is at a minimum and the skin friction drag becomes negative near to this Re. Above $Re=150$ the

flow is fully separated from the leading edge and the lift and drag both increase. The next major instability would appear to occur close to Re=850 at which point the drag and lift are both at a maximum and the skin friction is changing from negative to positive. This region would appear to correspond to region CD of Figure 2.3 which plots base pressure against Reynolds number for a circular cylinder. Williamson (1996a) attributed the fall in drag of region CD to the onset of small scale 3-D instabilities. This seems unlikely since the 2-D DVM simulation has captured the drag maximum and fall in a similar manner to that measured experimentally by Okajima (1995). It is possible that the increase in vortex formation length associated with a fall in drag is forced by developing 2-D small-scale instabilities and that their appearance is adequately represented in the simulation since the DVM represents the flow by infinitesimal vortex elements. It would be interesting to note whether a direct numerical simulation could predict the drag to a similar level of accuracy without alteration of the mesh since any instabilities smaller than the cell sizes cannot be accounted for in the simulation.

The rate of interaction between the separating shear layers governs the Strouhal number and the calculations of St made in the DVM simulation are not in accordance with the measured values beyond Re=500. This suggests that 3-D mechanisms are increasingly responsible for controlling this interaction as Re increases even though there is no apparent jump in behaviour evident in the Strouhal curve.

5.4.2 Combined effect of *Re* and *B/A* variation

The laminar flow calculations presented in Section 5.3 showed quite different C_D vs. B/A characteristics from the turbulent flow behaviour (see Figure 2.7). It is therefore expected that the Re dependence will vary with side ratio as there must exist a Reynolds number beyond which a critical geometry exists. Since the drag seems to be predicted fairly consistently with experiment up to Re=2000 for the B/A=1.0 cylinder and there is also broad agreement with the corresponding results of Sohankar *et al* at Re=200 for B/A variation, it would thus appear sensible to attempt to predict the drag variation with Reynolds number of some other geometries as maybe the critical drag phenomena will begin to occur at a higher Re.

Rectangles of side ratio, B/A=0.2, 0.5, 1.0 and 2.0 were tested for $Re<10^3$ and the results are presented in Figure 5.6. The B/A=2.0 cylinder shows little variation in drag coefficient with Re. At B/A=0.2 and 0.5 the drag increases with Re and although the gap between the two has narrowed at Re=500 there is no evidence for a critical drag side ratio below $Re=10^3$. The Strouhal frequency variationis shown in Figure 5.6(b). There is little variation in St for the B/A=0.5 cylinder and a slight decrease in St for the B/A=0.2 cylinder as Re increases from 200 to 1000. For the B/A=2.0 cylinder the Strouhal number increases from a value of around St=0.13 at Re=100 to St=0.20 at Re=500 before decreasing slightly. These values are a little higher than the laboratory measurements shown in Figure 2.12(b).

5.5 Effect of flow at an angle of attack

Results for the flow at an angle of attack are given in Figure 5.7. Only the B/A=1.0 cylinder was tested due to time constraints and since Sohankar *et al* (1996) have already tested the variation for a family of rectangles with B/A=1.0, 2.0, 3.0 and 4.0. It was anticipated that any results from the DVM would not differ greatly from those of Sohankar since broad agreement was shown in the variation of B/A earlier. A direct comparison with the findings of Sohankar *et al* can be seen. Sohankar has only plotted pressure drag but there is an excellent agreement between his findings and the results of this study with pressure drag falling to a minimum value close to α=6°, before rising to a maximum value of around C_{Dp}=1.7 at α=45°. A notable difference however is seen in the Strouhal number curve (Figure 5.7(b)); Sohankar found that the Strouhal number initially increased with angle of attack until α=6°; St then fell to a minimum value near α=10° before recovering to a maximum value of St=0.2 at α=45°. In contrast the DVM simulation has produced a smooth increase in St with increasing incidence. At a first glance it appears that perhaps Sohankar's data point at α=10° is a mistake since it is possible to visualise where it might be placed to smoothen the curve but reference to Figure 2.19(a) shows that Sohankar has predicted similar minima occurring for other B/A values.

This fundamental difference is further complicated by examination of the variation in lift with angle of attack, Figure 5.7(c). Sohankar *et al* do not state that they have plotted only the pressure component of lift but this would appear to be the case since the agreement between their DNS results and DVM is far greater when the pressure component is plotted. The lift coefficient is initially negative with a minimum at α=6°, which corresponds to the point of minimum drag. It then rises becoming positive at $\alpha\approx$20°, but remains relatively small and eventually falls back towards zero as α approaches 45°. The r.m.s lift plotted in Figure 5.7(d) agrees well for α>20°. Below this range there is substantial difference from Sohankar's results which cannot be accounted for by neglect of skin friction lift since at low incidence both the mean and r.m.s. values of skin friction lift are small. It should be noted however that Sohankar *et al* found the values of $C_{L(rms)}$ to vary substantially with simulation conditions. The α=0° cylinder showed a range of $0.20<C_{L(rms)}<0.36$ depending on mesh parameters and it is expected that the cylinder would show a similar variance at other angles of attack. The value of $C_{L(rms)}$=0.36 at α=0° is closest to that found in this DVM study and corresponds to the most refined grid used by Sohankar *et al*. However the grid did not influence other calculated values such as C_D and St to such an extent and so they chose a less refined grid set-up probably because this enabled considerable savings in run times to be made.

The force time histories of Figure 5.8 demonstrate that a non-symmetric bluff profile induces vortex shedding almost immediately with steady lift and drag curves established soon after the impulsive start. Strangely, at α=45° the drag does not oscillate in a uniform manner at twice the shedding frequency but appears to indicate that vortex shedding might be favoured from one side. Further examination of Figure 5.7(c) reveals that the mean lift is not quite zero at α=45°. This gives further evidence for some asymmetry in the vortex shedding process but the reasons for this behaviour remain unclear at present.

5.6 Flow visualisation

In the previous sections we have concentrated on analysis of the mean parameters, which can be calculated from the simulation, such as lift, drag and Strouhal number. Although no maximum in the drag curve was reported there did appear to be a maximum in the r.m.s lift and the Strouhal number occurring close to B/A=0.3. These quantitative results are useful in themselves but a qualitative analysis of the flow visualisation might provide some further insight into the physics responsible for such mechanisms. As described in Chapter 2, the work of Laneville and Yong (1983) and Ohya (1994) has helped to provide a better understanding of why we expect a critical drag phenomenon at higher Reynolds number.

The flow pattern analysis of this study has been split into two categories; firstly a near wake analysis of the time evolving flow pattern and associated surface pressure distribution is given and then the far wake flow patterns are compared for several cylinders.

Each of the visualisations shows the distribution of individual point vortices at instants of the DVM simulation. Each of the vortices has an associated circulation strength Γ_k and a visualisation scheme was chosen such that the strength of the point vortices is indicated by their colour. The colour coding scheme varies through fifty shades, with red indicating strong positive (anticlockwise) vorticity, green weak positive, blue weak negative and violet strong negative vorticity.

In the full analysis approximately 100 frames were made of each shedding cycle and these were made into loopable videos of the shedding process. A video of vortex shedding past a B/A=1.0 cylinder has been made into an 'animated gif' file format so that it could be made available on the internet. This video may be viewed at the following World Wide Web address: *http://vortex.mech.surrey.ac.uk/FluidsGroup/People/steggel*

5.6.1 Near wake visualisation

Figures 5.9-5.14 show visualisation time sequences and corresponding surface pressure distributions for rectangles in the range $0.2 \leq B/A \leq 4.0$. The visualisations were produced at four points of the shedding cycle determined from the lift curve: (a) C_L zero; (b) C_L is minimum; (c) C_L zero; (d) C_L maximum. These instants were chosen as they are easily identifiable from the force time history curve.

The surface pressure coefficient is defined as

$$C_P = 1 - \frac{\Delta p}{q_0}, \tag{5.3a}$$

where

$$q_0 = \tfrac{1}{2}\rho U_0^2. \tag{5.3b}$$

Δp is measured from the centre of the front surface, assumed to be a stagnation point, and found from the pressure integral expressions of Chapter 4; q_0 is the dynamic pressure.

The pressure distribution plots then show the variation in surface pressure from the centre of the front surface around the rectangle in a clockwise direction. The pressure differential between the base and front surfaces is primarily responsible for the drag and that between the upper and lower side surface for lift, although there will also be a small amount of lift and drag due to skin friction. Clear similarities can be observed between each set of frames and at the corresponding snapshots and the following description is made with particular reference to Figure 5.9, with B/A=0.2, since the vortex shedding process is very apparent in this case.

(a) The surface pressure distribution is symmetric implying zero lift force. A positive vortex is just about to be shed and a new one is forming close to the lower side surface.

(b) This vortex then rolls up strongly resulting in a reduced pressure along the lower portion of the base and the lower side surface. Meanwhile the anticlockwise vortex has moved further from the base of the body, resulting in a higher pressure along the upper portion of the base surface, and the separating shear layer is now at a more inclined angle to the upper surface, which also increases the pressure along the upper side surface. As a result the lift attains a minimum value at this point. The effect of the positive vortex close to the base outweighs that of the negative one and thus drag is also maximum at this point.

(c) At this moment the inverse to situation (a) is attained as the positive vortex begins to move away from the base, the negative vortex is about to be shed and a new one is forming close to the upper surface. A balance in the pressure distribution has again been obtained and hence the lift force becomes zero once again.

(d) It would appear that the negative vortex has been shed at some point in-between (c) and (d). The term 'shed' is used loosely here but a sensible definition might be the point at which an old vortex is no longer directly attached by a 'string' of vorticity to the newly forming vortex of the same sign. The inverse to plot (b) has now been obtained with a negative vortex rolling up strongly along the base resulting in reduced pressure along the upper surface portion.

The above description holds in many respects for the flow about the cylinders of larger side ratio. The phase of vortex shedding with respect to the lift force remains identical throughout the B/A range studied but the size and position of the vortex formation varies considerably as we would expect since the drag force decreases as the afterbody lengthens. A comparison between Figures 5.9(a)-5.14(a) shows that with increasing B/A the vortex which is forming near the lower surface is pushed further from the base of the cylinder and no longer rolls up as tightly. This is particularly evident in Figures 5.9(b)-5.14(b) as the vortex becomes more elongated in the streamwise direction and its centre appears further from the base.

An attempt can now be made to describe the reasons for the peak in the lift and Strouhal number close to B/A=0.3. Separation occurs at the cylinder corner and the shear layer grows along the cylinder side surface. At the rear of the cylinder the vortex shedding process dominates but this results in an oscillation of the shear layer. This oscillation leads to a difference in the pressure distribution along the top and bottom surfaces and hence an oscillatory lift results. As indicated by the visualisations at minimum lift, Figures 5.9(b)-5.14(b), and maximum lift, Figures 5.9(d)-5.14(d), there is a clear difference between the angles of inclination of the separating shear layers from the lower and upper surfaces. At low B/A it appears that this angle can oscillate substantially during the shedding cycle, a low surface pressure corresponding to the moment at which the shear layer is closest to the surface. Near to the leading edge the oscillation of the shear layer during the shedding cycle is small since it must remain attached to the front edge. Moving further downstream away from the leading edge the shear layer has more freedom of oscillation. As the afterbody is extended the trailing edge begins to interact with the separated layer damping out its oscillations and thus the surface pressure along the side surfaces can no longer oscillate as freely and lift begins to fall. The connection with the Strouhal peak remains unclear.

A simple analysis was carried out in an attempt to compare these visualisations, quantitatively, with those of Laneville and Yong (1983) who made laboratory measurements at $Re=7\times10^4$. They have defined the vortex formation position (see Figure 2.8) with time-averaged quantities V_p the distance of the vortex centre from the cylinder base and V_c the distance between vortex centres. In their laboratory visualisations the flow patterns could be time-averaged by an oil film technique and the quantities V_p and V_c are taken as the point of maximum oil accumulation, clearly identifiable from Figure 2.10. V_p and V_c are non-dimensionalised by B and plotted against B/A in Figure 2.9.

It is more difficult to define vortex centres in the DVM visualisations and these have simply been approximated visually from each of the near-wake plots. An average over the four instants of vortex shedding has then been taken in an attempt to estimate the mean position over the whole cycle. This is not particularly satisfactory as a means of finding V_p and V_c since it not only introduces spatial inaccuracies from the visual identification of vortex centres but temporally there will be inaccuracies introduced from averaging at only four instants of the shedding cycle. In hindsight a more effective method would be to average the mesh values of vorticity over a number of shedding periods and assume that the positions of high vorticity would correspond directly to the positions where oil accumulates in Laneville and Yong's technique. However the visual identification method should be useful for a preliminary investigation.

B/A	V_p/A	V_c/A
0.2	0.5	0.8
0.5	0.7	0.4
1.0	1.1	0.57
2.0	1.5	0.53
3.0	1.7	-
4.0	2.4	-

Table 5.8 Effect of B/A on vortex formation positions

Table 5.8 gives values for the variation in vortex formation position with B/A. Beyond B/A=2.0 the clarity with which the vortex centre position can be identified from the visualisations is greatly reduced and although it is possible to estimate V_p, the error in any estimation of V_c would have been quite large and thus these values were not determined. Clearly V_p/A increases with increasing B/A which is consistent with a rise in the base pressure or, equivalently, a reduction in the drag as shown in Figure 5.2(a). This differs from the result found by Laneville and Yong (see Figure 2.9) who found that V_p/A is minimum close to B/A=0.6. The changes in V_c/A from the DVM simulation are less clear. Laneville and Yong's work showed a rapid decrease in V_c/A as B/A increases from 0.2 to 0.64. At B/A=0.64, V_c/A is almost zero as the vortices are forming virtually along the wake centre line. With a further increase in B/A they found the formation positions moved away from the wake centre line. The DVM results do show evidence for a minimum value of V_c/A occurring between B/A=0.2 and 1.0 but it would appear that the vortices do not form close to the wake centreline as was found by Laneville and Yong for a higher Reynolds number.

5.6.2 Far wake visualisation

Wake visualisations of cylinders with side ratios in the range $0.2<B/A<4.0$ are plotted in Figure 5.15. The scales of the rectangle widths are the same in each picture and the colour coding of vortex particles is identical to that used in the near-wake visualisations. Two main structures are observed. Firstly a primary structure is observed in which the vortices are arranged in staggered pairs with the longer dimension of each vortex oriented in a cross stream direction. This structure becomes fully established further downstream in the wake as B/A is increased. A secondary structure evolves as the vortices roll up such that their longer dimension is now aligned with the flow direction. This structure appears almost immediately in the B/A=0.2 case with only a single pair observed in the primary structure and appears further downstream in the B/A=0.5 case. It is evident that the vortices are beginning to roll up into the secondary structure at the downstream end of the B/A=1.0 visualisation; one might anticipate that the secondary structure would appear at an increasing distance downstream as B/A is increased beyond B/A=1.0 although the wake visualisations of Figures 5.15(d)-(f) do not

go far enough downstream to verify this assertion. For the B/A=0.2 cylinder the secondary structure quickly breaks down into a less orderly configuration which was not observed for the cylinders of larger side ratio.

Wake visualisations of the B/A=1.0 cylinder at an angle of attack are shown in Figure 5.16. The same two main wake structures are observed with the secondary structure appearing further upstream as α increases up to 30°. However at α=45° the secondary structure appears slightly further downstream than at α=30°. Since the body is symmetric at α=45°, the shedding process should be symmetric and it is possible that the primary structure is more stable under symmetric shedding and hence breaks down further downstream. This suggests that there exists a limit between α=20° and α=45° at which point the primary structure is least stable. The maximum wake width observed decreases from around 8d at α=0° to 6d at α=45°, where d is the maximum cross-stream dimension.

5.7 Future use of the code for uniform flow calculations

Developing three-dimensional instabilities are considered to be the main hindrance to simulation accuracy at these low Re and they may manifest themselves in different forms and at different Re depending on the afterbody geometry. A two-dimensional model cannot therefore be expected to provide a good representation of a real flow which exhibits strongly three-dimensional behaviour. For the future use of this code in its present format it is recommended that a Reynolds number limit of Re=500 and a side ratio range of 0.25<B/A<3.0 be used. The upper limit for Re is chosen purely on the basis that for B/A=1.0 satisfactory agreement was obtained with existing measurements for the variation in Strouhal number and drag coefficients. It should not however be taken for granted that other side ratios will show agreement over a similar range if and when laboratory measurements become available for comparison.

Introducing the parameter M_{in} helped make the mesh more user-friendly since the values of $\Delta\eta_{min}$ and J_{min} could be controlled such that the diffusion time-step limit did not become too small. However there is still a problem with the grid at extremes of B/A caused by an increasing disparity between the grid spacing near the rectangle corners and at the side surface mid-points. An upper limit of B/A=3.0 is given simply because the mesh does not place enough cells within the wake region at higher B/A. This maybe what causes the noisy force time histories shown for B/A=3.0 and 4.0. Simulation at an angle of attack does not appear to present any extra difficulty.

A few main suggestions are given for future development of the code as a tool for uniform flow simulations past rectangles. Firstly vortex formation positions could be more precisely determined by analysis of the grid vorticity values, averaged over a number of shedding cycles. A comparison with the work of Laneville and Yong (1983) could then be more rigorously undertaken. In addition the time variation of skin friction plotted in a

similar manner to the time variation of surface pressure may prove beneficial in attempting to explain the changes responsible for the lift and Strouhal peaks at B/A=0.3 since the direction of flow along the body surface is quite difficult to interpret from the near-wake visualisations.

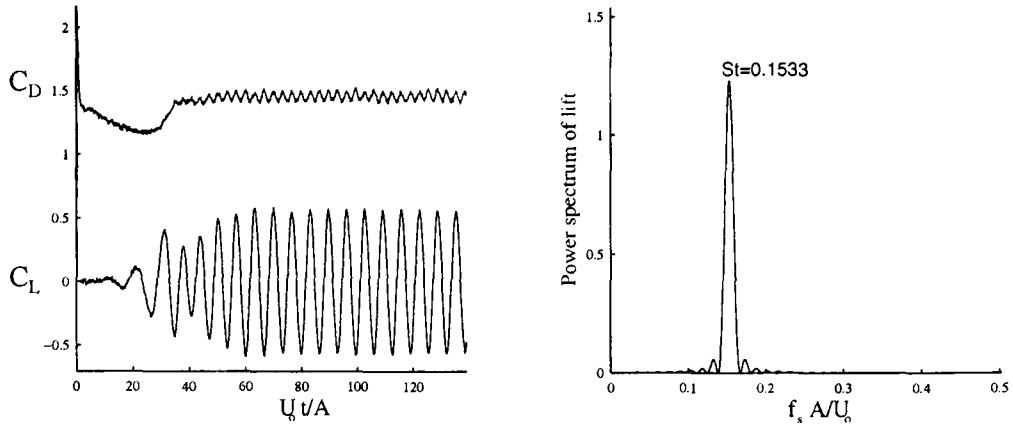

(a) M_{out}=160

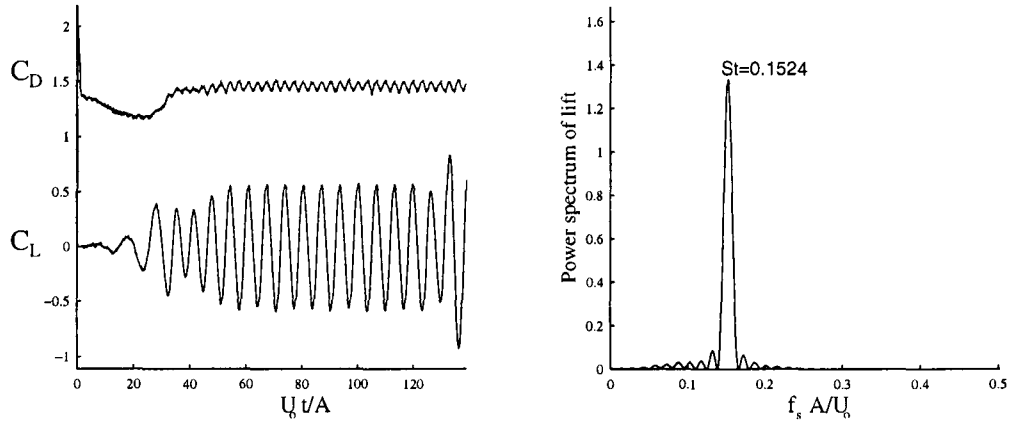

(b) M_{out}=130

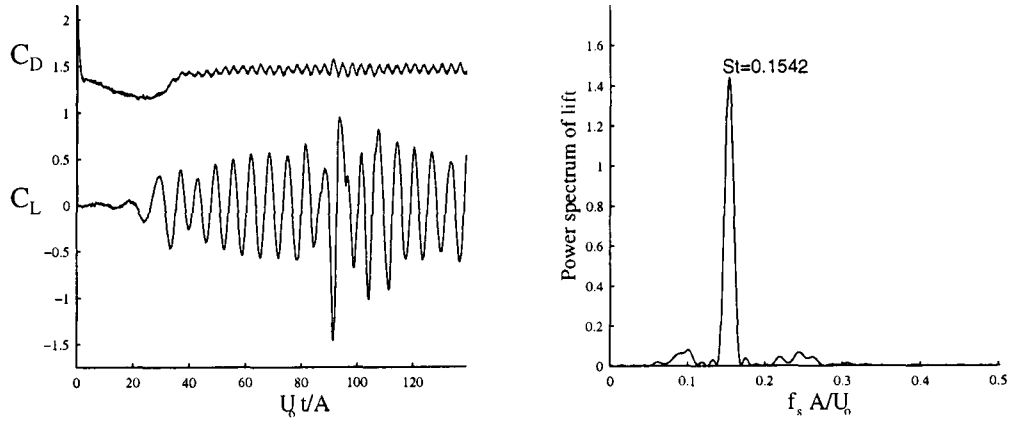

(c) M_{out}=70

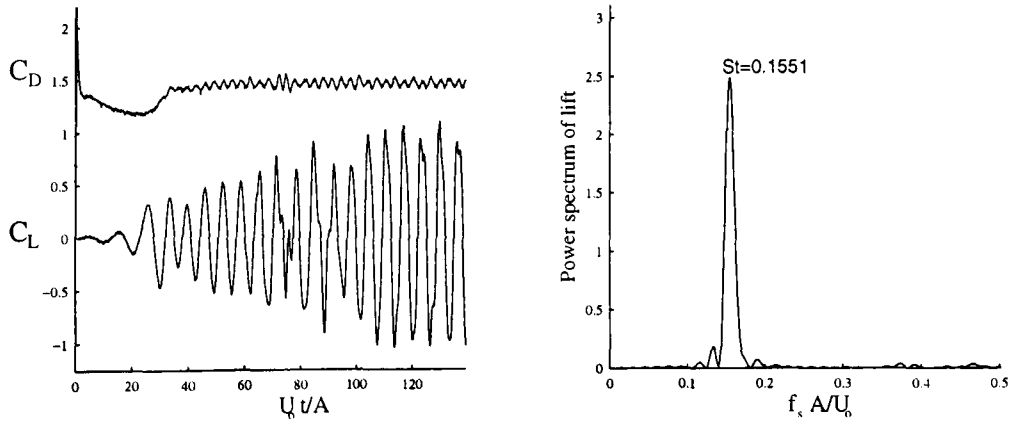

(d) M_{out}=50

Figure 5.1 Force time histories, B/A=1.0 cylinder, Re=200;
Effect of varying M_{out} (M_{in}=0.025, Δt=0.005, σ_{min}=0.00075, J_{min}=0.01).

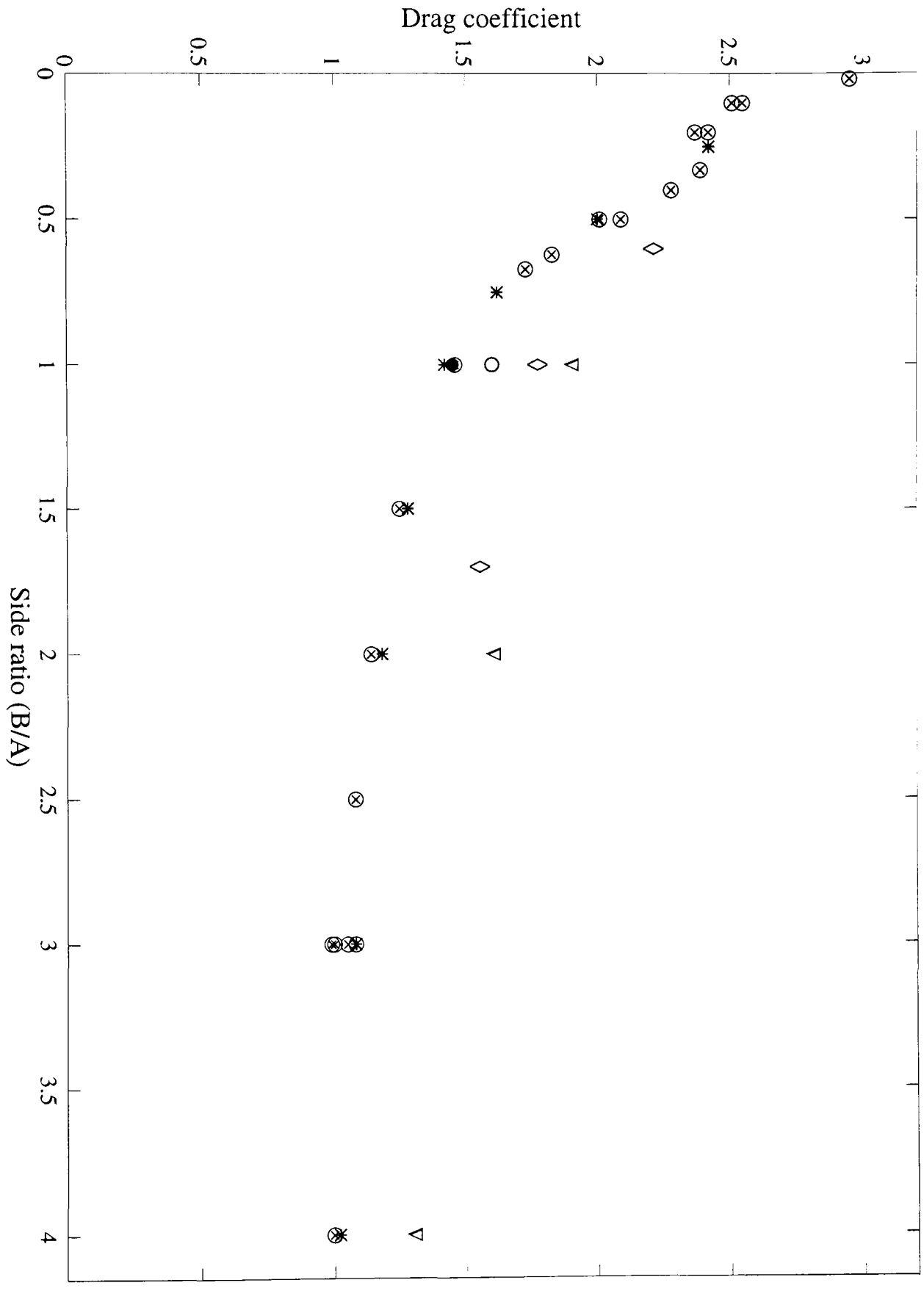

Figure 5.2(a) Drag coefficient vs Side Ratio, *Re*=200.

⊗ Present calculations ∗ Sohankar *et al* (1996) • Okajima(1995)
∇Okajima *et al* (1993) o Franke *et al*(1990) ◊Davis & Moore(1982)

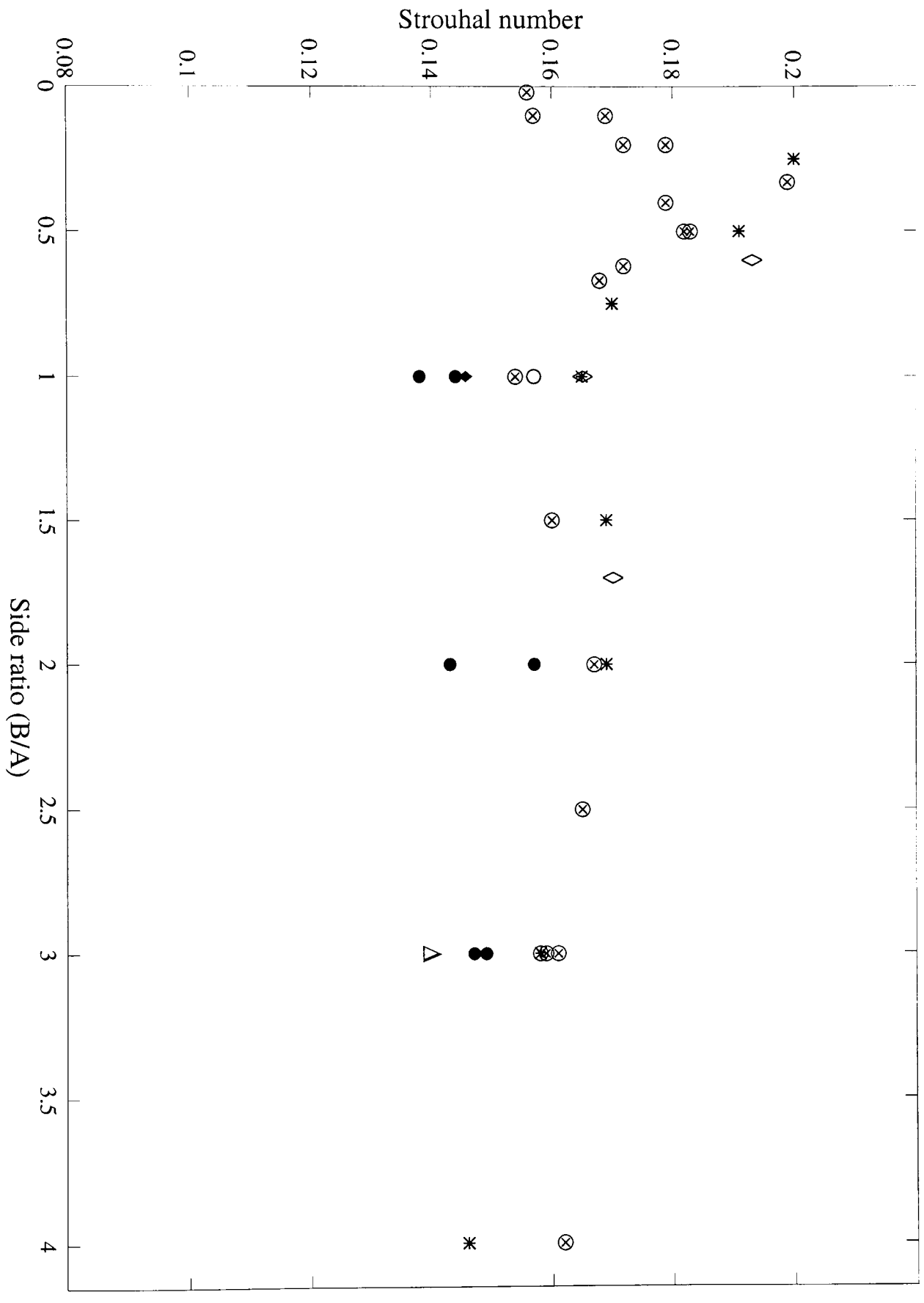

Figure 5.2(b) Strouhal number vs Side Ratio, *Re*=200.

⊗ Present calculations ∗ Sohankar *et al* (1996) • Okajima(1995)
Δ Nakayama *et al* (1993) o Franke *et al*(1990) ◊, ♦ Davis & Moore(1982)

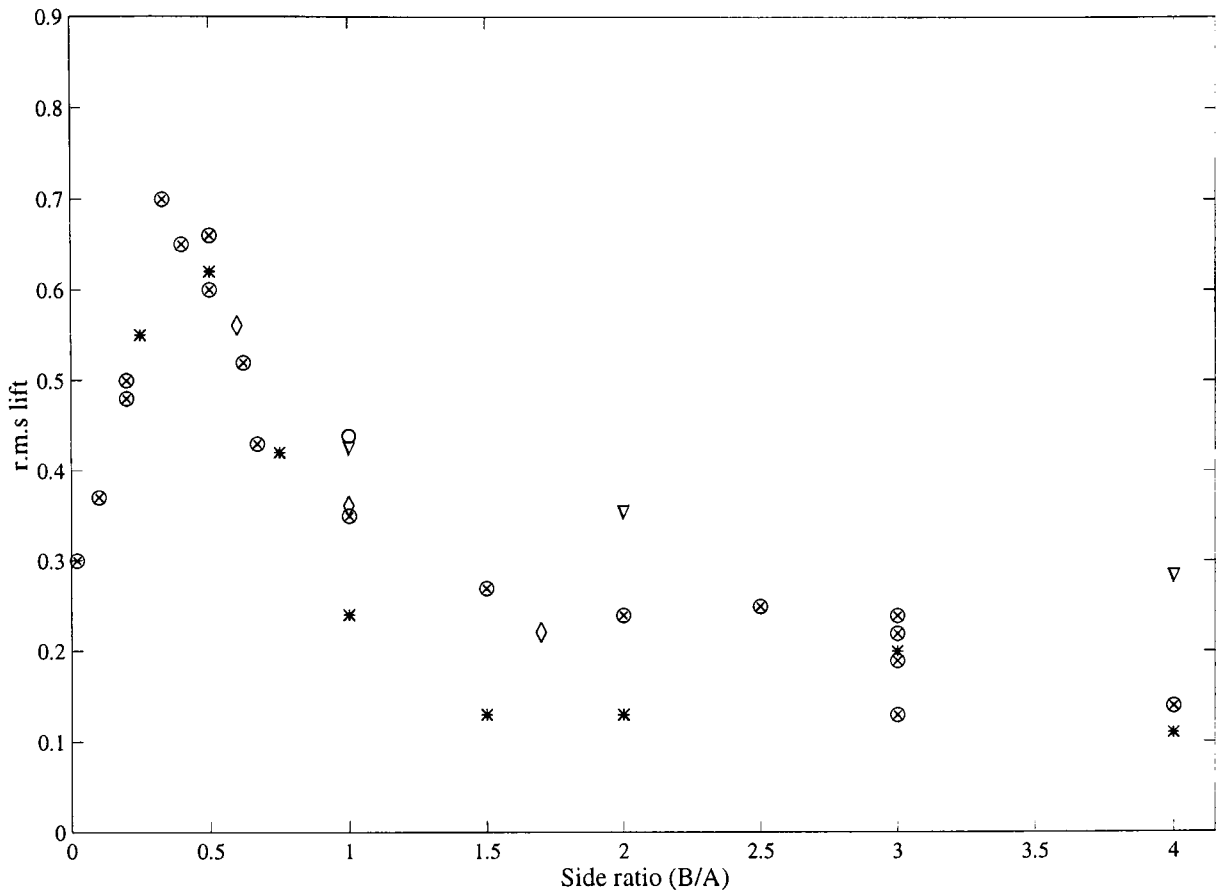

Figure 5.2(c) $C_{L(rms)}$ vs Side Ratio, *Re*=200.
⊗ Present calculations ∗ Sohankar *et al* (1996)
∇Okajima *et al* (1993) o Franke *et al*(1990) ◊Davis & Moore(1982)

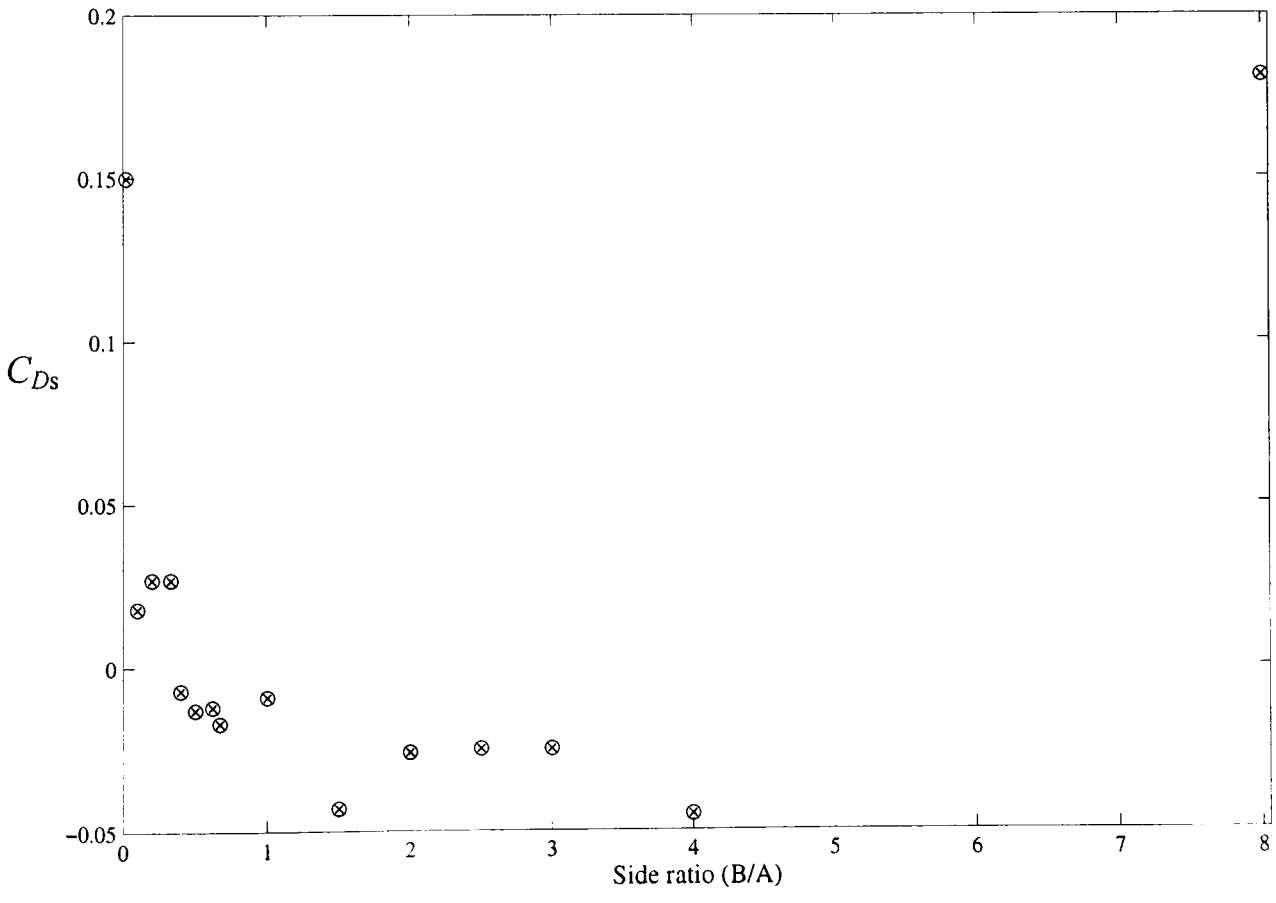

Figure 5.2(d) C_{Ds}vs Side Ratio, *Re*=200.
⊗ Present calculations

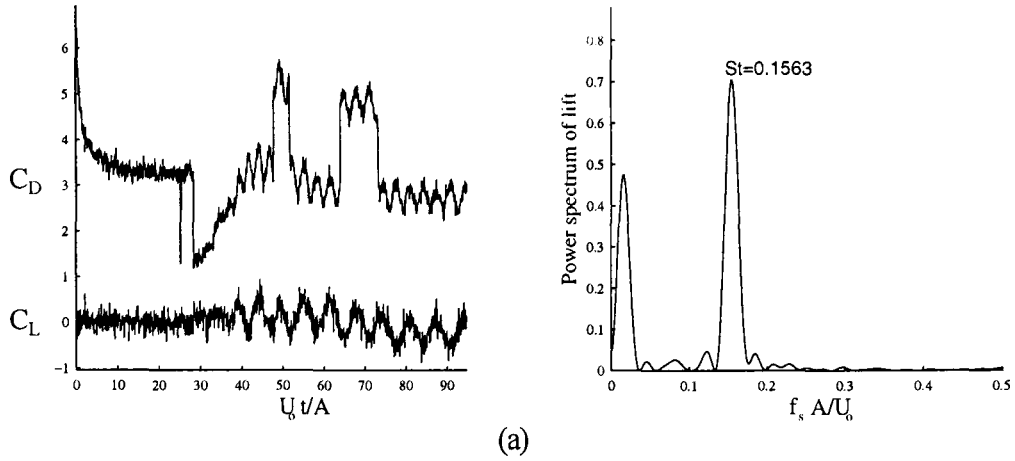

(a)

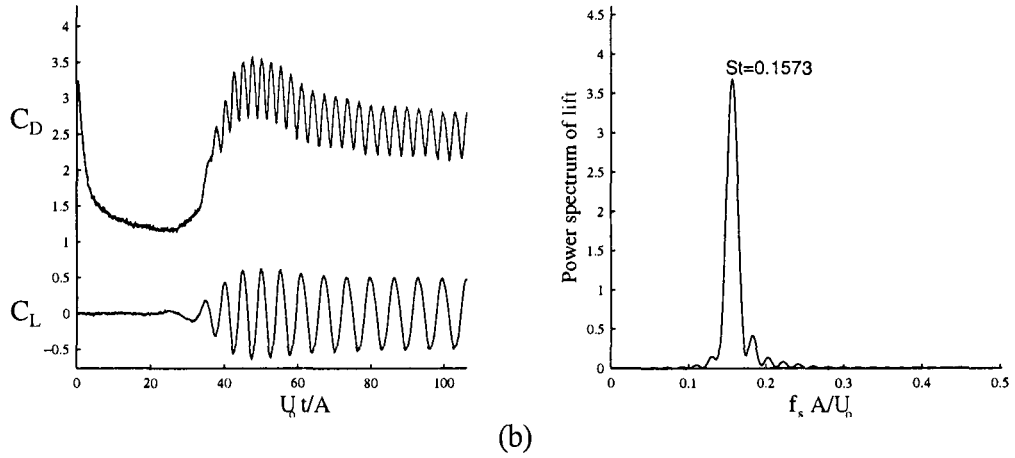

(b)

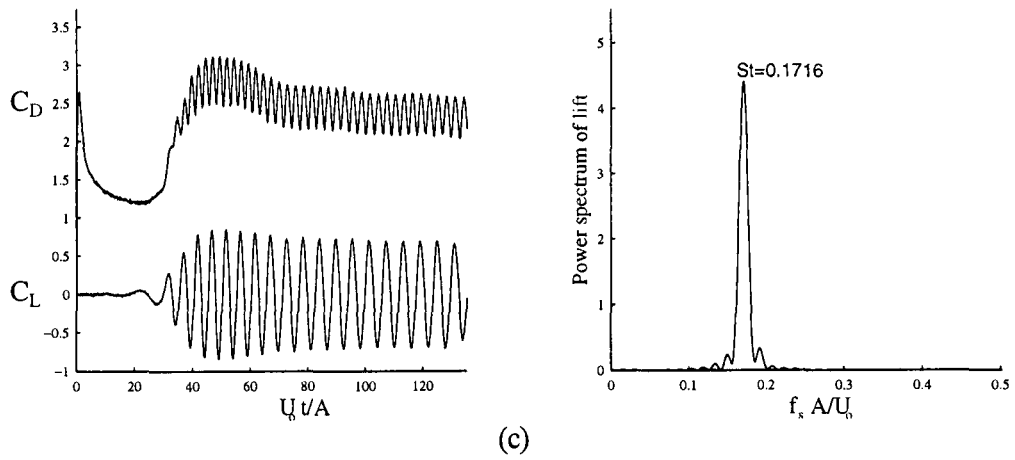

(c)

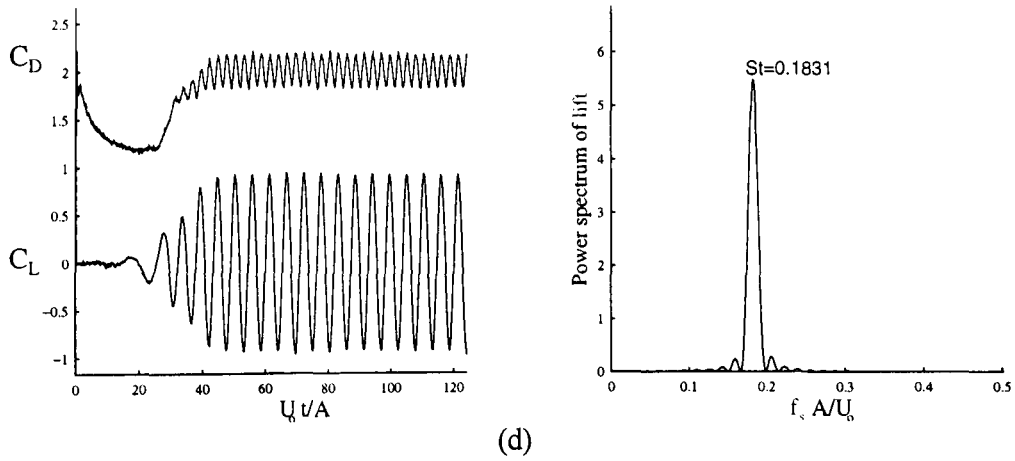

(d)

Figure 5.3 Force time histories, *Re*=200
(a) *B/A*=0.02; (b) *B/A*=0.1; (c) *B/A*=0.2; (d) *B/A*=0.5

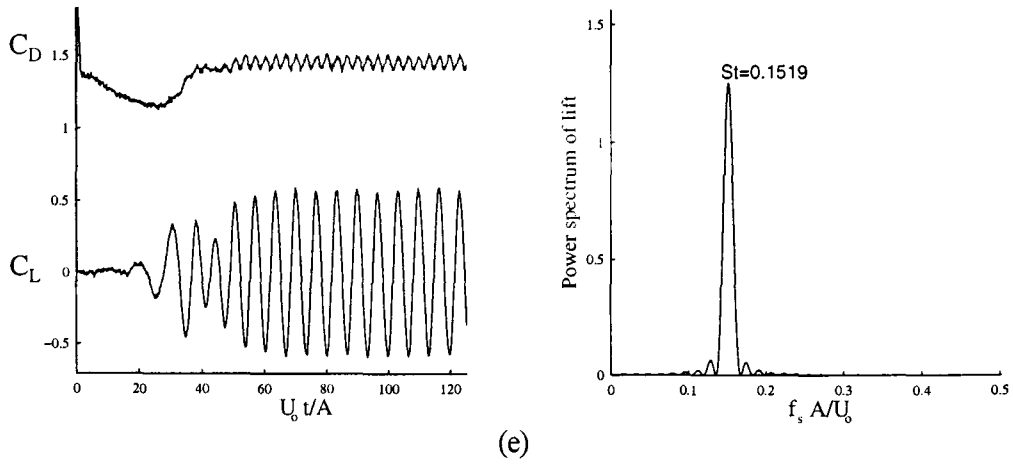

(e)

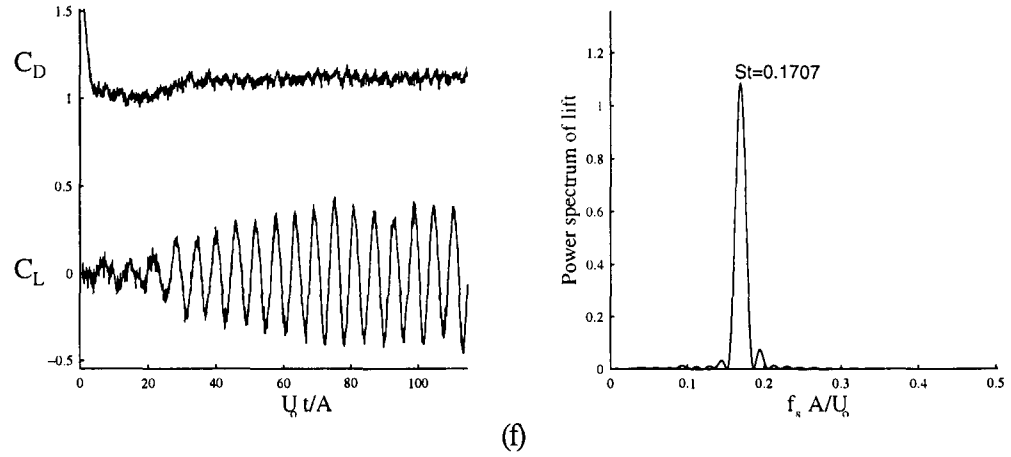

(f)

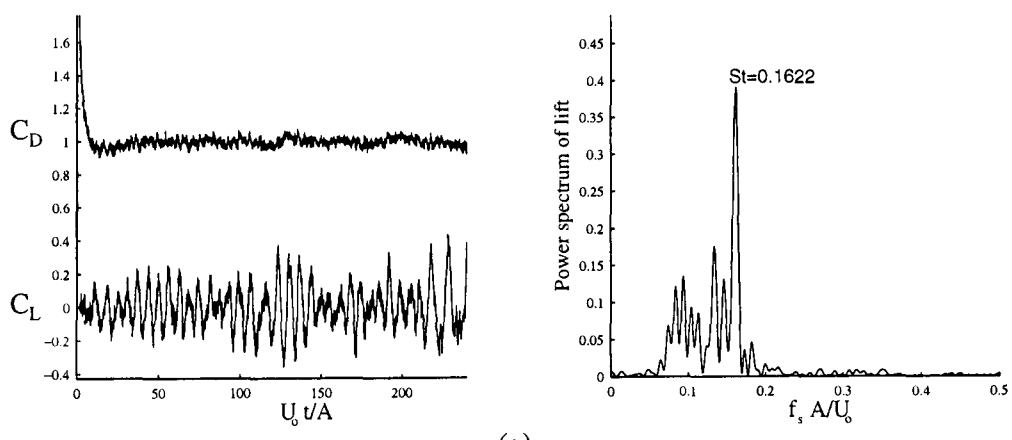

(g)

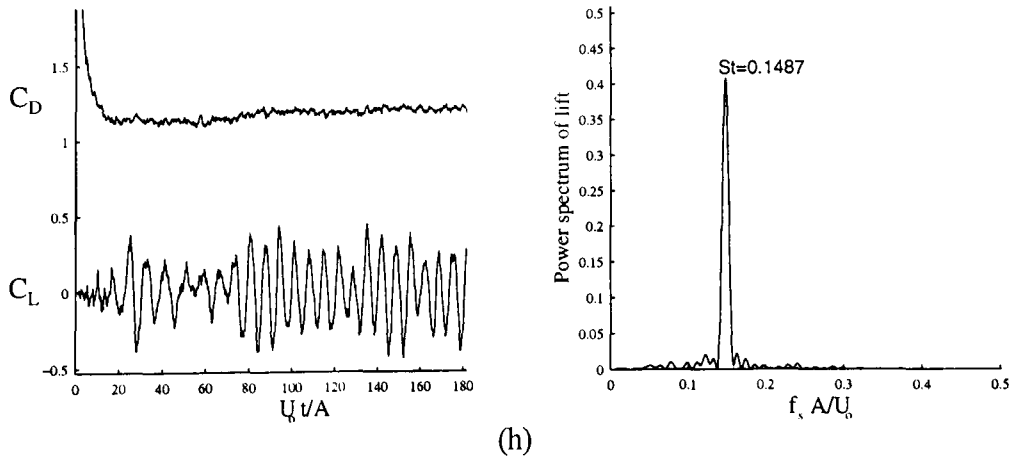

(h)

Figure 5.3 (cont) Force time histories, *Re*=200
(e) *B/A*=1.0; (f) *B/A*=2.0; (g) *B/A*=4.0; (h) *B/A*=8.0

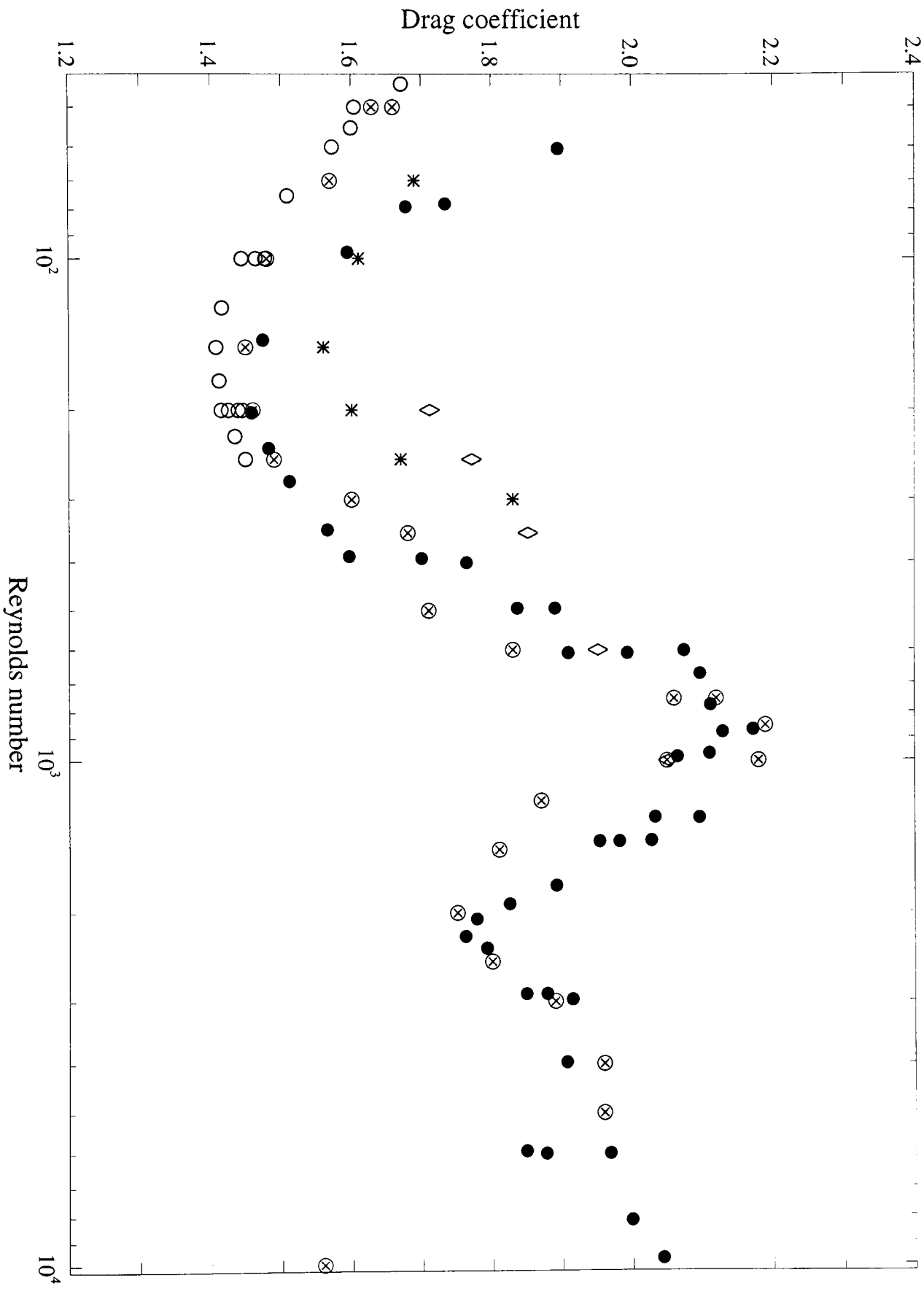

Figure 5.4(a) Drag coefficient vs Reynolds number, B/A=1·0 cylinder.
⊗ Present calculations o Sohankar *et al* (1996) • Okajima(1995)
*Franke *et al*(1990) ◊Davis & Moore(1982)

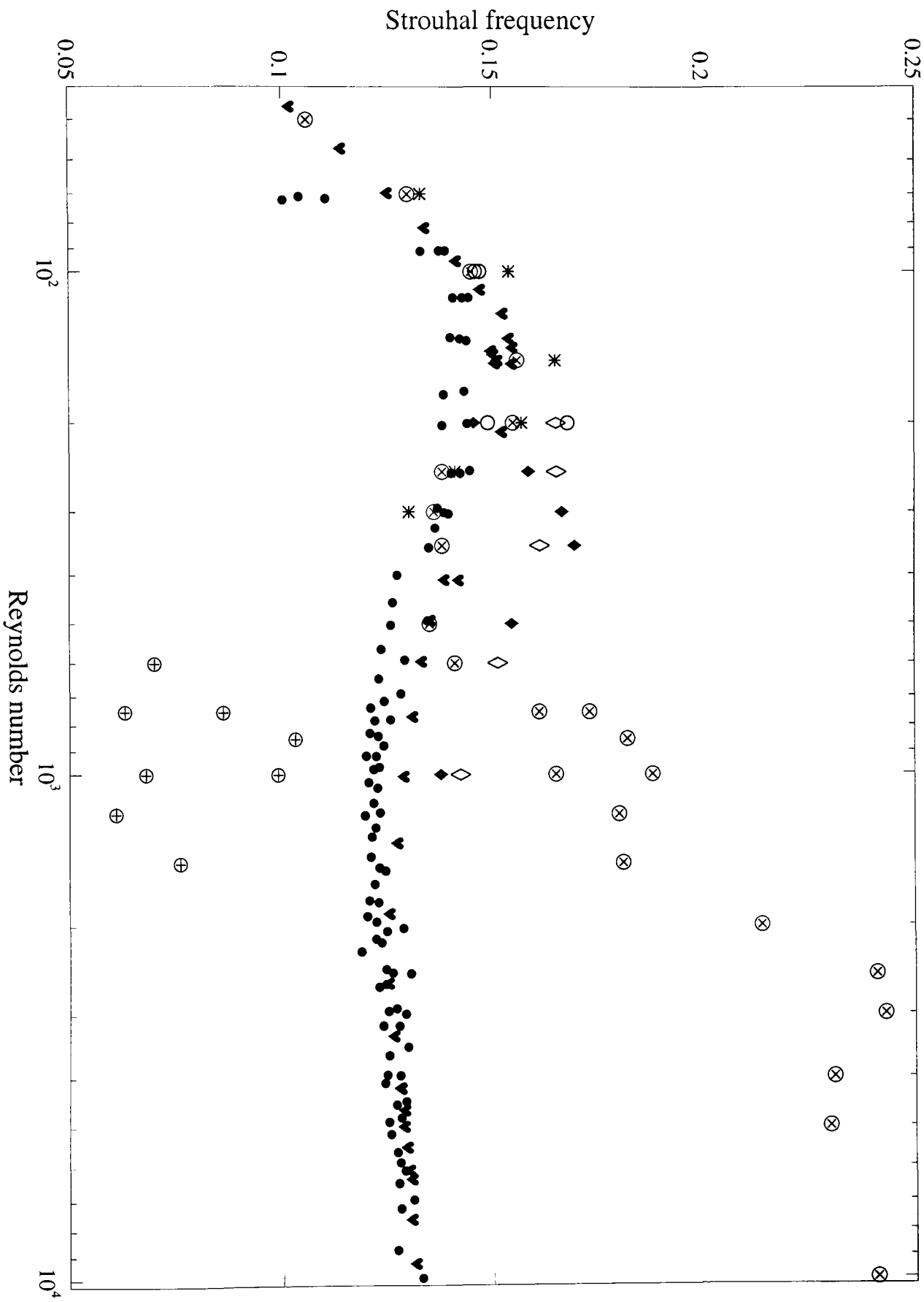

Figure 5.4(b) Strouhal frequency vs Reynolds number, B/A=1·0 cylinder.
⊗ Present calculations o Sohankar *et al* (1996) ♥ Norberg (1993, 1996)
∗Franke *et al*(1990) ◊(num), ♦(exp) Davis & Moore(1982) • Okajima(1982)

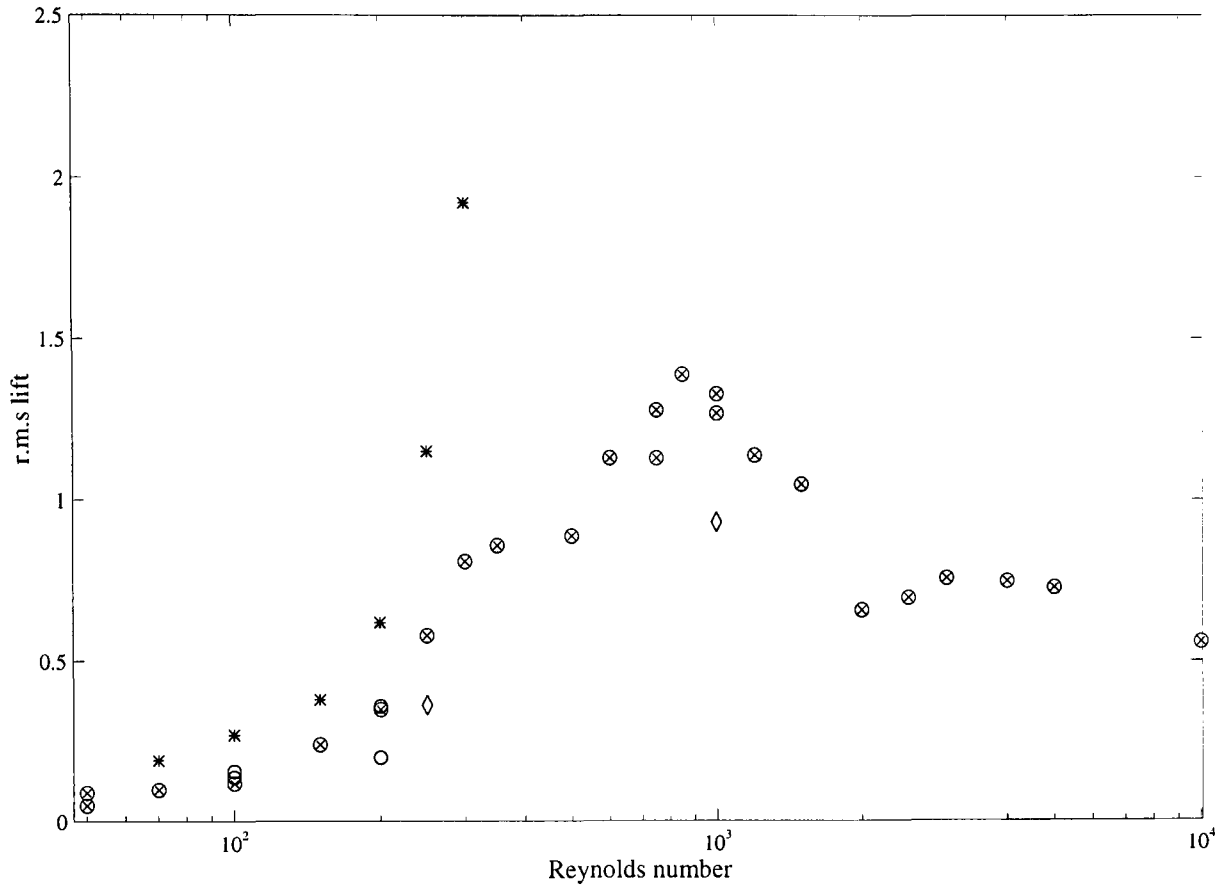

Figure 5.4(c) $C_{L(rms)}$ vs Reynolds number, B/A=1.0 cylinder
⊗ Present calculations o Sohankar *et al* (1996) ∗ Franke *et al*(1990) ◊ Davis & Moore(1982)

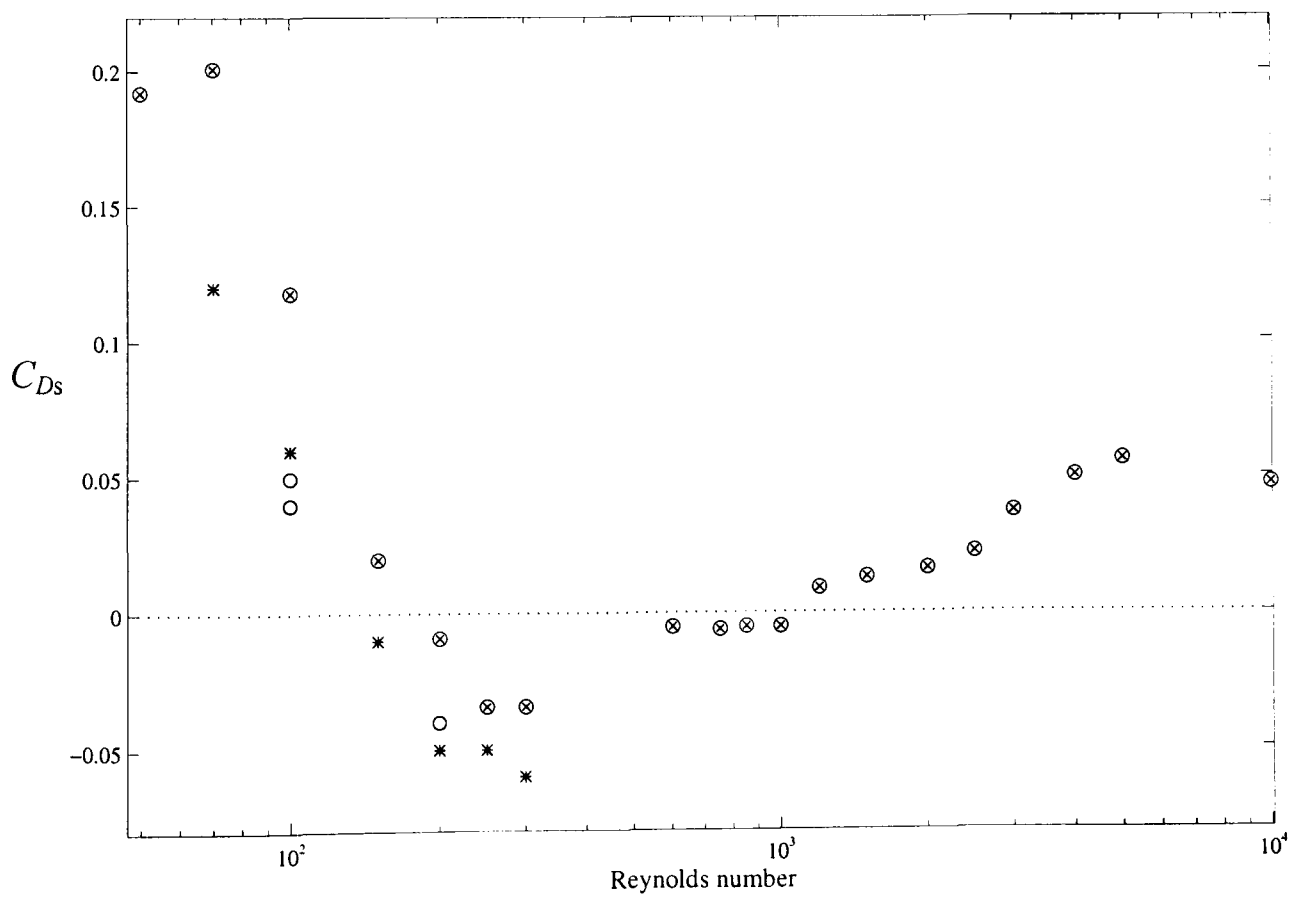

Figure 5.4(d) C_{Ds}vs Reynolds number, B/A=1.0 cylinder
⊗ Present calculations o Sohankar *et al* (1996) ∗ Franke *et al*(1990)

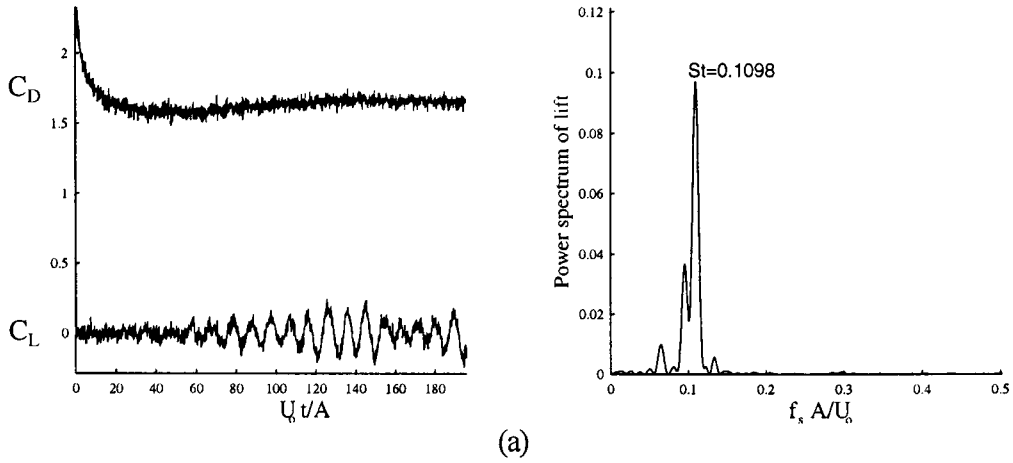

(a)

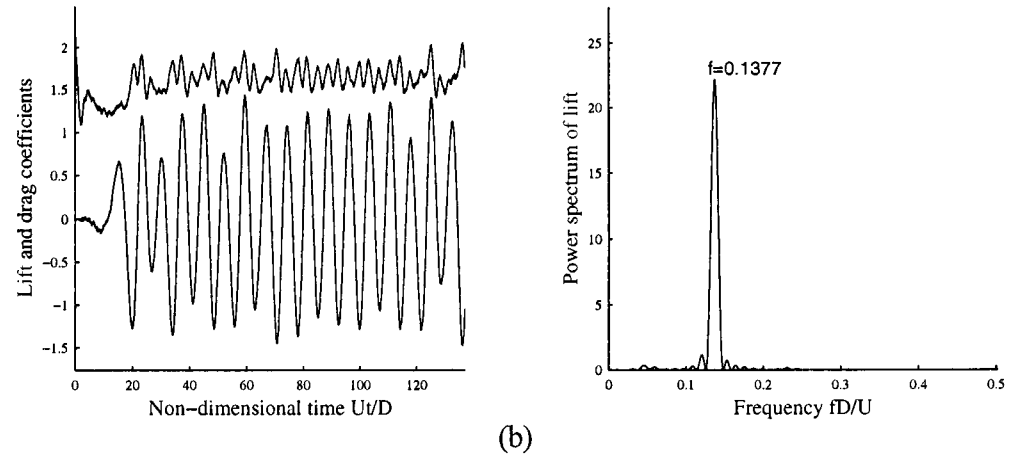

(b)

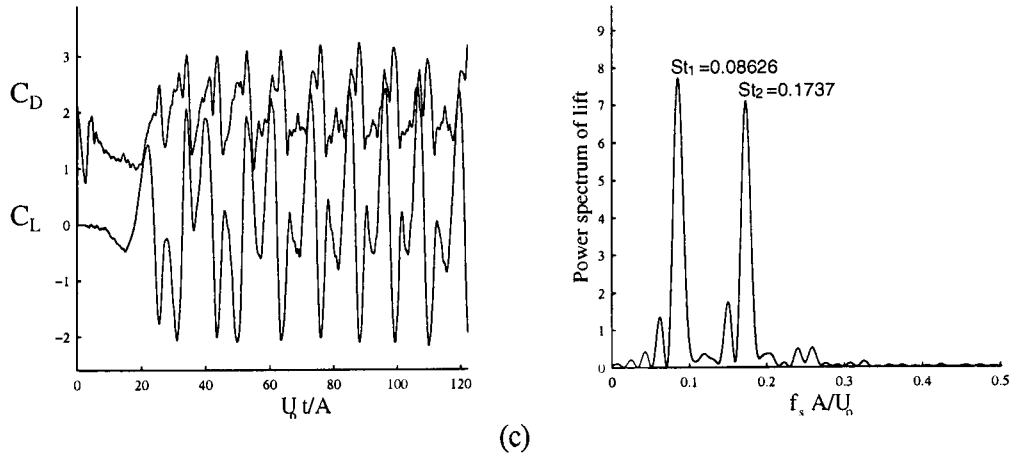

(c)

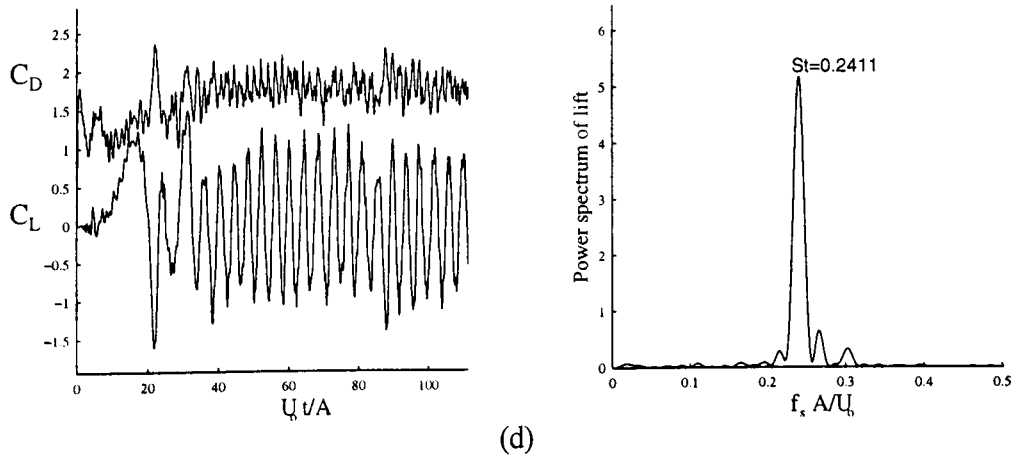

(d)

Figure 5.5 Force time histories, *B/A*=1.0 cylinder.
(a) *Re*=50; (b) *Re*=350; (c) *Re*=750; (d) *Re*=2500

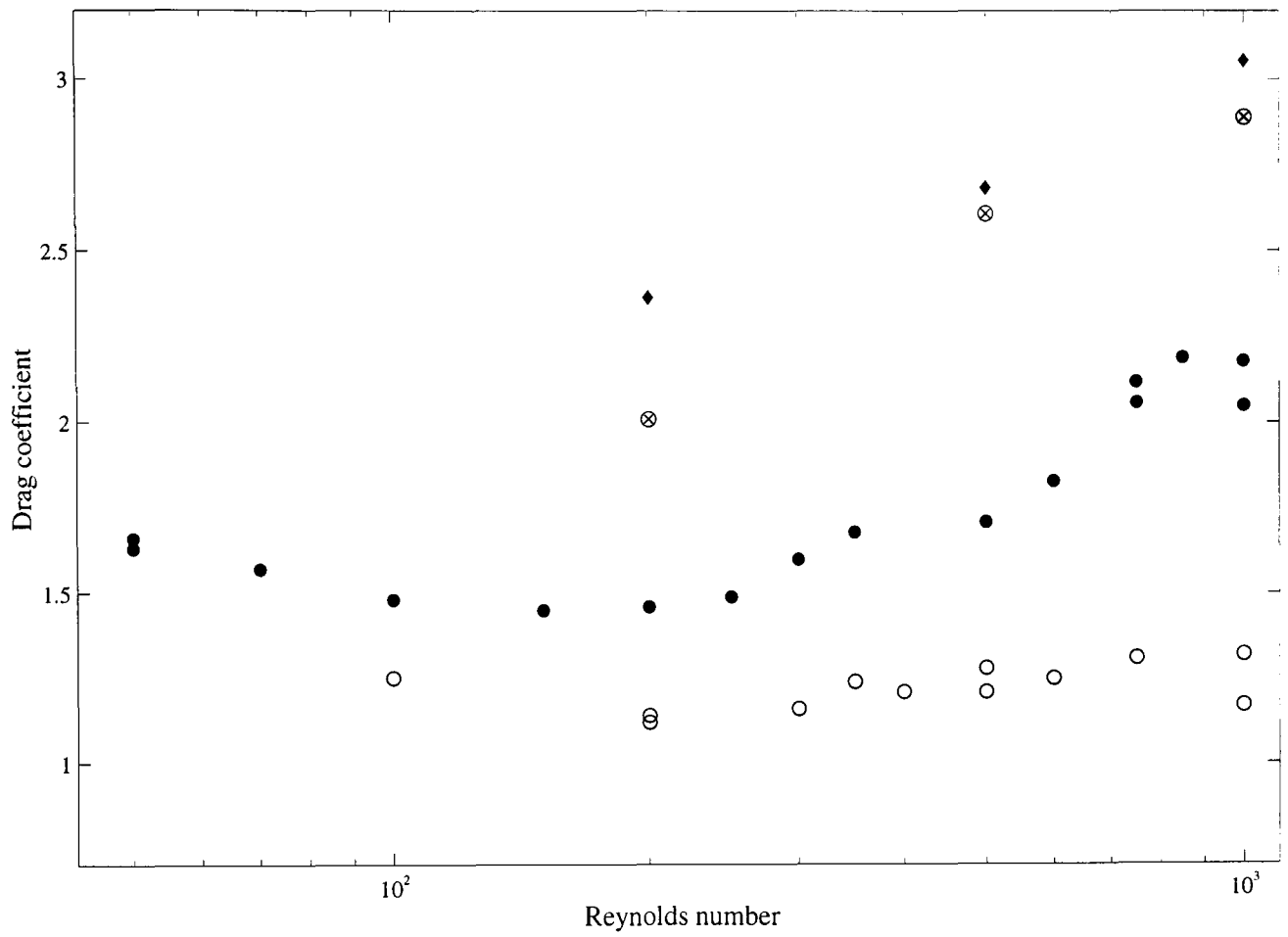

Figure 5.6(a) Drag coefficient vs Reynolds number
♦ B/A=0·2; ⊗ B/A=0·5; • B/A=1·0; o B/A=2·0

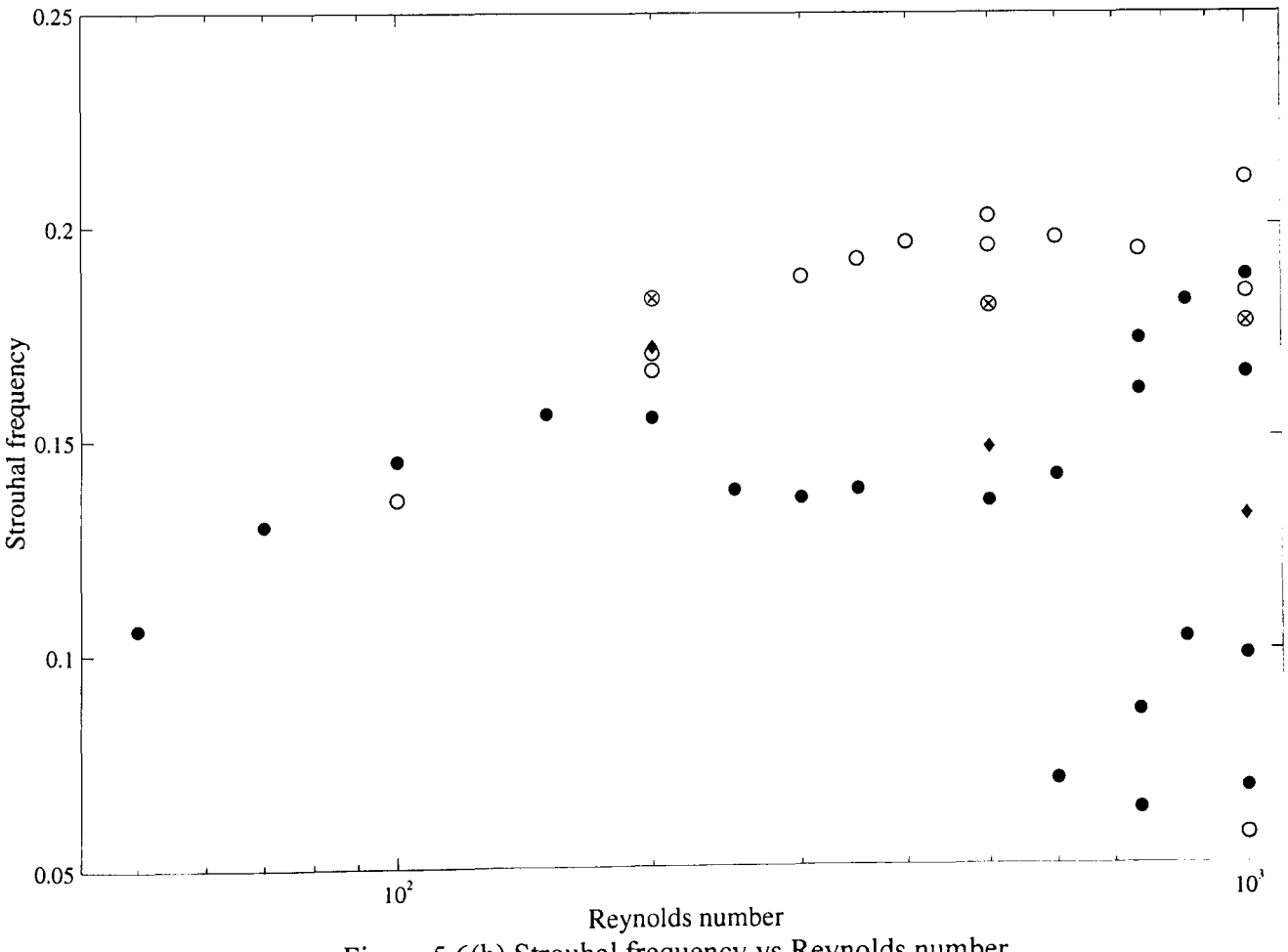

Figure 5.6(b) Strouhal frequency vs Reynolds number
♦ B/A=0·2; ⊗ B/A=0·5; • B/A=1·0; o B/A=2·0

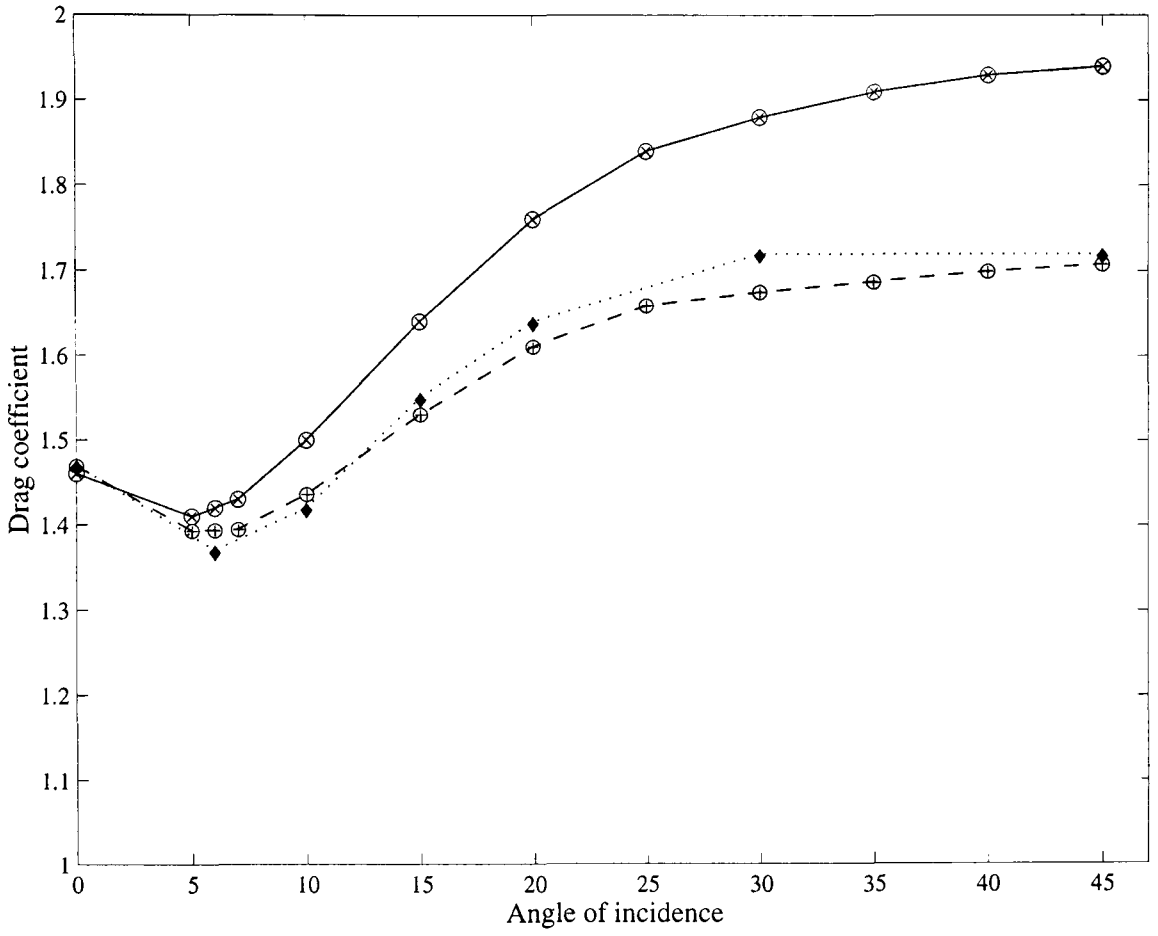

Figure 5.7(a) Drag coefficient vs Angle of incidence, *B/A*=1.0, *Re*=200.
⊗ C_D, ⊕ C_{Dp} Present calculations, ♦ C_{Dp} Sohankar *et al* (1996)

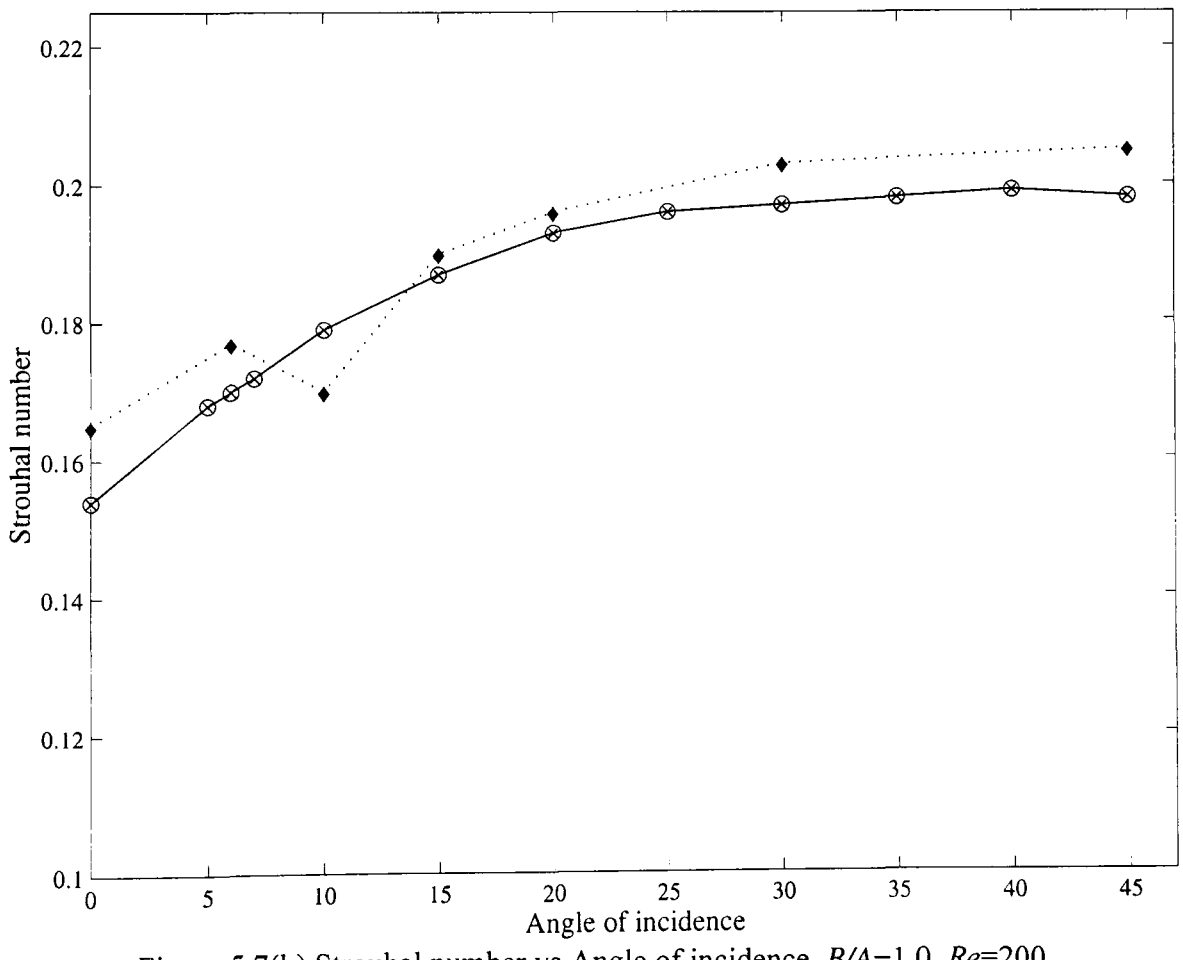

Figure 5.7(b) Strouhal number vs Angle of incidence, *B/A*=1.0, *Re*=200.
⊗ Present calculations, ♦ Sohankar *et al* (1996)

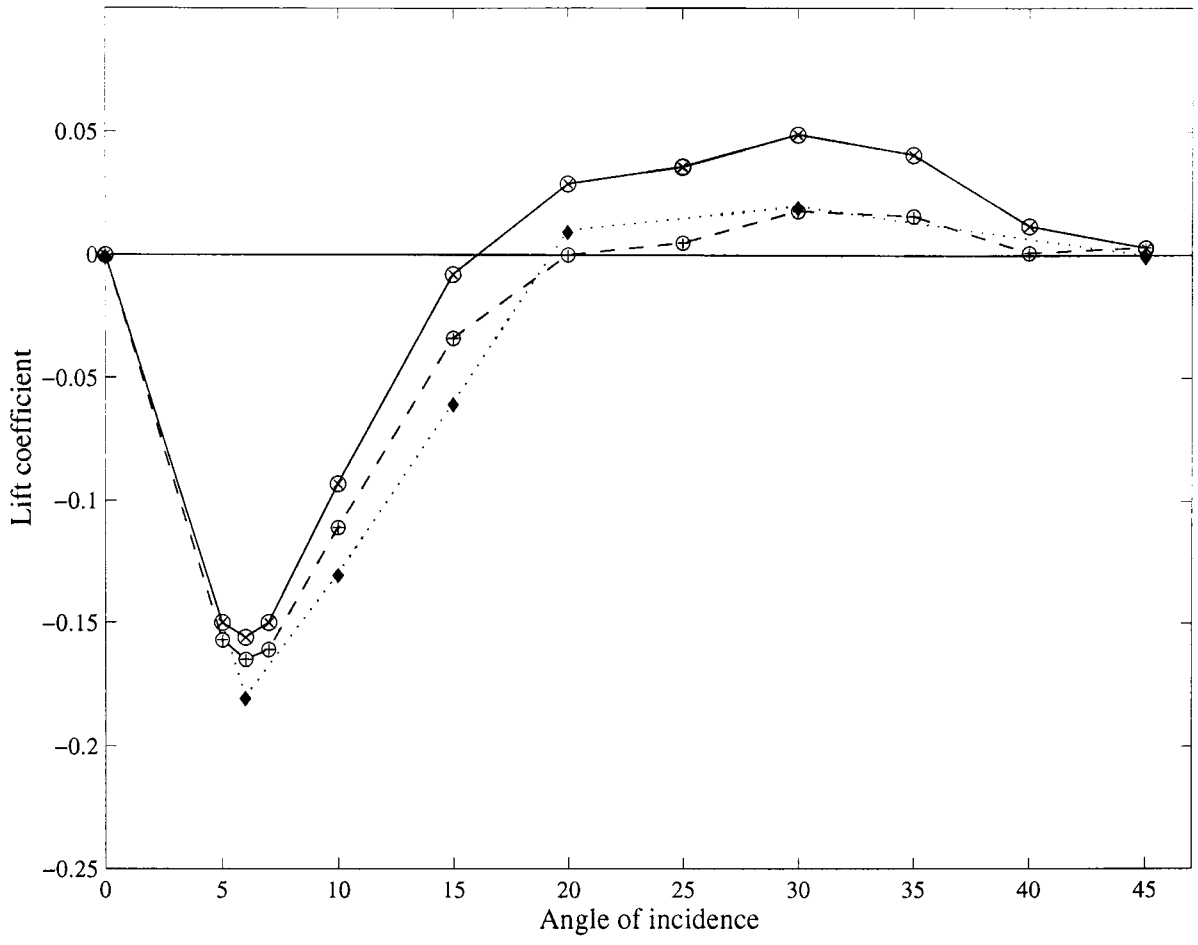

Figure 5.7(c) C_L vs Angle of incidence, *B/A*=1.0, *Re*=200.
⊗, ⊕ C_{Lp} Present calculations, ♦ Sohankar *et al* (1996)

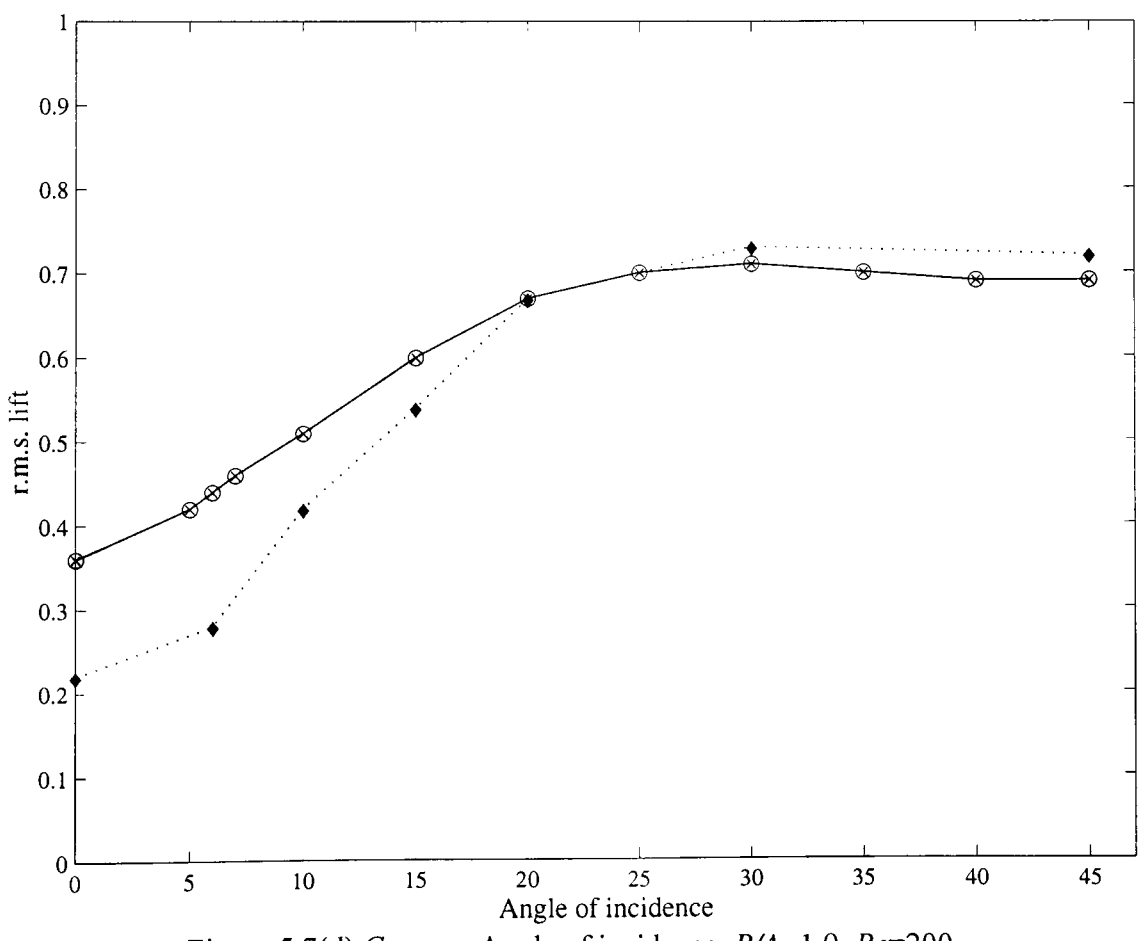

Figure 5.7(d) $C_{L(rms)}$ vs Angle of incidence, *B/A*=1.0, *Re*=200.
⊗ Present calculations, ♦ Sohankar *et al* (1996)

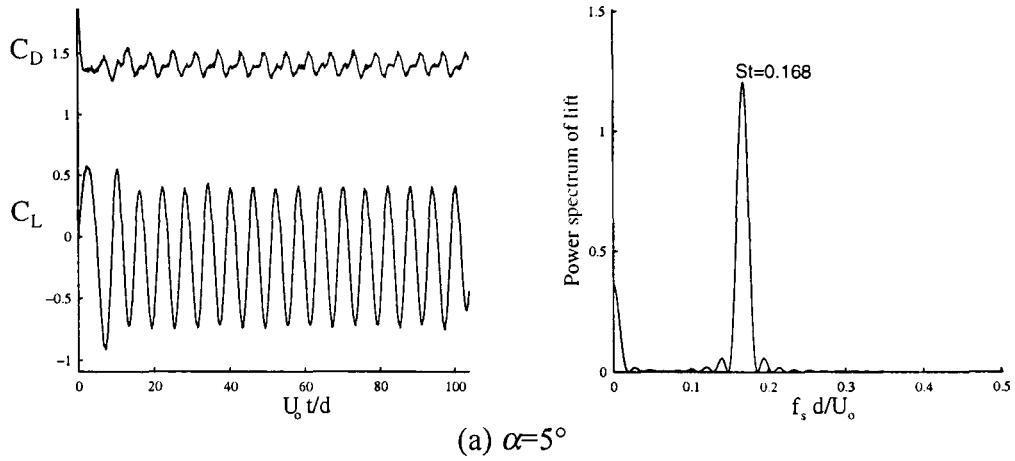

(a) α=5°

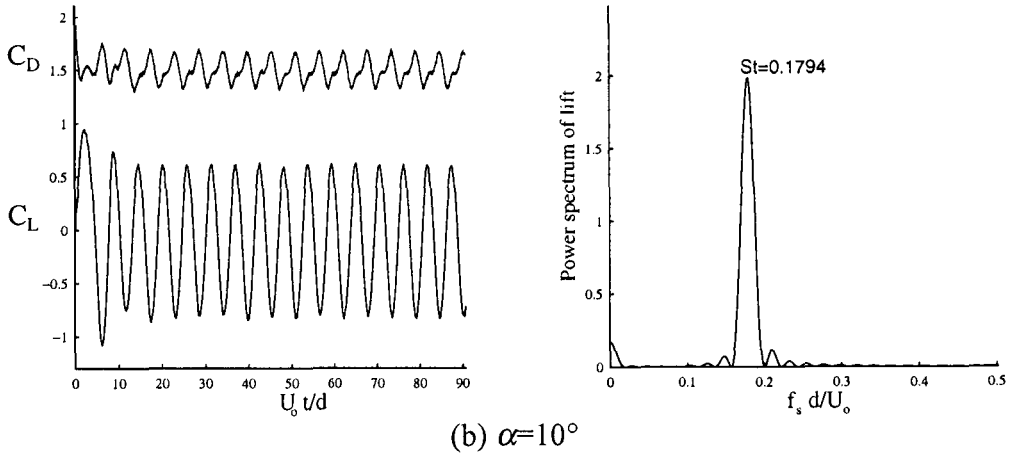

(b) α=10°

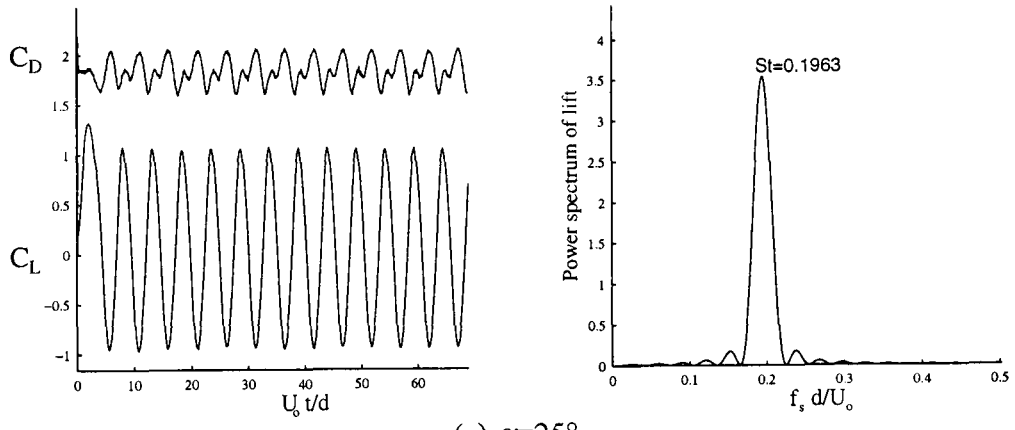

(c) α=25°

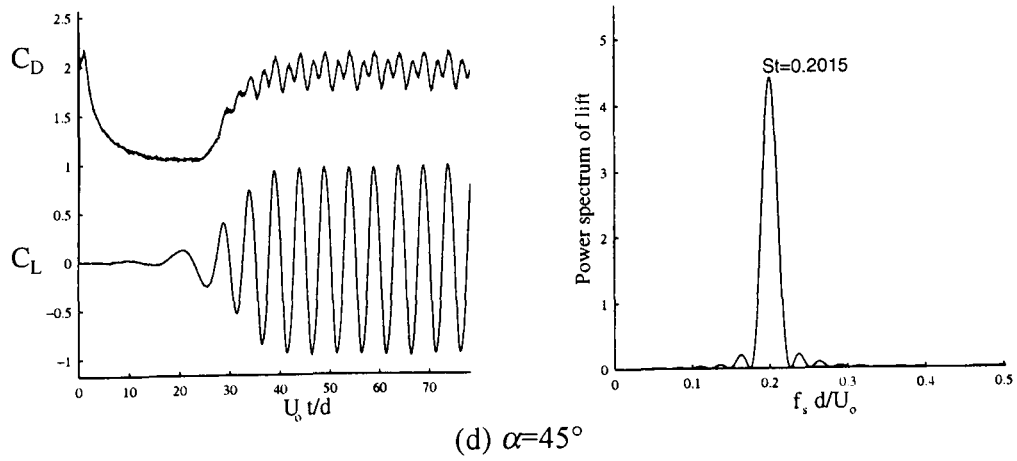

(d) α=45°

Figure 5.8 Force time histories, *B/A*=1.0, *Re*=200
(a) α=5°; (b) α=10°; (c) α=25°; (d) α=45°

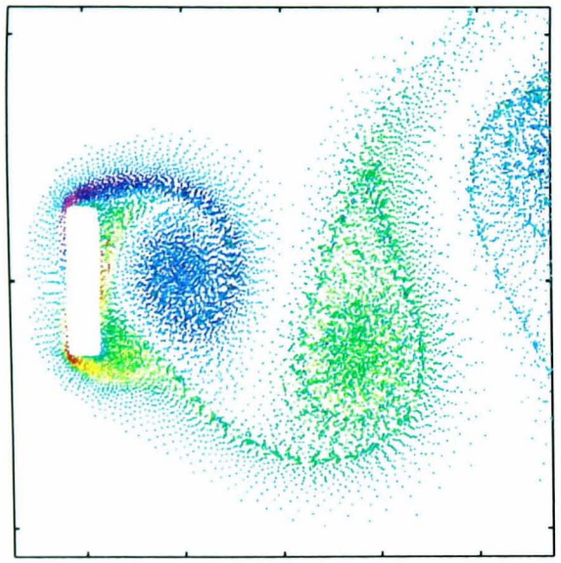

(a) C_L zero

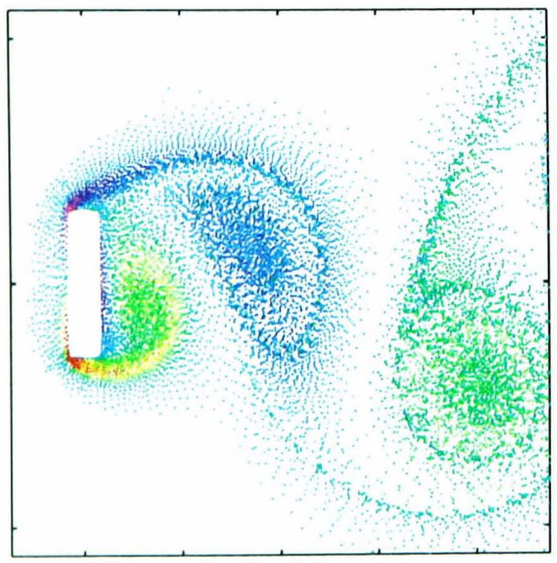

(b) C_L minimum

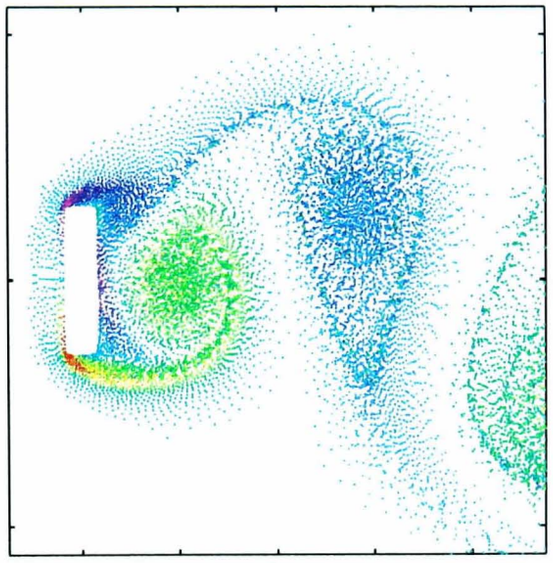

(c) C_L zero

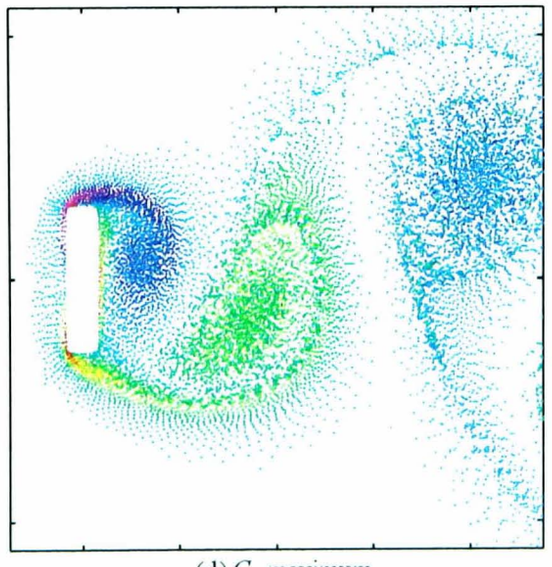

(d) C_L maximum

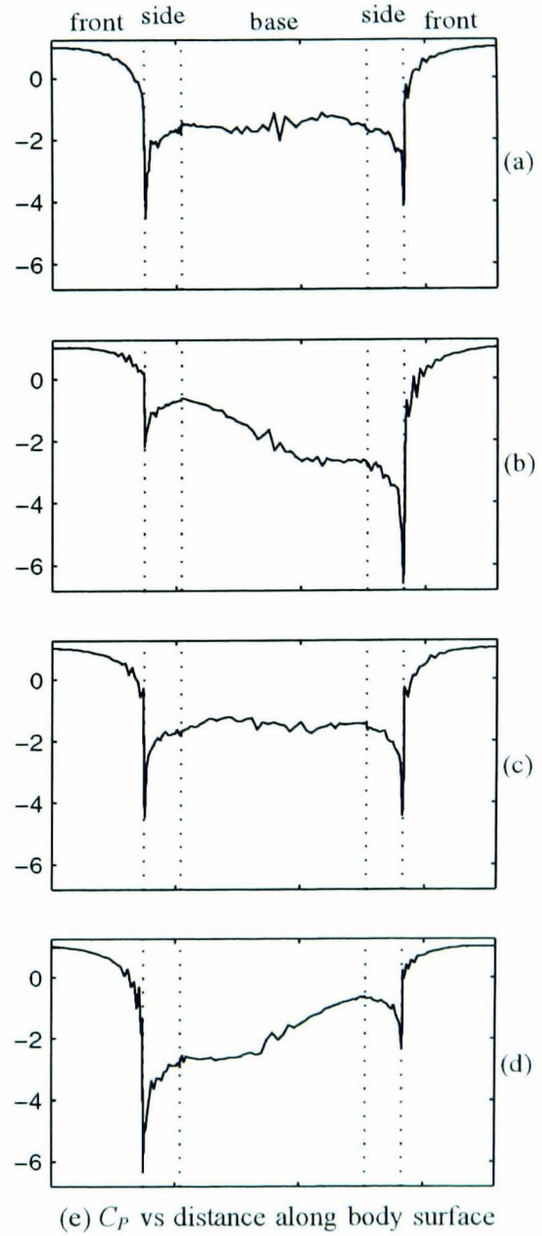

(e) C_P vs distance along body surface

Figure 5.9 Flow visualisation and surface pressure sequences, B/A=0.2, Re=200

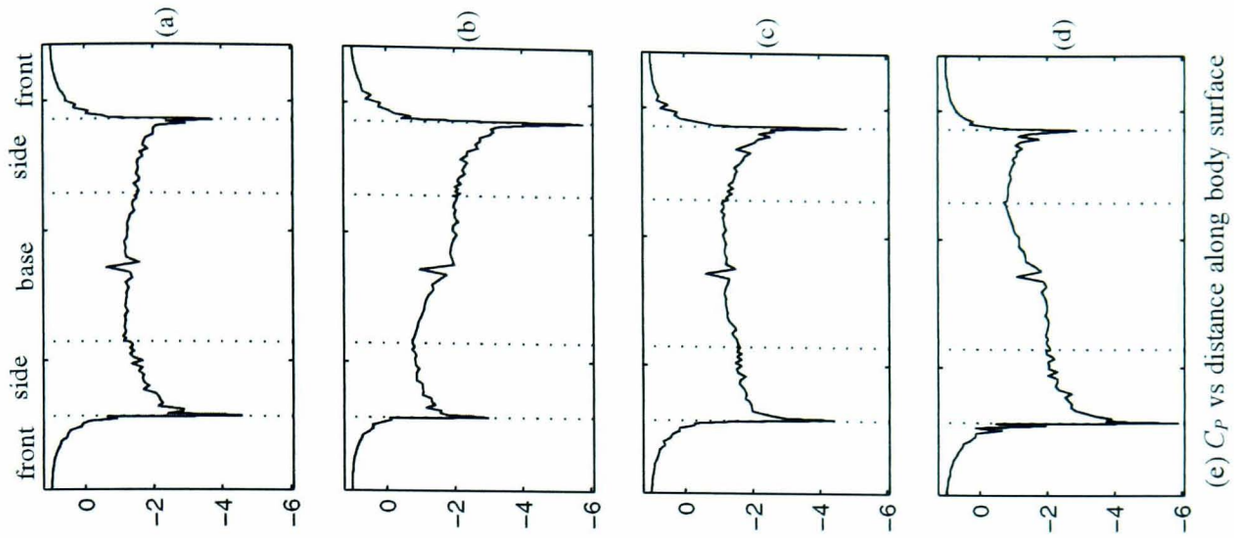

(e) C_P vs distance along body surface

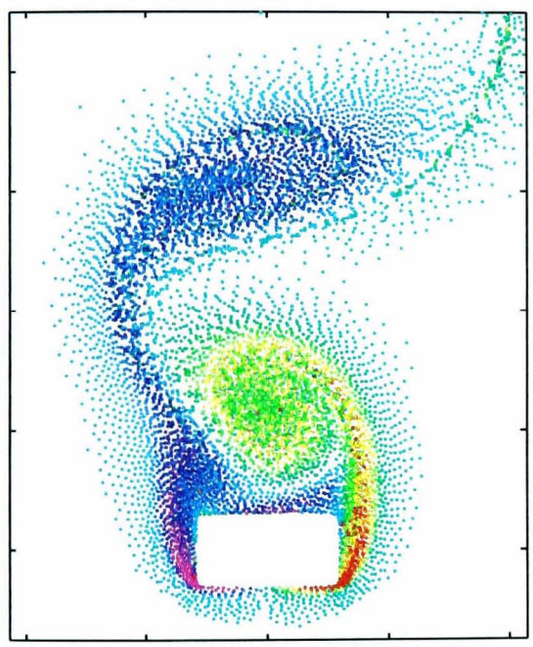

(c) C_L zero

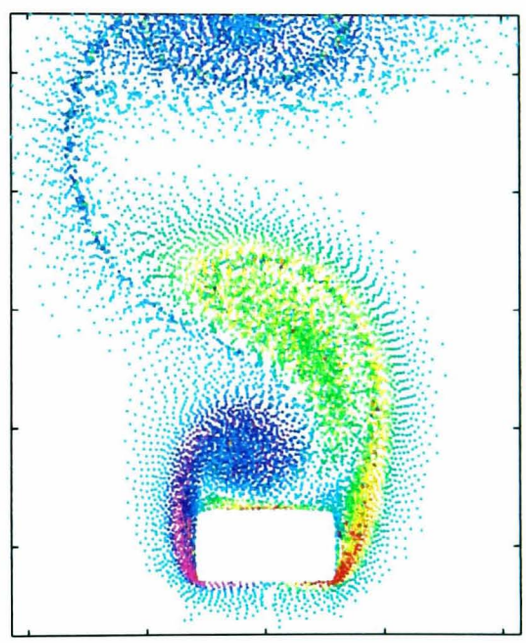

(d) C_L maximum

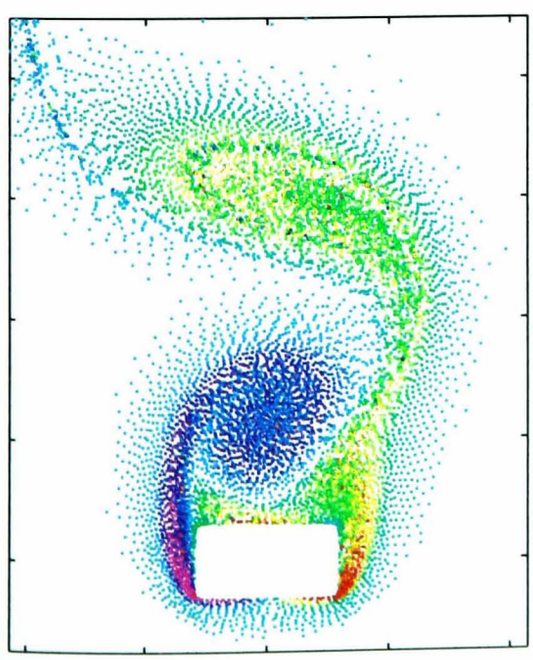

(a) C_L zero

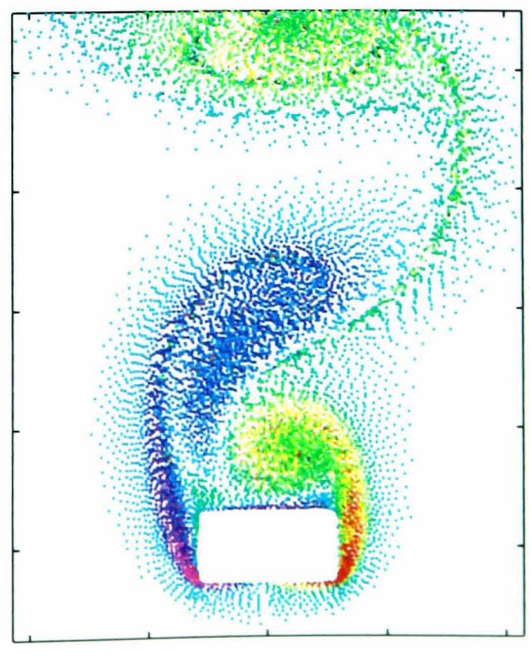

(b) C_L minimum

Figure 5.10 Flow visualisation and surface pressure sequences, B/A=0.5, Re=200

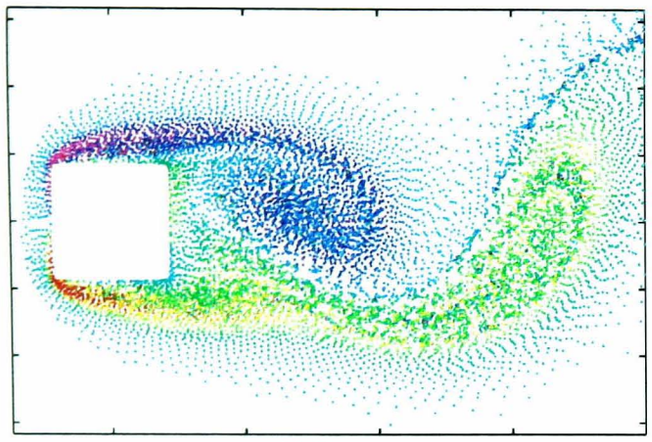

(a) C_L zero

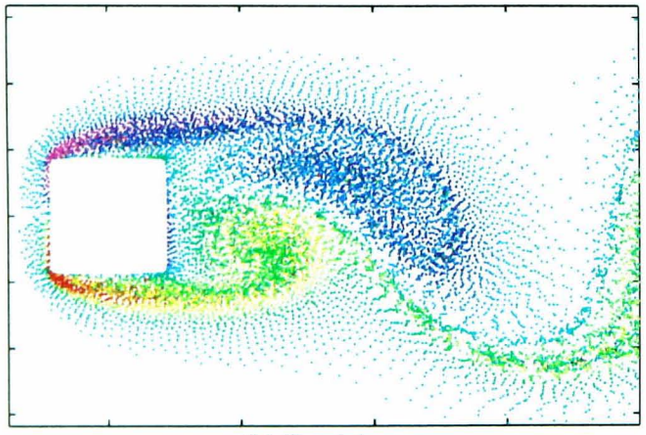

(b) C_L minimum

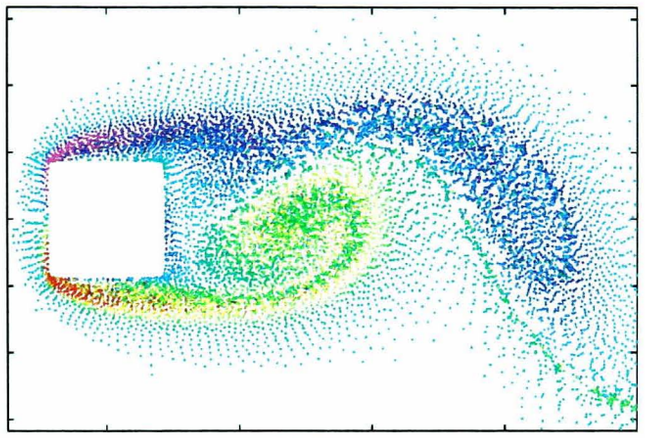

(c) C_L zero

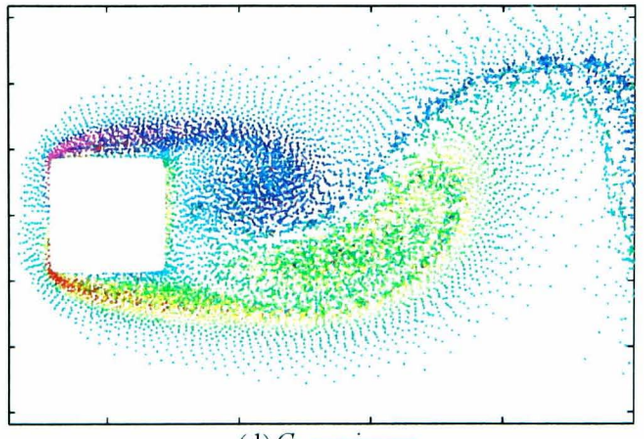

(d) C_L maximum

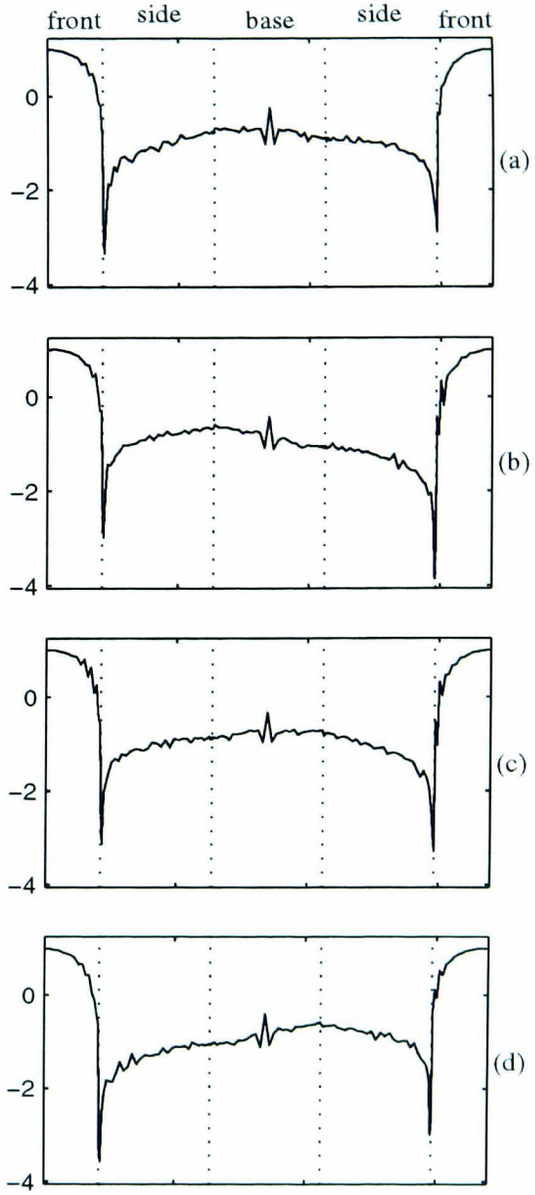

(e) C_P vs distance along body surface

Figure 5.11 Flow visualisation and surface pressure sequences, B/A=1.0, Re=200

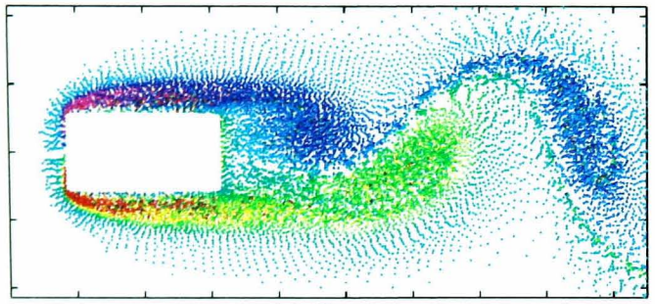

(a) C_L zero

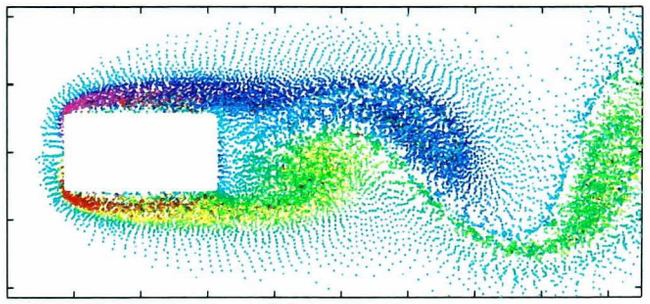

(c) C_L zero

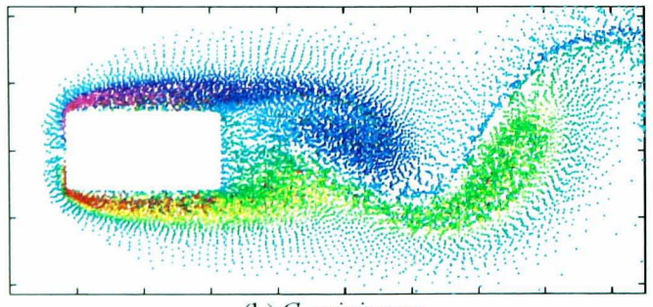

(b) C_L minimum

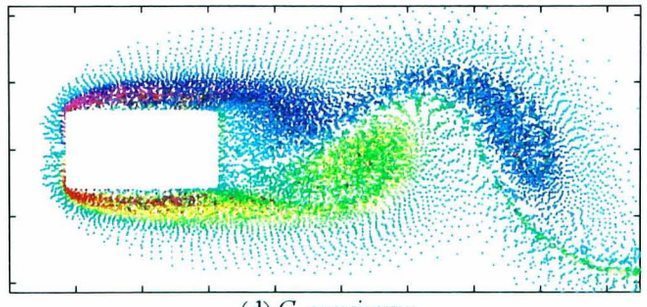

(d) C_L maximum

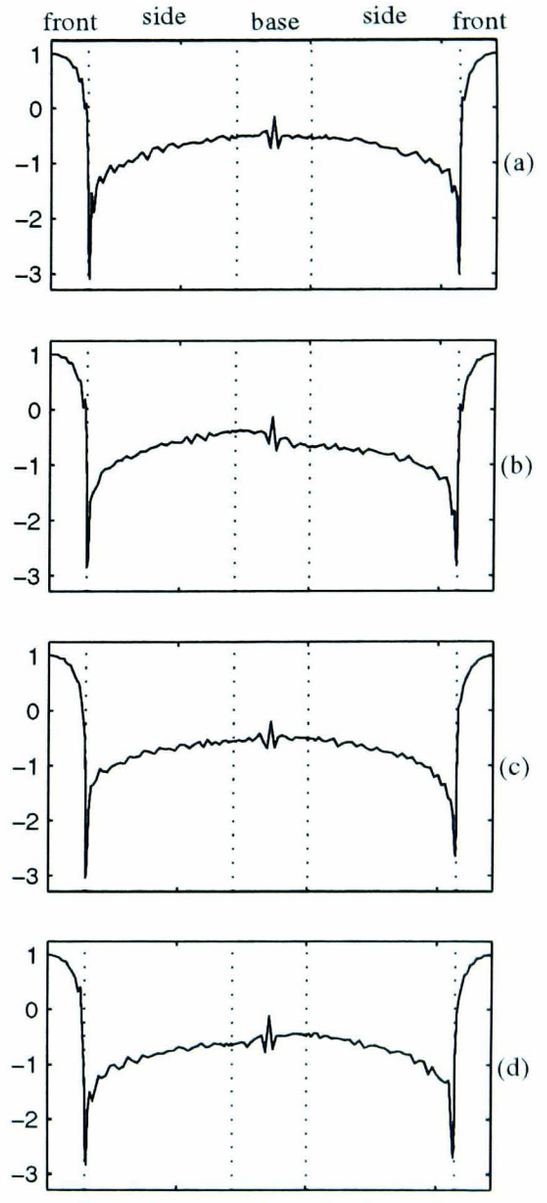

C_P vs distance along body surface

Figure 5.12 Flow visualisation and surface pressure sequences, B/A=2.0, Re=200

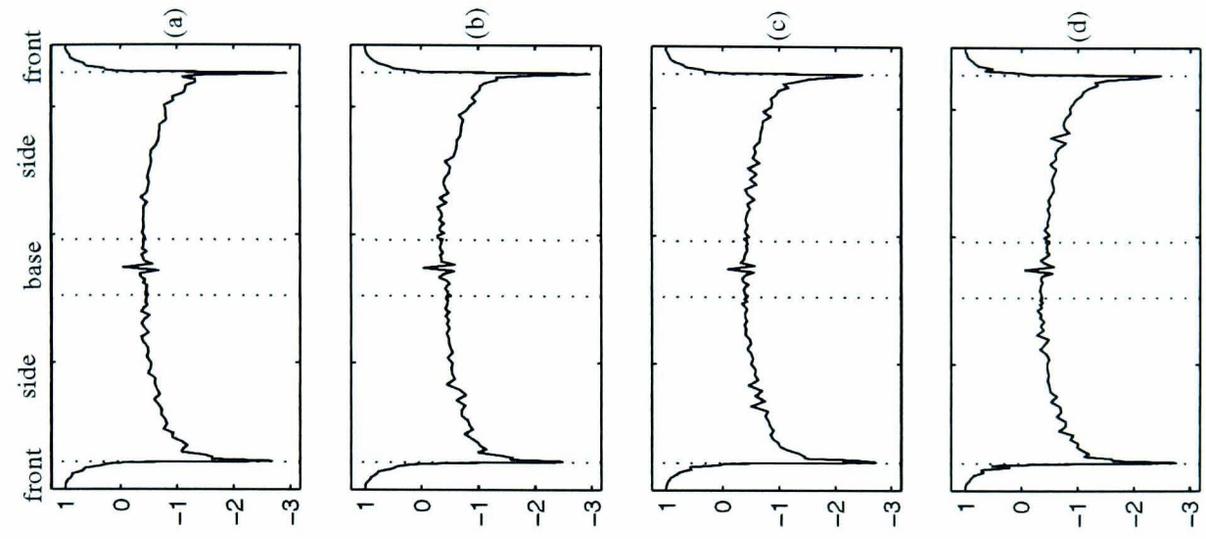

C_P vs distance along body surface

Figure 5.13 Flow visualisation and surface pressure sequences, B/A=3.0, Re=200

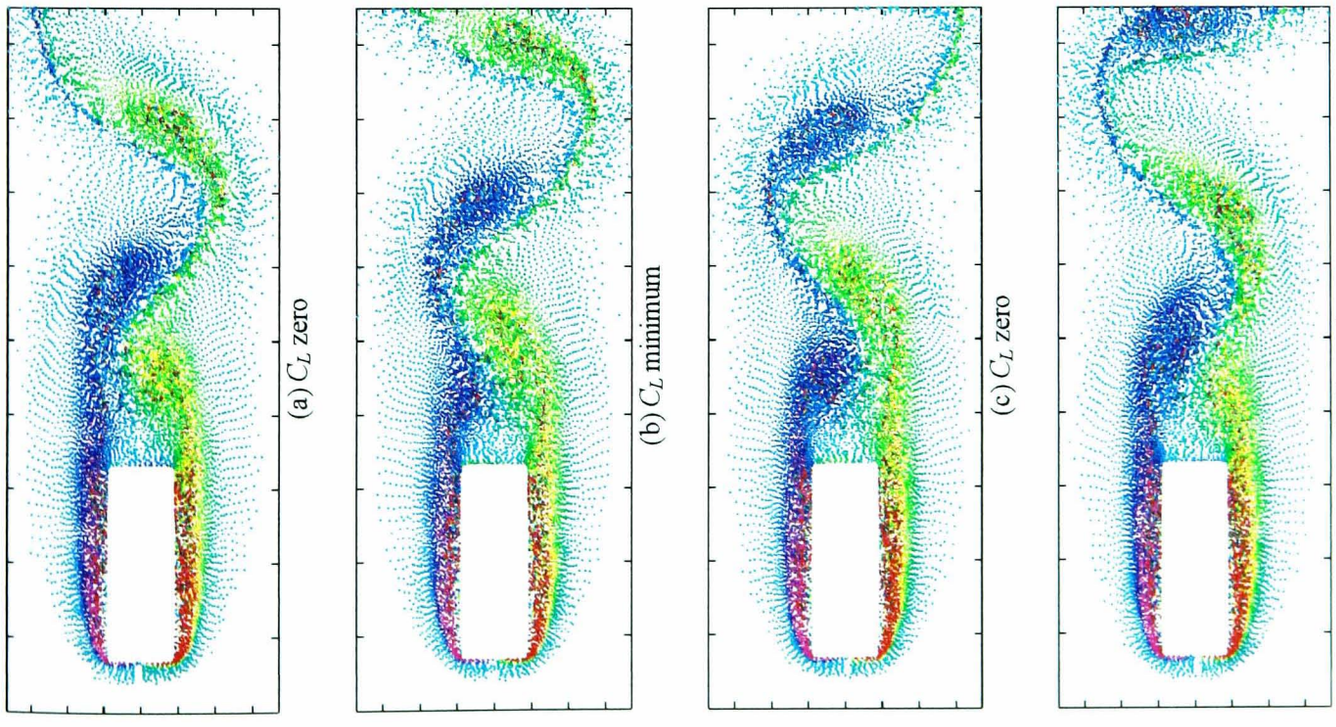

(a) C_L zero

(b) C_L minimum

(c) C_L zero

(d) C_L maximum

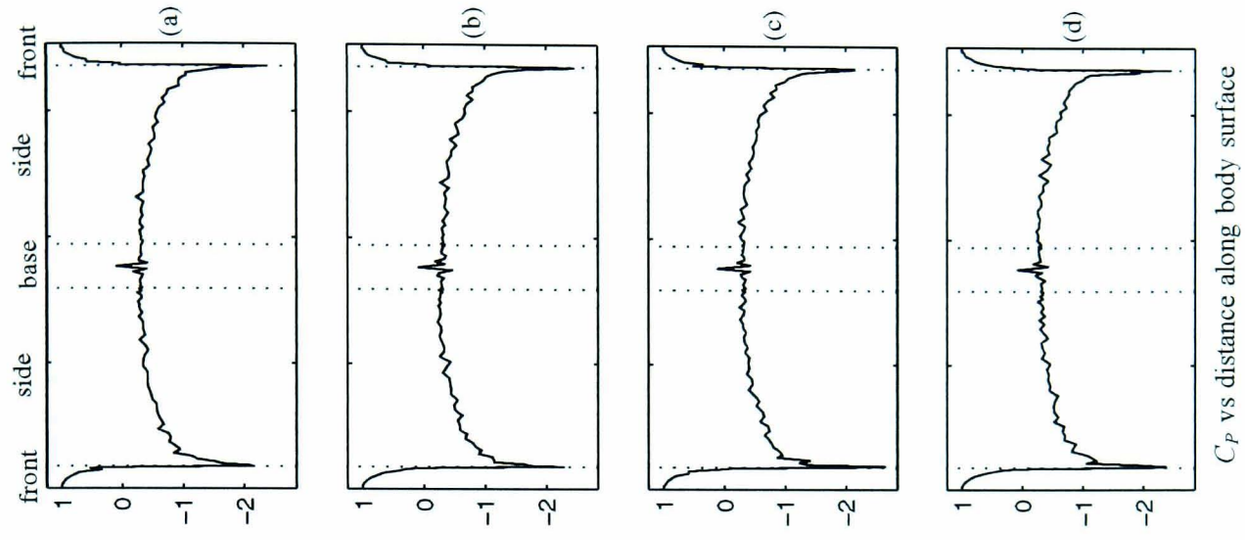

C_P vs distance along body surface

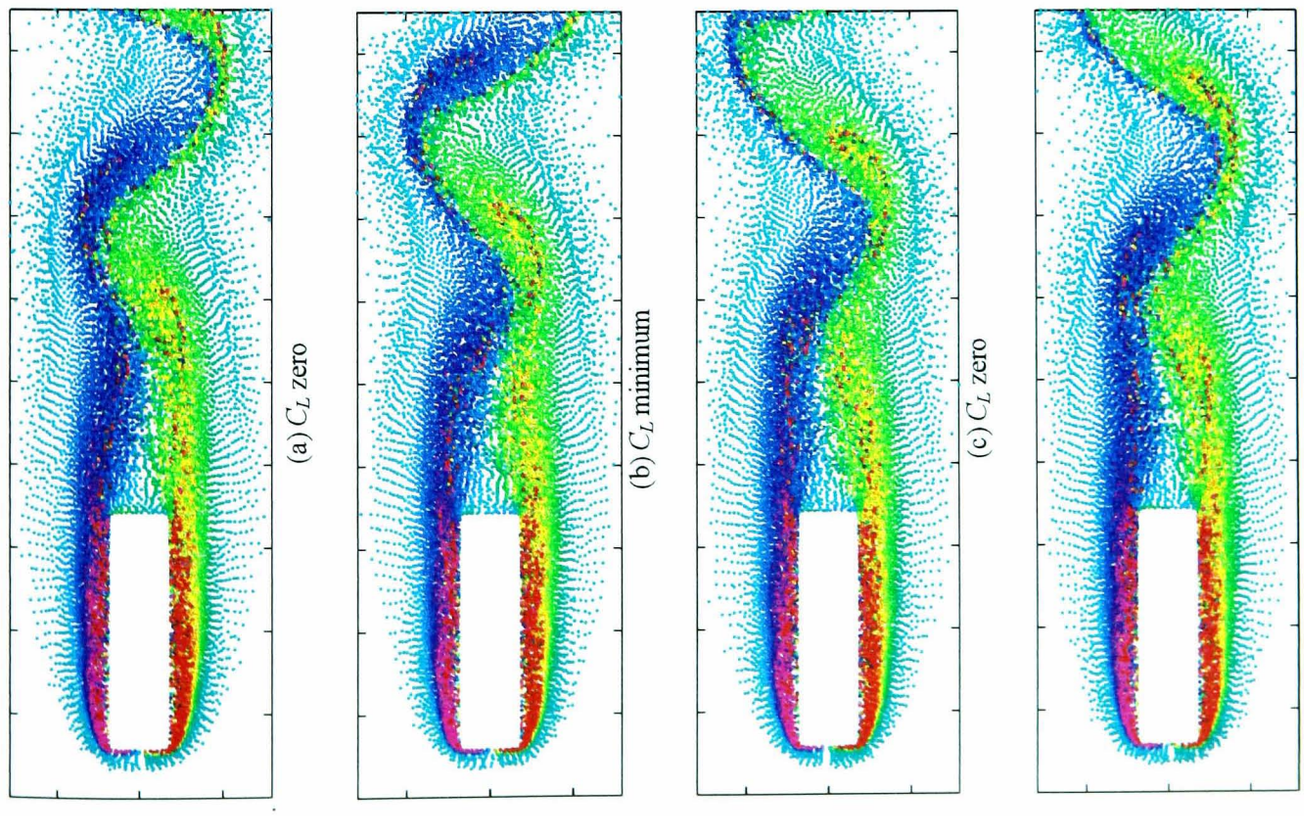

(a) C_L zero

(b) C_L minimum

(c) C_L zero

(d) C_L maximum

Figure 5.14 Flow visualisation and surface pressure sequences, B/A=4.0, Re=200.

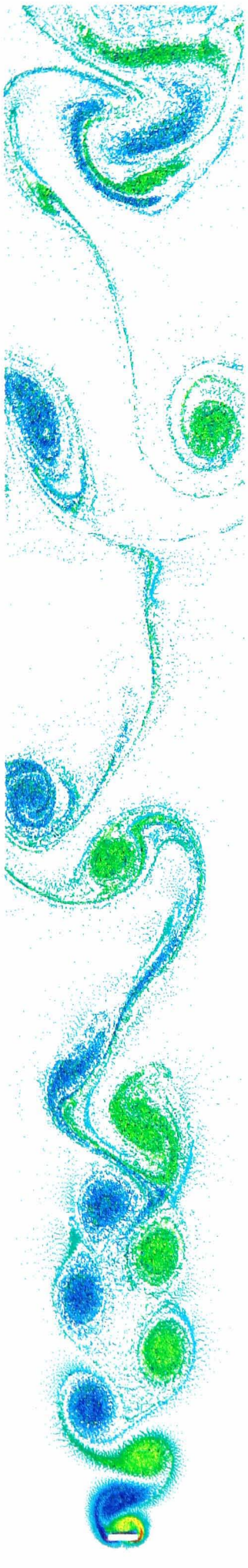

(a) B/A=0.2

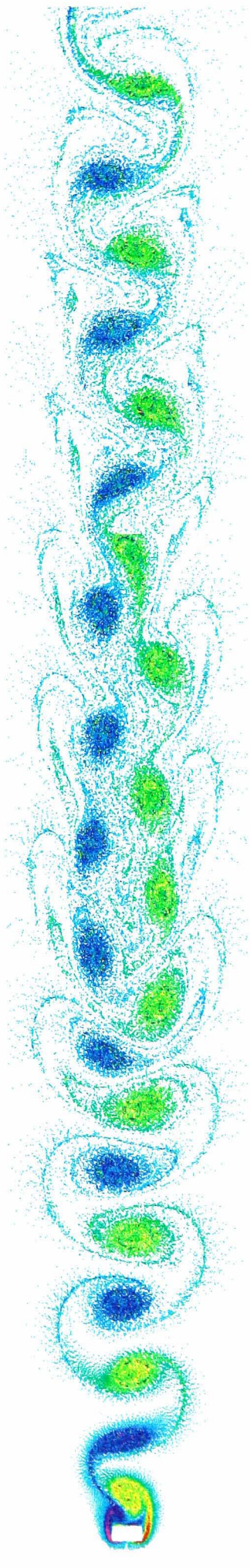

(b) B/A =0.5

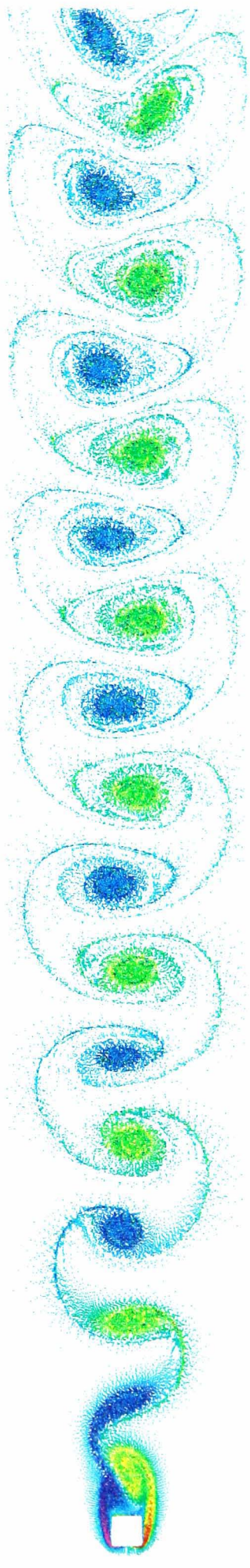

(c) B/A =1.0

Figure 5.15 Flow visualisation of the effect of side ratio on the vortex street, Re=200.

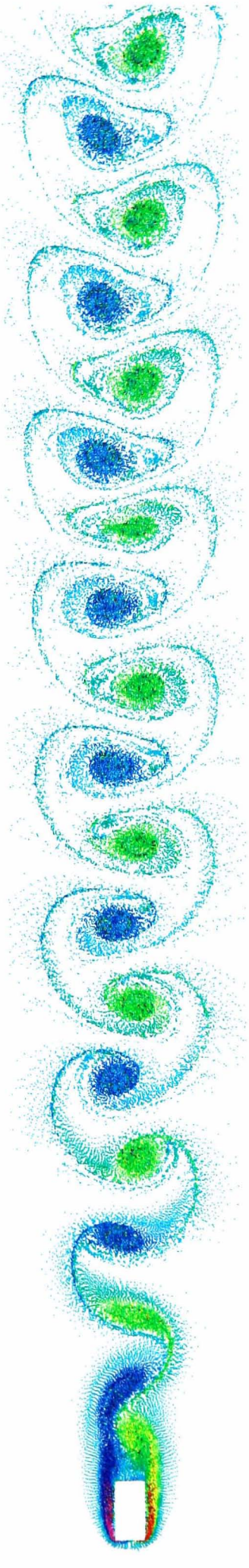

(d) B/A=2.0

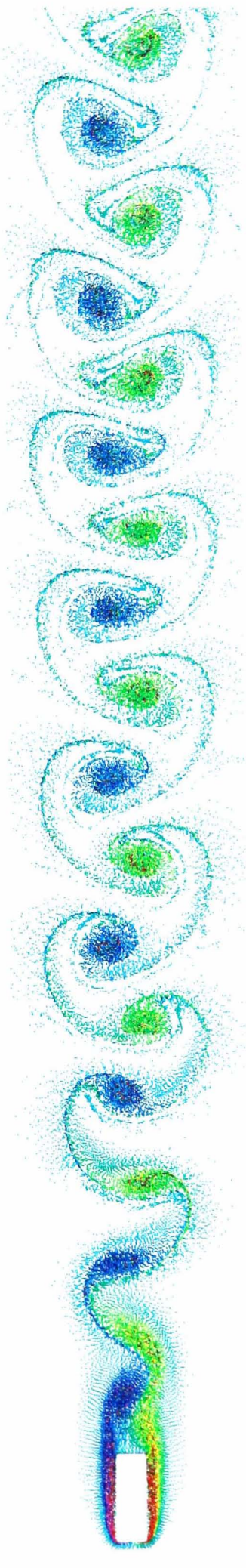

(e) B/A =3.0

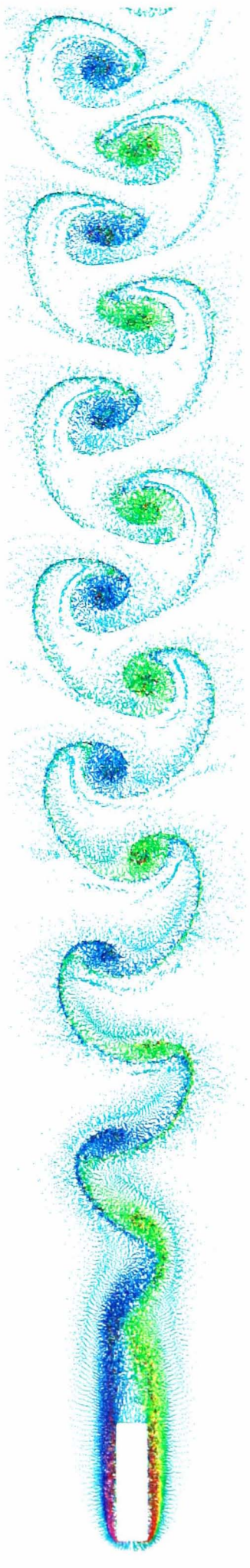

(f) B/A =4.0

Figure 5.15 (cont) Flow visualisation of the effect of side ratio on the vortex street, Re=200.

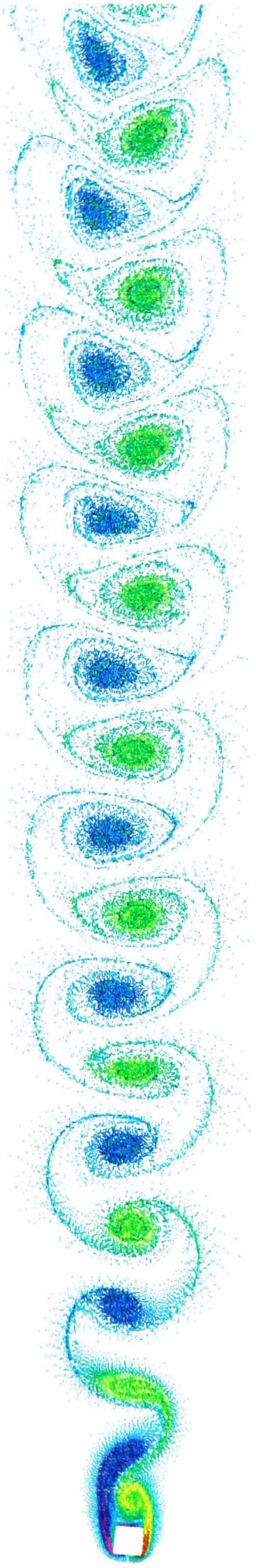

(a) α=5°.

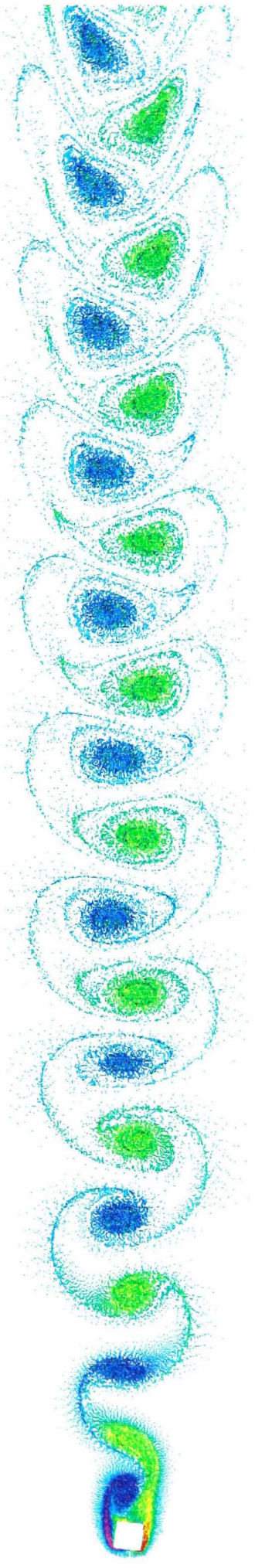

(b) α=7°.

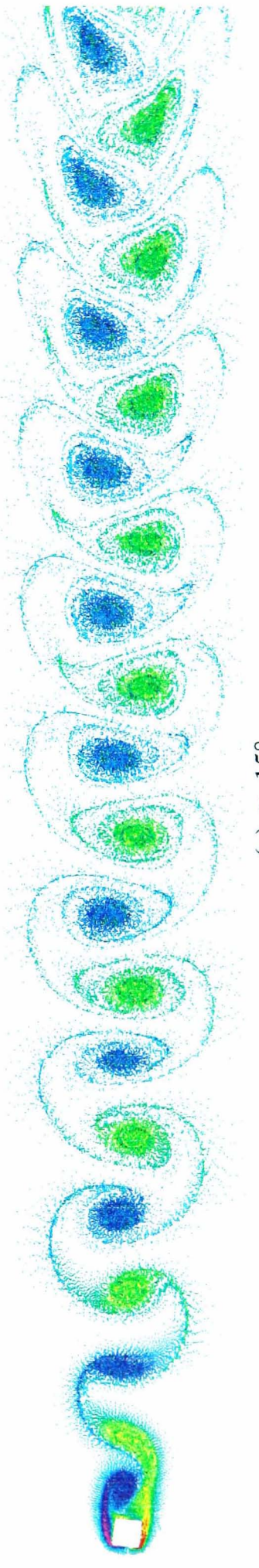

(c) α=15°.

Figure 5.16 Flow visualisation of the effect of incidence angle on the vortex street, B/A=1.0 cylinder, Re=200.

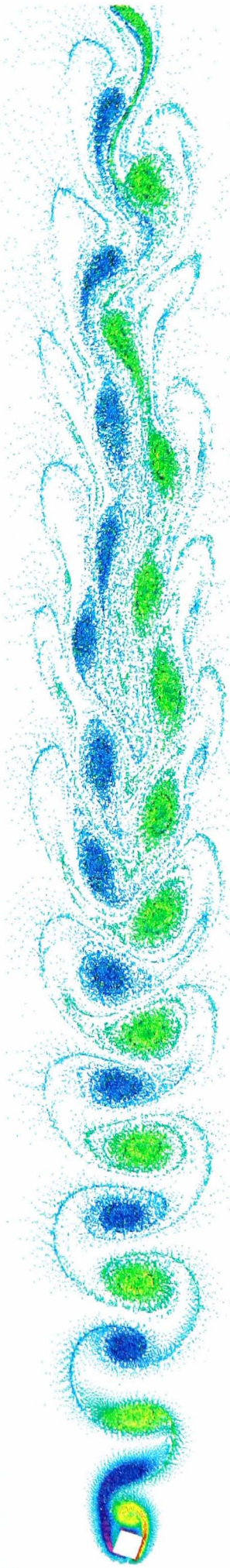

(d) α=20°.

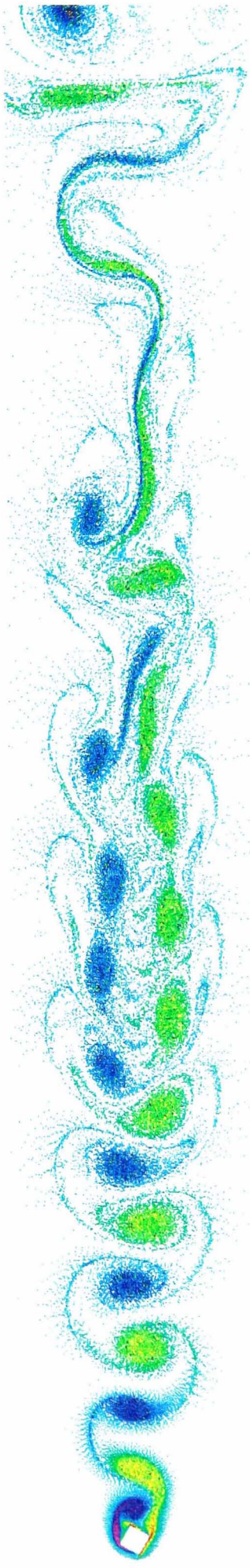

(e) α=30°.

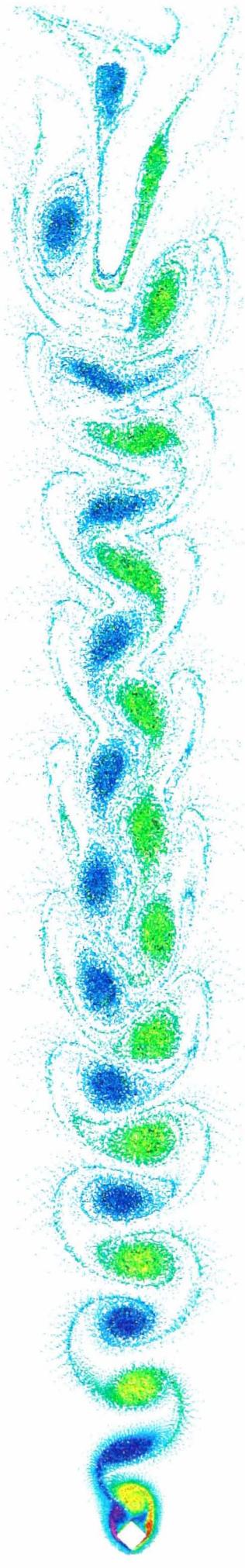

(f) α=45°.

Figure 5.16 (cont) Flow visualisation of effect of incidence angle on vortex street, B/A=1.0 cylinder, Re=200.

Chapter 6

Oscillatory Flow Results

6.1 Introduction

Literature on oscillatory flow topics was reviewed in Section 2.5 and broadly categorised into two distinct areas, cross-stream oscillations and in-line oscillations. One of the initial purposes of this project was to make numerical calculations of pulsating flows past typical vortex-shedding flowmeter geometries. Cross-stream simulations have thus not been pursued here although there is no reason why the code should not be used to make such a study as a future project.

As discussed in Chapter 2 pulsating flows can induce interactions between the shedding frequency f_s and the forcing frequency f_e. The primary resonant mode, referred to here as lock-in, occurs where vortices are shed in a Karman wake at half the forcing frequency. This regime is expected to occur when the forcing frequency is close to double the natural shedding frequency f_0 and above some threshold amplitude of oscillation. A symmetric shedding mode has also been observed in which a pair of oppositely signed vortices are shed at the same moment in each cycle. Within the symmetric mode $f_s=f_e$ and the induced forces on the cylinders are generally considerably lower than those found under uniform flow conditions. This contrasts with the primary mode for which forces are generally found to increase.

Relevant studies of in-line oscillatory motion include the laboratory findings of Ongoren and Rockwell (1988b) who have examined flows past circular cylinders. Their flow visualisations, Figure 2.35, clearly show the competition which exists between symmetric and primary modes. The measurements of Al-Asmi and Castro (1992) demonstrate that the range of oscillation amplitudes and frequencies over which lock-in can occur (Figure 2.37) is highly dependent on body geometry. Numerical studies of in-line pulsations are limited. Okajima and Kitajima (1993) have used a Direct Numerical Simulation to calculate pulsating flows about rectangles, $1.0<B/A<3.0$, at $Re=10^3$. Both the primary resonant mode and the symmetric mode were observed in their study with the mean calculated forces greatly reduced within the symmetric mode (Figure 2.38). However a comparison between a 2-D and 3-D simulation at $Re=10^3$ (Figure 2.31) by the same authors for cross-stream oscillations suggests that the 2-D calculations over-estimate the range of conditions under which resonance modes are predicted. A less comprehensive study by Minewitsch *et al* (1994) details calculations for the in-line oscillations

past square, $B/A=1.0$, cylinders. A primary resonant mode was clearly identified and the authors reported that symmetric shedding was possible under certain conditions although no evidence for this could be deduced from those results presented.

Two of the main questions which still arise in oscillatory flow topics were identified by Bearman (1984) in his review of the subject. Firstly, what effect does the afterbody geometry have on the appearance of resonant modes, and secondly, under what conditions does phase switching across the synchronisation range take place?

Six geometries were chosen for the simulation of pulsating flows. These were a circular cylinder and rectangular cylinders of side ratios $B/A=0.62$, 1.0, 2.0 and 3.0. A $B/A=1.0$ cylinder inclined to the flow at 45°, hereafter referred to as a diamond cylinder, was also tested. Their relevant parameters calculated under uniform flow conditions are given in Table 6.1. for each cross section. Although initially only the rectangular cylinders were to be considered the circular cross section has been included since the bulk of the literature in oscillatory flow topics refers to the flow about circular cylinders.

GEOMETRY	St_0	C_{D0}	$C_{L0(rms)}$	Flow vis.
Circular	0.190	1.39	0.43	Fig 6.6
Diamond	0.202	1.95	0.69	Fig 5.16(f)
$B/A=0.62$	0.172	1.83	0.52	-
$B/A=1.0$	0.154	1.46	0.35	Fig 5.15(c)
$B/A=2.0$	0.167	1.15	0.24	Fig 5.15(d)
$B/A=3.0$	0.161	1.05	0.21	Fig 5.15(e)

Table 6.1 Mean calculated parameters under uniform flow conditions and flow visualisation Figure number.

Some frequencies quoted in this chapter have been non-dimensionalised according to

$$St_0 = \frac{f_0 d}{U_0};\ St_e = \frac{f_e d}{U_0};\ St_s = \frac{f_s d}{U_0};\ St_n = \frac{f_n d}{U_0};\qquad (n = 1,2,3,...) \tag{6.1}$$

where St is used to represent a non-dimensional and f a dimensional frequency. St_0 is the Strouhal frequency or frequency under uniform flow conditions, St_e is the oscillatory forcing frequency and St_n are the dominant frequencies found from spectral analysis of the lift curve. St_s is the shedding frequency under oscillatory

conditions and is usually equated to St_1. The pulsations are characterised by the form of the upstream flow velocity,

$$U = U_0 + U_A \cos(2\pi f_e t), \tag{6.2}$$

where U_A represents the amplitude of the imposed flow velocity. In the literature most researchers refer to a maximum displacement amplitude x_e of the cylinder defined by

$$x_e = \frac{U_A}{2\pi f_e}. \tag{6.3}$$

The defining parameters of the flow are then the ratios f_e/f_0 and x_e/d.

6.1.1 Lock-in chart categories

For each cross-section examined, a lock-in chart has been prepared which shows the range of oscillatory amplitudes x_e/d and frequencies f_e/f_0 over which the geometry was tested. These are shown in Figures 6.4, 6.10, 6.14, 6.18, 6.22 and 6.26 for each of the cylinders considered. Each combination of x_e/d and f_e/f_0 has been placed within one of three categories: (i) quasi-symmetric shedding; (ii) asymmetric synchronisation; or (iii) outside the synchronisation regimes. The definitions used for the synchronisation regimes follow.

Across the asymmetric synchronisation range the vortex shedding is expected to take place at $f_s=f_e/2$. For practical purposes a less rigorous criterion is applied. The expression (6.4) gives a range of values for f_s which imply that the shedding frequency has been significantly altered from its freestream value to the extent that we may consider the flow to be controlled by the forcing oscillation.

$$1.1\left|\frac{f_e}{2} - f_0\right| > |f_s - f_0| > 0.9\left|\frac{f_e}{2} - f_0\right| \tag{6.4}$$

It should also be noted that, although expression (6.4) implies asymmetric synchronisation, several different modes of shedding were found within this range as will be evident from the flow visualisations discussed in the following sections. No attempt was made to further subdivide the asymmetric synchronisation range into these alternative modes. These modes will be referred to according to the definitions given by Williamson and Roshko (1988), Figure 2.28.

The onset of a symmetric shedding mode implies reduced lift forces. Shedding frequencies could not always be detected from the lift time history and where they could they referred to the asymmetric part of the wake which developed further downstream. An examination of the drag curve reveals that the drag force is controlled by the forcing frequency over a larger range and cannot be used to determine synchronisation of the shedding process.

For these calculations it was decided that the flow could be termed quasi-symmetric provided the r.m.s. value of the lift coefficient was reduced significantly from its freestream value. A 50% reduction was chosen:

$$C_{L(rms)} < \frac{C_{L0(rms)}}{2}. \tag{6.5}$$

6.1.2 Mean forces, dominant frequencies and shedding modes

For each simulation force time histories were produced as in the uniform flow case. Some examples of the lift time histories and lift power spectra are presented in Figures 6.1-6.3 for the circular cylinder. Spectral analysis of the lift curve was used to obtain the dominant frequencies and the shedding frequency St_s was assumed equal to the dominant frequency St_1. Mean values for C_D and $C_{L(rms)}$ were obtained by ignoring the initial interval during which the vortex shedding establishes itself and averaging the force time histories over an integer number of shedding periods. Across quasi-symmetric regions (see Figure 6.3(d)) the lift force was small and irregular such that the shedding frequency could not be determined from analysis of the lift curve. Any frequencies which could be detected for quasi-symmetric modes relate to the far wake since asymmetric behaviour develops further downstream.

Together with the lock-in charts figures are presented (see Figures 6.5, 6.11, 6.15, 6.19, 6.23 and 6.27) which show the variation of C_D, $C_{L(rms)}$ and f_e/f_s with f_e/f_0 for each geometry at set displacement amplitudes. On the curves of f_e/f_s vs. f_e/f_0 two additional lines are plotted. If the upstream oscillations had not affected the shedding frequency then we would expect the points to lie on the line $f_e/f_s = f_e/f_0$, i.e. $f_s = f_0$. On the other hand asymmetric synchronisation is signified by points lying on the line $f_e/f_s = 2.0$.

Instantaneous plots of the vortex street are also presented for each cylinder. The colour coding scheme was described previously in Chapter 5 (p108). The shedding modes have been termed according to the definitions of Williamson and Roshko (see Figure 2.28).

6.2 Circular cylinder (Figures 6.1 - 6.8)

Under uniform flow conditions the mean measured values of the key parameters were $St_0 = 0.190$, $C_{D0} = 1.39$ and $C_{L0(rms)} = 0.43$. The effect of the addition of an upstream pulsating flow component was tested over the ranges $0.5 \leq f_e/f_0 \leq 3.0$ and $x_e/d \leq 0.30$. All those combinations of frequency and amplitude which were simulated are displayed in Figure 6.4 together with the results of Barbi *et al* (1986) and Okajima *et al* (1993).

Asymmetric resonance was found for amplitudes above $x_e/d = 0.05$ and the lower frequency bound for asymmetric resonance shifted to lower frequencies at higher amplitudes. Quasi-symmetric shedding was possible for amplitudes at or above $x_e/d = 0.2$ and again the lower frequency bound for quasi-symmetric synchronisation was

reduced at the higher amplitude. This also had the effect of reducing the upper frequency limit for asymmetric resonance. The curve deduced by Barbi *et al* (1986) shows the amplitude threshold required to induce resonance of an asymmetric kind at a higher Reynolds number. Their curve does not continue beyond f_e/f_0=2.4 since the authors reported competition between asymmetric and symmetric shedding modes at higher forcing frequencies. This phenomenon was also reported by Ongoren and Rockwell (1988b).

One can clearly observe that the amplitude threshold found by DVM is larger than those obtained by Barbi *et al* (1986). However this is consistent with the result presented in Barbi *et al* which suggests that the required amplitude threshold decreases with increasing Reynolds number. Okajima and Kitajima (1993) made some numerical studies of the lock-in bounds at Re=1000 for a single oscillatory amplitude, x_e/d=0.14. Their calculations predicted lock-in for $1.32<f_e/f_0<1.98$ which indicates a similar lower frequency bound and a slightly smaller upper frequency bound than observed in this study. This difference contradicts two previous statements. Firstly that the frequency bound for lock-in tends to increase with increasing Re and secondly that a 2-D calculation applied above the Reynolds number limit for fully 2-D flow will over-estimate the lock-in bounds. However it appears likely that as Re increases the threshold amplitude for the appearance of quasi-symmetric modes is reduced and this may be responsible for the smaller upper frequency bound found by Okajima and Kitajima (1993).

Mean forces and shedding frequencies are plotted in Figure 6.5 for fixed amplitudes of x_e/d=0.05, 0.10, 0.15 and 0.30. Lift and drag forces are clearly seen to increase within the asymmetric synchronisation region and decrease across the quasi-symmetric regime. As the amplitude increases, the lift and drag maxima are shifted to lower frequencies. The asymmetric range is clearly visible at each of the four amplitudes plotted and can be seen to shift to lower frequencies with increasing amplitude. Outside the synchronisation range we might expect that the shedding frequency would return to the uniform flow value but clearly the frequency can be considerably altered even beyond this range. For the highest amplitude x_e/d=0.3, no frequency could be detected from the lift force at $f_e/f_0 \geq 1.7$ since the shedding was quasi-symmetric in this region. It is assumed that the shedding is locked on at f_e/f_s=1.0 throughout the quasi-symmetric region since the drag force oscillates at the shedding frequency. However the drag force oscillates at the forcing frequency across a broad range of frequencies and this is not necessarily related to the shedding pattern but may be caused by the pressure change on the upstream surface. This pressure is not affected by the vortex shedding process and is controlled directly by the upstream oscillations. Thus it would not be wise to use this for prediction of the shedding frequencies.

Flow visualisations over the range of oscillatory conditions tested are displayed in Figures 6.7-6.9. The uniform flow case is given in Figure 6.6 as a reference. At low amplitudes of oscillation the conditions are insufficient to induce resonance and the Karman vortex street remains intact, Figure 6.7, although it is noticeable that the Strouhal number has increased slightly from the uniform flow value. However at higher oscillatory amplitudes the shedding process may be altered even beyond the frequency ranges for resonance.

Initially the amplitude is set at x_e/d=0.15. For a low frequency ratio, f_e/f_0=0.5 (Figure 6.8a), the shedding process is not directly controlled by the forcing frequency and the mean forces are virtually unaltered from their steady flow values. However the vortex shedding has clearly been influenced by the upstream oscillations which results in the appearance of a secondary frequency, St_2. This frequency is a combination of the shedding and forcing frequencies, i.e. $St_2=St_s+St_e$. The combination frequency persists throughout the asymmetric lock-in range, $1.3<f_e/f_s<2.1$, at this amplitude but three quite distinct shedding modes are observed across the synchronisation range. At the lower frequency bound, Figure 6.8(b), vortices are shed alternately and of opposite circulation in each cycle and the centres of each vortex appear to be positioned near to the wake centreline. At an increased frequency, Figure 6.8(c), the shedding alternates between a pair of oppositely signed vortices and a single vortex per cycle. This corresponds to mode ***P+S*** in the work of Williamson and Roshko (1988, see Figure 2.28). Near the upper frequency bound, Figure 6.8(d), the process again consists of alternate shedding of clockwise and counter clockwise vortices. The vortex alignment now differs from that observed at the lower frequencies and the centres of each vortex are now positioned slightly away from the wake centre line. An explanation for the difference in vortex alignment can be given. As the forcing frequency increases the shedding frequency, f_s, must also increase while the flow remains synchronised. This increase in f_s reduces the separation distance between the vortices causing them to roll up and change their alignment relative to the flow.

A higher amplitude of x_e/d=0.30 has been set in Figure 6.9. At a low forcing frequency, Figure 6.9(a), the mean force parameters are similar to the steady flow values and the shedding frequency has been slightly reduced, St_s=0.186. Although the flow is not fully controlled by the upstream oscillations it is clear that a new pattern of shedding has been induced which we may term a ***P+2S*** mode following the definitions from Williamson and Roshko, Figure 2.28. Four vortices are shed per cycle consisting of a pair of vortices and two single vortices of opposite circulation. The combination frequency, St_2=0.0903, differs from that found at the lower amplitude, x_e/d=0.15, since it is now given by $St_2=St_s-St_e$. The reason for this difference in combination frequencies is not clear since the shedding pattern resembles that displayed in Figure 6.8(a). This ***P+2S*** mode must however be considered unique since the frequency of the forcing oscillation has been set at exactly half the natural shedding frequency, $f_e=0.5f_0$.

Figures 6.9(b), (c) and (d) span the asymmetric resonant range at x_e/d=0.30. Two modes of shedding were observed. For frequencies in the middle of this range, Figure 6.9(c), Type ***2P*** shedding was found, and this was sandwiched between type ***P+S*** shedding. For frequency ratios $f_e/f_0 \geq 1.8$, Figures 6.9(e) and (f), quasi-symmetric shedding was induced and a striking wake pattern emerges with a 'Chinese Dragon' appearance. The vortices in the near-wake region are seen to be considerably smaller than those shed within asymmetric modes and a close examination reveals that a pair of oppositely signed vortices are shed from each side of the cylinder per cycle. Vortex amalgamation occurs downstream in which an asymmetric pattern is established. The wake position of this vortex amalgamation moves further downstream as the forcing frequency is increased.

An immediate question which arises from these results is why in the case of the ***P+S*** and ***P+2S*** type shedding should the vortex pair favour one side of the wake? The ***P+S*** type shedding has been observed under cross-flow oscillations by Meneghini and Bearman (1993) and in their calculations the favoured side for the vortex pair could be altered by changing the initial direction of the cross-flow oscillations. For in-line oscillations changing the initial oscillatory direction would not alter the symmetry and one may suggest that the arrangement will be dependant on the side of the wake into which the start-up vortex is shed. This implies that the favoured side for the vortex pair is random under in-line oscillations.

6.3 Diamond cylinder (Figures 6.10-6.13)

The mean calculated parameters for the diamond cylinder under uniform flow conditions were St_0 =0.202, C_{D0}=1.95 and $C_{L0(rms)}$=0.69. Figure 6.10 displays the combinations of frequencies and amplitudes which were tested and as before the shedding patterns have been categorised into symmetric and asymmetric synchronisation and outside the synchronisation range. No previous data exists for this configuration to the author's knowledge.

The variations in lift, drag and the ratio f_e/f_s against increasing f_e/f_0 are plotted for four fixed displacement amplitudes (x_e/d=0.05, 0.10, 0.20, 0.30) in Figure 6.11. Similar characteristics are observed as were found with the circular cylinder case. Lift and drag both increase across the asymmetric synchronisation range, which shifts to lower frequencies at the higher amplitudes. At x_e/d=0.20 and 0.30, symmetric shedding is possible provided f_e/f_0>2.0 and lift is greatly reduced in this regime although the drag is not significantly lower than its uniform flow value.

At x_e/d=0.05 asymmetric synchronisation was found in the range $1.6<f_e/f_0<2.0$. The asymmetric synchronisation range was shifted to a lower frequency band $1.4<f_e/f_0<1.8$ at x_e/d=0.10. At higher frequencies, no evidence for any symmetric shedding was found at this amplitude but the shedding frequencies have been significantly altered from their uniform flow value while $C_{L(rms)}$ values are found to be around 15% lower. This suggests the onset of a symmetric range and indeed at higher amplitudes symmetric shedding is found.

In Figure 6.11(c) the reduction in lift force is clearly seen and the arbitrary 50% reduction is achieved for f_e/f_0>2.2 at x_e/d=0.20 and for f_e/f_0>1.8 at x_e/d=0.30. Asymmetric resonance was found over the range $1.2<f_e/f_0<1.6$ for x_e/d=0.20 and x_e/d=0.30. However at x_e/d=0.30 the situation is a little more complicated since resonance was also found for a lower forcing frequency f_e/f_0=0.8 but not at f_e/f_0=1.0. There is also evidence for lock-in with f_e/f_s=1.0 at f_e/f_0=0.7.

Vortex streets at x_e/d=0.05 are displayed in Figure 6.12. Figure 6.12(a) shows the shedding pattern at a low forcing frequency but the Karman vortex street is only sustained for around four or five shedding cycles downstream. Within the resonant regime, Figure 6.12(b), the street is sustained for a slightly longer period but

there is a strong indication of some vortex pairing occurring in the centre of this visualisation. This pairing becomes more apparent at a higher frequency, Figure 6.12(c), beyond the synchronisation range. In the immediate near wake the vortices are shed asymmetrically but after travelling a short distance they appear to pair off favouring one side of the wake centre line, in this instance the lower side. Further downstream the vortices have paired off on the opposite side of the wake centre line which suggests some form of intermittency is present in this shedding arrangement.

The visualisations at x_c/d=0.30, Figure 6.13, are further evidence of the complex shedding processes which have been found for this geometry. At a low frequency, Figure 6.13(a), the vortices have paired off onto one side of the wake in a similar manner to that found for high frequency oscillations at a lower amplitude. In Figure 6.13(b) at f_c/f_0=0.9 the Strouhal number deduced from the lift force suggests that the flow is synchronised with f_c/f_s=2.0 but this appears unlikely on inspection of the vortex street and the secondary frequency is probably more closely associated with the shedding frequency in this case. At a synchronised frequency, Figure 6.13(c), the paired vortices are now shed alternately from either side of the diamond. As the forcing frequency is increased across the synchronisation range, $1.1<f_c/f_0<1.6$, the alignment of these paired vortices changes by ninety degrees. At higher frequencies symmetric shedding is induced with pairs of vortices shed simultaneously from each side. The vortices are somewhat smaller than those shed in non-symmetric regimes but contain very strong cores. This arrangement breaks down in the far wake into something resembling a giant Karman street.

The main point of observation for this cylinder is the strong tendency for vortex pairing resulting in the ***P*** type mode, Figures 6.12(b),(c) and 6.13(a),(b), and the ***2P*** mode across the synchronisation range at x_c/d=0.03, Figures 6.13(c),(d) and(e). Pairing is also evident in the quasi-symmetric shedding case, Figure 6.13(f).

6.4 *B/A*=0.62 cylinder (Figures 6.14-6.17)

The lock-in diagram for this cylinder is presented in Figure 6.14 together with the threshold amplitudes found by Al-Asmi and Castro (1992) for a flat plate and a *B/A*=0.67 cylinder. Under uniform flow conditions the mean calculated parameters for the *B/A*=0.62 cylinder were St_0 =0.172, C_{D0}=1.83 and $C_{L0(rms)}$=0.52. It is clear that at x_c/d=0.05 the lock-in boundaries lie close to those found for a *B/A*=0.67 cylinder by Al-Asmi and Castro (1992) although their measurements were taken at a higher Reynolds number, *Re*=7000-50000.

The variation in mean forces and shedding frequencies is displayed in Figure 6.15. Flow visualisations for this cylinder are shown in Figures 6.16 and 6.17. At a low oscillatory amplitude, x_c/d=0.05, asymmetric synchronisation is possible in the range $1.8\leq f_c/f_0\leq 2.2$. There is no noticeable change in the vortex street arrangement, shown in Figure 6.16, across this range. Outside this range the dominant frequency (see Figure 6.15(b)) is only slightly altered from its uniform flow value. At x_c/d=0.10 the lower bound is extended such that

asymmetric synchronisation is found over the range $1.6<f_e/f_0<2.2$. The mean forces increase marginally across the lock-in range at $x_e/d=0.05$ and 0.10.

A greater increase in the mean forces is found at the higher amplitudes shown in Figure 6.15(c). As the amplitude is increased to $x_e/d=0.20$ the synchronisation range broadens to $1.4\leq f_e/f_0\leq 2.3$. There is a sudden decrease in the upper frequency bound for asymmetric resonance at $x_e/d=0.30$ and the range is shifted to $1.2<f_e/f_0<1.6$. Some evidence is found for quasi-symmetric shedding at $x_e/d=0.30$ near $f_e/f_0=1.8$ but clearly the reduction in the r.m.s. lift is not as significant as was observed in the case of the circular and diamond cylinders and occurs over a shorter range of forcing frequencies. At $x_e/d=0.30$ with $f_e/f_0\geq 2.2$ the dominant frequency is clearly significantly different from the uniform flow value, and follows a straight line fit. This straight line did not appear to be given by any obvious fractional combination of f_e and f_0 but could be approximated by $f_s = 0.93f_e + f_0$.

The visualisations in Figure 6.17 encompass the range of oscillatory frequencies tested at $x_e/d=0.30$. Asymmetric resonance was found from the lift spectra over the range $1.2\leq f_e/f_0\leq 1.6$ but simulations were not undertaken for frequency ratios lower than $f_e/f_0=1.2$. The flow patterns in these cases are complex and it is difficult to define the shedding mode or deduce that the flow is controlled by the forcing oscillations from these visualisations. At $f_e/f_0=1.2$ and 1.6, Figures 6.17(a) and (c), this may have resulted from not allowing the simulation a suitable time to fully settle down as the vortex street does not show a regular pattern in the wake. However at $f_e/f_0=1.4$, Figure 6.17(b), a regular street is observed although the mode of shedding is debatable and dependent on the reference position. There are certainly four vortices shed in each cycle and if we examine the near wake we may categorise this as type ***2P*** shedding. However as we move downstream one of the vortices from the pair shed into the lower half of the wake begins to interact with the pair shed into the upper half. This may be termed type ***T+S*** shedding since the arrangement consists of three vortices in the upper half of the wake and a single vortex in the lower half. At higher forcing frequencies, Figures 6.17(d, e and f), the flow appears to consist of many small vortices shed into the near wake which amalgamate downstream to produce a vortex street.

6.5 *B/A*=1.0 cylinder (Figures 6.18-6.21)

Under uniform flow conditions the mean calculated parameters for the $B/A=1.0$ cylinder were St_0 =0.154, $C_{D0}=1.46$ and $C_{L0(rms)}=0.35$. Some previous research has been undertaken to determine the lock-in boundary for this cylinder and these results are displayed in Figure 6.18. Minewitsch *et al* (1994) determined the lower and upper frequency threshold for asymmetric resonance at $Re=200$ but their calculations indicated a slightly narrower synchronisation range than found by the DVM simulations. The DVM study indicates that this range ceases to widen beyond $x_e/d=0.15$ but Minewitsch's study shows the synchronisation width continues to increase up to $x_e/d=0.20$. Okajima *et al* (1993), working at $Re=1000$, chose a fixed displacement amplitude $x_e/d=0.14$ and

obtained somewhat different values to those found in this study at a lower Re. The frequency range over which they determined asymmetric synchronisation was given by $1.7<f_e/f_o<2.7$ which compares to the range determined by DVM of $1.5<f_e/f_o<2.4$ at a fixed amplitude of $x_e/d=0.15$. Okajima also found lock-in of type $f_e/f_s=1.0$ for a range $0.6<f_e/f_o<1.35$. Neither this DVM study nor the Minewitsch calculations found any evidence for such behaviour at Re=200.

Figure 6.19 shows the forces and shedding frequencies observed for displacement amplitudes $x_e/d\leq0.50$ with the square cylinder. No evidence for any quasi-symmetric behaviour was found for this cylinder but the asymmetric synchronisation range was wide, varying from $1.8<f_e/f_0<2.2$ at $x_e/d=0.05$ to $1.5<f_e/f_0<2.4$ at $x_e/d=0.20$. At $x_e/d=0.30$, the range had narrowed to $1.6<f_e/f_0<2.3$ and by $x_e/d=0.50$ no asymmetric lock-in was observed. At the high displacement amplitude $x_e/d=0.50$ and with $f_e/f_0\geq1.4$, Figure 6.19(f), the dominant shedding frequency follows a straight line fit similar to that found for the B/A=0.62 cylinder with $f_s = 0.91f_e + f_0$.

Flow visualisations are shown across the synchronisation ranges at $x_e/d=0.10$ and 0.30. At $x_e/d=0.10$, Figure 6.20, only type ***2S*** shedding is found. This remains the case at $x_e/d=0.30$, Figure 6.21, although the vortices are beginning to change their orientation in the far wake at $f_e/f_0=2.3$, Figure 6.21(c), as the separation between the vortices decreases. In summary the B/A=1.0 cylinder shows a wide range of asymmetric type ***2S*** shedding but no alternative modes of shedding or quasi-symmetric behaviour were observed for $x_e/d\leq0.30$.

6.6 B/A=2.0 cylinder (Figures 6.22-6.25)

The mean calculated parameters for the B/A=2.0 cylinder under uniform flow conditions were St_0 =0.167, C_{D0}=1.15 and $C_{L0(rms)}$=0.24. Figure 6.22 shows the lock-in chart for this geometry. The mean forces and shedding frequencies are displayed in Figure 6.23 and vortex shedding plots have been reproduced at displacement amplitudes of $x_e/d=0.10$, Figure 6.24, and $x_e/d=0.30$, Figure 6.25. At $Re=10^3$ Okajima *et al* (1993) found lock-in of type $f_e/f_s=1.0$ across the range $0.6<f_e/f_o<2.5$ and of type $f_e/f_s=2.0$ across the range $2.5<f_e/f_o<3.0$. This is clearly quite different from the lock-in values found in this study and is probably due to the difference in Reynolds numbers between the calculations. The shedding characteristics under uniform flow conditions alter substantially as the Reynolds number increases for this geometry. The Strouhal number vs. Re curve was reproduced in Figure 2.12(b) and shows a discontinuity close to Re=400. This is due to intermittent reattachment along the side surfaces. At Re>600 the flow remains attached and thus there is a distinct difference between the fully separated flow at Re=200 and the reattached flow at Re=1000. It is thus not surprising that the characteristics under oscillatory flow conditions found in this study should be so different from those found by Okajima *et al.*

In the DVM simulations the range of forcing frequencies which induced asymmetric synchronisation varies little with forcing amplitude. As the displacement amplitude increased from $x_e/d=0.05$ to 0.30 the lower bound for

asymmetric synchronisation decreased from f_e/f_0=1.7 to f_e/f_0=1.5 while the upper bound decreased from f_e/f_0=2.1 to f_e/f_0=1.9. Quite different behaviour from that of the rectangles of shorter side ratio is observed since the pulsations are strongly inclined to induce quasi-symmetric shedding for certain ranges of forcing frequency. The quasi-symmetric shedding mode begins to emerge at x_e/d=0.10 and at higher amplitudes is dominant for f_e/f_0>2.0. Above the upper frequency bound for asymmetric synchronisation one can observe a sharp decline in the mean forces, particularly the rms lift as the flow changes abruptly to exhibit quasi-symmetric behaviour.

The visualisations show the different shedding modes observed for this geometry. At x_e/d=0.10, Figure 6.24, only type ***2S*** shedding was observed, although at f_e/f_0=2.2 the calculations indicate a reduced lift force (see Figure 6.23(a)) and hence quasi-symmetric shedding is implied. It is rather difficult to detect any great difference in the near-wake regions between Figure 6.24(b) and (c) but at this low amplitude the near-wake symmetry may well be intermittent. At a higher amplitude, x_e/d=0.30, the shedding mode changes from type ***2S*** at f_e/f_0=1.5, Figure 6.25(a), to type ***2P*** at f_e/f_0=1.7, Figure 6.25(b), across the asymmetric synchronisation range. At higher frequencies the quasi-symmetric mode is induced, Figure 6.25(c), and the symmetry in the near wake now extends to several body widths downstream before breaking down into an asymmetric vortex street.

6.7 *B/A*=3.0 cylinder (Figures 6.26-6.28)

Figure 6.26 displays the lock-in chart found for this cylinder. Under uniform flow conditions the mean calculated parameters for the *B/A*=3.0 cylinder were St_0 =0.161, C_{D0}=1.05 and $C_{L0(rms)}$=0.21. The effect of in-line oscillations on mean forces and shedding frequencies is shown in Figure 6.27 and a series of shedding plots have been plotted at the displacement amplitude x_e/d=0.30, Figure 6.28. As a reference the uniform flow shedding pattern has been plotted in the previous chapter, Figure 5.15(e). Asymmetric synchronisation was not observed below a forcing amplitude of x_e/d=0.10 or above a forcing frequency of f_e/f_0=2.0. This compares with the upper limit found by Okajima *et al* (1993) of f_e/f_0=1.9. The lower limit decreased from f_e/f_0=1.6 at x_e/d=0.10 to f_e/f_0=1.2 at x_e/d=0.30 although at the higher amplitude this lower limit has not been fully investigated. Okajima's study found a lower limit to the asymmetric resonance and also found shedding with f_e/f_s=1.0 for forcing frequencies above and below the range for f_e/f_s=2.0.

This cylinder exhibits behaviour similar to the *B/A*=2.0 cylinder within the asymmetric range but no quasi-symmetric behaviour could be deduced from examination of the lift forces in Figures 6.27(a) and (c). It is clear that the lift is never reduced significantly as was observed for the circular, diamond and *B/A*=2.0 cylinders and none of the simulations for this geometry could be termed quasi-symmetric according to the definition of a 50% reduction in the mean r.m.s. lift.

At x_e/d=0.3, f_e/f_0=1.2, Figure 6.28(a), the near wake shows strong quasi-symmetric behaviour, particularly if comparison is made to the uniform flow shedding appearance, Figure 5.15(e). However further downstream the

asymmetric vortex street is locked onto the forcing frequency at f_s/f_s=2.0 and since this was dominant in the spectral analysis of the lift curve the flow is considered to be within the asymmetric synchronisation region. As the frequency is increased through the asymmetric synchronisation range the shedding pattern changes to mode ***2P***, Figures 6.28(b) and (c). Beyond the synchronised region at $f_s/f_0 \geq 1.8$ the shedding pattern is similar to what was previously observed for quasi-symmetric shedding with a near-wake region in which pairs of vortices are shed into the flow before breaking down into an asymmetric vortex street further downstream. However careful examination of the near-wake region reveals that the symmetry is not as well maintained as was the case for other geometries. This perhaps explains why the lift force does not reduce substantially and suggests that although using the reduction in lift force is perhaps a sufficient condition to define quasi-symmetry in the near wake it is not a necessary one. With this longer geometry the lift coefficient under uniform conditions is already quite small since the afterbody delays the onset of any asymmetry from the vortex interaction and hence the quasi-symmetric mode is no longer well defined by an examination of the mean lift.

6.8 Pseudo-phase shift across the asymmetric resonance range

A phase shift across the synchronisation range has been found for cross-flow oscillations by Ongoren and Rockwell (1988a) amongst others. Their results indicate a sudden jump in the phase difference as the forcing frequency increases across the synchronisation range. Figure 2.26 has been reproduced from Ongoren and Rockwell's (1988a) laboratory study on cross flow oscillations. We can observe that at f_s/f_0=1.0 a vortex has just been shed from the lower surface. At f_s/f_0=1.17 the vortex is shed from the upper surface at the equivalent moment of the oscillation cycle. This implies that the phase of the vortex shedding with respect to the oscillatory motion has shifted by approximately 180° in this frequency range.

This phase change has not been observed for in-line oscillations although Okajima *et al* (1993) examined the phase of the drag with respect to the forcing oscillation for pulsating flows about rectangular and circular cylinders. Their findings showed only a small shift in the phase angle and across the synchronisation range the phase remained quite constant. It is not clear why the drag was used to determine this phase change instead of the lift which would appear to relate more clearly to the vortex shedding process. A possible explanation is that the drag normally oscillates at twice the frequency of the lift. For in-line oscillations this implies that the drag will oscillate at the forcing frequency and thus a phase difference can be readily calculated. Across the asymmetric synchronisation range the lift oscillates at half the forcing frequency and so a phase difference cannot be defined in precise mathematical terms.

There is also a fundamental difference between the phase shift for an in-line and a cross-flow oscillation which can be appreciated by reference to Figures 6.29-6.31. Two moments of vortex shedding, shown in Figure 6.29, are chosen which coincide with the moments of maximum and minimum lift. [It should be noted that Figures 6.29(a) and (b) are taken from uniform flow visualisations but should be sufficient for illustrative purposes]. For

cross-flow oscillations ϕ_V is defined as the phase difference between these moments of vortex shedding and the forcing oscillation. ϕ_V is defined to be zero if vortex A is shed at the moment of maximum oscillatory velocity and vortex B is shed at the moment of minimum oscillatory velocity, Figure 6.30(a). ϕ_V=180° if this arrangement is reversed, Figure 6.30(b). The phase change between Figures 6.30(a) and (b) then corresponds to the type of behaviour shown in Ongoren and Rockwell's work, Figure 2.26.

For in-line oscillations, and across the asymmetric synchronisation range, the frequency of vortex shedding is half the forcing oscillation frequency and a phase shift cannot be properly defined. A pseudo-phase shift is therefore defined as shown in Figure 6.31. ϕ_V is defined to be zero if both vortex A and vortex B are shed consecutively at moments of maximum oscillatory velocity. ϕ_V=180° if both vortices are shed consecutively at moments of minimum oscillatory velocity.

It must be emphasised that the laboratory-determined phase difference involves a difference in phase between the forcing oscillation and the shedding process. The numerical calculations are concerned with a difference between the forcing oscillations and the force time histories. It is certainly far simpler to calculate a phase shift by referring to the difference between the forcing oscillations and the force time histories, particularly if only small shifts are involved. For this study a pseudo-phase difference ϕ_L will therefore be defined which relates a moment of the lift cycle to a moment of the forcing oscillation. A phase lag ϕ_D will also be calculated which relates a moment of the drag cycle to a moment of the forcing oscillation.

The phase differences were calculated by plotting a sine curve of frequency f_e on the same graph as the force time history. The sine curve was given an amplitude and displacement similar to the lift (or drag). Shifts of ϕ_L and ϕ_D degrees were applied to the lift and drag curves respectively such that the force curves coincided with the sinusoidal forcing oscillation at particular moments of the cycle. For the lift curve these moments were given when both the lift and the forcing oscillation were changing from negative to positive. For the drag curve the chosen coincident moments were not as vital since the drag time history oscillates in an approximately sinusoidal manner at the forcing frequency f_e. It is important to note that ϕ_L can only be defined across the asymmetric synchronisation range. The drag was found to be controlled by the forcing oscillation over a much greater range of frequencies than the lift and so ϕ_D could be defined over a wider frequency range. A discussion of the findings for ϕ_L and ϕ_D for each cylinder follows.

6.8.1 Circular cylinder (Figure 6.32)

Figure 6.32 shows the phase difference found between the lift and drag time histories and the forcing oscillations. The phase difference for the lift, ϕ_L, can only be defined across the asymmetric synchronisation region. A definite trend is exhibited in which ϕ_L gradually increases as the forcing frequency increases. The gradient of this increase appears to become shallower as the oscillatory amplitude is increased although it is unclear what significance this holds. ϕ_D, the phase of the drag with respect to the forcing oscillation, could be defined across a much broader range of frequencies since it is controlled over a wider range than the lift. The

phase change is small and shows similar characteristics independent of the forcing amplitude. For f_e/f_0>1.2 it remains roughly constant at approximately 260 degrees.

6.8.2 Diamond cylinder (Figure 6.33)

Figure 6.33 plots ϕ_L and ϕ_D found for the diamond cylinder. A similar trend is seen to the results for the circular cylinder with ϕ_L gradually increasing as the forcing frequency increases. However the change in ϕ_L is not as great as was observed for the circular cylinder. ϕ_D=335° at f_e/f_0=0.8 and gradually decreases until f_e/f_0>2.0 at which point it remains constant at approximately ϕ_D=290°.

6.8.3 Rectangular cylinders (Figures 6.34-6.37)

The phase of the drag remains approximately constant at ϕ_D=270°-290° for each cylinder above f_e/f_0=2.0. Below this value the change in ϕ_D is small and will not be considered further. There is some difference between the cylinders in the way ϕ_L is observed to vary. The results for the B/A=0.62 and B/A=2.0 cylinders shown in Figures 6.34 and 6.36 indicate similar behaviour to the circular and diamond cylinders as for these cylinders an increase in amplitude is accompanied by a decrease in the gradient of the phase change across the synchronisation range. However if one considers f_e/f_0 fixed then an increase in amplitude results in an increase in ϕ_L for the B/A=0.62 and B/A=2.0 cylinders. This contrasts with the findings for the B/A=1.0 and B/A=3.0 cylinders for which the value of ϕ_L decreases for increasing amplitude at a fixed f_e/f_0.

At an amplitude of x_e/d=0.15 the B/A=1.0 cylinder, Figure 6.35(a), shows a particularly rapid increase in ϕ_L over the range 2.1≤f_e/f_0≤2.4. ϕ_L changes by approximately 180 degrees over this region. This implies that an examination of the vortex shedding taken at equivalent moments of the oscillatory flow cycle at f_e/f_0 =2.1 and f_e/f_0=2.4 would reveal a shift in the phase of the vortex shedding similar to that indicated in Figure 6.31.

6.9 Comparison between geometries

Figures 6.38 and 6.39 show comparison of the lift and phase shift found for each cylinder. Figure 6.40 displays the lock-in boundaries found for each cylinder. In Figure 6.38 the ratio $C_{L(rms)}/C_{L0(rms)}$ has been plotted against f_e/f_0. $C_{L0(rms)}$ refers to the value calculated for uniform flow conditions. In effect this means that the curve shows the relative change to the lift from its uniform flow value.

At x_e/d=0.05, Figure 6.38(a), the differences between the cylinders are not large. For forcing frequencies less than f_e/f_0=1.5 the lift is unaltered from its uniform flow value for the circular, diamond, B/A=2.0 and B/A=3.0 cylinders. However the rectangles of shorter side ratio, B/A=0.62 and B/A=1.0, show a slight increase . All the cylinders show a decrease in the lift for slightly higher f_e/f_0 with minima occurring in the range 1.6≤f_e/f_0≤1.8. Across the asymmetric synchronisation ranges the lift increases by a similar amount for all but one of the cylinders. The B/A=2.0 cylinder shows different characteristics at this displacement amplitude as the lift reaches a

sharp peak close to f_e/f_0=2.0 before falling sharply to a value around 0.8 times its uniform flow value. The main difference between the cylinders when the forcing amplitude is low is that the B/A=2.0 cylinder shows signs of developing quasi-symmetric behaviour with a reduced lift force above f_e/f_0=2.0.

At a higher displacement amplitude, Figure 6.38(b), the differences in the behaviour for each cylinder are more noticeable. The B/A=2.0, circular and diamond cylinders all have a distinct range across which the lift is reduced to near zero, indicating quasi-symmetric shedding. The B/A=2.0 and 3.0 cylinders have a large increase in their lift, 4-5 times their respective uniform flow values across the asymmetric synchronisation range. For the other cylinders the maximum increase is between two and two and a half times the uniform flow value. Secondary peaks in the lift curves can be observed near f_e/f_0=1.0 for the B/A=1.0, .2.0, 3.0 and circular cylinders. This is possibly evidence for a small range of lock-in where f_e/f_s=1.0 but this was not investigated further.

Values of ϕ_L across the synchronisation range are displayed in Figure 6.39. At the low amplitude, x_e/d=0.05, Figure 6.39(a), there is a clear difference between the cylinders. The B/A=1.0 and circular cylinders show a large change in ϕ_L of almost 180 degrees. The exact moment at which the vortices were shed with respect to the forcing oscillation cycle was not investigated. However if one assumes that the vortices are shed at the moment of maximum forward acceleration near the lower frequency bound for resonance then a 180 degree shift across the synchronisation range implies that the vortices will then be shed at the moment of maximum deceleration. Smaller changes in ϕ_L are observed for the other cylinders. At the higher displacement amplitude, Figure 6.39(b), ϕ_L increases slowly across the synchronisation range. For the B/A=3.0 cylinder there is actually a slight decrease in ϕ_L.

The frequency bounds for lock-in are shown in Figure 6.40. The dashed lines represent the lower frequency bound and the dotted lines the upper bounds for asymmetric synchronisation in each case. There is clearly considerable difference in the frequency ranges between the geometries. The smallest lock-in bounds are seen for the diamond cylinders and the rectangles of side ratio B/A=2.0 and 3.0. The shorter rectangles of side ratio B/A=0.62 and 1.0 have the widest lock-in ranges.

In summary this in-line oscillatory flow study has revealed substantial differences in the lock-in characteristics of several geometries. All the cylinders exhibited primary asymmetric resonance within which f_e/f_s=2.0 and the mean forces increase although the lock-in boundaries and shedding modes varied between cylinders. The circular, diamond and B/A=2.0 cylinders exhibited quasi-symmetric type shedding in which the near wake takes on a symmetric appearance and the far wake reverts to an asymmetric vortex street. The lift force was substantially reduced from its uniform flow value for quasi-symmetric type shedding. The B/A=0.62 and 1.0 cylinders gave some indication that quasi-symmetric behaviour may emerge at higher forcing amplitudes. An investigation of the pseudo-phase difference between the lift and the forcing oscillation showed that at low amplitude a large change in ϕ_L took place across the asymmetric synchronisation range at low forcing amplitudes. However this change was reduced significantly at higher amplitudes.

The above results perhaps offer more new questions rather than resolving any old ones. For example what is the mechanism responsible for producing vortex pairs instead of individual vortices? How does the change from asymmetric shedding, e.g. Figure 6.13(e), to symmetric shedding, e.g. Figure 6.13(f), occur? Are there regions close to the boundaries for asymmetric and quasi-symmetric resonance which exhibit intermittent behaviour? Does the side of the wake into which the vortex pair is shed depend on the side of the wake into which the start-up vortex is shed? What is the link between the shedding mode, lift time history, and phase difference? It is evident that further work must be carried out before an explanation for these questions can be offered. Greater understanding may be found from an examination of the near wake at several moments of the forcing oscillation. More comprehensively it would be useful to create a series of loopable videos of each shedding mode. Each video should also include a time evolution of the force histories and upstream oscillations so that a link between these processes can possibly be deduced. It may also be useful to undertake some simulations within which the forcing frequency is gradually increased, particularly at frequencies close to the lock-in boundary.

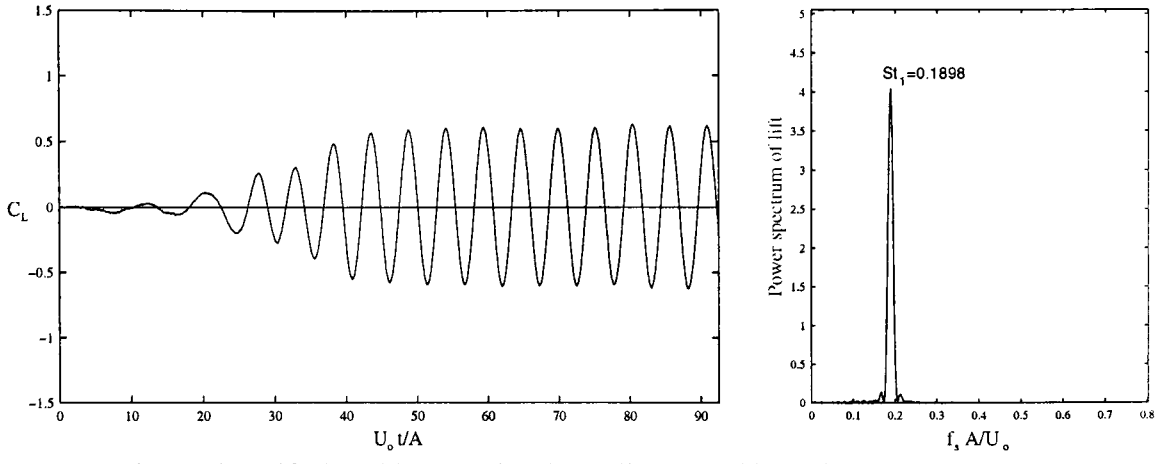

Figure 6.1 Lift time history, circular cylinder, uniform flow, $C_{L(rms)}$=0.43.

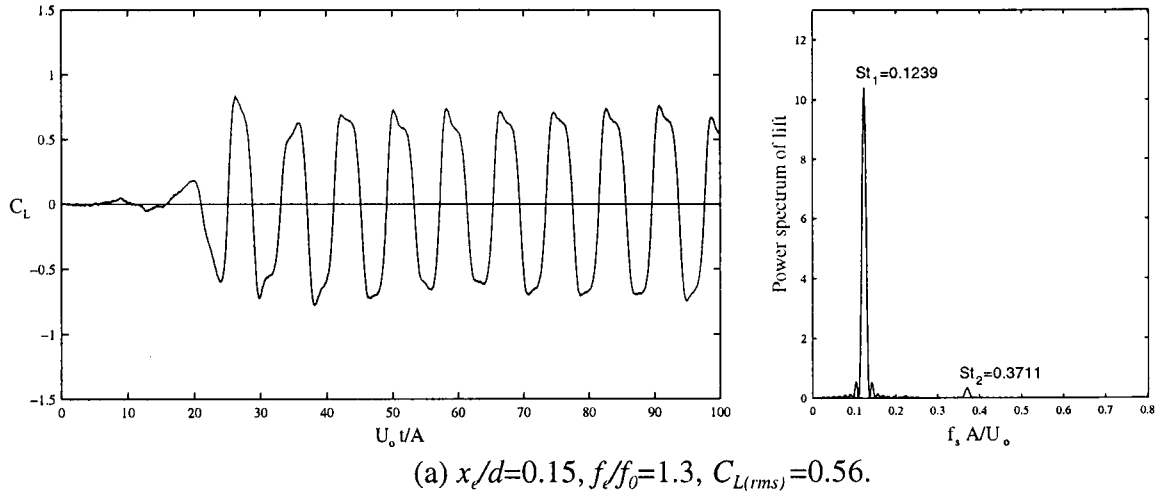

(a) x_e/d=0.15, f_e/f_0=1.3, $C_{L(rms)}$=0.56.

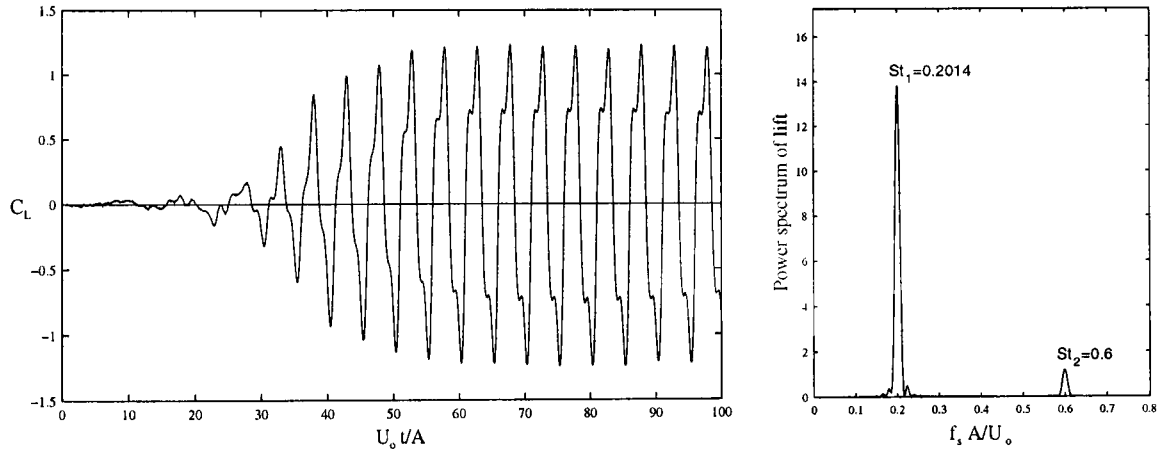

(b) x_e/d=0.15, f_e/f_0=1.75, $C_{L(rms)}$=0.87.

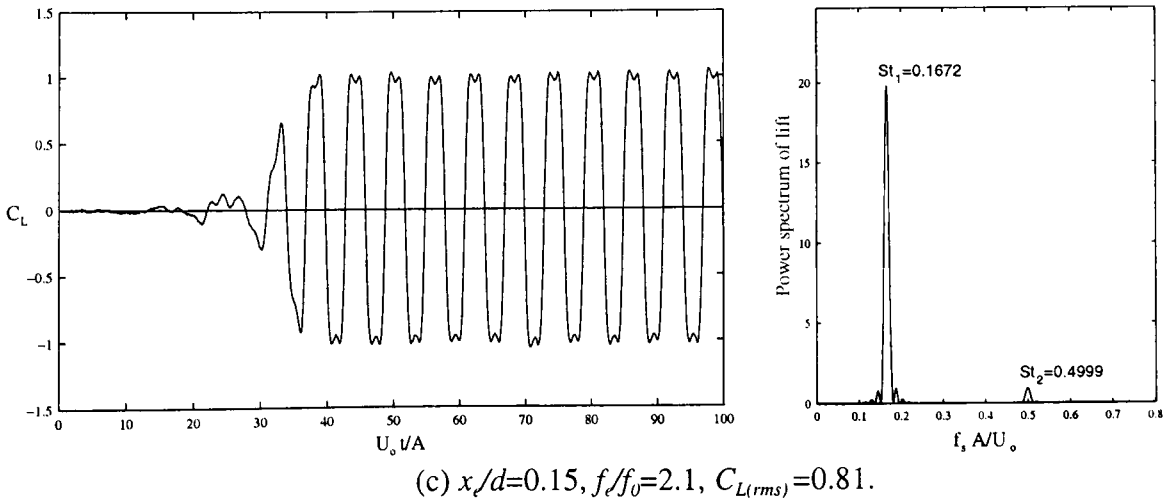

(c) x_e/d=0.15, f_e/f_0=2.1, $C_{L(rms)}$=0.81.

Figure 6.2 Lift time histories, circular cylinder, x_e/d=0.15, Re=200.

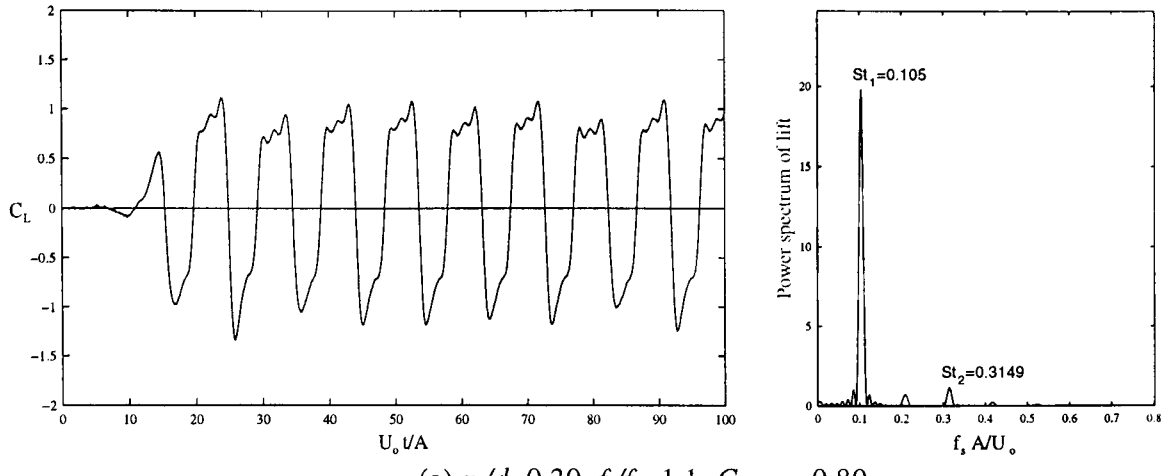

(a) x_e/d=0.30, f_e/f_0=1.1, $C_{L(rms)}$=0.80.

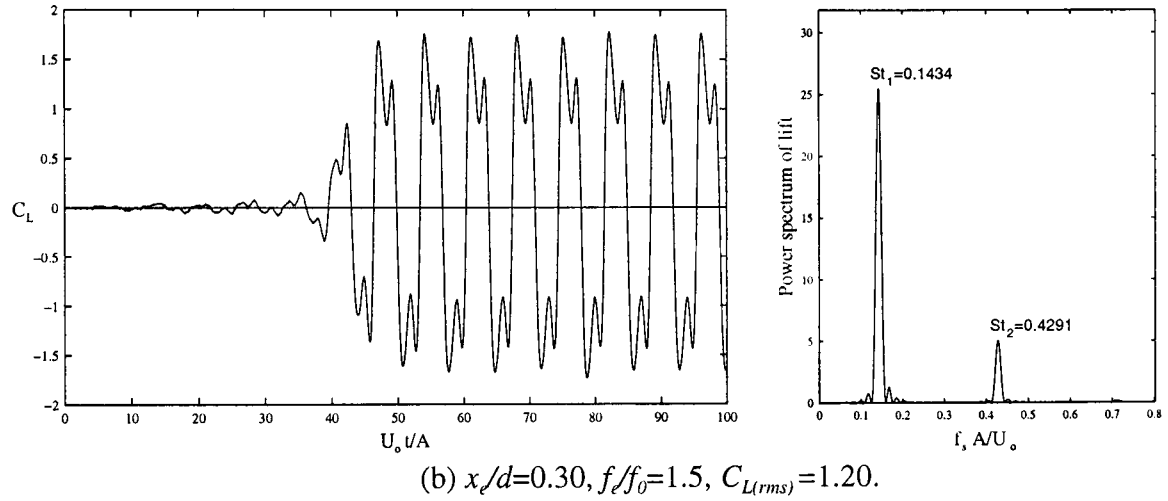

(b) x_e/d=0.30, f_e/f_0=1.5, $C_{L(rms)}$=1.20.

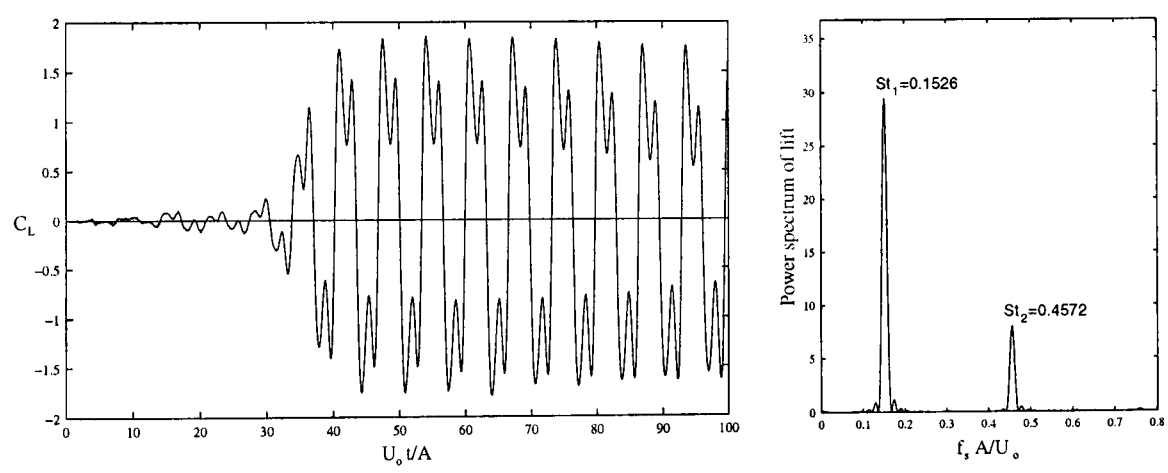

(c) x_e/d=0.30, f_e/f_0=1.6, $C_{L(rms)}$=1.20.

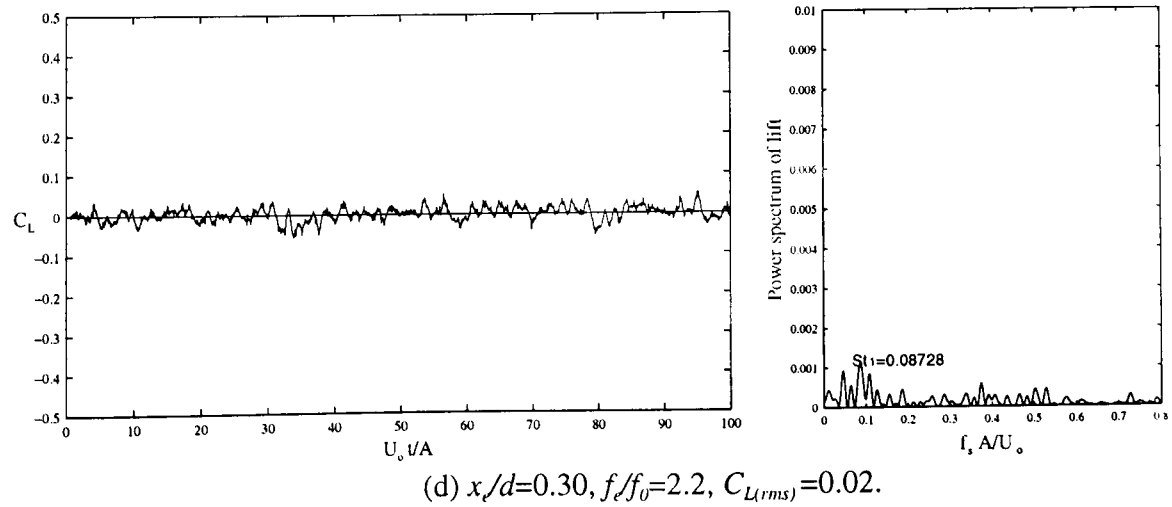

(d) x_e/d=0.30, f_e/f_0=2.2, $C_{L(rms)}$=0.02.

Figure 6.3 Lift time histories, circular cylinder, x_e/d=0.30, Re=200.

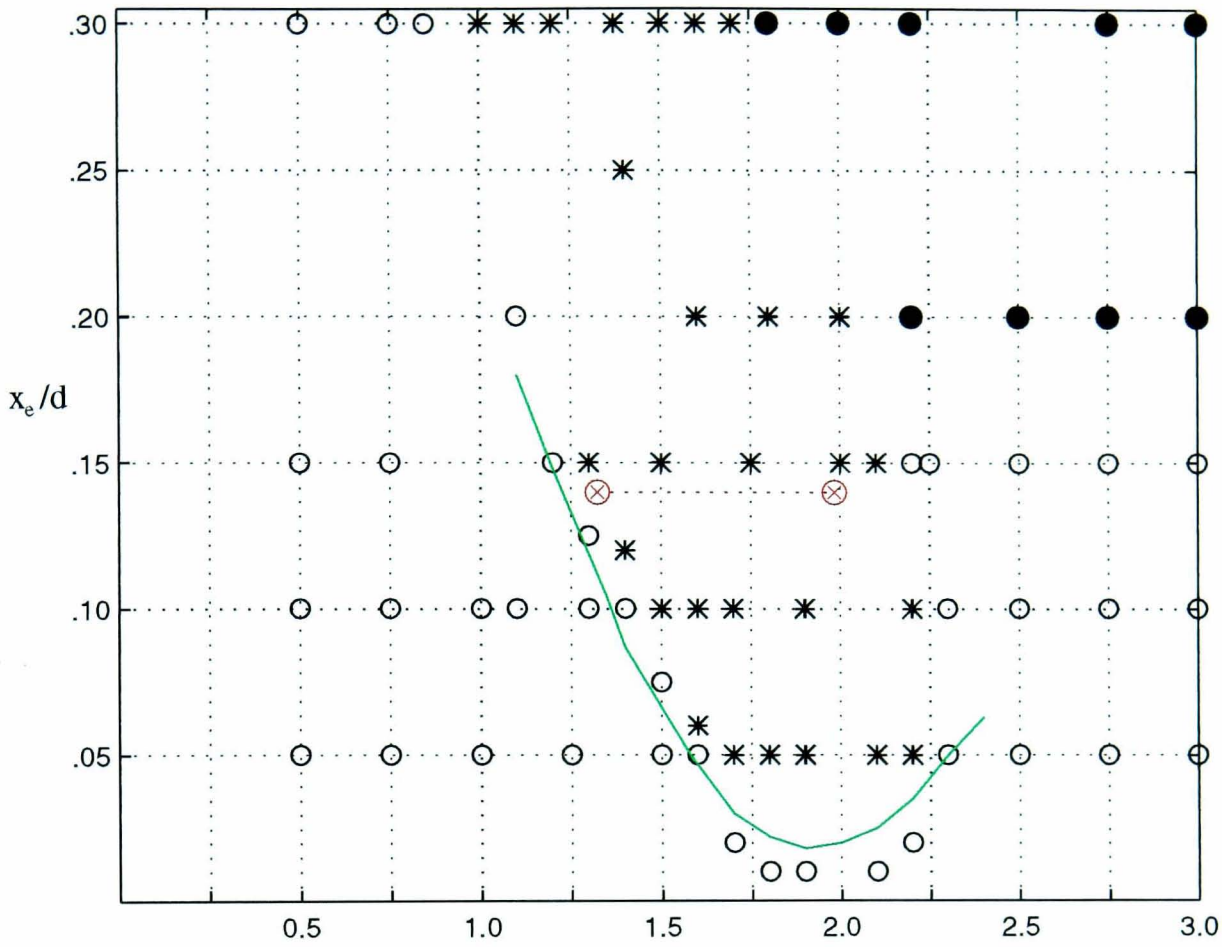

Figure 6.4 Shedding regimes for circular cylinder, *Re*=200.

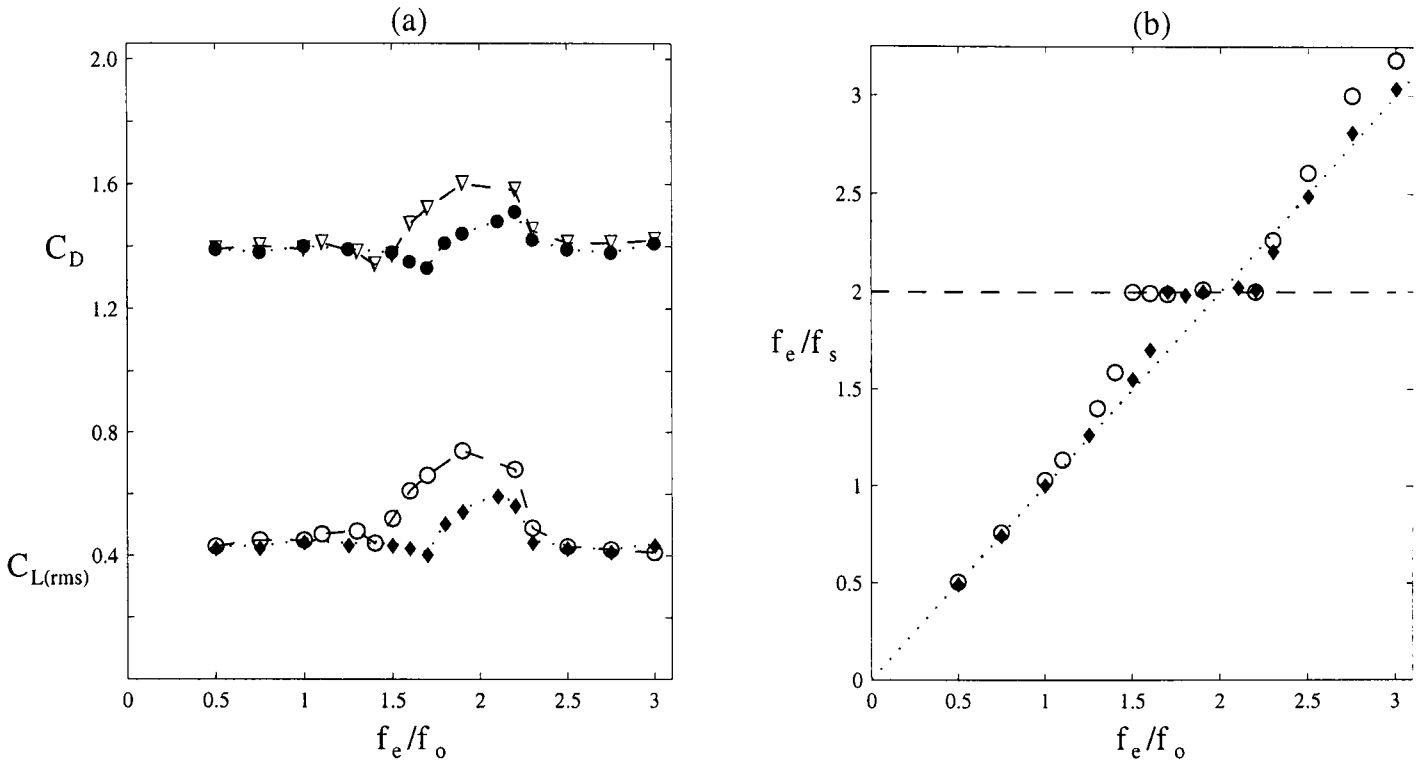

(a) $C_{L(rms)}$ vs. f_e/f_0, ♦ - x_e/d=0.05, o - x_e/d=0.10
C_D vs. f_e/f_0, • - x_e/d=0.05, ∇ - x_e/d=0.10
(b) f_e/f_s vs. f_e/f_0, ♦ - x_e/d=0.05, o - x_e/d=0.10

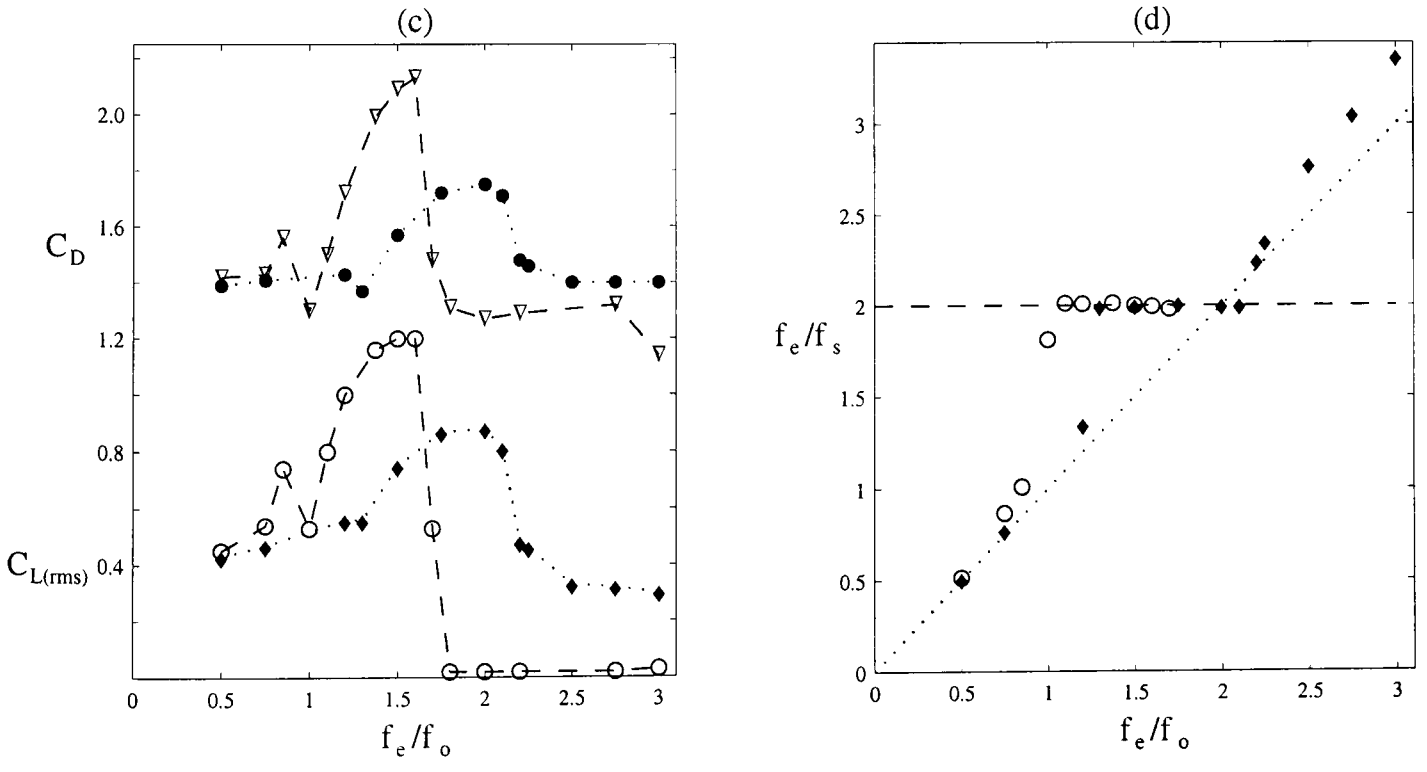

(c) $C_{L(rms)}$ vs. f_e/f_0, ♦ - x_e/d=0.15, o -x_e/d=0.30
C_D vs. f_e/f_0, • - x_e/d=0.15, ∇ - x_e/d=0.30
(d) f_e/f_s vs. f_e/f_0, ♦ - x_e/d=0.15, o - x_e/d=0.30

Figure 6.5 Effect of in-line oscillations on mean forces and shedding frequency; Circular cylinder; *Re*=200.

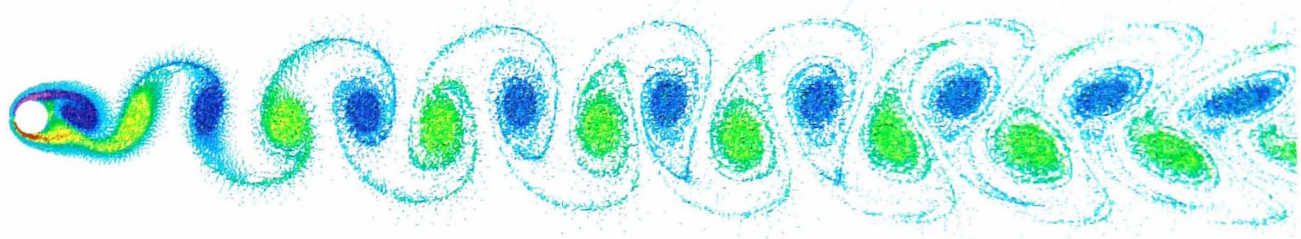

Figure 6.6 Vortex shedding past circular cylinder; Uniform flow; Re=200;
St_0=0.191, C_D=1.39, $C_{L(rms)}$=0.43

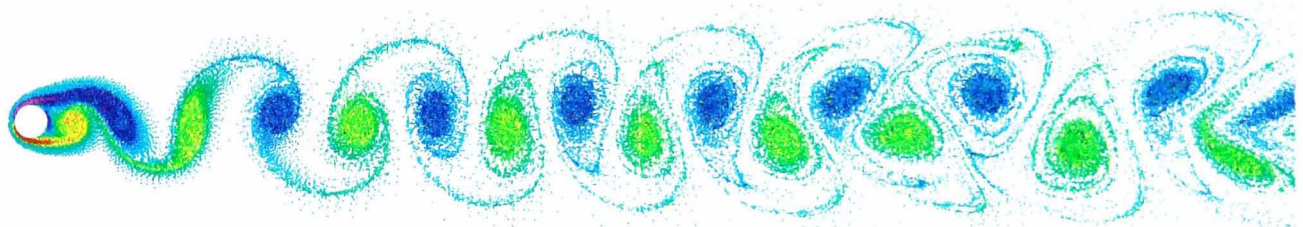

Figure 6.7 Effect of in-line oscillations on vortex shedding; Circular cylinder; Re=200.
x_e/d=0.02, f_e/f_0=2.2, St_1=0.194, C_D=1.36, $C_{L(rms)}$=0.42

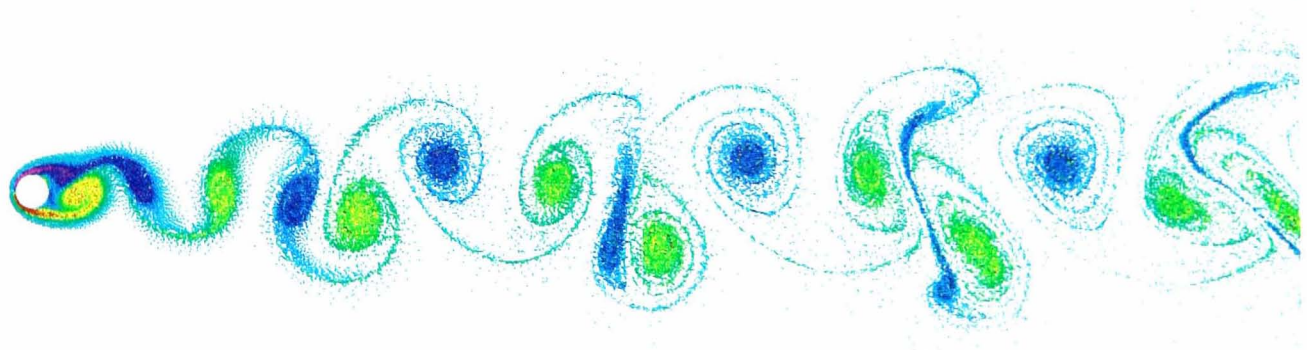

(a) x_e/d=0.15, f_e/f_0=0.5, St_1=0.189, St_2=0.283, C_D=1.39, $C_{L(rms)}$=0.43

Figure 6.8 Effect of in-line oscillations on vortex shedding; Circular cylinder; x_e/d=0.15; Re=200.

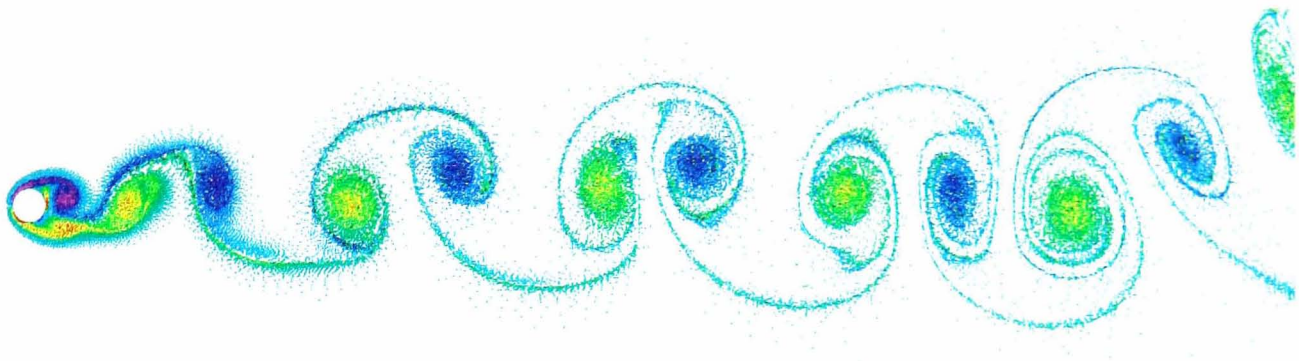

(b) x_e/d=0.15, f_e/f_0=1.3;
St_1=0.125, St_2=0.371, C_D=1.37, $C_{L(rms)}$=0.56, ϕ_L=65.

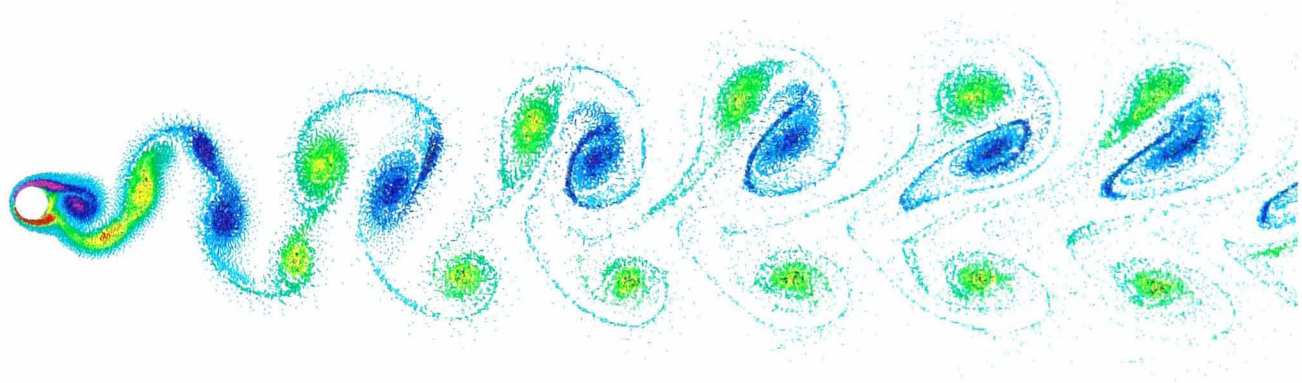

(c) x_e/d=0.15, f_e/f_0=1.75;
St_1=0.167, St_2=0.501, C_D=1.72, $C_{L(rms)}$=0.87, ϕ_L=105.

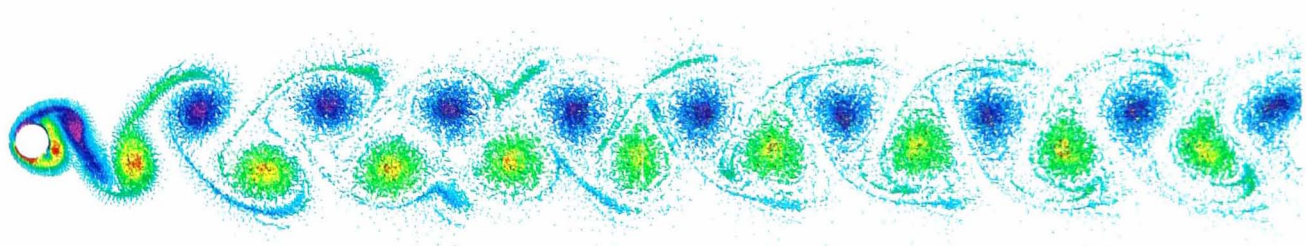

(d) x_e/d=0.15, f_e/f_0=2.1;
St_1=0.201, St_2=0.600, C_D=1.71, $C_{L(rms)}$=0.81, ϕ_L=145.

Figure 6.8 (cont) Effect of in-line oscillations on vortex shedding; Circular cylinder; x_e/d=0.15.

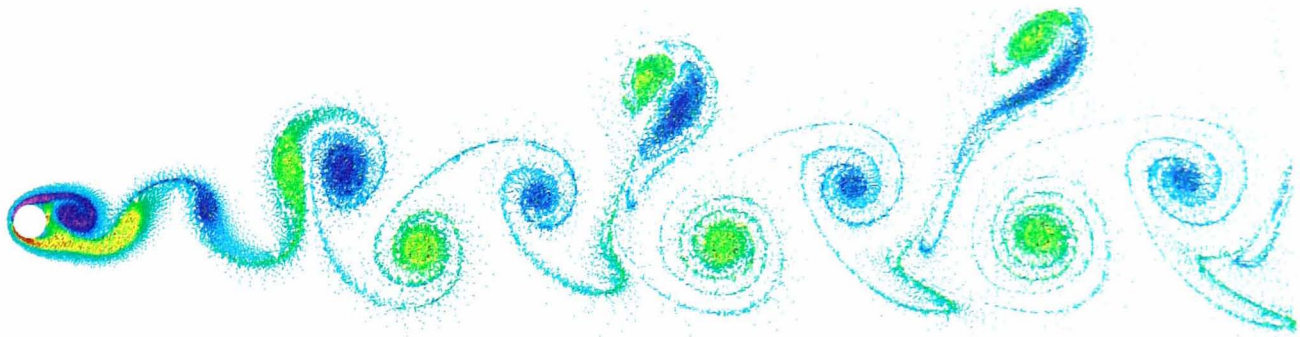

(a) x_e/d=0.30, f_e/f_0=0.5;
St_1=0.186, St_2=0.090, C_D=1.42, $C_{L(rms)}$=0.45.

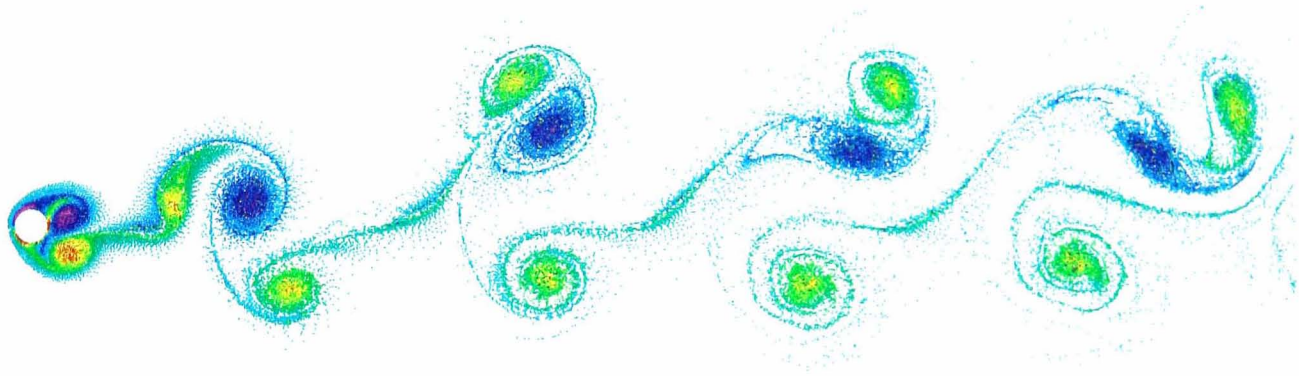

(b) x_e/d=0.30, f_e/f_0=1.1;
St_1=0.105, St_2=0.315, C_D=1.50, $C_{L(rms)}$=0.80, ϕ_L=65.

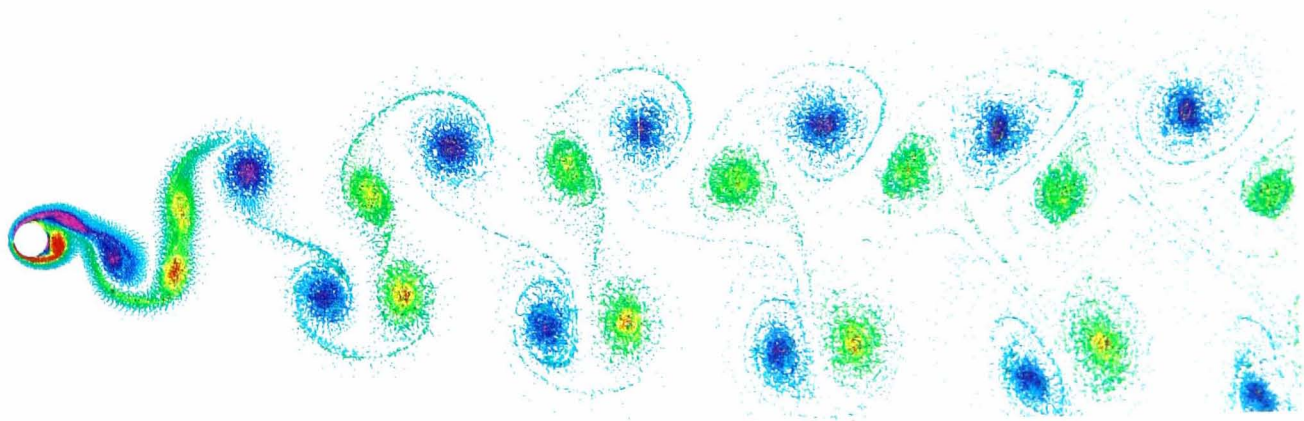

(c) x_e/d=0.30, f_e/f_0=1.5;
St_1=0.144, St_2=0.430, C_D=2.09, $C_{L(rms)}$=1.20, ϕ_L=90.

Figure 6.9 Effect of in-line oscillations on vortex shedding; Circular cylinder; x_e/d=0.30.

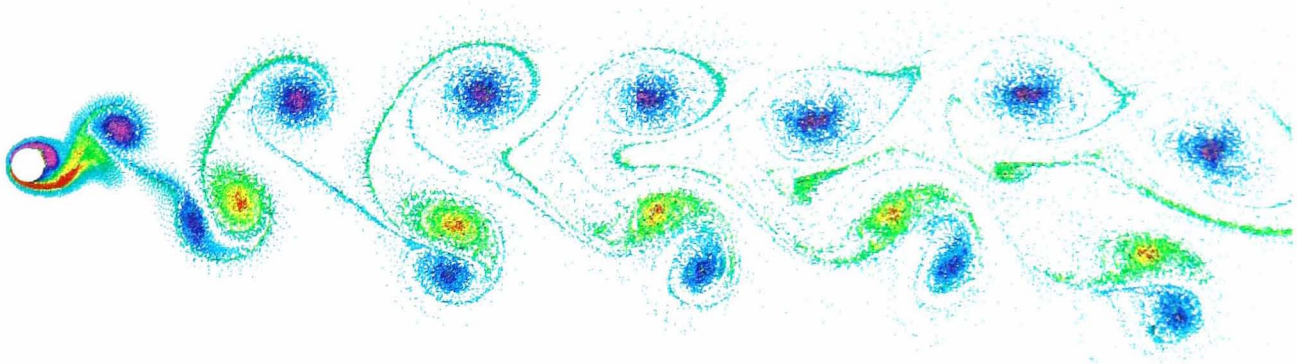

(d) x_e/d=0.30, f_e/f_0=1.6;
St_1=0.154, St_2=0.458, C_D=2.13, $C_{L(rms)}$=1.20, ϕ_L=100.

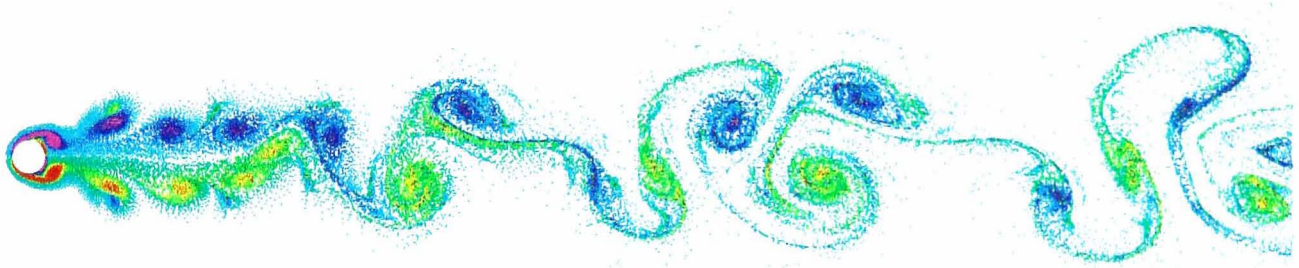

(e) x_e/d=0.30, f_e/f_0=1.8;
C_D=1.31, $C_{L(rms)}$=0.02.

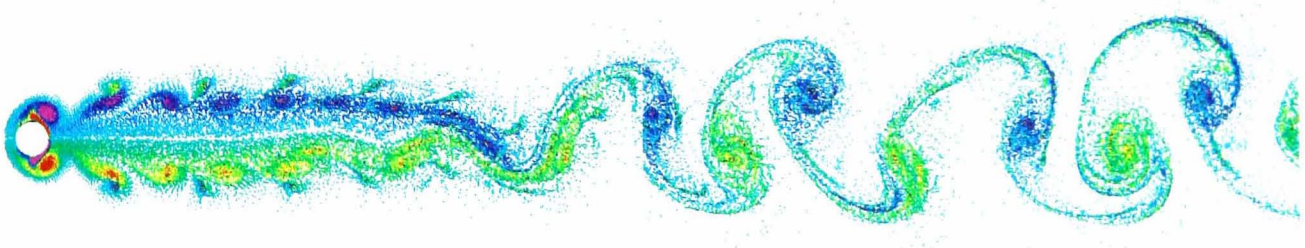

(f) x_e/d=0.30, f_e/f_0=2.2;
C_D=1.29, $C_{L(rms)}$=0.02.

Figure 6.9 (cont) Effect of in-line oscillations on vortex shedding; Circular cylinder; x_e/d=0.30.

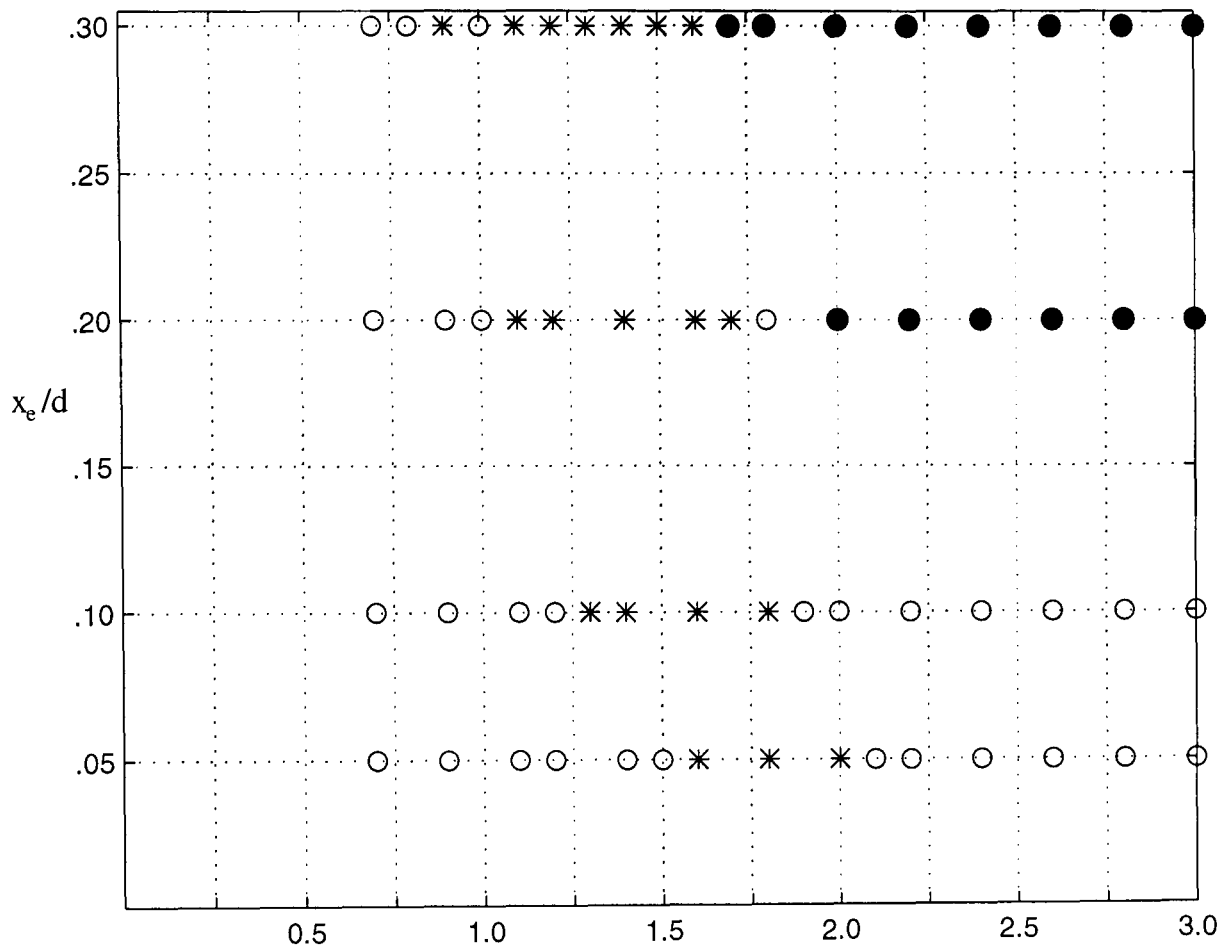

Figure 6.10 Shedding regimes for diamond cylinder.

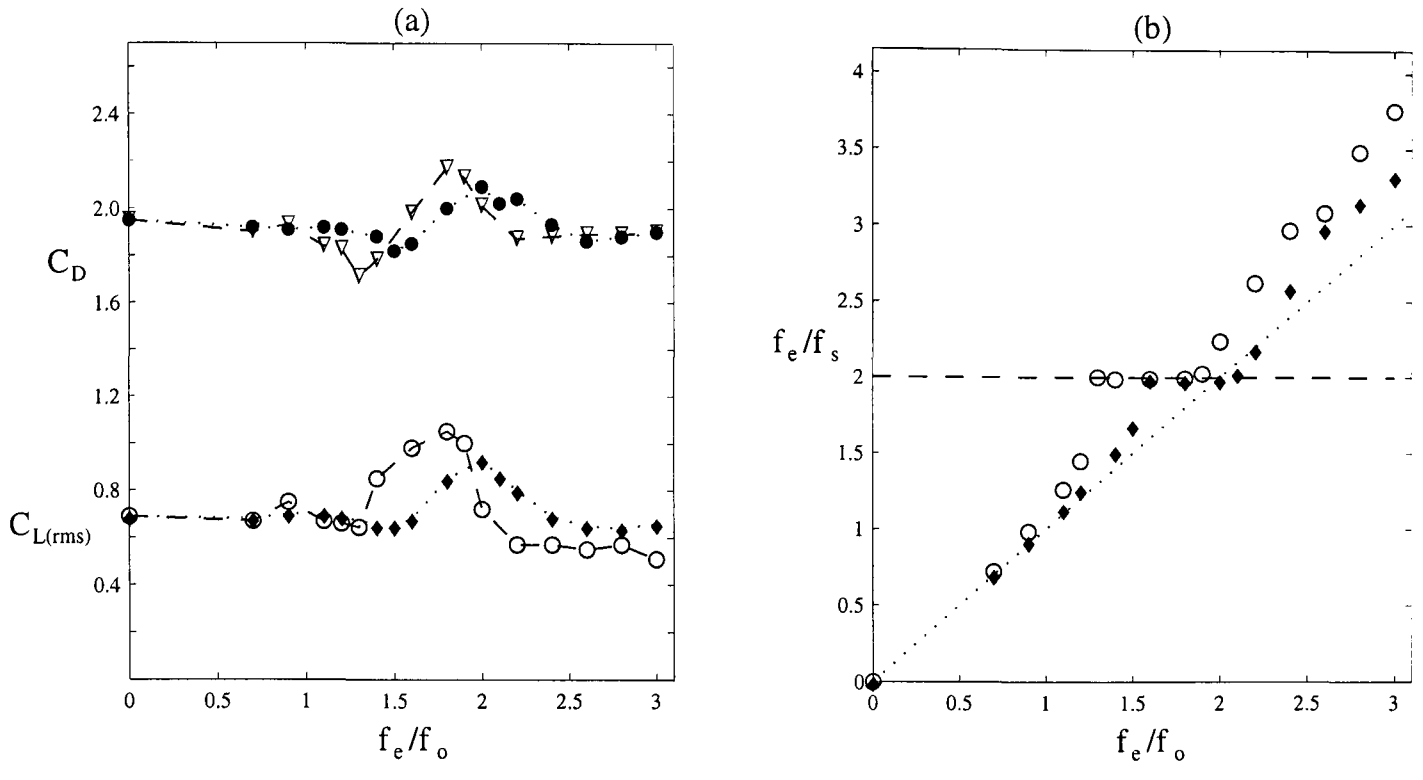

(a) $C_{L(rms)}$ vs. f_e/f_0, ♦ - x_e/d=0.05, o -x_e/d=0.10
C_D vs. f_e/f_0, • - x_e/d=0.05, ∇ - x_e/d=0.10
(b) f_e/f_s vs. f_e/f_0, ♦ - x_e/d=0.05, o - x_e/d=0.10

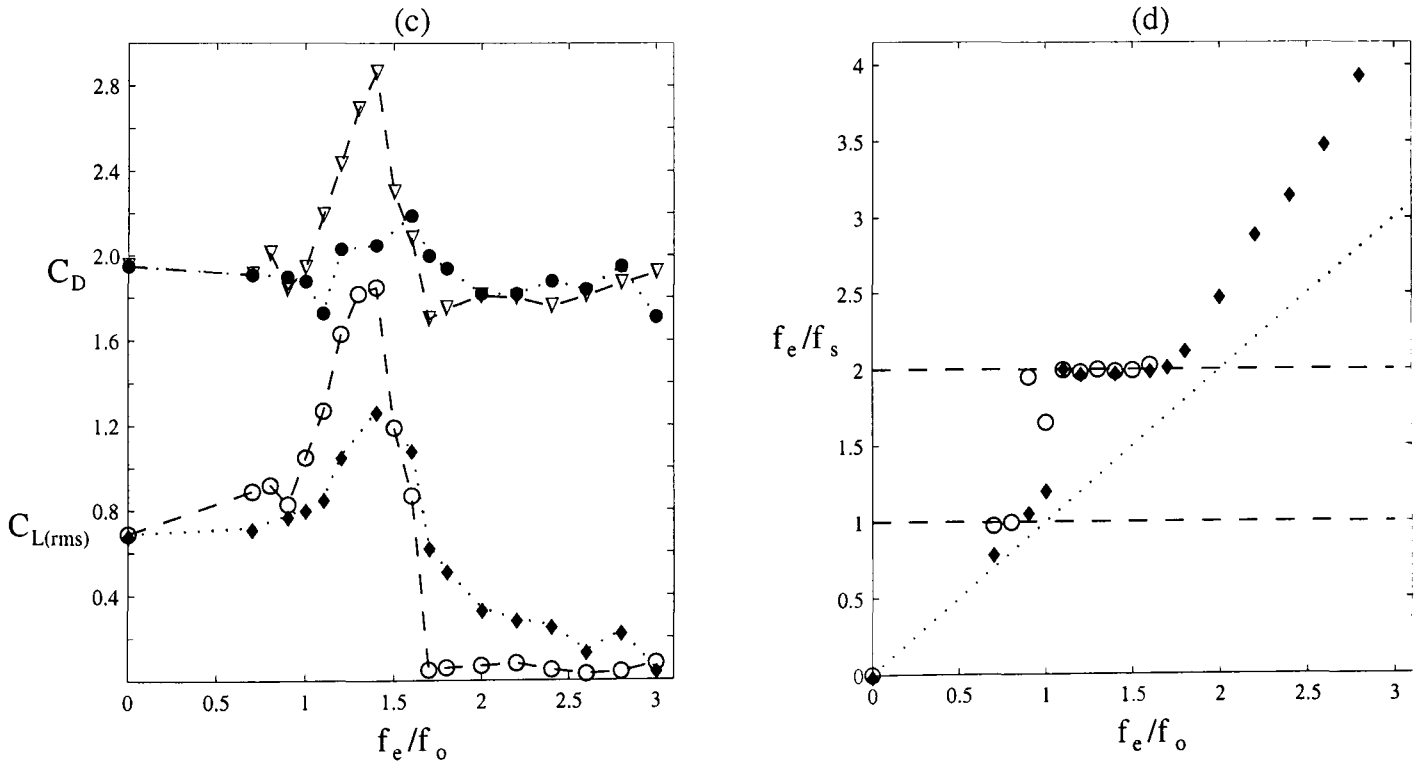

(c) $C_{L(rms)}$ vs. f_e/f_0, ♦ - x_e/d=0.20, o -x_e/d=0.30
C_D vs. f_e/f_0, • - x_e/d=0.20, ∇ - x_e/d=0.30
(d) f_e/f_s vs. f_e/f_0, ♦ - x_e/d=0.20, o - x_e/d=0.30

Figure 6.11 Effect of in-line oscillations on mean forces and shedding frequencies; Diamond cylinder.

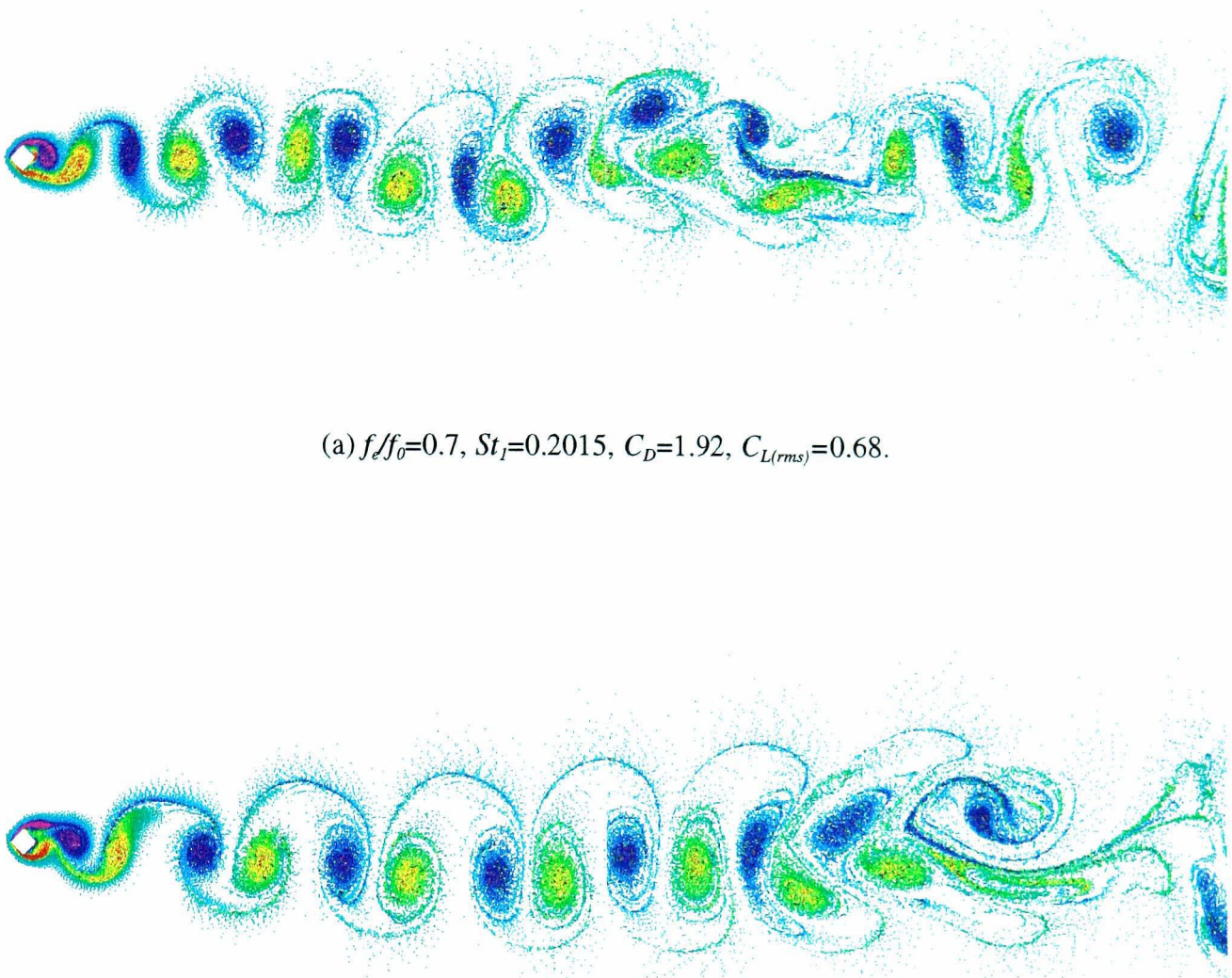

(a) f_e/f_0=0.7, St_1=0.2015, C_D=1.92, $C_{L(rms)}$=0.68.

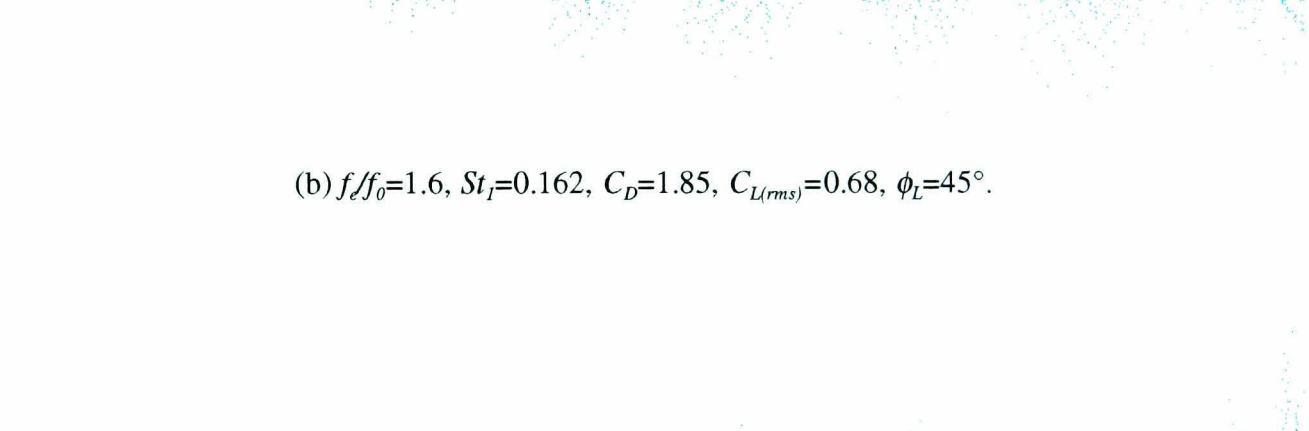

(b) f_e/f_0=1.6, St_1=0.162, C_D=1.85, $C_{L(rms)}$=0.68, ϕ_L=45°.

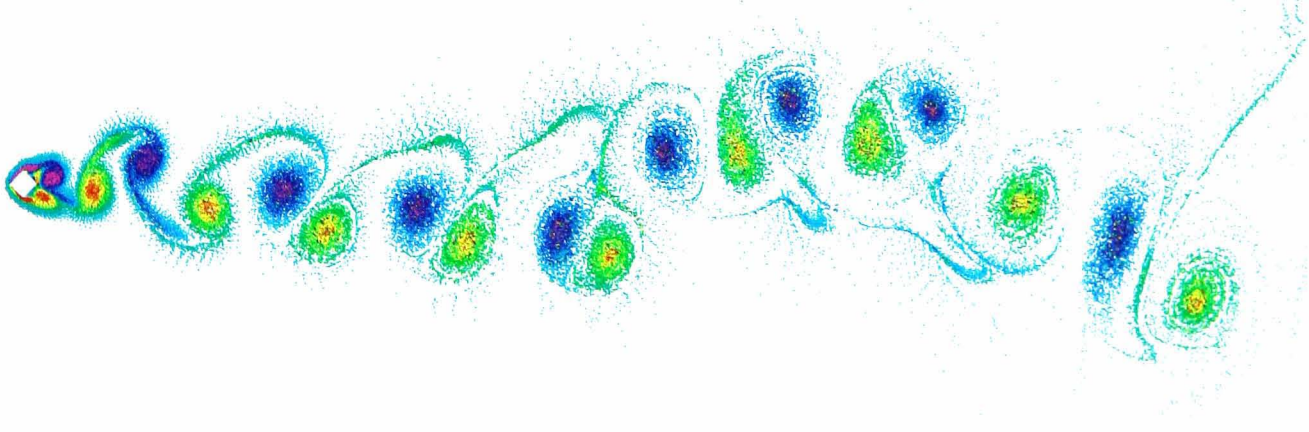

(c) f_e/f_0=2.8, St_1=0.179, C_D=1.88, $C_{L(rms)}$=0.64.

Figure 6.12 Effect of in-line oscillations on vortex shedding; diamond cylinder; x/d=0.05.

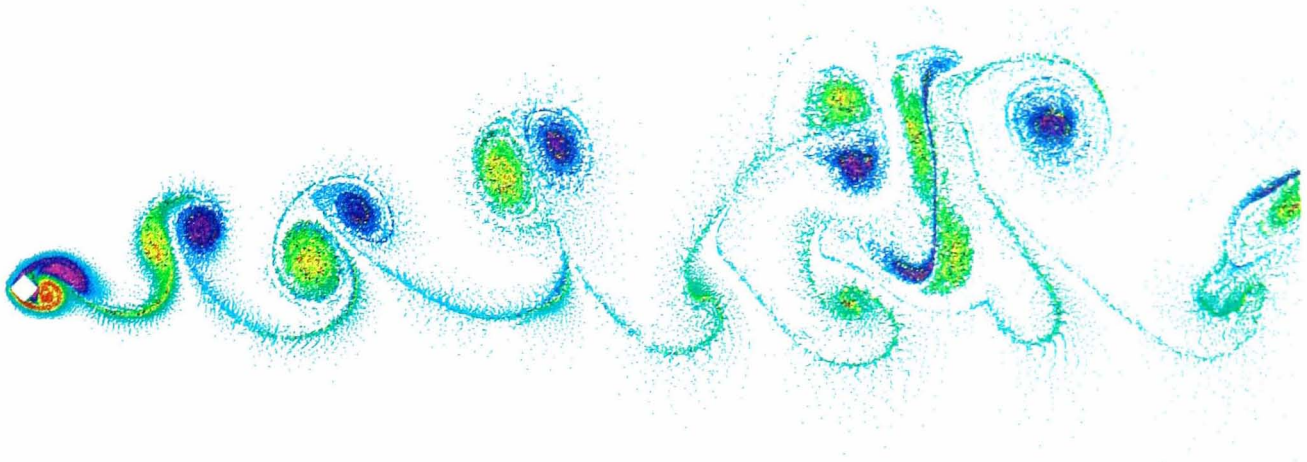

(a) f_e/f_0=0.7, St_1=0.144, C_D=1.91, $C_{L(rms)}$=0.89.

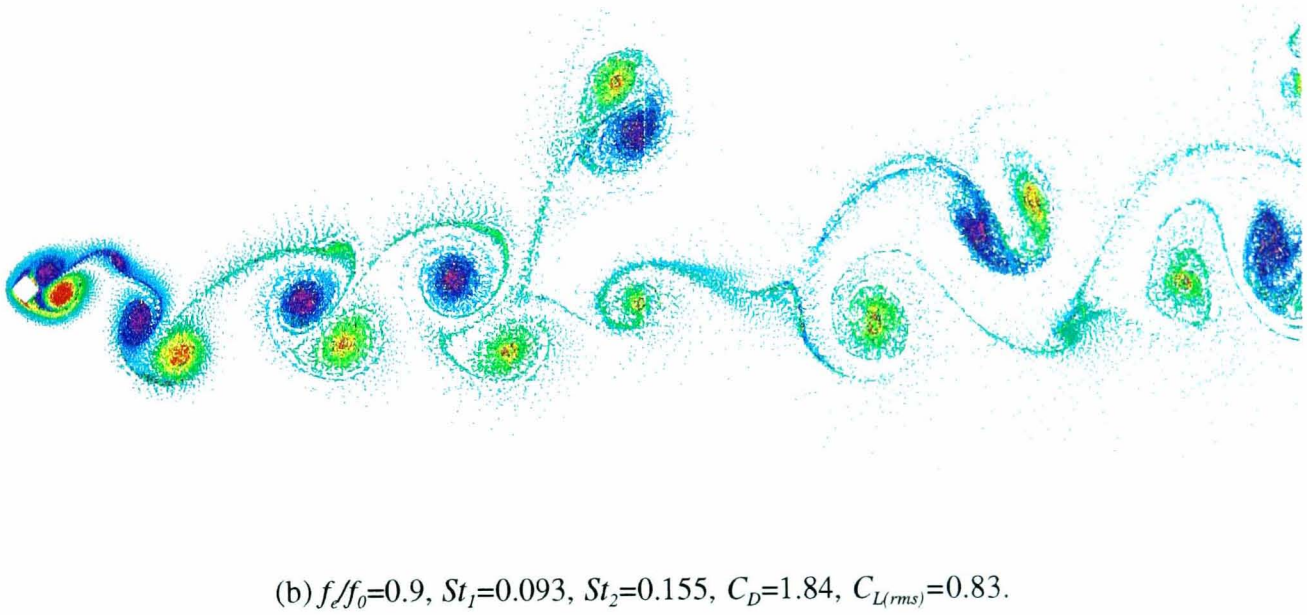

(b) f_e/f_0=0.9, St_1=0.093, St_2=0.155, C_D=1.84, $C_{L(rms)}$=0.83.

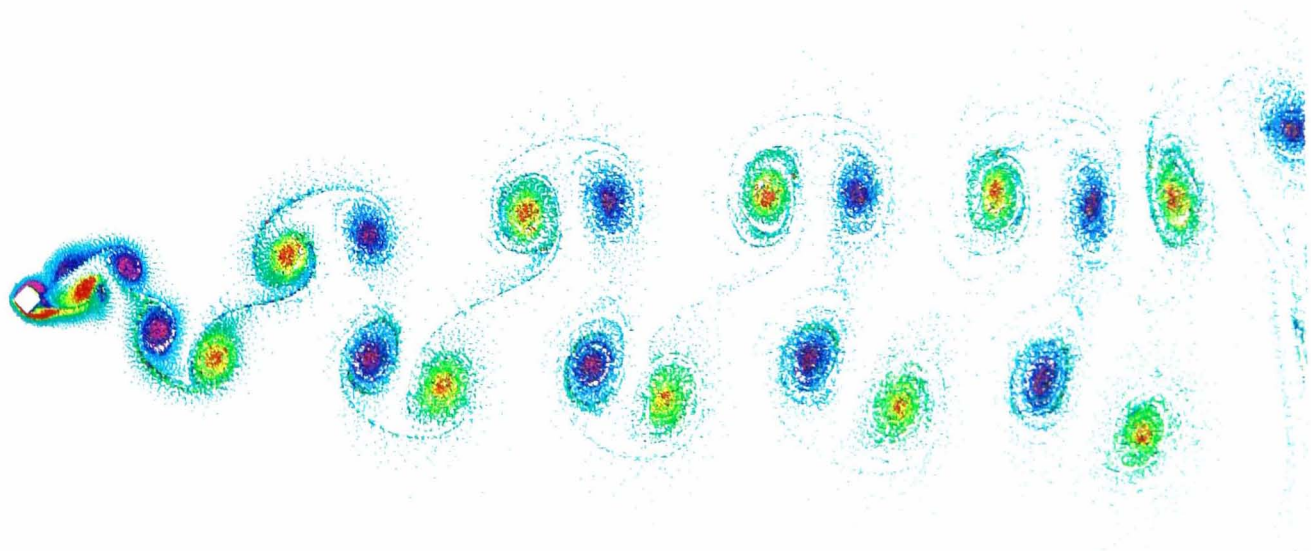

(c) f_e/f_0=1.1, St_1=0.111, St_2=0.336, C_D=2.19, $C_{L(rms)}$=1.27, ϕ_L=30°.

Figure 6.13 Effect of in-line oscillations on vortex shedding; Diamond cylinder; x/d=0.30.

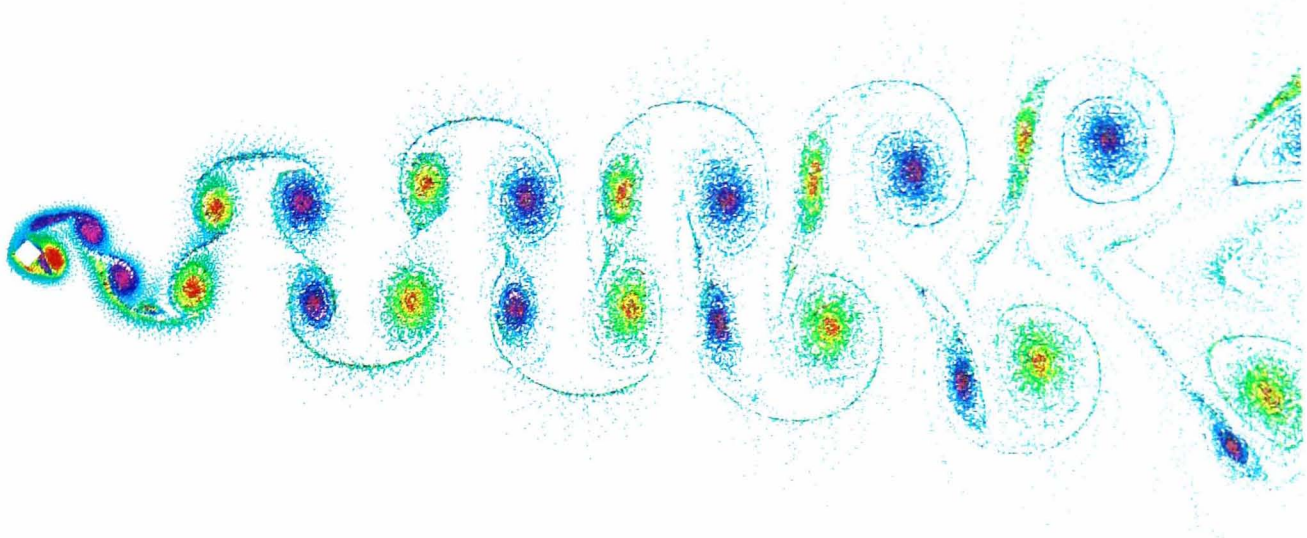

(d) f_e/f_0=1.2, St_1=0.142, St_2=0.425, C_D=2.24, $C_{L(rms)}$=1.65, ϕ_L=60°.

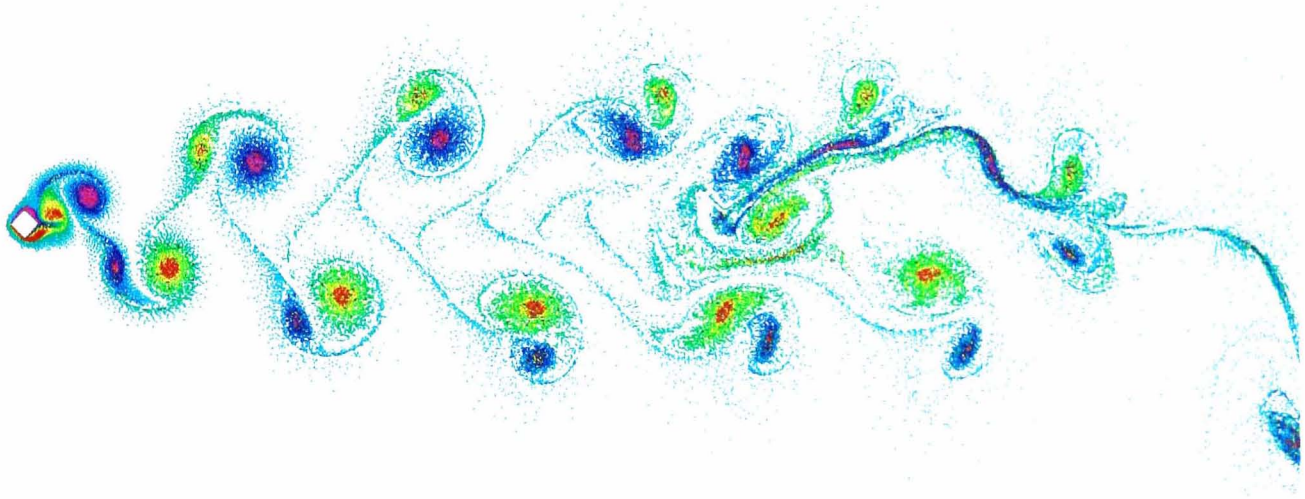

(e) f_e/f_0=1.4, St_1=0.159, St_2=0.485, C_D=2.08, $C_{L(rms)}$=0.87, ϕ_L=100°.

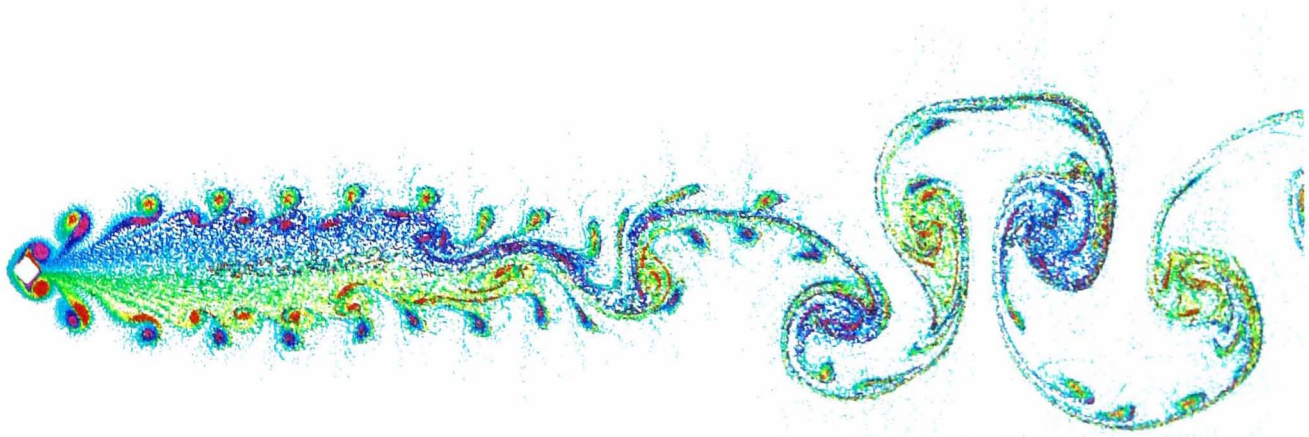

(f) f_e/f_0=2.4, C_D=1.76, $C_{L(rms)}$=0.05.

Figure 6.13 (cont) Effect of in-line oscillations on vortex shedding; Diamond cylinder; x/d=0.30.

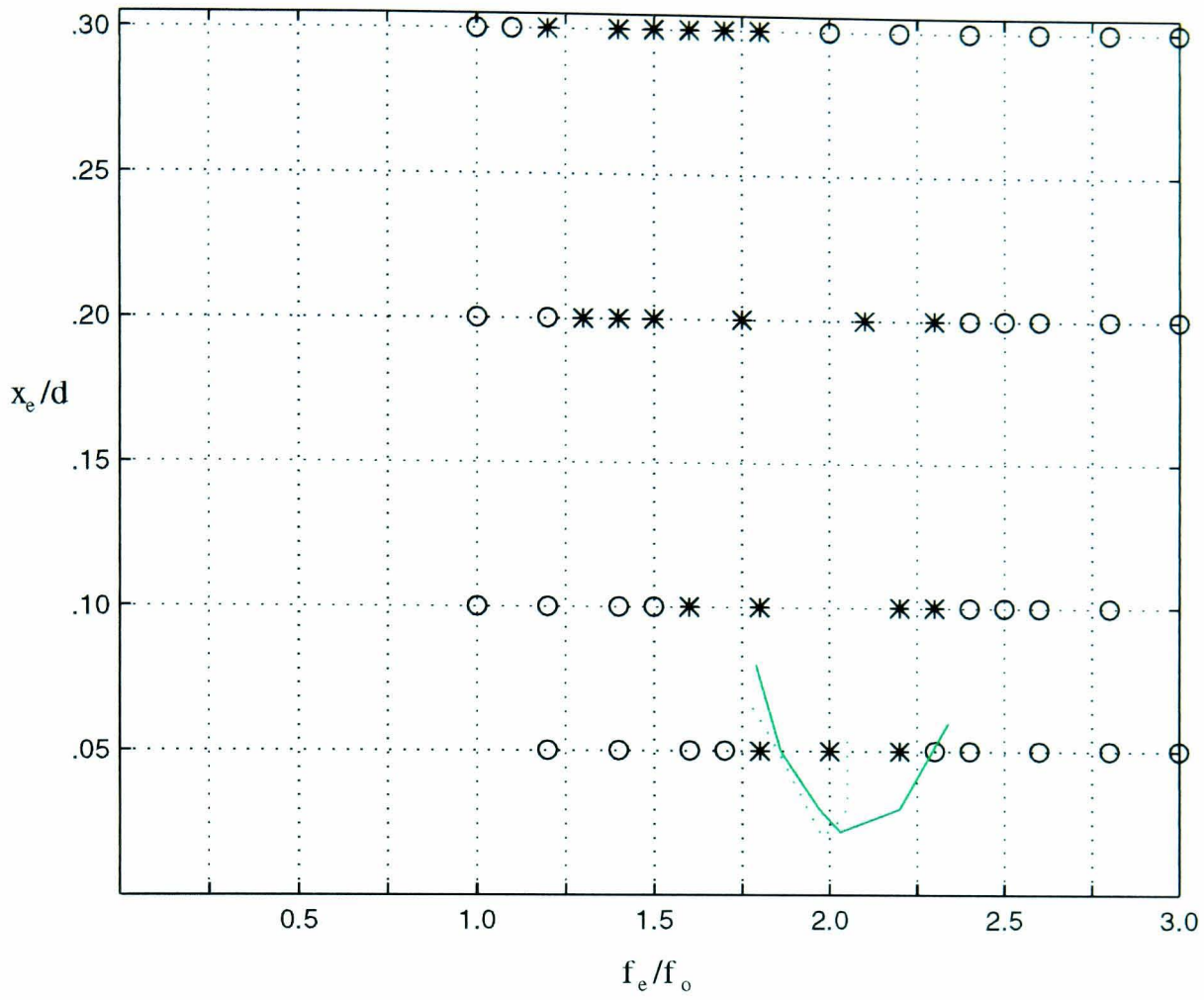

Figure 6.14 Shedding regimes for rectangular cylinder, *B/A*=0.62.

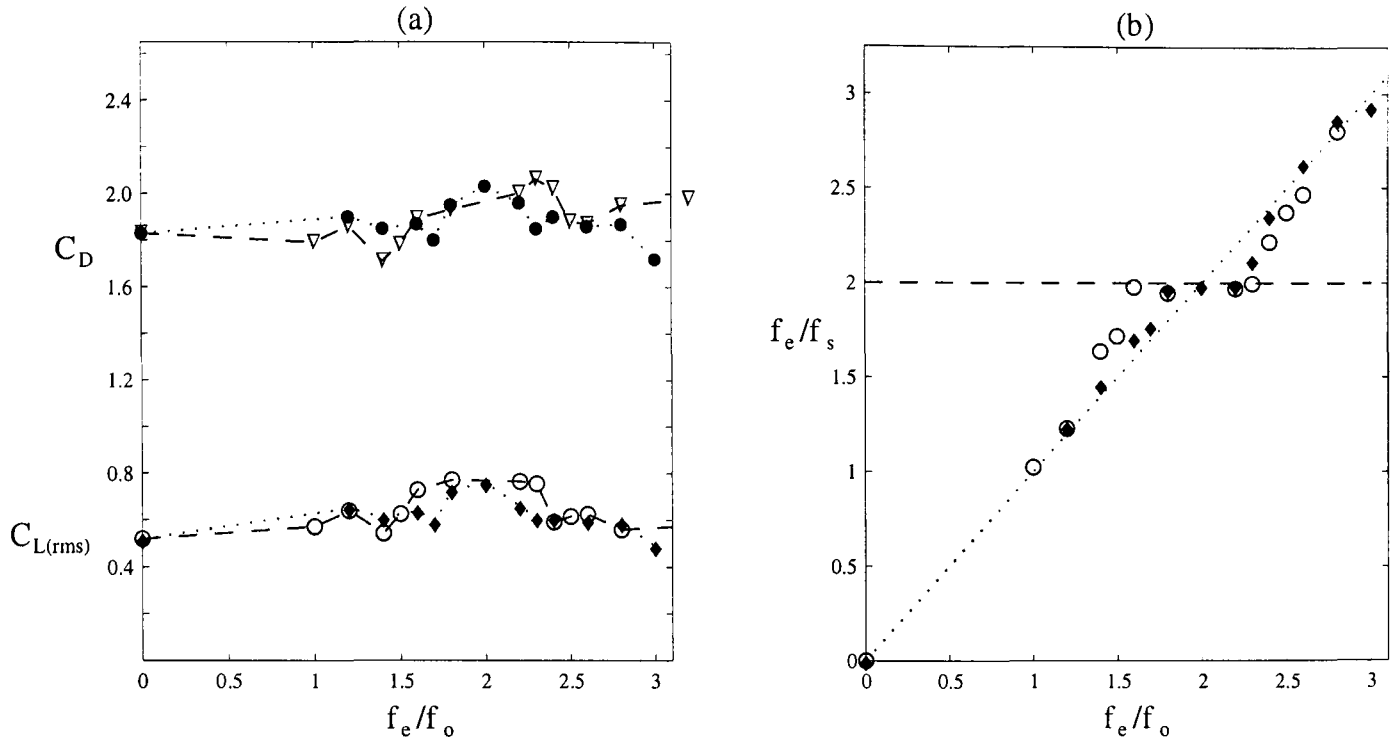

(a) $C_{L(rms)}$ vs. f_e/f_0, ♦ - x_e/d=0.05, o -x_e/d=0.10
C_D vs. f_e/f_0, • - x_e/d=0.05, ∇ - x_e/d=0.10
(b) f_e/f_s vs. f_e/f_0, ♦ - x_e/d=0.05, o - x_e/d=0.10

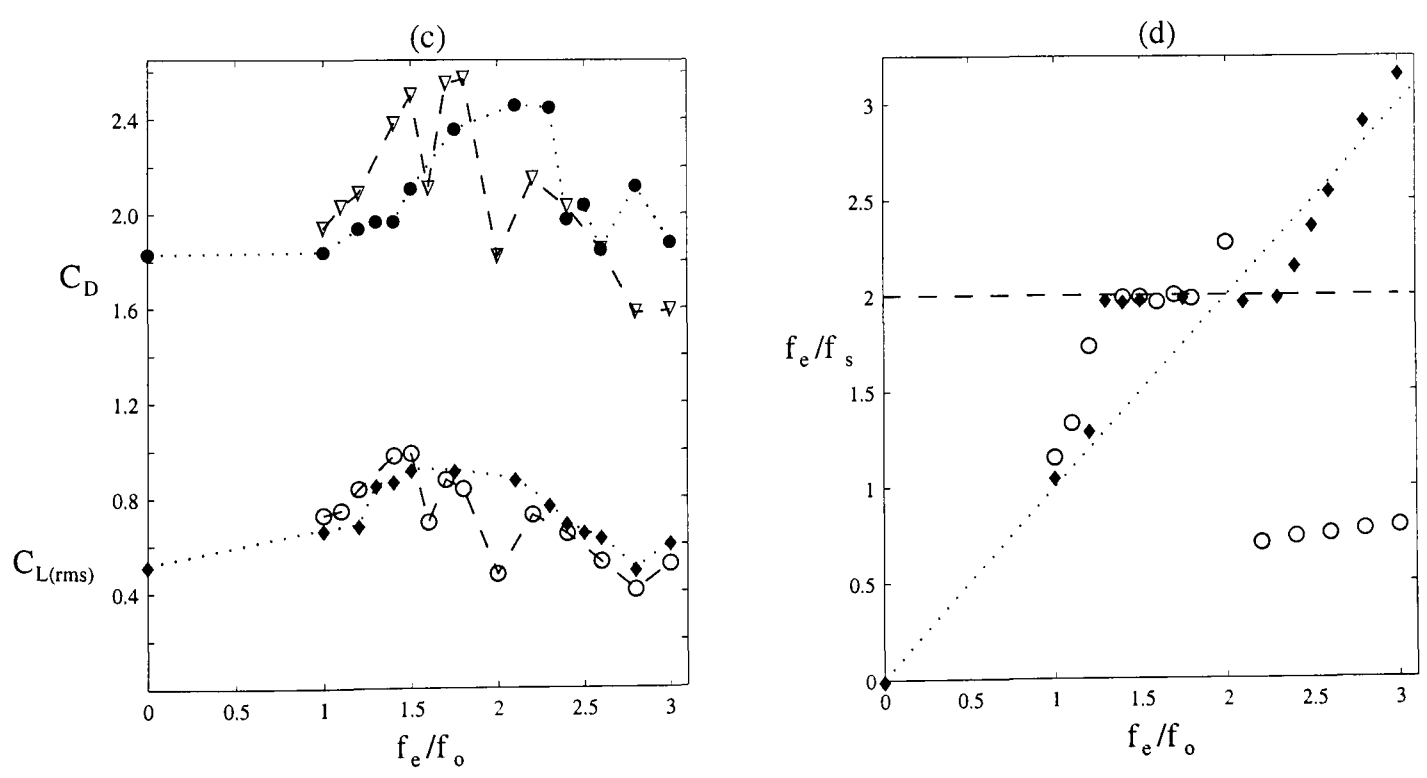

(c) $C_{L(rms)}$ vs. f_e/f_0, ♦ - x_e/d=0.20, o -x_e/d=0.30
C_D vs. f_e/f_0, • - x_e/d=0.20, ∇ - x_e/d=0.30
(d) f_e/f_s vs. f_e/f_0, ♦ - x_e/d=0.20, o - x_e/d=0.30

Figure 6.15 Effect of in-line oscillations on mean forces and shedding frequencies; B/A=0.62 cylinder.

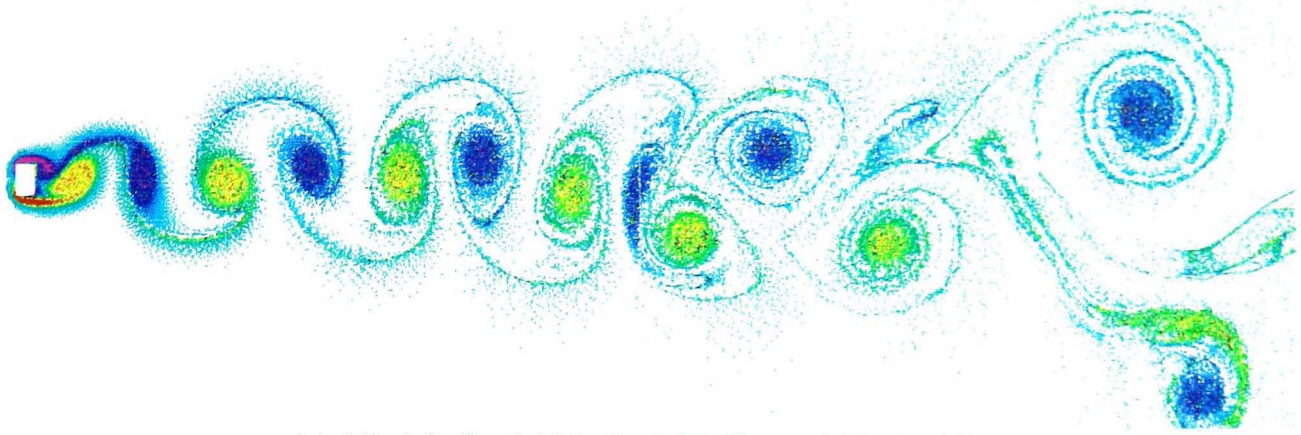

(a) f_e/f_0=1.8, St_1=0.157, C_D=1.95, $C_{L(rms)}$=0.73, ϕ_L=42°.

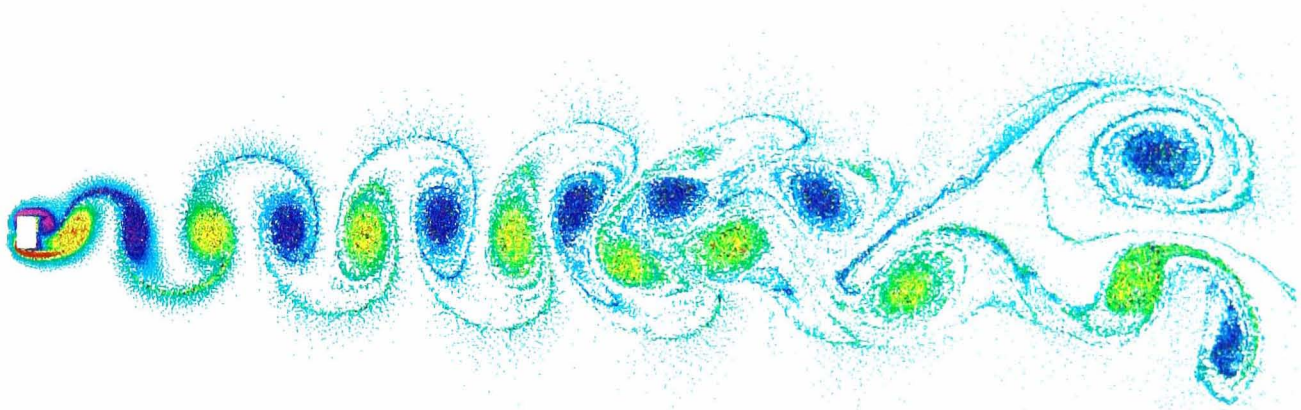

(b) f_e/f_0=2.0, St_1=0.173, C_D=2.03, $C_{L(rms)}$=0.76, ϕ_L=67°.

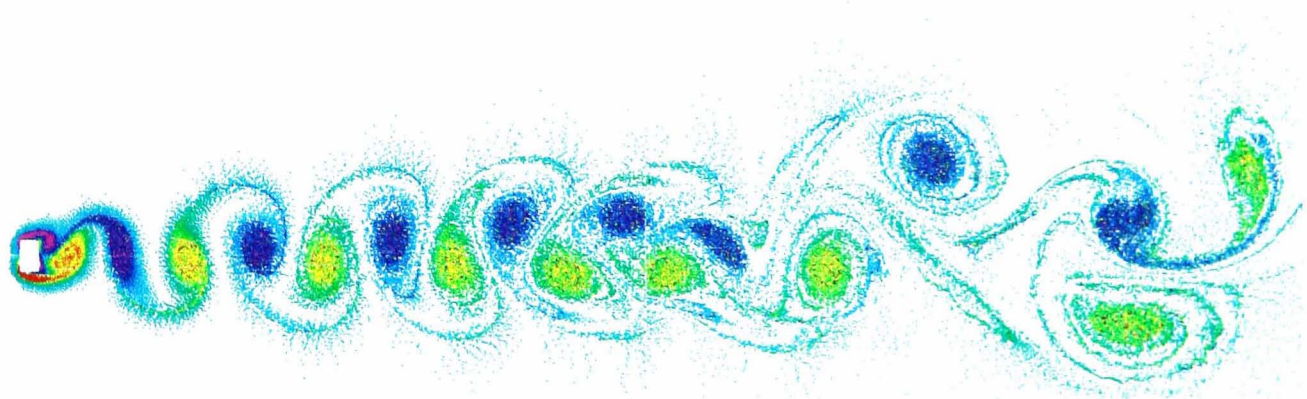

(c) f_e/f_0=2.2, St_1=0.190, C_D=1.96, $C_{L(rms)}$=0.66, ϕ_L=113°.

Figure 6.16 Effectof in-line oscillations on vortex shedding; B/A=0.62 cylinder; x_e/d=0.05.

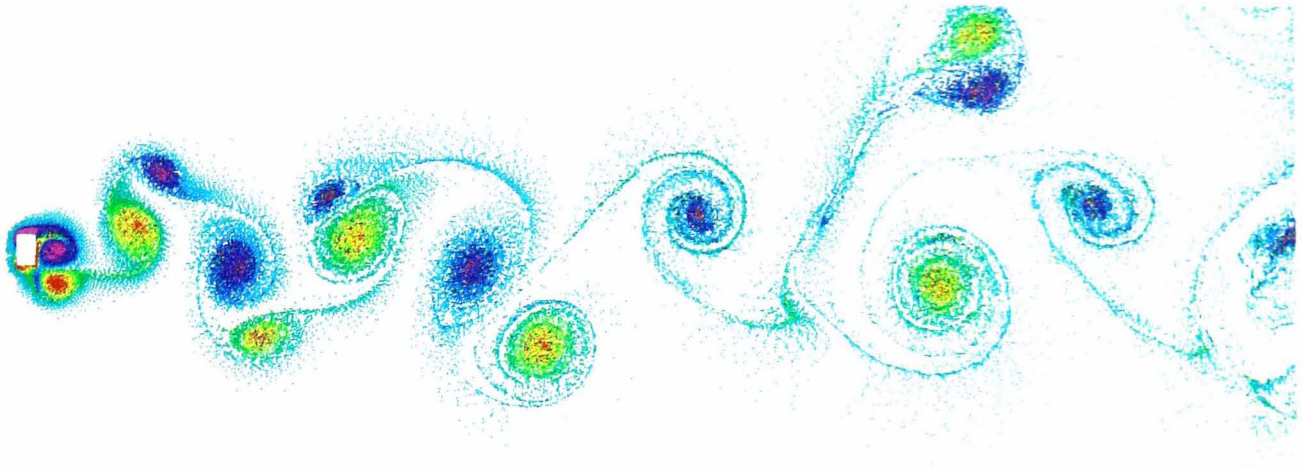

(a) f_e/f_0=1.2, St_1=0.119, C_D=2.09, $C_{L(rms)}$=0.84, ϕ_L=60°.

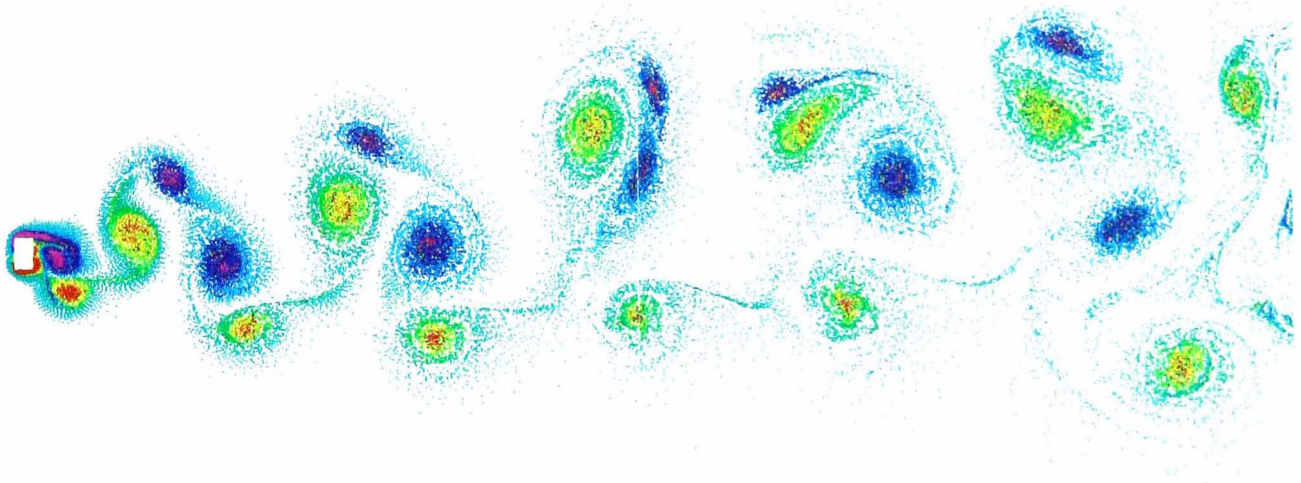

(b) f_e/f_0=1.4, St_1=0.121, St_2=0.368, C_D=2.38, $C_{L(rms)}$=0.98, ϕ_L=75°.

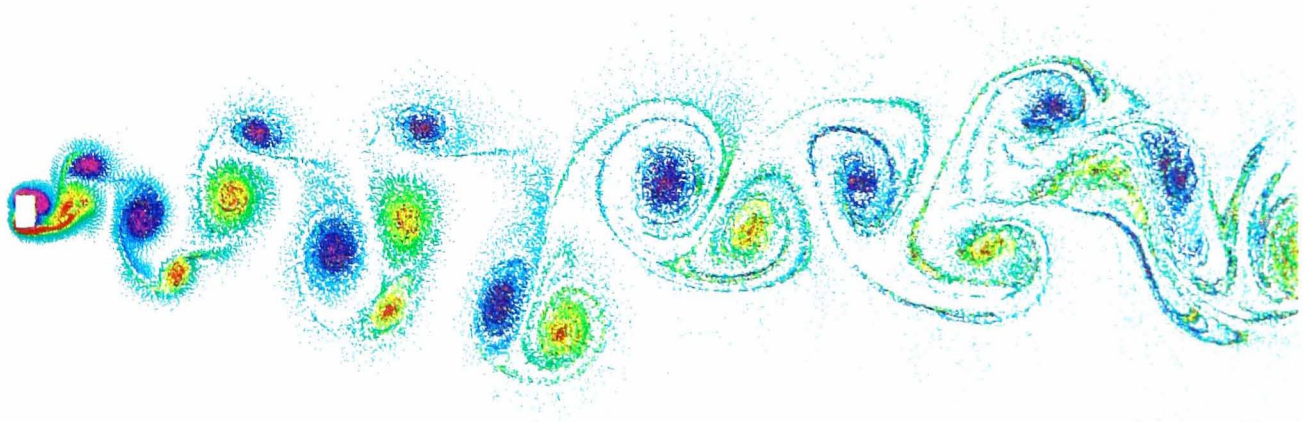

(c) f_e/f_0=1.6, St_1=0.140, St_2=0.416, C_D=2.11, $C_{L(rms)}$=0.70, ϕ_L=80°.

Figure 6.17 Effect of in-line oscillations on vortex shedding; B/A=0.62 cylinder; x/d=0.30.

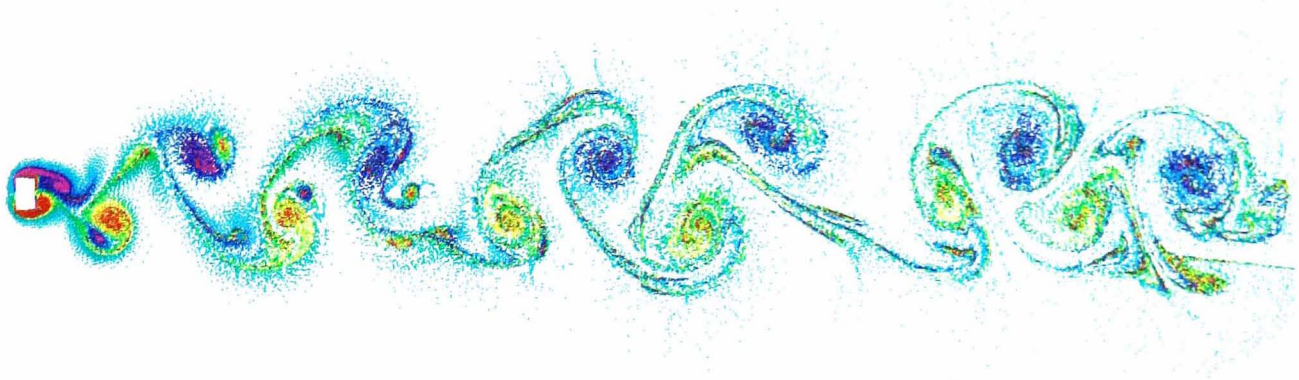

(d) f_e/f_0=1.8, St_1=0.130, St_2=0.442, C_D=1.50, $C_{L(rms)}$=0.25.

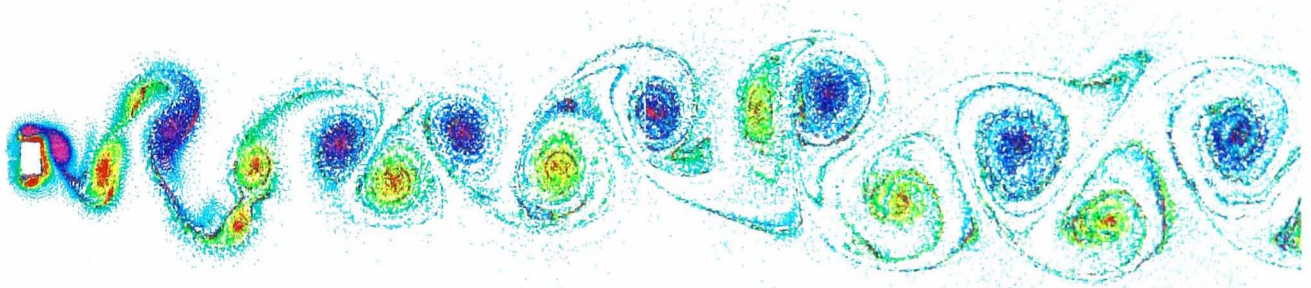

(e) f_e/f_0=2.2, St_1=0.537, St_2=0.225, C_D=2.15, $C_{L(rms)}$=0.73.

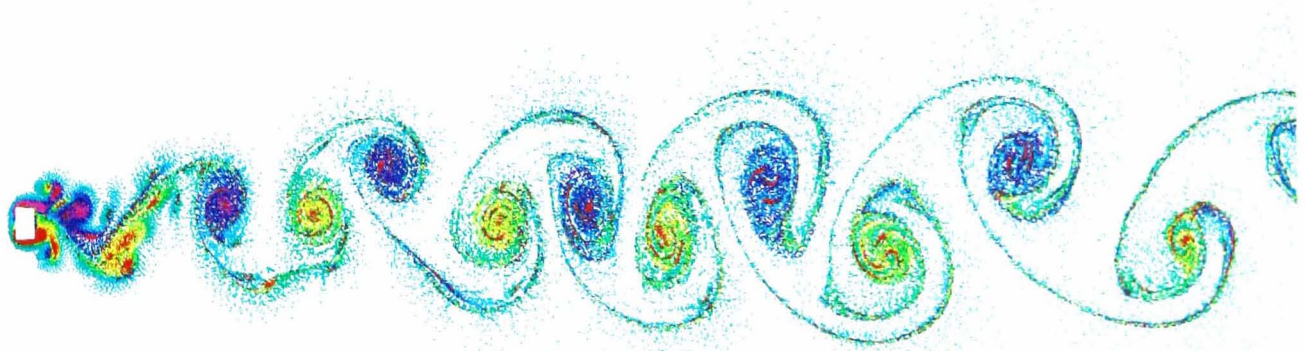

(f) f_e/f_0=2.8, St_1=0.621, St_2=0.144, C_D=1.58, $C_{L(rms)}$=0.41.

Figure 6.17 (cont) Effect of in-line oscillations on vortex shedding; B/A=0.62 cylinder; x/d=0.30.

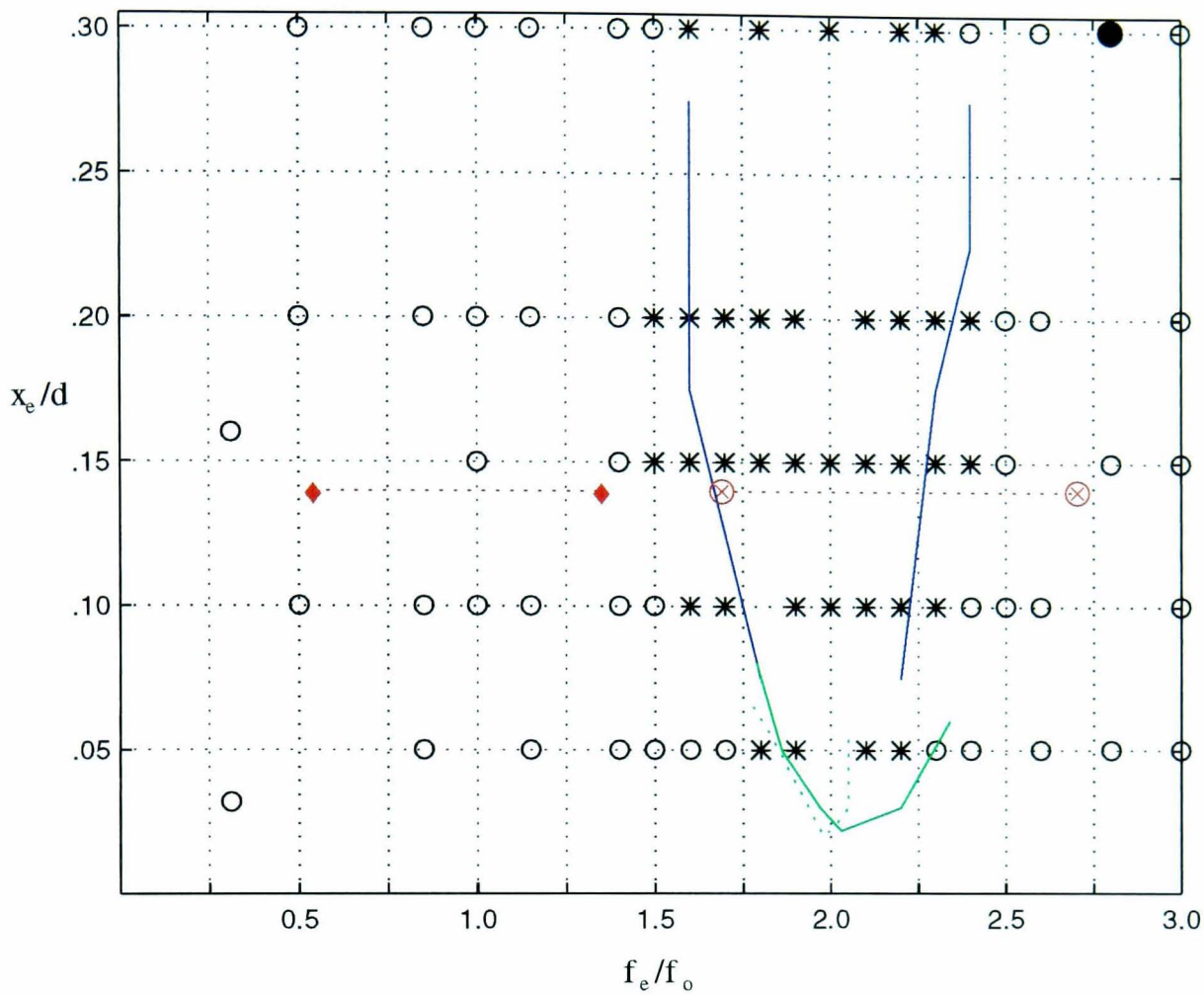

● – Quasi–Symmetric shedding

✳ – Asymmetric synchronisation

○ – Outside synchronisation regimes

——— – Minewitsch et al (1995), B/A=1.0, Re=200

⊗ · · · ⊗ – Okajima et al (1993), B/A=1.0, Re=1000, f_e/f_s =2.0

♦ · · · ♦ – Okajima et al (1993), B/A=1.0, Re=1000, f_e/f_s =1.0

——— – Al–Asmi and Castro (1992), B/A=0.67, Re=7000–50000

. . . . . – Al–Asmi and Castro (1992), Flat plate, Re=7000–50000

Figure 6.18 Shedding regimes for rectangular cylinder, *B/A*=1.0.

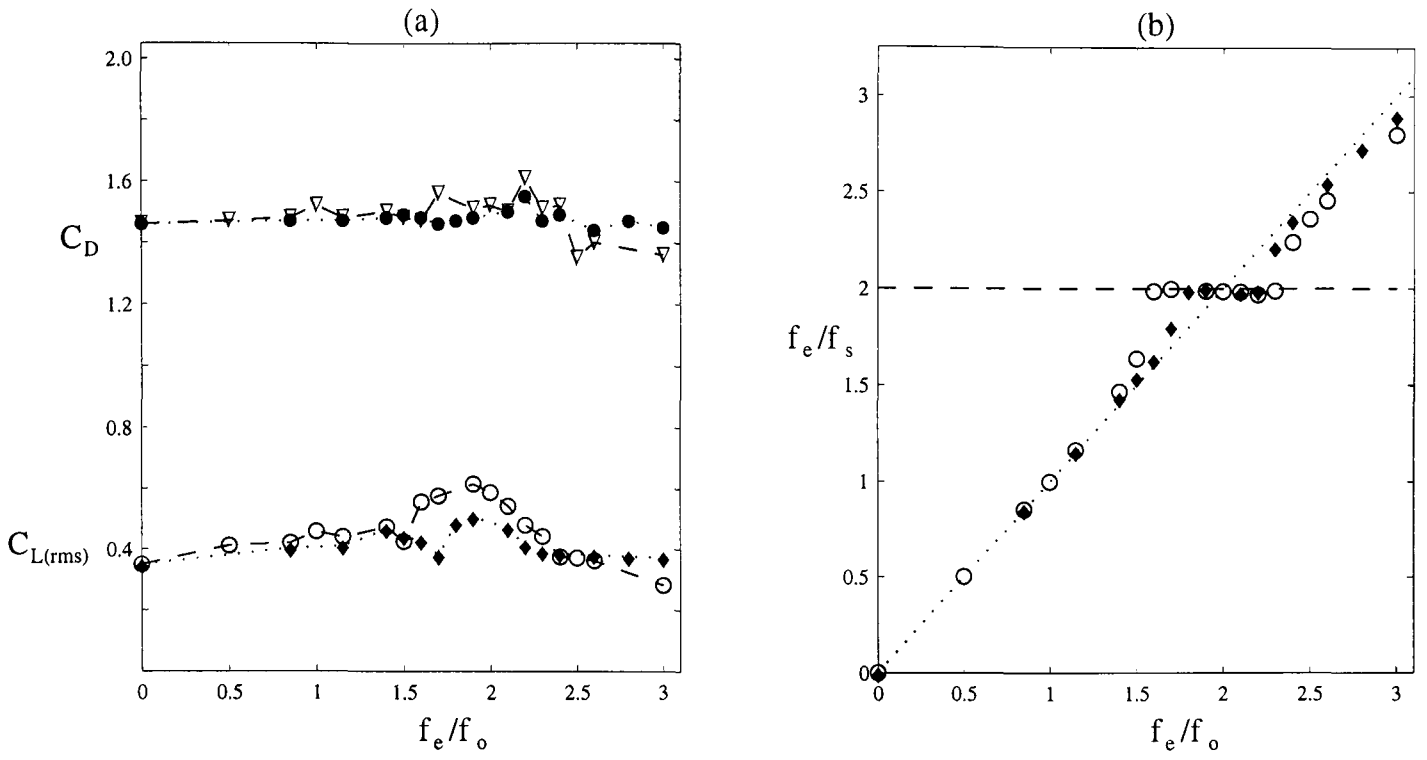

(a) $C_{L(rms)}$ vs. f_e/f_0, ♦ - x_e/d=0.05, o -x_e/d=0.10
C_D vs. f_e/f_0, • - x_e/d=0.05, ∇ - x_e/d=0.10
(b) f_e/f_s vs. f_e/f_0, ♦ - x_e/d=0.05, o - x_e/d=0.10

(c) $C_{L(rms)}$ vs. f_e/f_0, ♦ - x_e/d=0.15, o -x_e/d=0.20
C_D vs. f_e/f_0, • - x_e/d=0.15, ∇ - x_e/d=0.20
(d) f_e/f_s vs. f_e/f_0, ♦ - x_e/d=0.15, o - x_e/d=0.20

Figure 6.19 Effect of in-line oscillations on mean forces and shedding frequencies; B/A=1.0 cylinder.

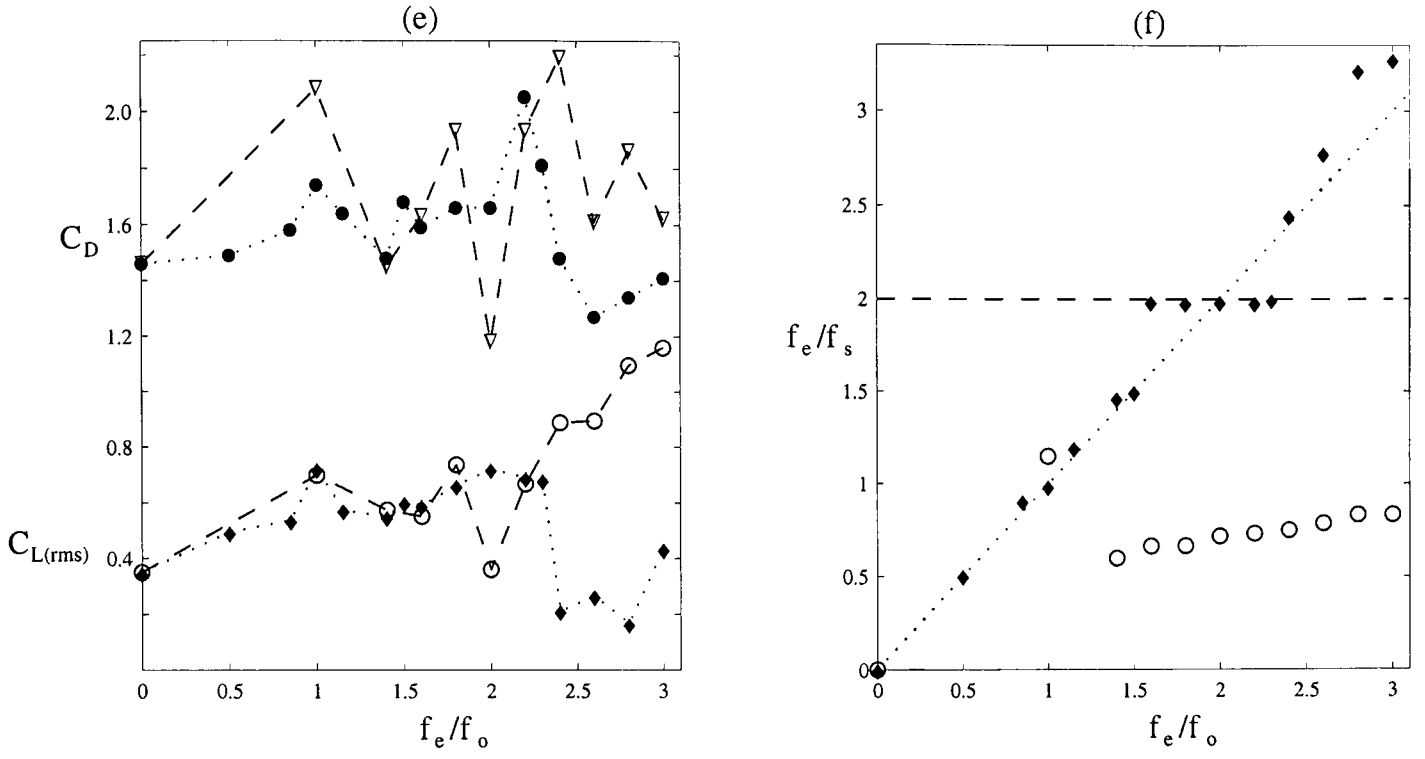

(e) $C_{L(rms)}$ vs. f_e/f_0, ♦ - x_e/d=0.30, o -x_e/d=0.50
C_D vs. f_e/f_0, • - x_e/d=0.30,∇ - x_e/d=0.50
(f) f_e/f_s vs. f_e/f_0, ♦ - x_e/d=0.30, o - x_e/d=0.50

Figure 6.19(cont) Effect of in-line oscillations on mean forces and shedding frequencies; *B/A*=1.0 cylinder.

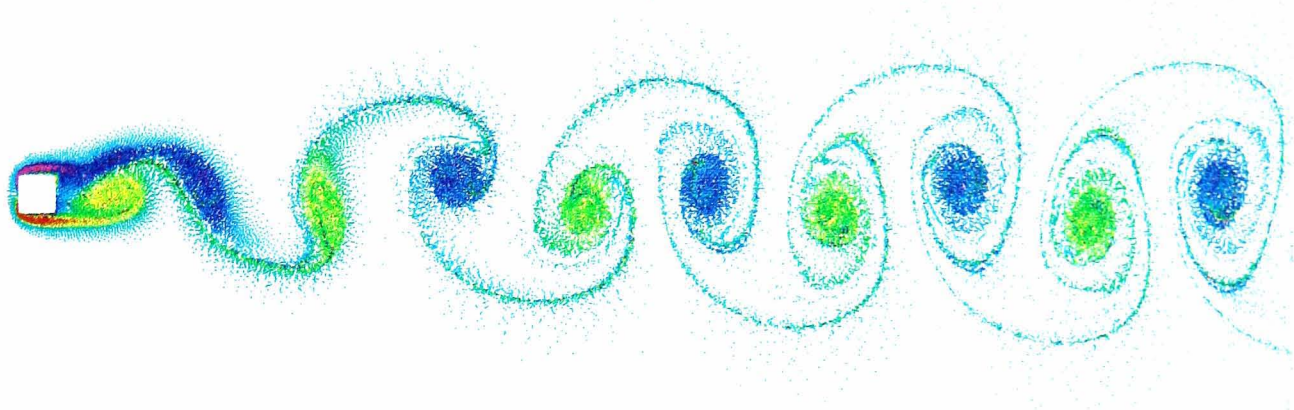

(a) f_e/f_0=1.7, St_1=0.141, C_D=1.48, $C_{L(rms)}$=0.43.

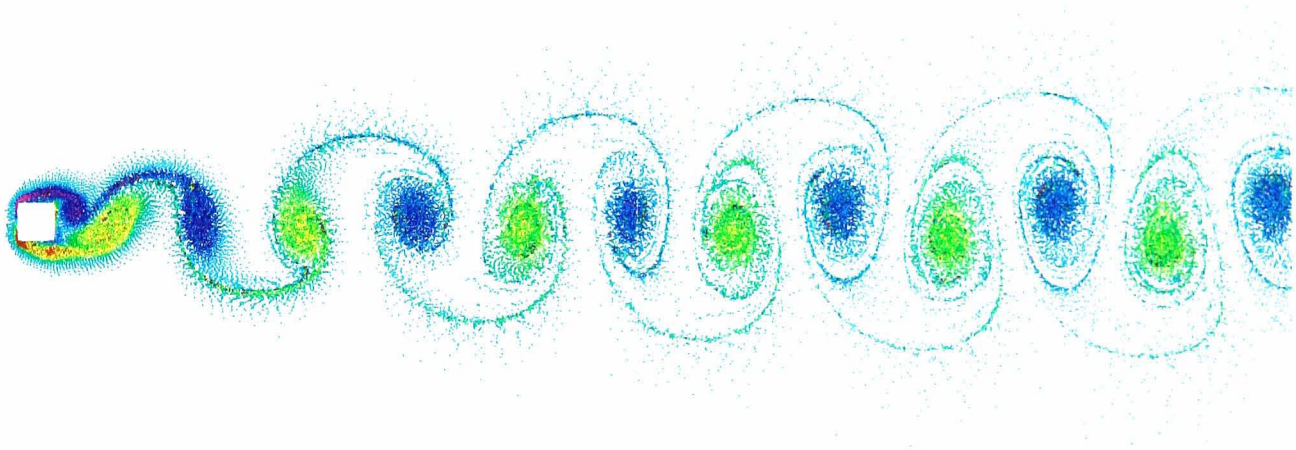

(b) f_e/f_0=2.0, St_1=0.154, C_D=1.56, $C_{L(rms)}$=0.58, ϕ_L=120°.

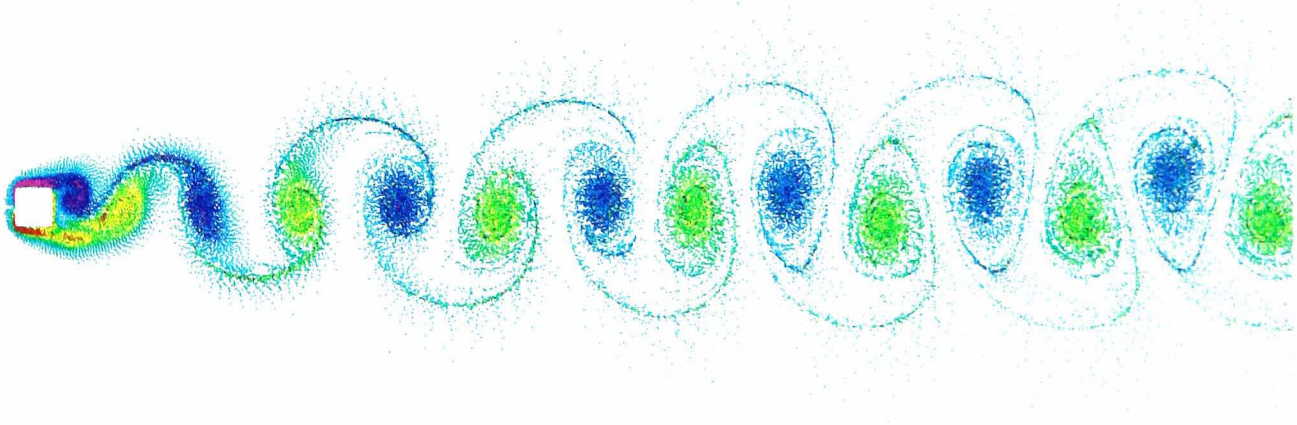

(c) f_e/f_0= 2.2, St_1=0.172, St_2=0.513, C_D=1.61, $C_{L(rms)}$=0.48, ϕ_L=225°.

Figure 6.20 Effect of in-line oscillations on vortex shedding; B/A=1.0 cylinder; x_e/d=0.10.

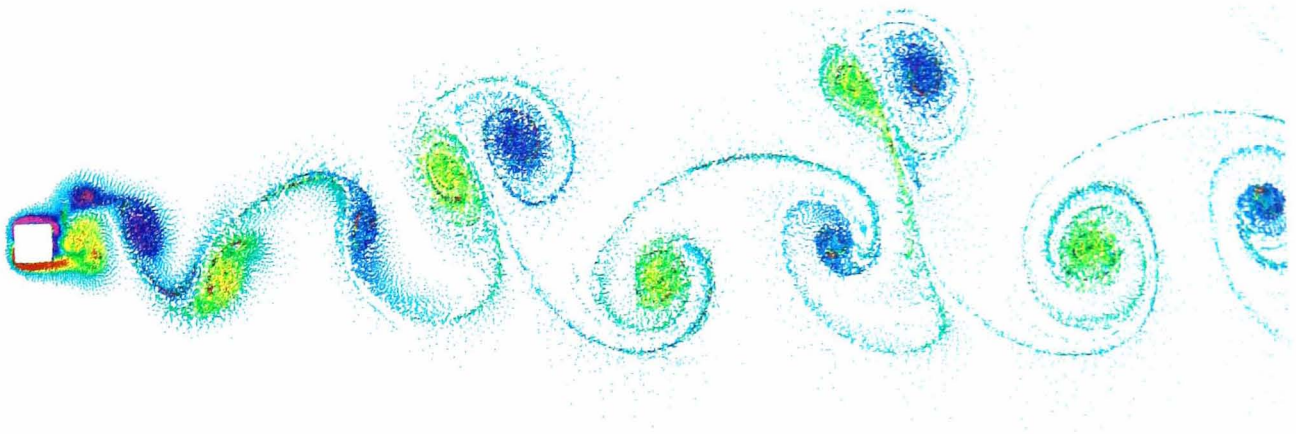

(a) f_e/f_0=1.5, St_1=0.154, St_2=0.386, C_D=1.68, $C_{L(rms)}$=0.60.

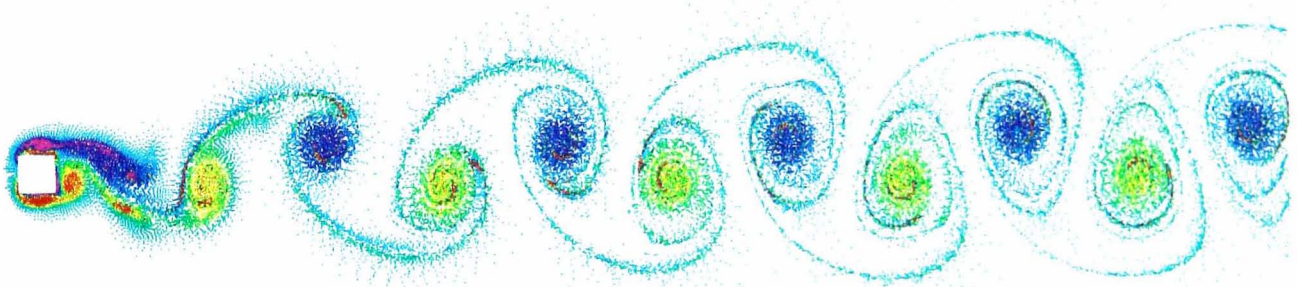

(b) f_e/f_0=1.8, St_1=0.140, St_2=0.417, C_D=1.66, $C_{L(rms)}$=0.66, ϕ_L=90°.

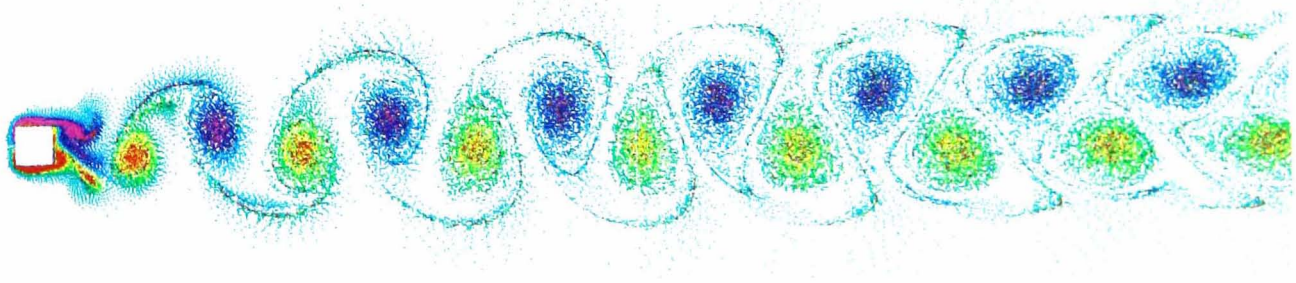

(c) f_e/f_0=2.3, St_1=0.177, St_2=0.532, C_D=1.81, $C_{L(rms)}$=0.68, ϕ_L=120°.

Figure 6.21 Effect of in-line oscillations on vortex shedding; B/A=1.0 cylinder; x/d=0.30.

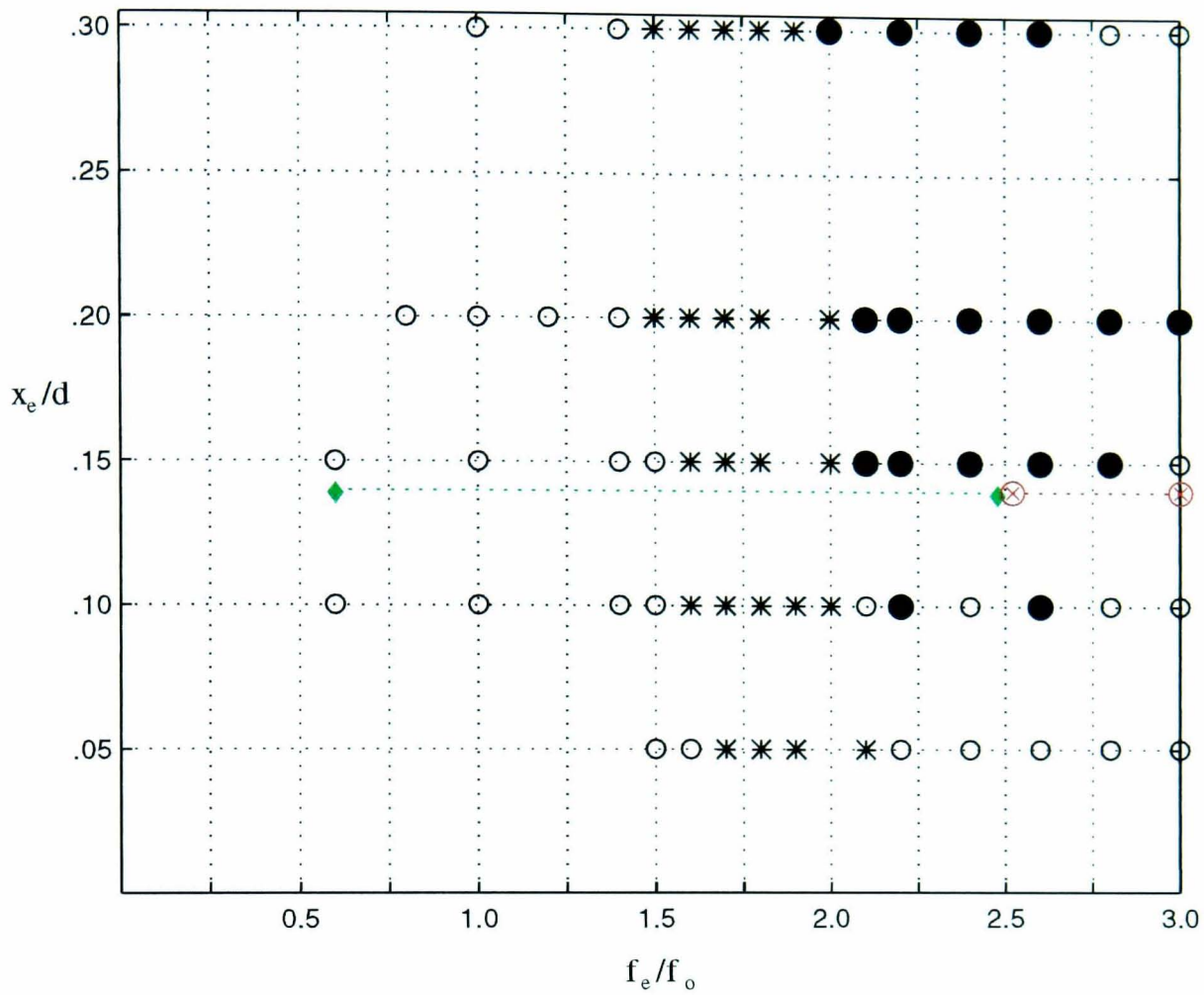

Figure 6.22 Shedding regimes for rectangular cylinder, *B/A*=2.0.

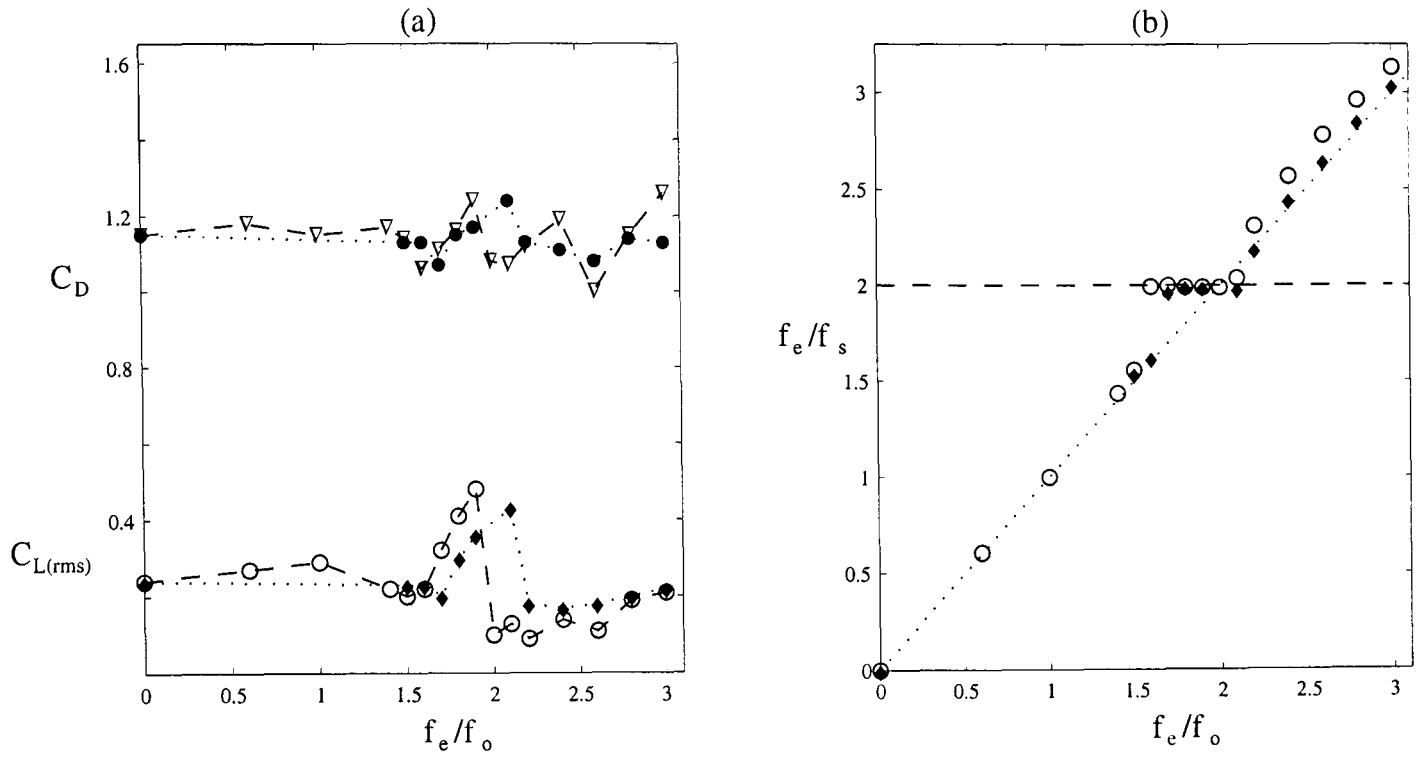

(a) $C_{L(rms)}$ vs. f_e/f_0, ♦ - x_e/d=0.05, o -x_e/d=0.10
C_D vs. f_e/f_0, • - x_e/d=0.05, ∇ - x_e/d=0.10
(b) f_e/f_s vs. f_e/f_0, ♦ - x_e/d=0.05, o - x_e/d=0.10

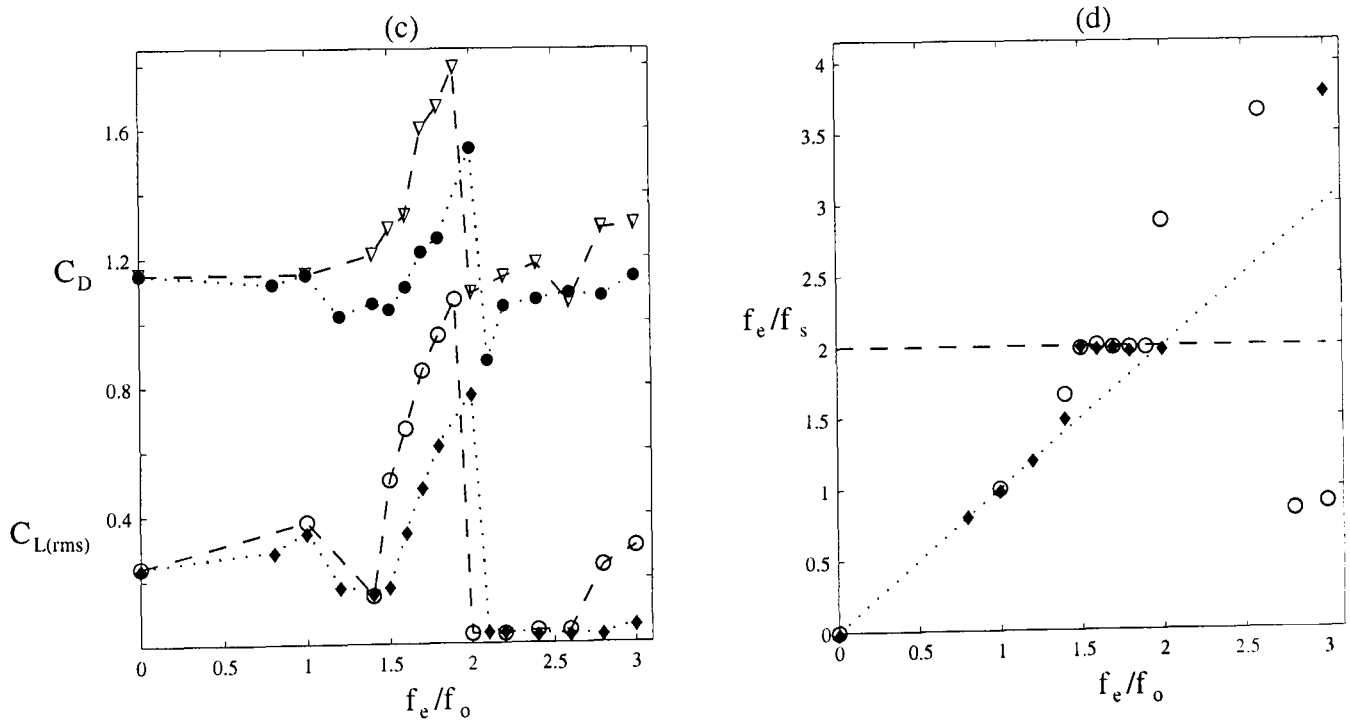

(c) $C_{L(rms)}$ vs. f_e/f_0, ♦ - x_e/d=0.20, o -x_e/d=0.30
C_D vs. f_e/f_0, • - x_e/d=0.20, ∇ - x_e/d=0.30
(d) f_e/f_s vs. f_e/f_0, ♦ - x_e/d=0.20, o - x_e/d=0.30

Figure 6.23 Effect of in-line oscillations on mean forces and shedding frequencies; B/A=2.0 cylinder.

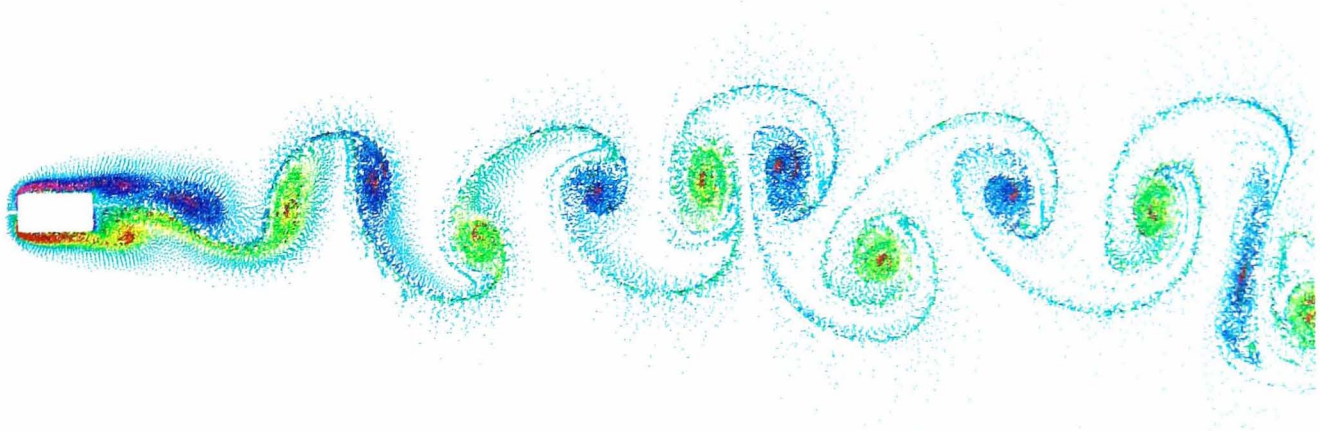

(a) f_e/f_0=1.5, St_1=0.161, St_2=0.091, C_D=1.14, $C_{L(rms)}$=0.20.

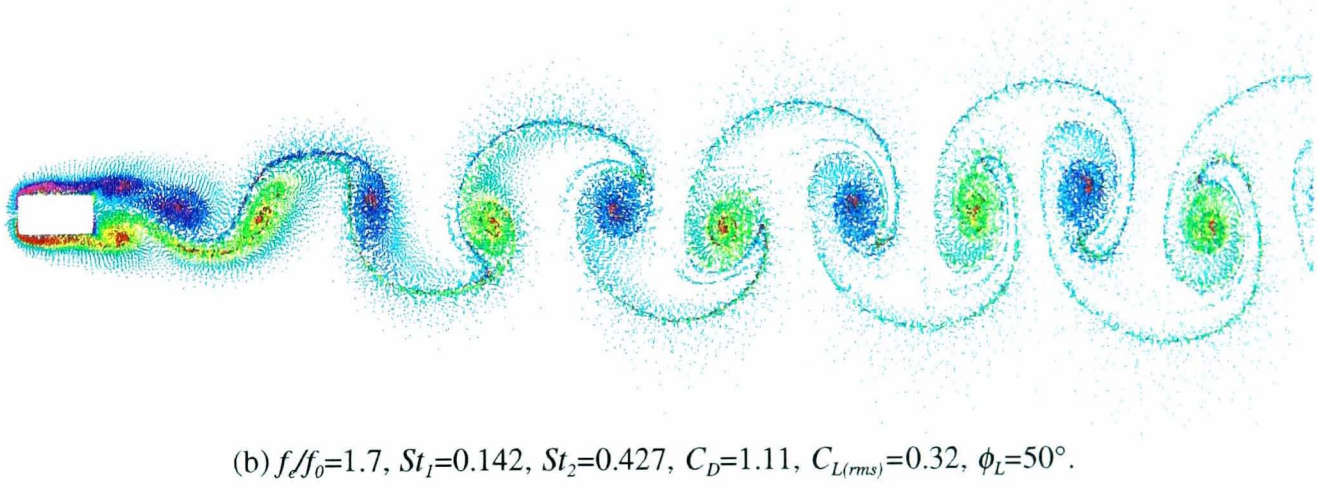

(b) f_e/f_0=1.7, St_1=0.142, St_2=0.427, C_D=1.11, $C_{L(rms)}$=0.32, ϕ_L=50°.

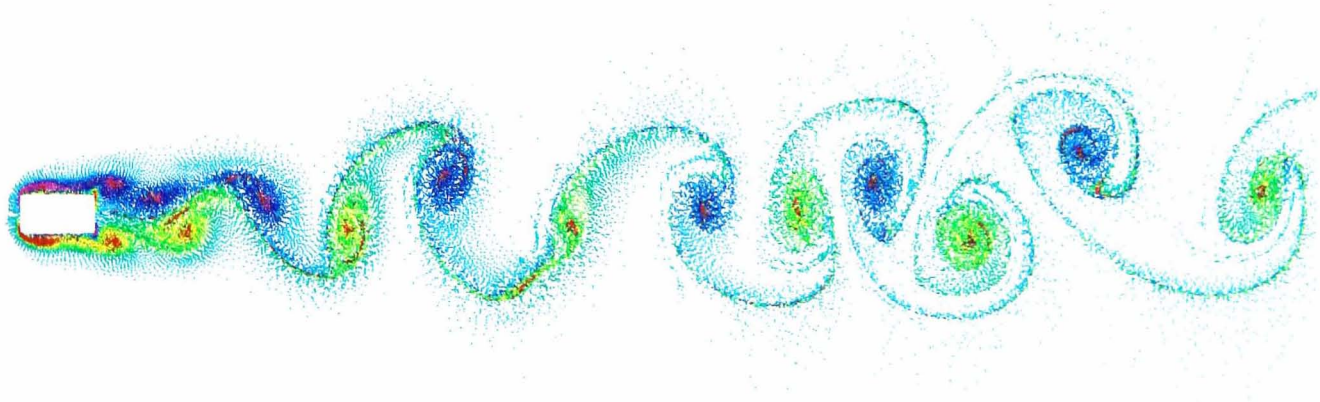

(c) f_e/f_0=2.2, St_1=0.159, C_D=1.12, $C_{L(rms)}$=0.09.

Figure 6.24 Effect of in-line oscillations on vortex shedding; B/A=2.0 cylinder; x_e/d=0.10.

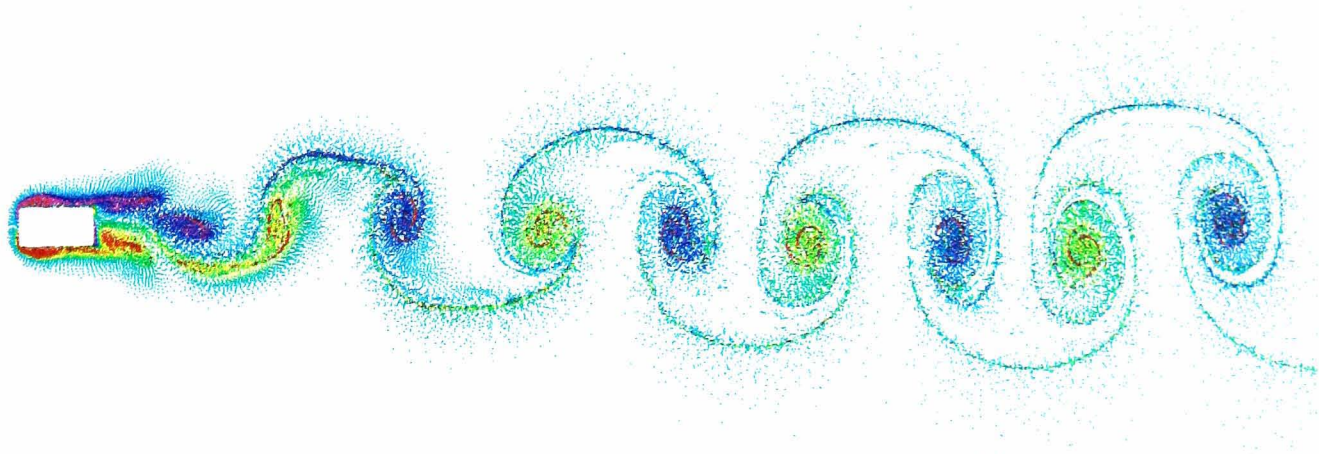

(a) f_e/f_0=1.5, St_1=0.126, St_2=0.375, C_D=1.29, $C_{L(rms)}$=0.51, ϕ_L=55°.

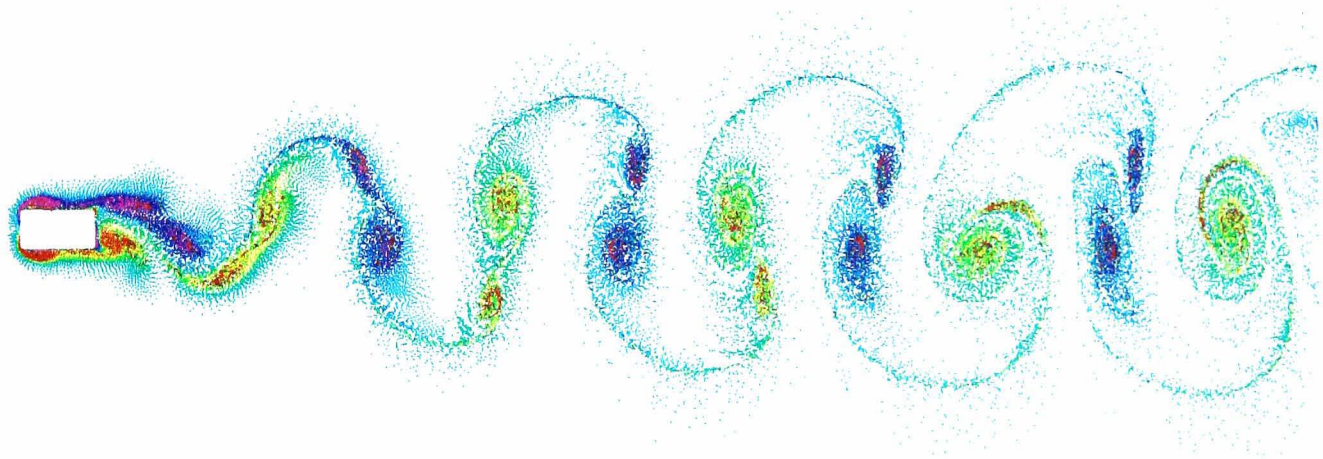

(b) f_e/f_0=1.7, St_1=0.143, St_2=0.425, C_D=1.60, $C_{L(rms)}$=0.85, ϕ_L=70°.

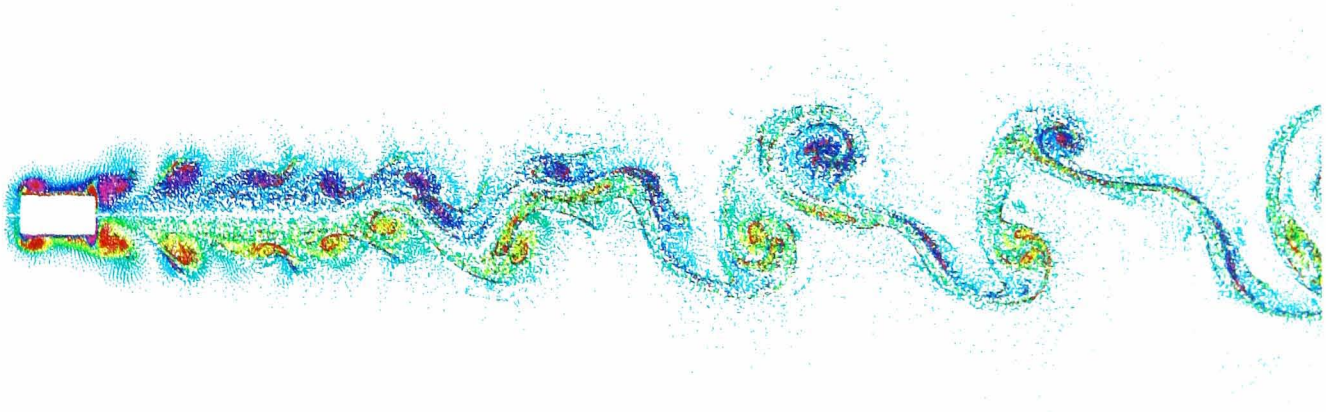

(c) f_e/f_0=2.2, C_D=1.12, $C_{L(rms)}$=0.03.

Figure 6.25 Effect of in-line oscillations on vortex shedding; B/A=2.0 cylinder; x_e/d=0.30.

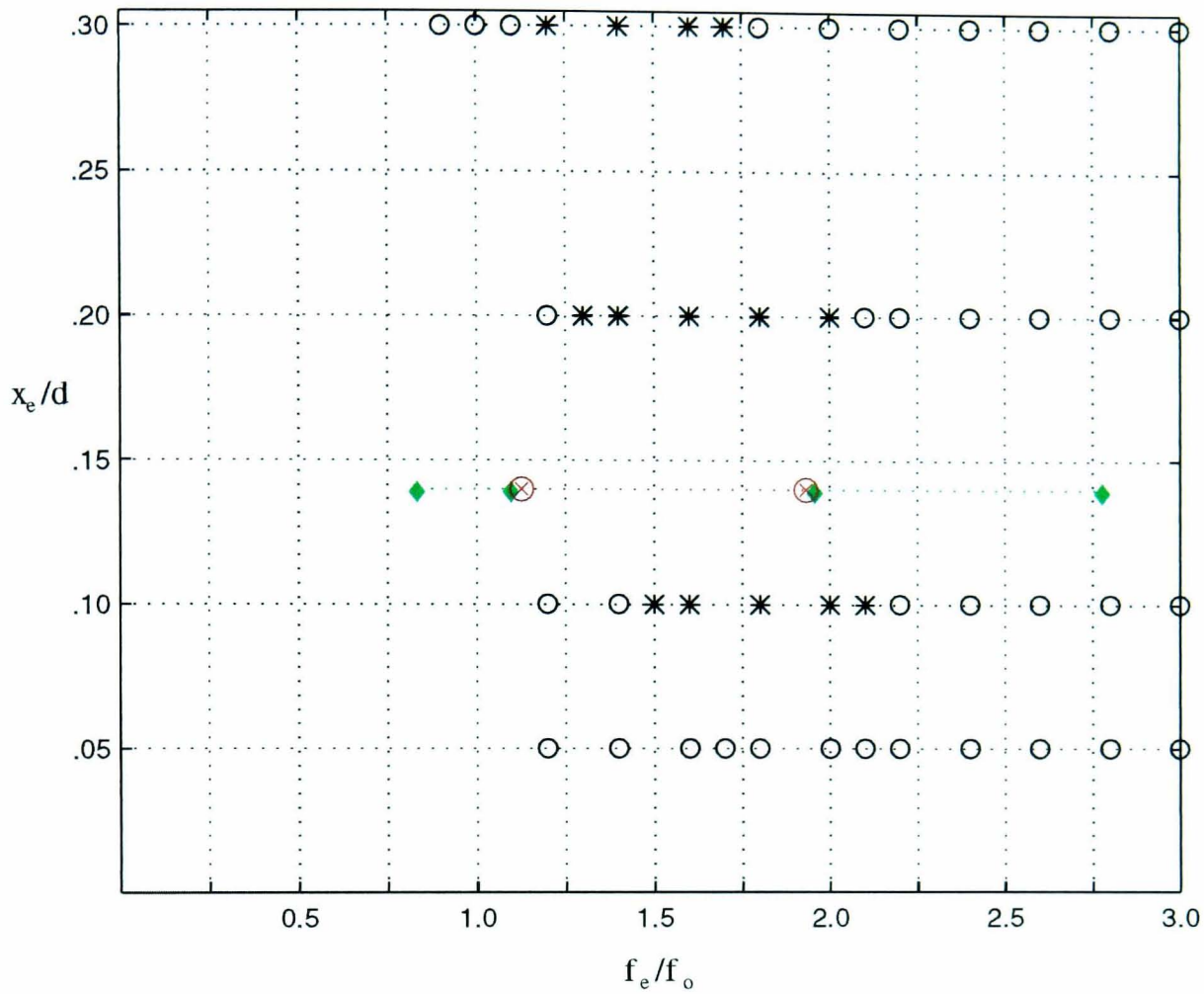

Figure 6.26 Shedding regimes for rectangular cylinder, *B/A*=3.0, *Re*=200.

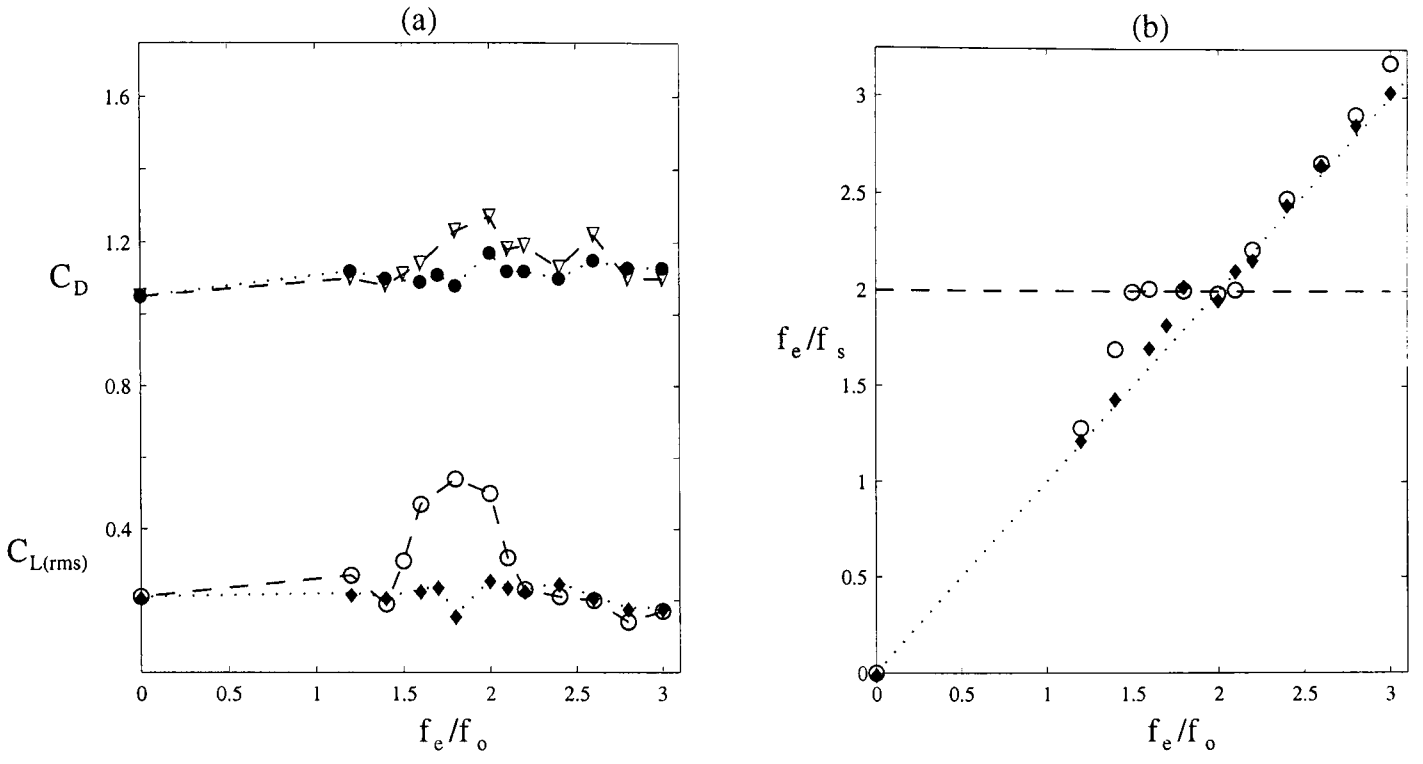

(a) $C_{L(rms)}$ vs. f_e/f_0, ♦ - x_e/d=0.05, o -x_e/d=0.10
C_D vs. f_e/f_0, • - x_e/d=0.05, ∇ - x_e/d=0.10
(b) f_e/f_s vs. f_e/f_0, ♦ - x_e/d=0.05, o - x_e/d=0.10

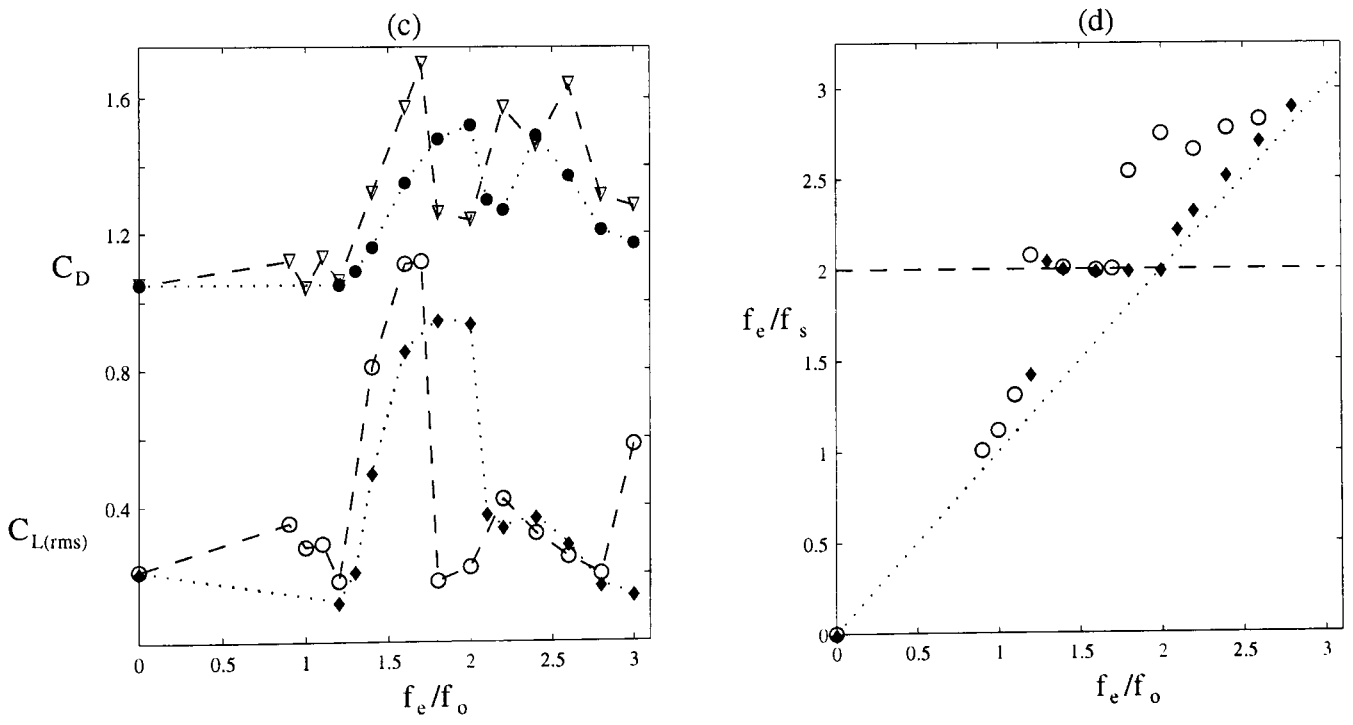

(c) $C_{L(rms)}$ vs. f_e/f_0, ♦ - x_e/d=0.20, o -x_e/d=0.30
C_D vs. f_e/f_0, • - x_e/d=0.20, ∇ - x_e/d=0.30
(d) f_e/f_s vs. f_e/f_0, ♦ - x_e/d=0.20, o - x_e/d=0.30

Figure 6.27 Effect of in-line oscillations on mean forces and shedding frequencies; *B/A*=3.0 cylinder.

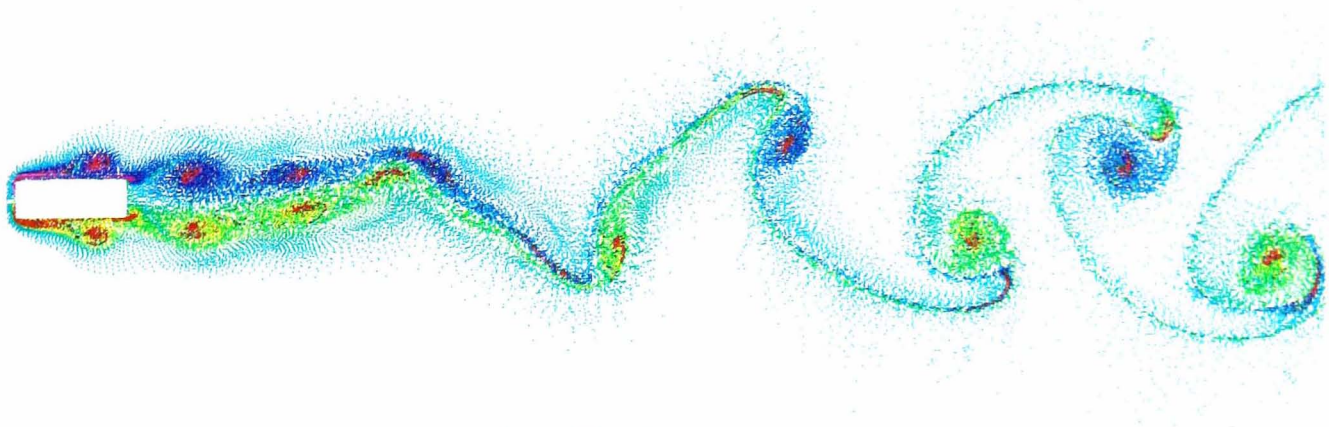

(a) f_e/f_0=1.2, St_1=0.093, C_D=1.06, $C_{L(rms)}$=0.18, ϕ_L=90°.

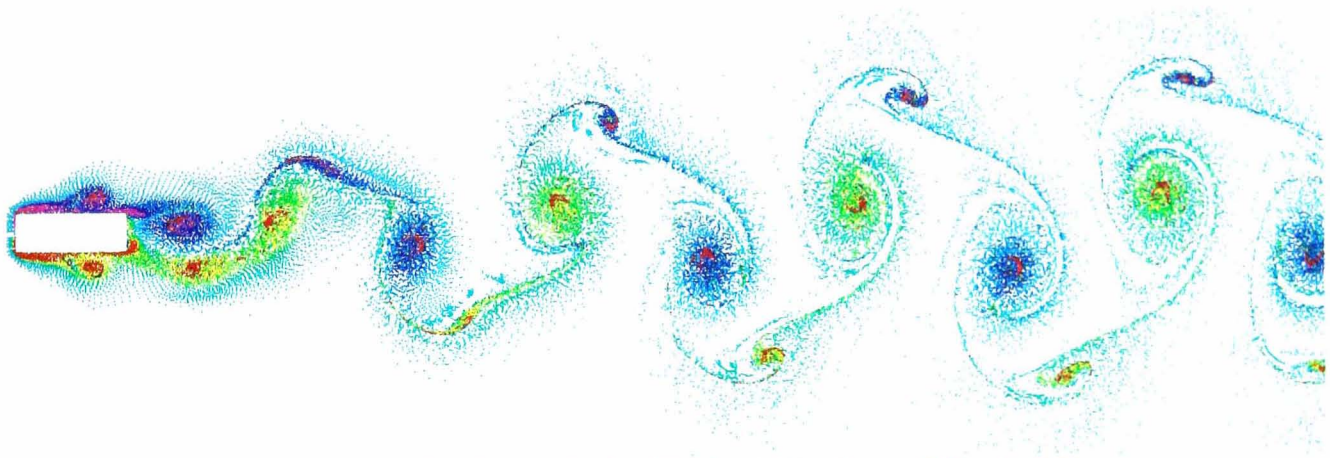

(b) f_e/f_0=1.4, St_1=0.112, St_2=0.336, C_D=1.32, $C_{L(rms)}$=0.81, ϕ_L=75°.

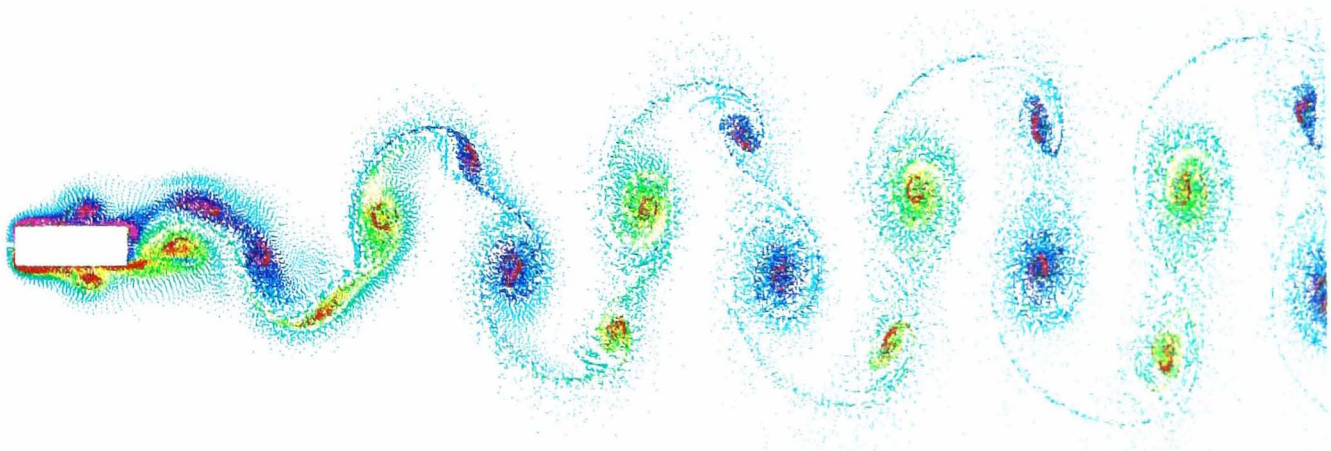

(c) f_e/f_0=1.6, St_1=0.129, St_2=0.383, C_D=1.57, $C_{L(rms)}$=1.11, ϕ_L=70°.

Figure 6.28 Effect of in-line oscillations on vortex shedding; B/A=3.0 cylinder x_c/d=0.30.

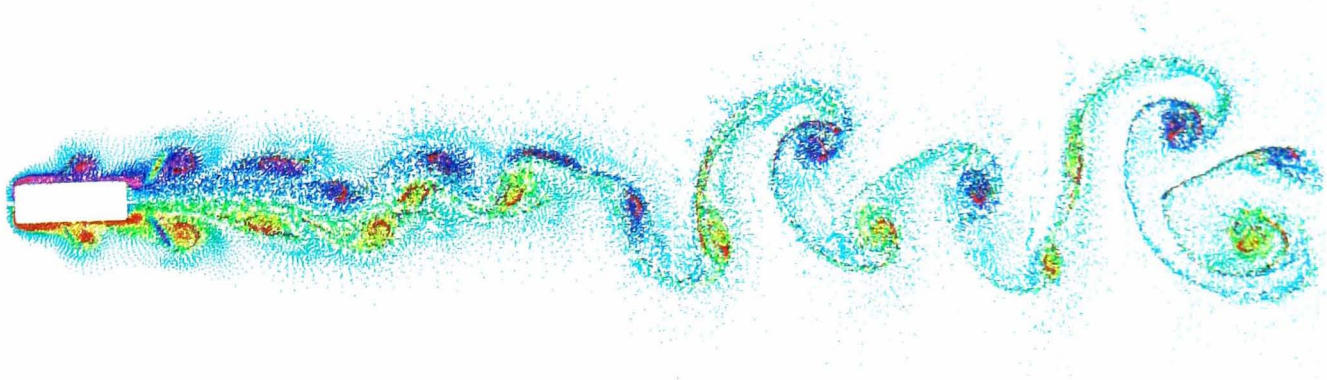

(d) f_e/f_0=1.8, St_1=0.114, St_2=0.397, C_D=1.26, $C_{L(rms)}$=0.18.

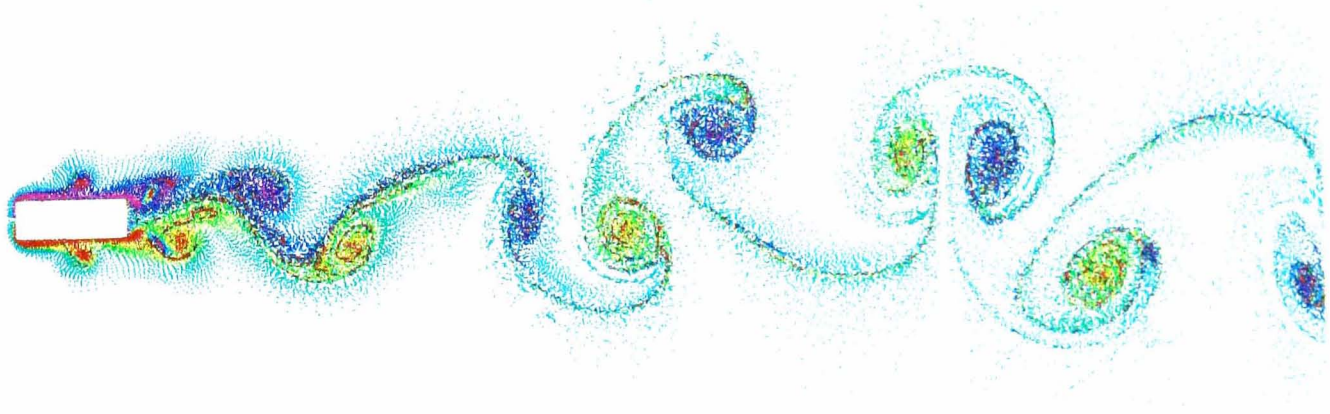

(e) f_e/f_0=2.2, St_1=0.117, St_2=0.438, C_D=1.51, $C_{L(rms)}$=0.42.

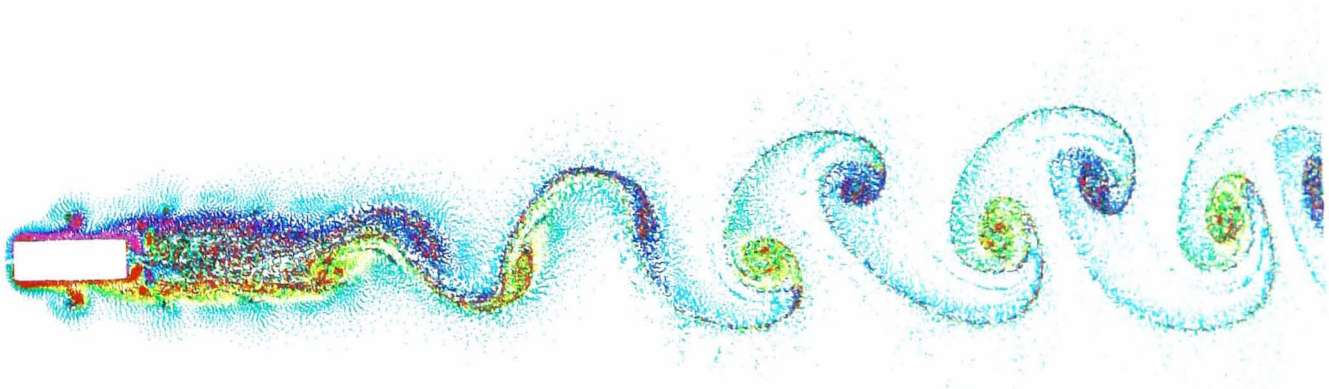

(f) f_e/f_0=2.8, C_D=1.60, $C_{L(rms)}$=0.85.

Figure 6.28 (cont) Effect of in-line oscillations on vortex shedding; B/A=3.0 cylinder x_e/d=0.30.

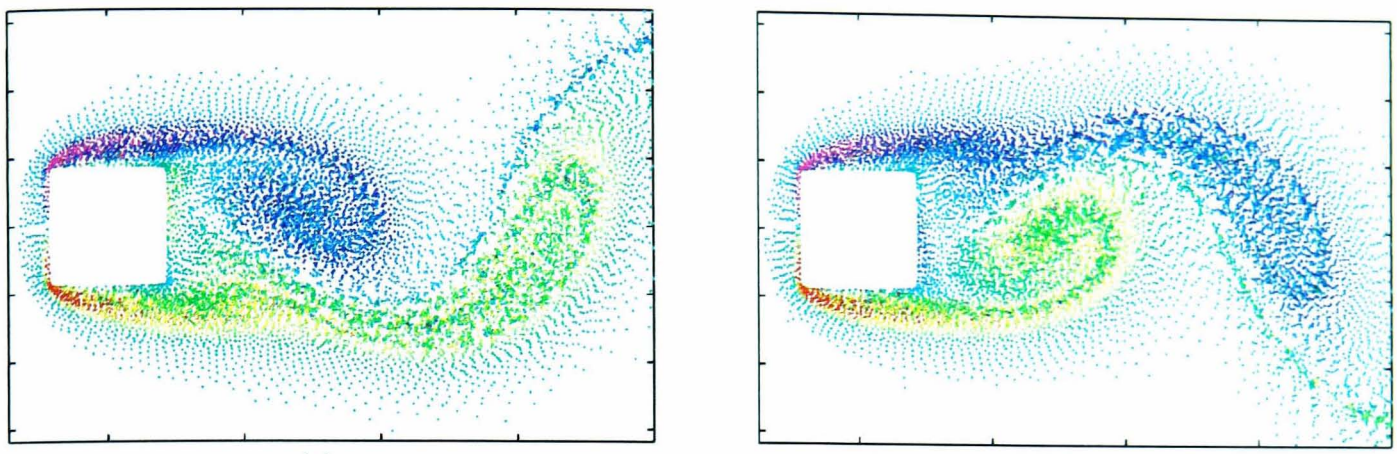

(a) (b)

Figure 6.29 Moment of vortex shedding for B/A=1.0 cylinder
(a) Vortex A shed from upper surface; Lift is maximum.
(b) Vortex B shed from lower surface; Lift is minimum.

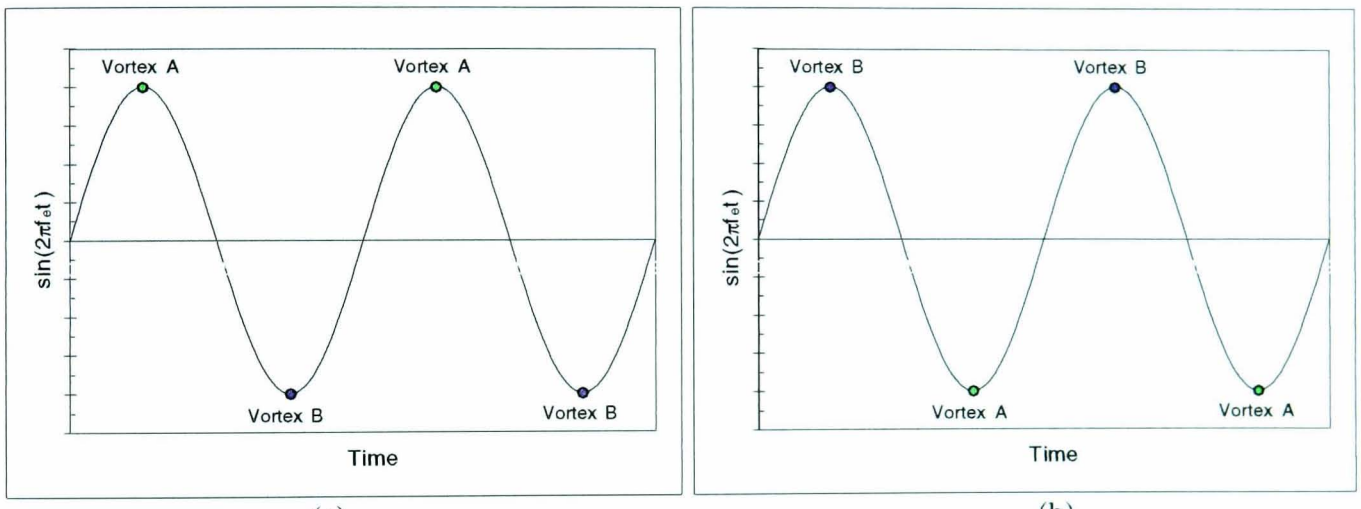

(a) (b)

Figure 6.30 Moment of vortex shedding with respect to phase of cross-flow oscillations
Phase shift: (a) ϕ_V=0°; (b) ϕ_V=180°.

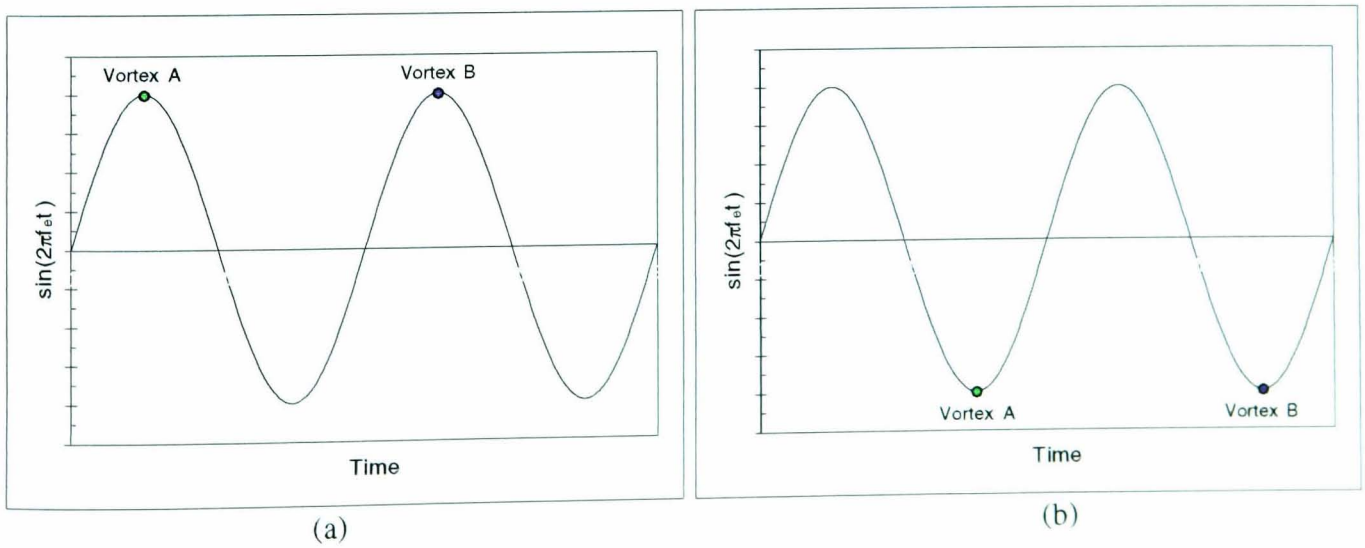

(a) (b)

Figure 6.31 Moment of vortex shedding with respect to phase of in-line oscillations
Pseudo-phase shift: (a) ϕ_V=0°; (b) ϕ_V=180°.

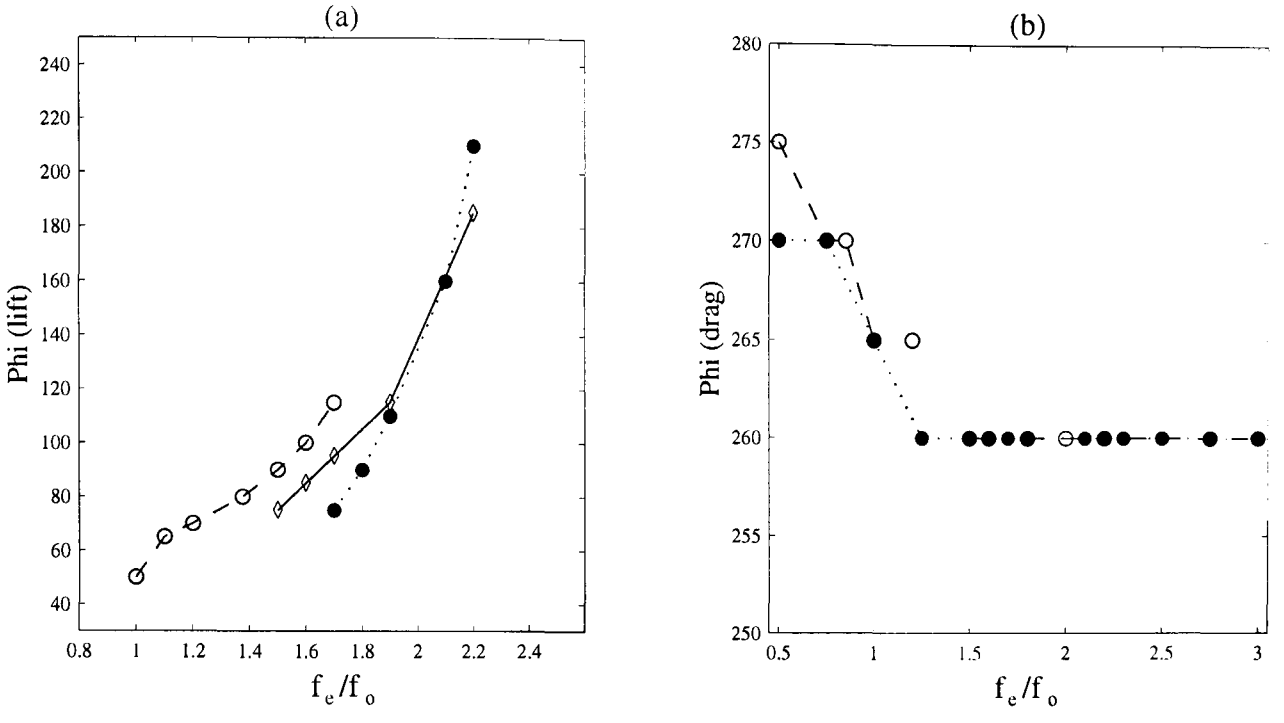

Figure 6.32 Pseudo phase lag of force time histories with respect to in-line oscillations; Circular cylinder.
(a) ϕ_L vs. f_e/f_0; •- x_e/d=0.05; ◊-x_e/d=0.10; o-x_e/d=0.30.
(b) ϕ_D vs. f_e/f_0; •-x_e/d=0.05; o-x_e/d=0.30.

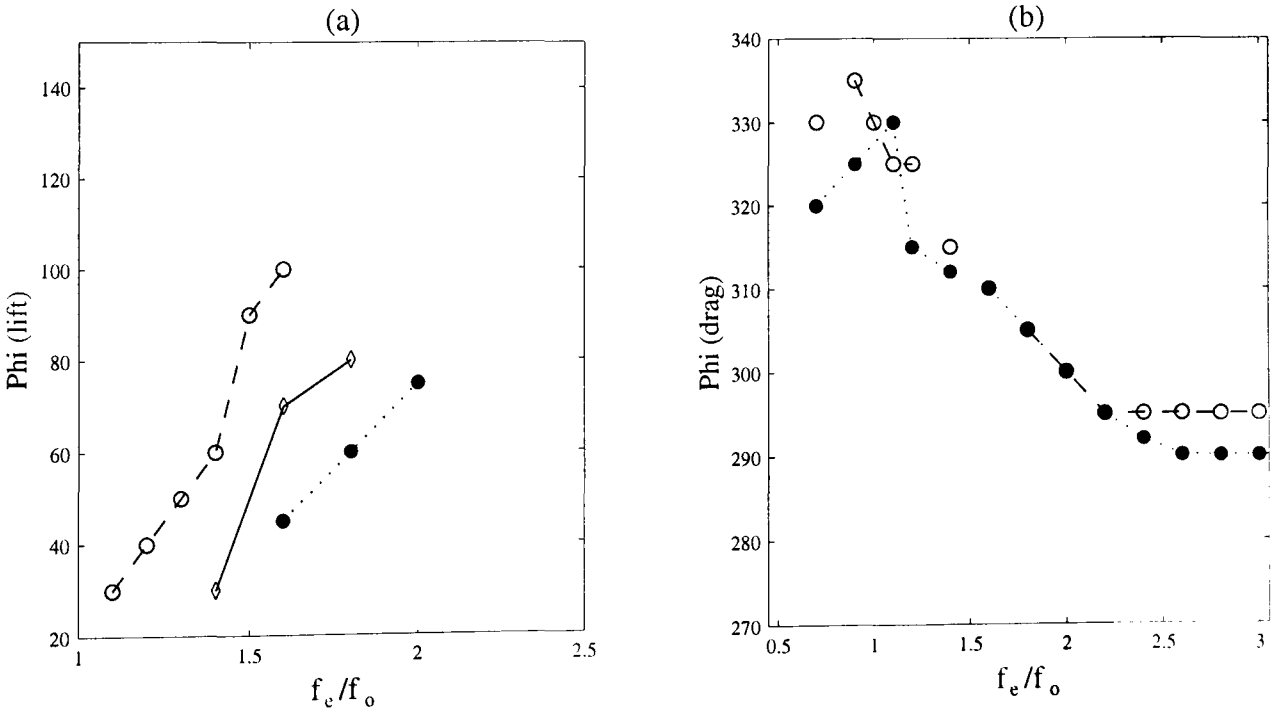

Figure 6.33 Pseudo phase lag of force time histories with respect to in-line oscillations; Diamond cylinder.
(a) ϕ_L vs. f_e/f_0; •-x_e/d=0.05; ◊-x_e/d=0.10; o-x_e/d=0.30.
(b) ϕ_D vs. f_e/f_0; •-x_e/d=0.05; o-x_e/d=0.30.

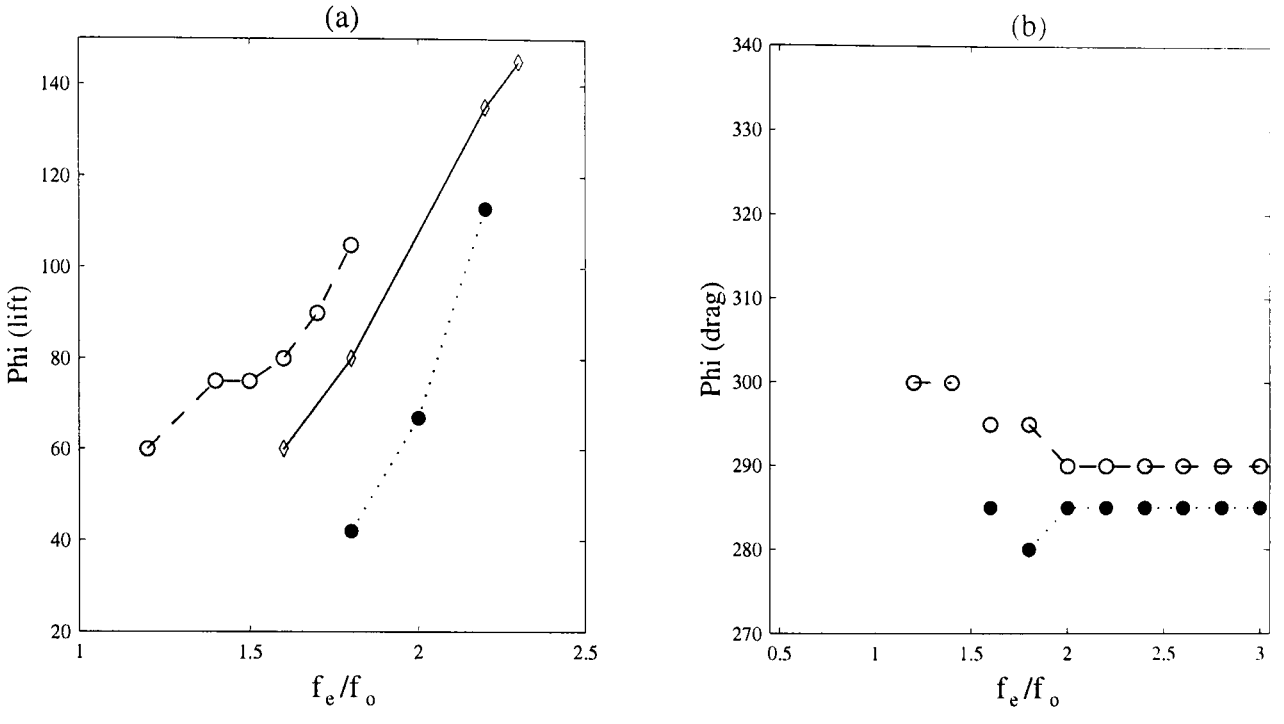

Figure 6.34 Pseudo phase lag of force time histories with respect to in-line oscillations; *B/A*=0.62 cylinder.
(a) ϕ_L vs. f_e/f_0; •-x_e/d=0.05; ◊-x_e/d=0.10; o-x_e/d=0.30.
(b) ϕ_D vs. f_e/f_0; •-x_e/d=0.05; o-x_e/d=0.30.

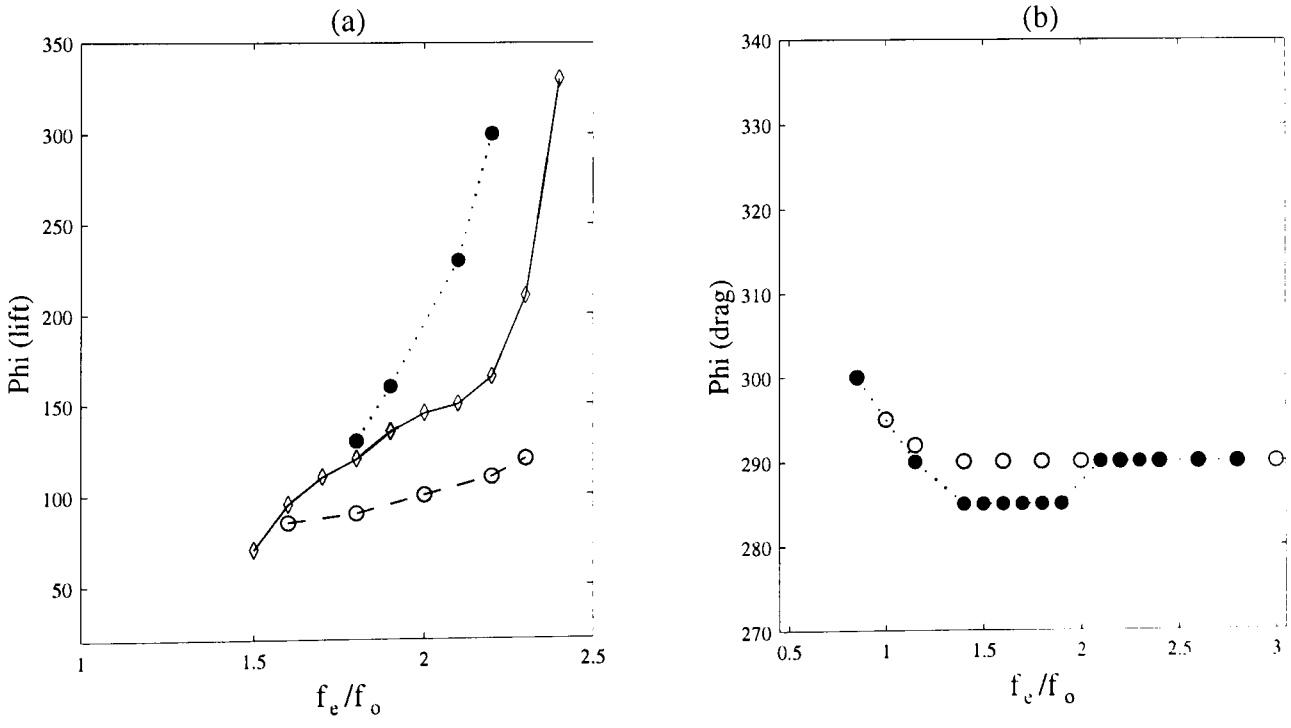

Figure 6.35 Pseudo phase lag of force time histories with respect to in-line oscillations; *B/A*=1.0 cylinder.
(a) ϕ_L vs. f_e/f_0; •-x_e/d=0.05; ◊-x_e/d=0.15; o-x_e/d=0.30.
(b) ϕ_D vs. f_e/f_0; •-x_e/d=0.05; o-x_e/d=0.30.

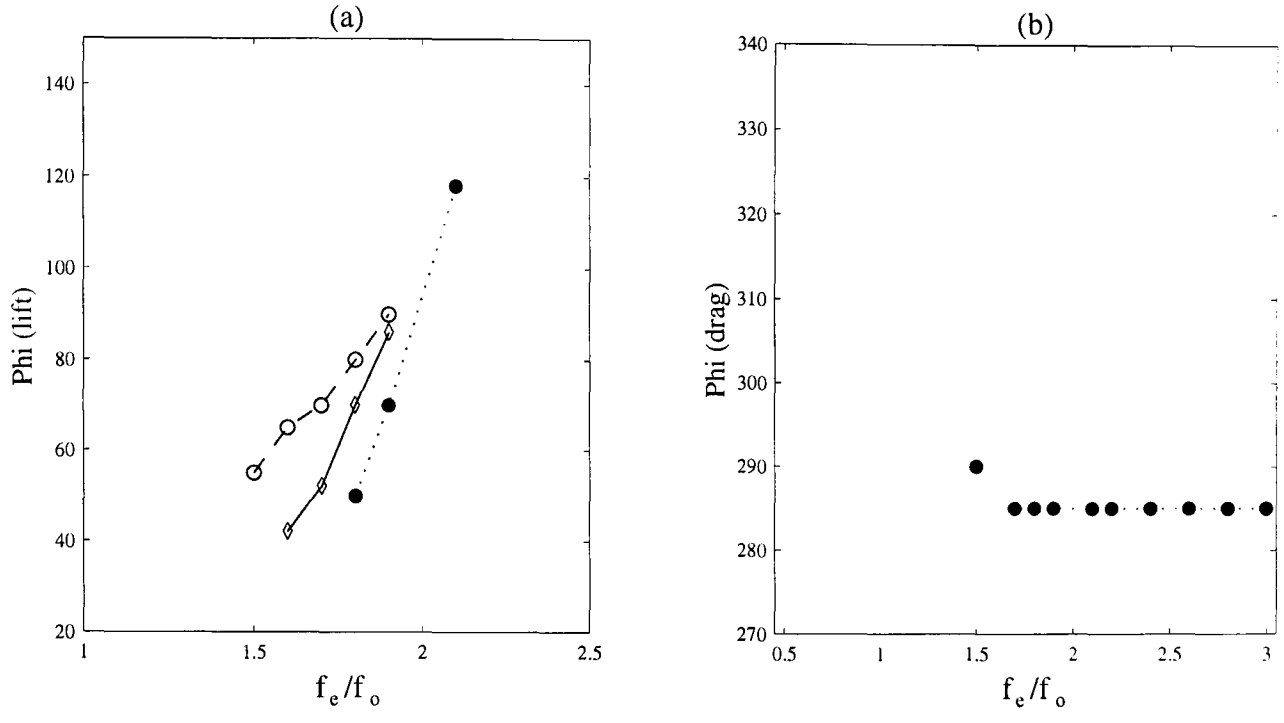

Figure 6.36 Pseudo phase lag of force time histories with respect to in-line oscillations; *B/A*=2.0 cylinder.
(a) ϕ_L vs. f_e/f_0; •-x_e/d=0.05; ◊-x_e/d=0.15; o-x_e/d=0.30.
(b) ϕ_D vs. f_e/f_0; •-x_e/d=0.05; o-x_e/d=0.30.

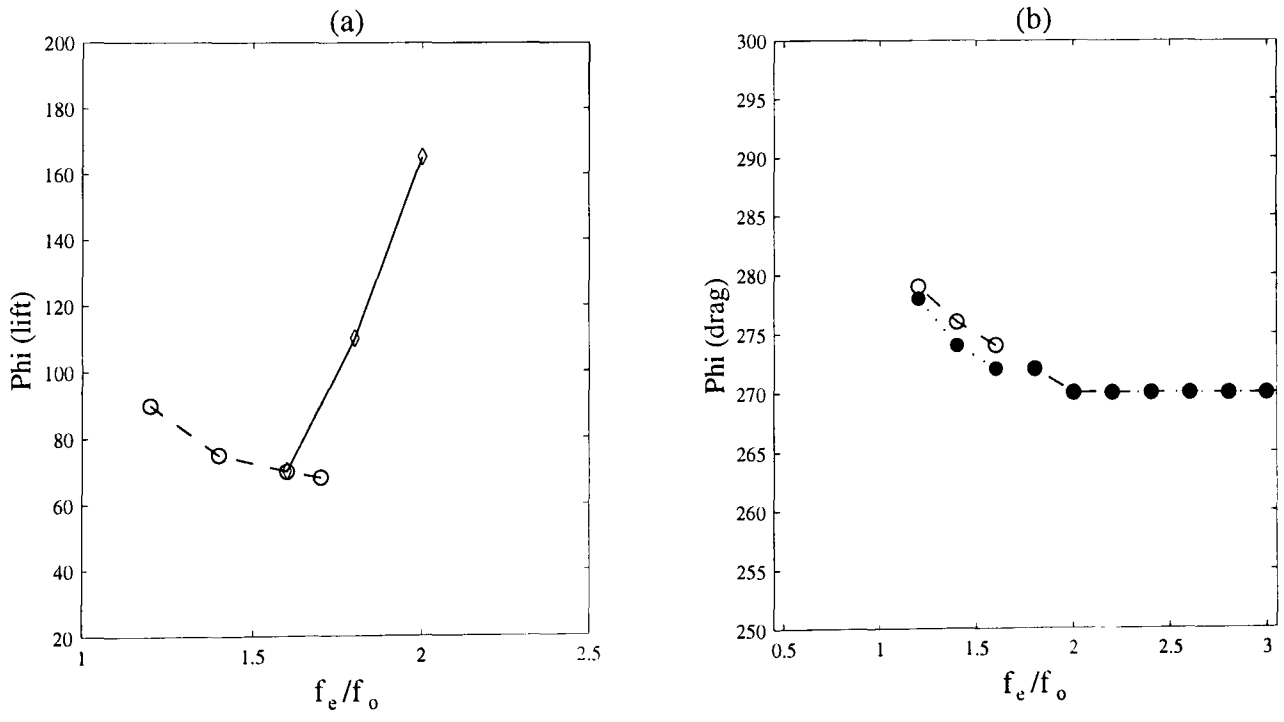

Figure 6.37 Pseudo phase lag of force time histories with respect to in-line oscillations; *B/A*=3.0 cylinder.
(a) ϕ_L vs. f_e/f_0; ◊-x_e/d=0.15; o-x_e/d=0.30.
(b) ϕ_D vs. f_e/f_0; •-x_e/d=0.05; o-x_e/d=0.30.

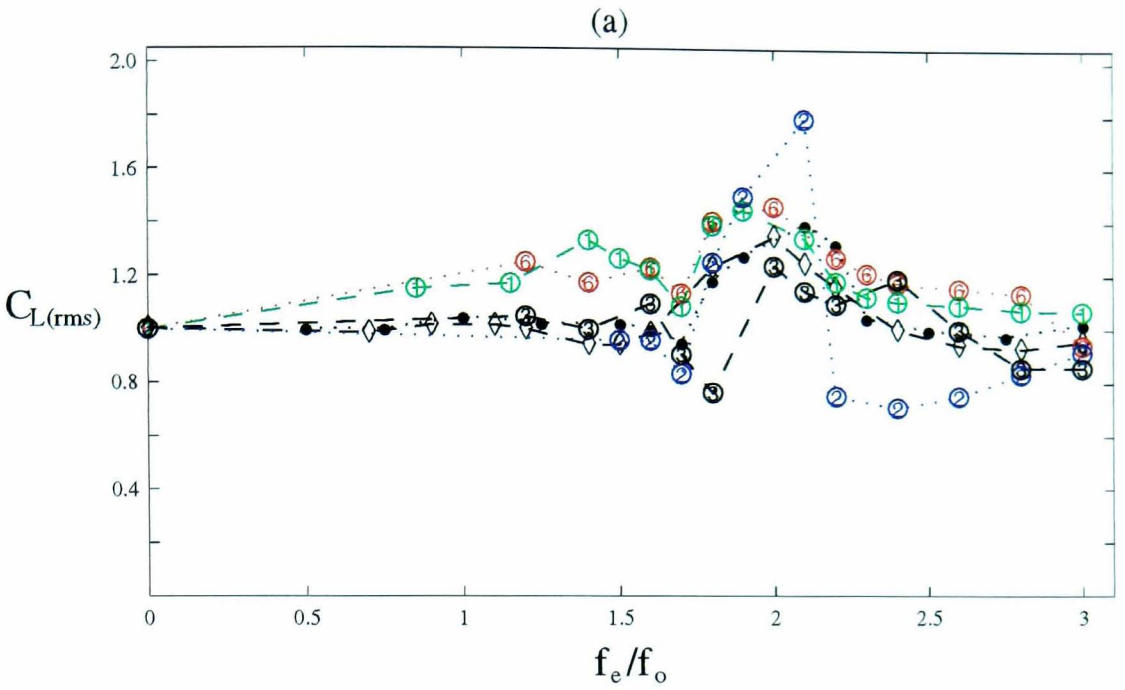

Figure 6.38 $C_{L(rms)}$ vs. f_e/f_0, Comparison between cylinders.

(a) x_e/d=0.05, (b) x_e/d=0.30

• - Circular, ◊ - Diamond , ⑥ - B/A=0.62

① - B/A=1.0, ② - B/A=2.0, ③ - B/A=3.0

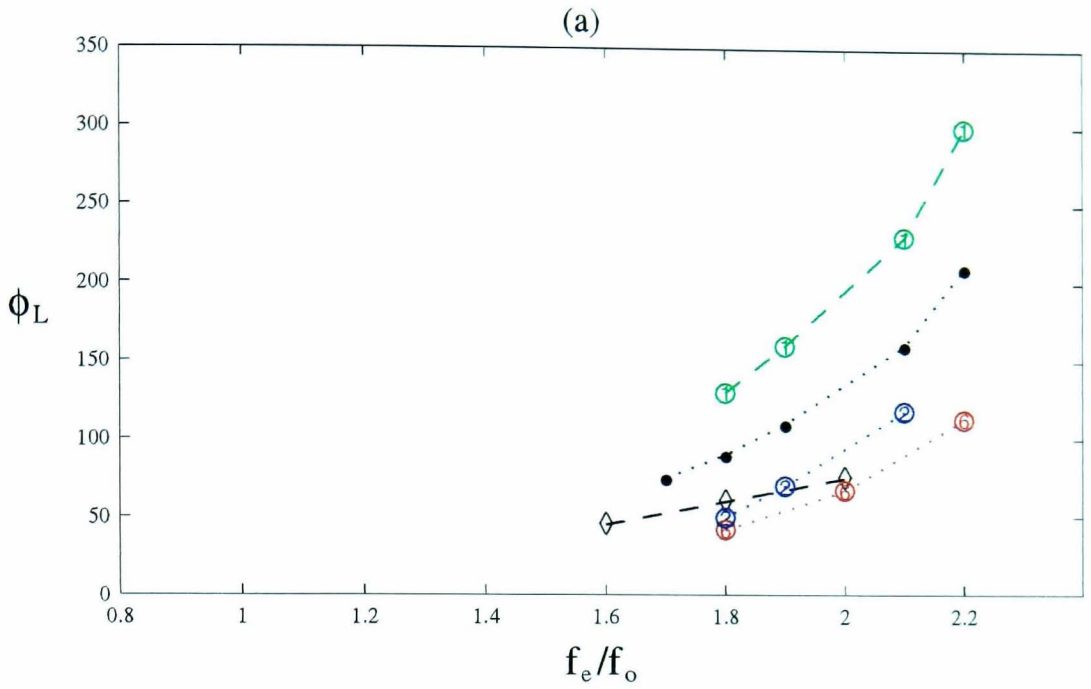

Figure 6.39 ϕ_L vs. f_e/f_o, Comparison between cylinders.

(a) x_e/d=0.05, (b) x_e/d=0.30

• - Circular, ◊ - Diamond , ⑥ - B/A=0.62

① - B/A=1.0, ② - B/A=2.0, ③ - B/A=3.0

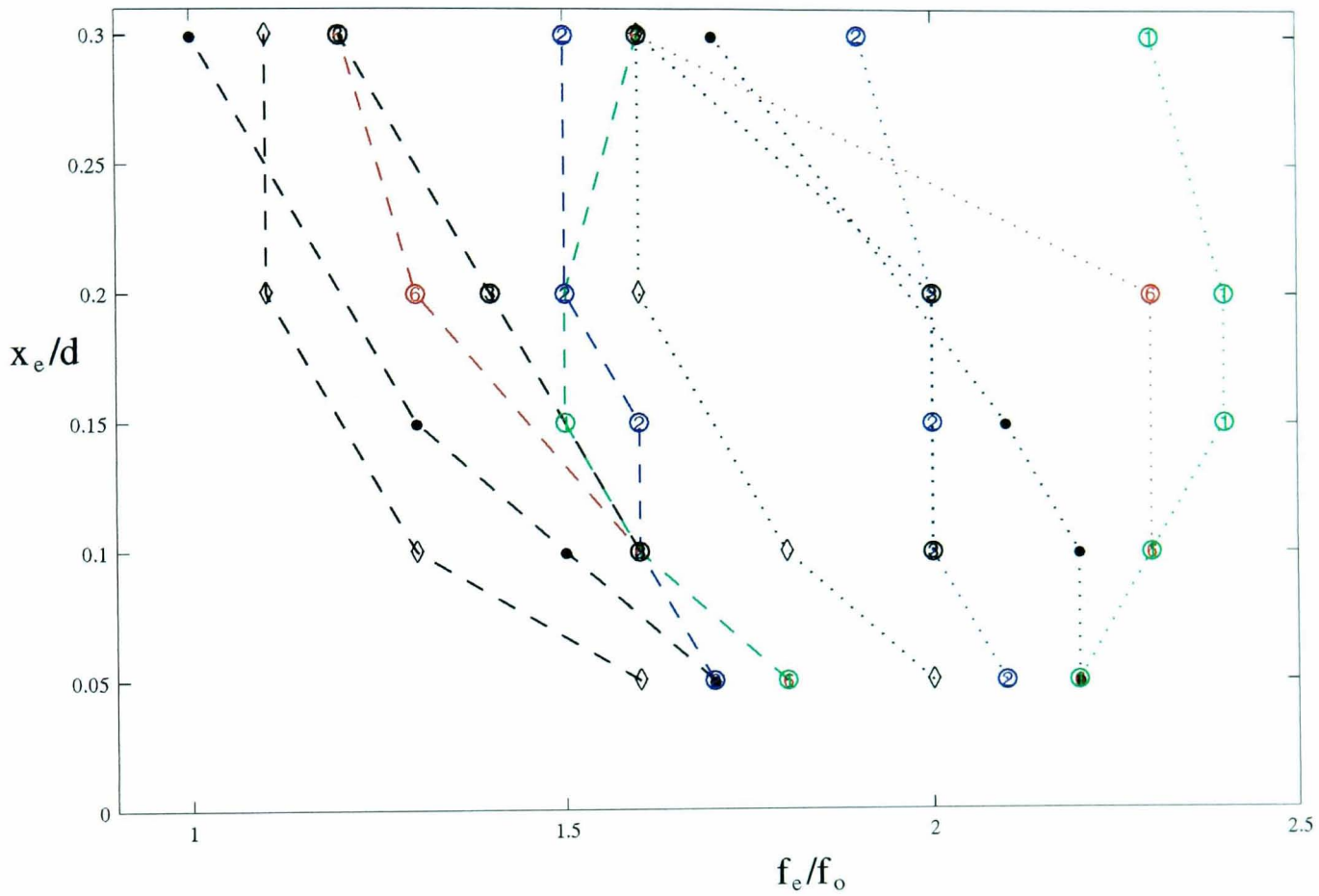

Figure 6.40 Frequency bounds for lock-in, $0.05 \le x_e/d \le 0.30$; Comparison between cylinders.

• - Circular, ◊ - Diamond , ⑥ - B/A=0.62

① - B/A=1.0, ② - B/A=2.0, ③ - B/A=3.0

Chapter 7

Conclusions

A numerical study was undertaken of the flow past a selection of bluff cylinders. For uniform flow conditions, attention was focussed on rectangular cylinders of side ratio in the range $0.02<B/A<4.0$, and the effects of varying the side ratio, the angle of incidence and the Reynolds number were all considered. The addition of an upstream in-line oscillatory flow component was tested on six cylinders.

In an earlier study Meneghini (1994) had applied the discrete vortex method to simulate the flow past a circular cylinder with an oscillatory component normal to the oncoming stream. The code used in Meneghini's study was adapted such that it was suitable to model flows about sharp-edged obstacles. Initially this was motivated by a desire to simulate the effects of in-line unsteadiness on the flows about typical vortex shedding flowmeter geometries. These include triangular, rectangular and T-shaped geometries. A variable rectangular transformation was chosen since a review of the literature revealed large gaps in the fundamental knowledge of flows even under uniform flow conditions past these geometries.

A summary of the code adaptations and main findings under uniform and oscillatory flow conditions follows. Finally a discussion of future code usage and possible developments will be given.

7.1 Code development

An integral expression was derived from the Schwarz-Christoffel relations which gave the transformation between a region exterior to any rectangle onto a semi-infinite strip in the computational domain. This transformation was incorporated into the DVM code together with an adaptation to the grid generation giving better user control on the mesh spacing. Improved smoothing of the Jacobian J in the region of the vertex singularities and a proper consideration of the variability of J with ξ in the diffusion calculations were also included. In previous versions of the code a Fast Fourier Transform algorithm was performed twice per timestep to solve the stream function. This appeared an unnecessary and computationally expensive operation and thus the code was modified to include only one FFT per timestep.

The most important and novel adaptation to the code was the derivation and implementation of a surface pressure solver. This was necessary since the methods applied in previous versions of the code were found to be inappropriate for this study. The Blasius method determines force coefficients but not surface pressure coefficients and becomes noisy as vortices leave the computational domain. The gradient of vorticity method is inappropriate for sharp-edged obstacles since the tangential direction cannot be defined at corners. An integral expression was derived which relates the spatial pressure gradients in a manner applicable to a general coordinate transformation. Ongoing projects have successfully applied the surface pressure solver to triangular, T-shaped and aerofoil cross-sections.

Simulations under uniform and oscillatory flow conditions have demonstrated the value of all these modifications. Ideally more thorough investigations would have been made of code convergence and the effects of altering the Jacobian smoothing scheme. However the prime objective of the project was not to provide highly accurate values for calculated parameters such as the Strouhal number and force coefficients and the emphasis is instead placed on the trends in these parameters which occur as the cylinder and flow geometry are varied. It is felt that where comparisons could be made the broad agreement between the DVM calculations and existing numerical and laboratory data justifies this methodology.

7.2 Uniform flow simulations

Rectangular cylinders of side ratio $0.02<B/A<4.0$ were tested. In addition to the side ratio, tests were done on the variation of the angle of attack and the Reynolds number, although these were confined mainly to the square, $B/A=1.0$, cylinder.

7.2.1 Effect of side ratio and angle of attack at $Re=200$

At $Re=200$, no drag maximum was found in the B/A range tested. This contrasts with the known result at higher Reynolds numbers, $Re=10^4$-10^5, for which a maximum drag occurs close to $B/A=0.6$. At higher Reynolds number this result has been attributed to a change in the vortex formation position caused by an interaction between the rectangle afterbody and the shear layer separating from the front corner of the rectangle. Some attempt was therefore made to estimate the vortex formation position and it was shown that the distance from the rear surface to the formation position increased across the range of side ratios investigated at $Re=200$. However the formation positions were not accurately determined and a more detailed analysis could have been made if the time-averaged values of mesh vorticity had been calculated.

Although no peak in the C_D vs. B/A curve was found, both the Strouhal number and the lift coefficient had maximum values close to $B/A=0.30$. A change was also observed in the skin friction drag coefficient which went from positive to negative at a similar side ratio. Some near-wake visualisations and surface pressure calculations were made at several moments of the shedding cycle for a few rectangles of differing side ratio. An explanation for the maximum lift coefficient which occurs close to $B/A=0.3$ was suggested from these results.

Separation occurs at the cylinder corner and the shear layer grows along the cylinder side surface. At the rear of the cylinder the vortex shedding process dominates but this results in an oscillation of the shear layer. This oscillation leads to a difference in the pressure distribution along the top and bottom surfaces and hence an oscillatory lifting force. As B/A increases initially since the oscillation magnitude is greater further downstream the lift oscillation also grows but as the side ratio increases beyond B/A=0.3 the afterbody begins to suppress the oscillation of the shear layer and hence the mean lift decreases.

The simulations for the B/A=1.0 cylinder were varied over the full range, $0°<\alpha<45°$, of the angle of incidence. The lift coefficient was found to be negative for $\alpha<15°$ with a minimum occurring near $\alpha=5°$. The drag was also minimum near $\alpha=5°$ and had a maximum at $\alpha=45°$. The Strouhal number increased gradually with incidence angle from St=0.155 at $\alpha=0°$ to St=0.20 at $\alpha=45°$.

7.2.2 Effect of Reynolds number

Vortex shedding was detected at Re=50 with the Strouhal frequency in close agreement with existing laboratory measurements. The agreement remained strong up to Re=500 at which point DVM predicted a dual-shedding mode in contrast to the accepted laboratory data which remains roughly constant at St=0.13 for Re>500. This may be explained by the appearance of three-dimensional instabilities which cannot be accounted for in a two-dimensional simulation. The scale of these instabilities will also decrease as the Reynolds number increases and thus the cell size will not be large enough to model them all.

One may have anticipated that other parameters estimated in the simulation would also become inaccurate as Re>500 since the vortex shedding process did not give a good representation of the laboratory observations. However the drag was found to give good agreement with the laboratory data up to Re=5000. This was a surprising result and suggests that although the vortex shedding frequency is not well simulated the strength and position of vortex shedding is predicted in accordance with the laboratory data. Since the drag could be predicted with some confidence for the B/A=1.0 cylinder some further simulations were made to predict the drag coefficient for rectangles of other side ratios. Those cylinders tested did show different Reynolds number dependencies but no critical side ratio was found for $Re<10^3$.

7.3 Oscillatory flow simulations

The addition of an in-line oscillatory upstream flow component was tested on six cylinders at a fixed Reynolds number, Re=200. A circular, a diamond and four rectangular cylinders, B/A=0.62, 1.0, 2.0 and 3.0, were chosen. The pulsations were varied over a range of forcing amplitudes, $x_o/d \leq 0.3$, and frequencies, $f_e/f_0 \leq 3.0$. At each combination the mean forces and dominant frequencies of the lift oscillation were determined. Three different resonant modes were detected and several shedding patterns observed as described below.

7.3.1 Resonant modes

All the cylinders exhibited primary lock-in within which the shedding frequency is controlled by the upstream oscillations at f_e/f_s=2.0. Across this synchronisation range the mean forces, particularly the lift, increased. The most significant increases relative to their uniform flow values occurred for the geometries of longer afterbody, the B/A=2.0 and 3.0 cylinders. As the forcing amplitude increased the synchronisation range became larger and the increase in the force coefficients was more pronounced.

For amplitudes in the range $0.2 \leq x_e/d \leq 0.3$ several cylinders also exhibited a secondary type of resonance. It was termed a quasi-symmetric mode since the near wake was characterised by symmetric vortex shedding and the symmetry broke down at some point downstream. Vortex shedding frequencies could not be determined from the force coefficients where this mode was excited. However the mode was characterised by a substantial reduction in mean forces and the bounds for quasi-symmetric synchronisation were defined in terms of the relative reduction to the lift coefficient from its uniform flow value. The mode initially occurred at $f_e/f_0 \geq 2.0$ but shifted to lower frequencies as the amplitude increased.

Some evidence was shown for a third resonant mode in which f_e/f_s=1.0. This was observed for the diamond and circular cylinders for forcing oscillations in the range $0.7 \leq f_e/f_0 \leq 0.8$ but was not thoroughly investigated.

7.3.2 Shedding patterns

Several different shedding patterns were observed and these were noted across the synchronisation ranges of each cylinder. At low forcing amplitudes type ***2S*** shedding was dominant for all cylinders. However some changes could be detected in the vortex alignment as the forcing frequency increased across the synchronisation range. At higher amplitudes new modes began to emerge.

Type ***P+S*** shedding was observed for the circular cylinder. A pair of vortices and a single vortex are shed per cycle but a question which remains to be resolved is the asymmetry of this arrangement. This same shedding pattern has been observed under cross-flow oscillations but the asymmetry in that case can be explained by the direction in which the oscillation is started.

Vortex pairing was clearly a common process for many of the flows examined. Type ***2P*** shedding was found in which two pairs of oppositely signed vortices are shed into each side of the wake per cycle. This mode was observed for all but the B/A=1.0 cylinder. However the kind of ***2P*** shedding differed both between cylinders and for different forcing combinations of amplitude and frequency. The ***2P*** shedding behind the circular and diamond cylinders contained vortex pairs in which both vortices were of similar size although the alignment varied. For the B/A=2.0 and 3.0 cylinders the vortices in each pair were of quite different sizes. The larger vortices were positioned near to the wake centre line and the small vortices were positioned further off centre.

In some cases, particularly for the B/A=0.62 cylinder, the shedding mode could not be determined although the frequencies deduced from the lift curve implied that the vortex shedding was controlled by the forcing oscillation.

Quasi-symmetric shedding was observed for the circular, diamond, B/A=2.0 and B/A=3.0 cylinders. This mode consists of vortices shed symmetrically from either side of the cylinder per cycle. The symmetry breaks down at some point downstream and an asymmetric vortex street emerges in the far-wake. In cases where the quasi-symmetry was strong vortex pairs were shed from each side per cycle. This led to a striking wake pattern with a 'Chinese dragon' appearance.

7.3.3. Pseudo-phase shift

The phase lag between vortex shedding and the forcing oscillation has been examined in previous experiments for cross-flow oscillations. These indicated a sudden jump in the phase difference as the forcing frequency increases across the synchronisation range.

Since the vortex shedding frequency locks in at half the forcing frequency for in-line oscillations a phase difference cannot be defined in precise mathematical terms. A pseudo-phase difference ϕ_L was therefore defined to relate a moment of the lift cycle to a moment of the forcing oscillation. ϕ_L showed a gradual change across the synchronisation range and for all cylinders considered the change was greater at lower amplitudes. This was particularly apparent for the circular and square cylinders at x_ϵ/d=0.05. ϕ_L changed by close to 180° across their respective sychronisation ranges at this amplitude. It is not entirely clear why this pseudo-phase difference does not change as much at higher amplitudes although it is possible that the different shedding modes observed at higher amplitudes in some way compensate for the smaller phase change.

7.4 Further work

In its present format the code could be used to provide further insight into the two-dimensional flows about rectangular cylinders. The Reynolds number dependence of other rectangular cylinders below Re=500 could be studied and the effects of cross flow oscillations could also be examined. In addition the effects of varying the angle of attack on the other rectangular cylinders could be examined although these have already been studied by Sohankar *et al* (1996). However the most valuable new information could be gained by undertaking more qualitative analysis of the simulations. Videos of the near-wake vortex shedding could be combined with time histories of the force coefficients and under oscillatory conditions the phase of the forcing oscillation could also be displayed. For uniform flow, analysis of these videos may reveal a better understanding of the peak in the lift curve which occurs close to B/A=0.3. With the added oscillatory flow component the relationship between the forces, the phase of the oscillatory flow and the mode of vortex shedding may become clearer. Ideally videos should be made under pulsating flow conditions which span the asymmetric resonance range of several cylinders. In this way it is hoped that a greater understanding of the pseudo-phase change phenomenon may be obtained.

Minor adjustments to the code could include the simulation of flows about other geometries. A few projects have already been undertaken to examine the flows about triangular and T-shaped obstacles. These studies simply involved a change to the conformal transformation although since the bodies were polygons they could still use the Schwarz-Christoffel transformations. Further changes to the geometry of the flow could include the addition of external boundaries, although the conformal transformation would lead to very distorted grids with subsequent computational inaccuracies.

More challenging code modifications could involve the implementation of a turbulence model or the adaptation of the code to a fully three-dimensional simulation. The former could be applied directly to the code in its present format and the differences between the simulation and laboratory experiments may provide some useful information on the appearance of 3-D instabilities.

In summary these uniform flow measurements have highlighted the ability of the DVM code to simulate two-dimensional low Reynolds number flows about bluff cylinders at least as well as contemporary DNS calculations such as those by Sohankar *et al* (1996) and Minewitsch *et al* (1994). It is hoped that the recommendations for making a series of videos will be undertaken as the implementation should be straightforward and the results informative. On a more general note solving three-dimensional turbulent flows about bluff obstacles must represent the ultimate goal for bluff body aerodynamicists. Since these flows are characterised by wakes in which vortical structures are dominant the extension of vortex methods to three-dimensional turbulent flow simulations should be encouraged.

APPENDIX A

Conformal Transformation of Rectangle to Strip

A conformal transformation is employed which transfers our physical (x,y) reference frame into a suitably defined computational (ξ,η) plane, periodic in the ξ-direction, in which a rectangular grid can be used and the equations are more easily discretised. As the ξ-axis from 0 to 2π now represents the body surface, boundary conditions can also be more easily applied than in the physical plane. It is desirable to have a non-uniform mesh in the η-direction with more grid points close to the body surface such that the boundary layer region is more satisfactorily resolved. An FFT algorithm is used to solve Poisson's equation and this necessitates that the mesh be uniformly spaced and periodic in one direction. Thus the grid spacing is chosen to be uniform in the ξ-direction.

The Schwarz-Christoffel formulae can be found in many standard textbooks on conformal mapping and complex analysis, e.g. Nehari (1952) and Phillips (1957). They give mappings between the regions exterior and interior of polygons to the regions exterior and interior of circles. Since we can also map from circles onto half-planes or strips a whole series of transformations exist which are useful in the fields of fluid dynamics and electrostatics. The following relationship, taken from Bieberbach (1953), maps the region exterior to the unit circle, $|t|\geq 1$, onto the exterior of a polygon with exterior angles $\alpha_k\pi$:

$$\frac{dz}{dt} = C_{ct}\frac{(t-a_1)^{\alpha_1}(t-a_2)^{\alpha_2}.....(t-a_n)^{\alpha_n}}{t^2}, \tag{A1}$$

where the constant C_{ct} is a complex correction factors which can adjust the polygon size and orientation. The constants a_k and α_k must satisfy the following conditions:

$$\sum \alpha_k = 2, \tag{A2a}$$

$$\sum a_k \alpha_k = 0, \tag{A2b}$$

$$|a_k| = 1. \tag{A2c}$$

The last of these implies that the a_k lie on the unit circle; these are the image points of the polygon vertices.

For a rectangle k=1,..4 and the α_k=1/2. Using symmetry, the vertex image points are chosen to lie at

$$a_1 = \beta + i\gamma,\ a_2 = \beta - i\gamma,\ a_3 = -\beta + i\gamma,\ a_4 = -\beta - i\gamma. \tag{A3}$$

Since the points a_k lie on the unit circle,

$$\beta^2 + \gamma^2 = 1, \tag{A4}$$

and so the expression (A1) simplifies to

$$\frac{dz}{dt} = C_{ct}\frac{\sqrt{t^4 - 2t^2(\beta^2 - \gamma^2) + 1}}{t^2}. \tag{A5}$$

The second stage is to transform from the region exterior to the unit circle onto a strip in the computational (ξ,η) plane. This is accomplished by the mapping

$$t = e^{-i(\Omega - \Omega_0)}, \tag{A6}$$

such that

$$\frac{dt}{d\Omega} = -ie^{-i(\Omega - \Omega_0)}. \tag{A7}$$

Substituting (A6) and (A7) into (A5) leads to an expression (A8) for the transformation from the computational plane $\Omega(\xi,\eta)$ to the physical plane $z(x,y)$:

$$\frac{dz}{d\Omega} = C_{ct}\sqrt{2}\sqrt{cos(2(\Omega - \Omega_0)) - (\beta^2 - \gamma^2)}. \tag{A8}$$

(A8) takes a strip in the computational plane onto the exterior of a general rectangle in the physical plane. However the ratio β/γ does not give the side ratio B/A directly although when β=γ the transformation to the exterior of a square is obtained,

$$\frac{dz}{d\Omega} = C_{ct}\sqrt{2}\sqrt{cos(2(\Omega - \Omega_0))}. \tag{A9}$$

APPENDIX B

Solution of Poisson's Equation

In terms of circulation Poisson's equation is expressed,

$$\left(\frac{\partial^2\psi}{\partial\xi^2}+\frac{\partial^2\psi}{\partial\eta^2}\right)\Bigg|_{i,j}=\frac{-2\Gamma_{i,j}}{\Delta\xi(\eta_{j+1}-\eta_{j-1})}. \tag{B1}$$

A finite difference representation of (B1) would yield a set of coupled linear equations. To obtain a set of uncoupled equations we can take the Discrete Fourier Transform of both sides first. The Discrete Fourier Transforms of functions the ψ, its derivatives and Γ are defined by

$$F(\psi)\equiv\Psi_{k,j}=\sum_{n=0}^{n=NX-1}\psi_{n,j}\,exp\left(\frac{-2\pi ikn}{NX}\right), \tag{B2a}$$

$$F(\Gamma)\equiv\Lambda_{k,j}=\sum_{n=0}^{n=NX-1}\Gamma_{n,j}\,exp\left(\frac{-2\pi ikn}{NX}\right), \tag{B2b}$$

$$F\left(\frac{\partial^2\psi}{\partial\xi^2}\right)\equiv\frac{\partial^2\Psi_{k,j}}{\partial\xi^2}=-k^2\Psi_{k,j}, \tag{B2b}$$

$$F\left(\frac{\partial^2\psi}{\partial\eta^2}\right)\equiv\frac{\partial^2\Psi_{k,j}}{\partial\eta^2}=\frac{2s}{s+1}\left[\frac{\Psi_{k,j+1}-(1+s)\Psi_{k,j}+s\Psi_{k,j-1}}{\Delta\eta_j{}^2}\right]. \tag{B2c}$$

where s is given by:

$$s=\frac{\Delta\eta_j}{\Delta\eta_{j-1}},\qquad\qquad \Delta\eta_j=\eta_{j+1}-\eta_j \tag{B2d}$$

(B2b) is a useful property which follows since the mesh is uniformly spaced in the ξ direction, see Arfken (1985) for a detailed explanation. (B2c) is the finite difference representation for an expanding mesh, derived in Appendix E.

Taking the Fourier Transform of (B1) yields the following expression,

$$\frac{2s}{s+1}(\Psi_{k,j+1}) - (k^2\Delta\eta_j^2 + 2s)\Psi_{k,j} + \frac{2s^2}{s+1}\Psi_{k,j-1} = -\frac{2\Lambda_{k,j}\Delta\eta_j^2}{\Delta\xi(\Delta\eta_j + \Delta\eta_{j-1})}. \tag{B3}$$

(B3) represents a set of linear equations for each value of k and can be written as

$$a_{kj}\Psi_{k,j+1} + b_{kj}\Psi_{k,j} + c_{kj}\Psi_{k,j-1} = d_{kj}. \tag{B4a}$$

The coefficients for this set of equations are given by

$$a_{kj} = \frac{2s}{s+1}, \tag{B4b}$$

$$b_{kj} = -k^2\Delta\eta_j^2 - 2s, \tag{B4c}$$

$$c_{kj} = \frac{2s^2}{s+1}, \tag{B4d}$$

$$d_{kj} = -\frac{2\Lambda_{k,j}\Delta\eta_j^{\,2}}{\Delta\xi(\Delta\eta_j + \Delta\eta_{j+1})}. \tag{B4e}$$

At each value of k the set of tridiagonal equations (B4) can be solved using Gaussian elimination techniques to yield values for $\Psi_{k,j}$. The stream function values, $\psi_{i,j}$, can then be deduced by taking inverse Fourier Transforms,

$$F^{-1}(\Psi) \equiv \psi_{k,j} = \sum_{n=0}^{n=NX-1} \Psi_{n,j}\, exp\left(\frac{2\pi ikn}{NX}\right) \tag{B5}$$

The Fourier Transforms of (B2a) and (B5) are speeded up by using FFT algorithms and these have been set up in the code in such a way that the number of mesh points in the ξ direction must be a power of two.

APPENDIX C

Irrotational Flow Solution

The freestream potential solution for irrotational, inviscid flow about an obstacle is required as this represents the instantaneous solution to the problem when the flow is started impulsively from rest, or equivalently the solution at the first time step. In subsequent time steps the stream function is found as a summation of the potential flow solution and the vorticity flowfield.

The uni-directional flow in an unbounded, inviscid and irrotational fluid has a simple complex potential solution,

$$\Omega(w) = Uw, \tag{C1}$$

where U is fluid velocity and w the complex position.

Transformation to the circular z-plane is achieved by means of the mapping function

$$w = z + \frac{a}{z^2} \tag{C2}$$

in which a is the radius of the circle and thus the complex potential becomes

$$\Omega(w) = U\left(z + \frac{a}{z^2}\right) \tag{C3}$$

The mapping function

$$z = Ae^{-i(\zeta-\zeta_0)} \tag{C4}$$

transforms from the z-plane to the ζ plane and complex potential becomes

$$z = UA(e^{-i(\zeta-\zeta_0)} + e^{i(\zeta-\zeta_0)}) \tag{C5}$$

Now since $\zeta=\xi+i\eta$ and $\zeta_0=\xi_0$ we can derive the result,

$$\Omega(\zeta) = UA\left[\cos(\xi-\xi_0)2\cosh\eta - i\sin(\xi-\xi_0)2\sinh\eta\right] \tag{C6}$$

and hence since $\Omega=\phi+i\psi$,

$$\phi = 2UA\cos(\xi-\xi_0)\cosh\eta \tag{C7a}$$

$$\psi = -2UA\sin(\xi-\xi_0)\sinh\eta \tag{C7b}$$

Considering equation (A9) the constant of the transformation is C_{ct}, since $\sqrt{2}$ is an explicit part of the conformal transformation. Hence the general result for the stream function in potential flow about a square cylinder is given,

$$\psi = -2UC_{ct}\sin(\xi-\xi_0)\sinh\eta \tag{C8}$$

APPENDIX D

Finite Difference Diffusion Scheme

Viscous diffusion has been incorporated into the simulation by splitting the vorticity transport equation (4.1) into convection and diffusion parts. (D1) represents the rate of change of vorticity due to viscous diffusion,

$$\left[\frac{\partial\tilde{\omega}}{\partial t}\right]_{diffusion} = \frac{\nu}{J}\nabla^2\tilde{\omega}. \tag{D1}$$

For the DVM code presented here (D1) is solved on a finite difference mesh, expanding in the η direction but constant in the ξ direction. An explicit difference representation of this equation is given by

$$\frac{\tilde{\omega}_{(i,j)}^{(t+\Delta t)} - \tilde{\omega}_{(i,j)}^{(t)}}{\Delta t} = \frac{\nu}{J_{(i,j)}}(\tilde{\omega}_{\xi\xi}^{(t)} + \tilde{\omega}_{\eta\eta}^{(t)}), \tag{D2}$$

but in the code the diffusion equation is solved explicitly in the ξ direction and uses a parameter, α, to control the degree of implicitness in the η direction.

$$\frac{\tilde{\omega}_{(i,j)}^{(t+\Delta t)} - \tilde{\omega}_{(i,j)}^{(t)}}{\Delta t} = \frac{\nu}{J_{(i,j)}}(\tilde{\omega}_{\xi\xi}^{(t)} + (1-\alpha)\tilde{\omega}_{\eta\eta}^{(t)} + \alpha\tilde{\omega}_{\eta\eta}^{(t+\Delta t)}) \tag{D3}$$

A derivation of the finite difference operators, $\tilde{\omega}_{\xi\xi}$ and $\tilde{\omega}_{\eta\eta}$ is presented in Appendix E. The code uses circulation to define vortex strengths and so (D3) must be altered accordingly. Vorticity and circulation are related as,

$$\tilde{\omega}_{(i,j)} = \frac{2\Gamma_{(i,j)}}{J_{(i,j)}\Delta\xi(\Delta\eta_j + \Delta\eta_{j-1})} \tag{D4}$$

Substituting (D4) into the expressions for $\tilde{\omega}_{\xi\xi}$ and $\tilde{\omega}_{\eta\eta}$ and with some manipulation of the expression (D2) leads to a finite difference diffusion equation in terms of circulation,

$$(1-\alpha\nu\Delta t\Theta^2_{(\eta)})\Delta\Gamma^{(t)}_{(i,j)} = \nu\Delta t(\Theta^2_{(\xi)}+\Theta^2_{(\eta)})\Gamma^{(t)}_{(i,j)}, \tag{D5a}$$

where,

$$\Delta\Gamma^{(t)}_{(i,j)} = \Gamma^{(t+\Delta t)}_{(i,j)} - \Gamma^{(t)}_{(i,j)} \tag{D5b}$$

The operators of (D5) are expressed:-

$$\Theta^2_{(\xi)}\Gamma^t_{(i,j)} = \frac{2}{\Delta\xi^2}\left\{\frac{\Gamma^t_{i-1,j}}{J_{i-1,j}} - \frac{2\Gamma^t_{i,j}}{J_{i,j}} + \frac{\Gamma^t_{i+1,j}}{J_{i+1,j}}\right\}, \tag{D6}$$

$$\Theta^2_{(\eta)}\Gamma^t_{(i,j)} = \frac{2}{\Delta\eta_j}\left\{\frac{s\Gamma^t_{i,j-1}}{J_{i,j-1}(\Delta\eta_{j-1}+\Delta\eta_{j-2})} - \frac{(1+s)\Gamma^t_{i,j}}{J_{i,j}(\Delta\eta_j+\Delta\eta_{j-1})} + \frac{\Gamma^t_{i,j+1}}{J_{i,j+1}(\Delta\eta_{j+1}+\Delta\eta_j)}\right\}, \tag{D7}$$

$$\Theta^2_{(\eta)}\Delta\Gamma^t_{(i,j)} = \frac{2}{\Delta\eta_j}\left\{\frac{s\Delta\Gamma^t_{i,j-1}}{J_{i,j-1}(\Delta\eta_{j-1}+\Delta\eta_{j-2})} - \frac{(1+s)\Delta\Gamma^t_{i,j}}{J_{i,j}(\Delta\eta_j+\Delta\eta_{j-1})} + \frac{\Delta\Gamma^t_{i,j+1}}{J_{i,j+1}(\Delta\eta_{j+1}+\Delta\eta_j)}\right\}. \tag{D8}$$

The system (D5) represents a set of tridiagonal equations which are solved by Gaussian elimination to yield values of $\Delta\Gamma_{(i,j)}$, the change in circulation at each mesh point. These changes are then re-interpolated onto the existing point vortices in a reverse VIC scheme or a new vortex is created at each mesh point with no neighbouring vortices.

APPENDIX E

Finite Difference Approximations for an Expanding Mesh

In order to solve the diffusion equation given by (D1) it is first necessary to form finite difference forms of the second derivatives for meshes with unequal grid spacing. The following work closely follows that given in Minkowycz *et al* (1988) and also Meneghini (1994). Notation is simplified to give a more compact form of equations:

$$s = \frac{\Delta\eta_j}{\Delta\eta_{j-1}}, \qquad \omega_\eta = \left.\frac{\partial\omega}{\partial\eta}\right|_{i,j}, \qquad \omega_{\eta\eta} = \left.\frac{\partial^2\omega}{\partial\eta^2}\right|_{i,j} \tag{E1}$$

The following expressions can be obtained by taking Taylor series expansions of the vorticity at grid points $(i,j+1)$ and $(i,j-1)$,

$$\omega_{i,j+1} = \omega_{i,j} + \omega_\eta \Delta\eta_j + \omega_{\eta\eta}\frac{(\Delta\eta_j)^2}{2!} + \omega_{\eta\eta\eta}\frac{(\Delta\eta_j)^3}{3!} + \ldots\ldots, \tag{E2}$$

$$\omega_{i,j-1} = \omega_{i,j} + \omega_\eta(-\Delta\eta_{j-1}) + \omega_{\eta\eta}\frac{(-\Delta\eta_{j-1})^2}{2!} + \omega_{\eta\eta\eta}\frac{(-\Delta\eta_{j-1})^3}{3!} + \ldots\ldots \tag{E3}$$

Multiplying (E2) by $1/s(s+1)$ and (E3) by $-s/(s+1)$ and adding the two equations yields:-

$$\left.\frac{\partial\omega}{\partial\eta}\right|_{i,j} = \frac{\omega_{i,j+1} + (s^2-1)\omega_{i,j} - s^2\omega_{i,j-1}}{s(s+1)\Delta\eta_{j-1}} + O(\Delta\eta)^2 \tag{E4}$$

Similarly multiplying (E2) by $1/s(1+s)$ and (E3) by $1/(1+s)$ and then adding yields

$$\left.\frac{\partial^2\omega}{\partial\eta^2}\right|_{i,j} = \frac{2s}{(s+1)}\left[\frac{\omega_{i,j+1}-(1+s)\omega_{i,j}+s\omega_{i,j-1}}{\Delta\eta_j^2}\right]+O(\Delta\eta)^2, \tag{E5}$$

or equivalently using the definition in (E1),

$$\omega_{\eta\eta} = \frac{2}{(\Delta\eta_j+\Delta\eta_{j-1})}\left[\frac{\omega_{i,j+1}-\omega_{i,j}}{\Delta\eta_j}-\frac{\omega_{i,j}-\omega_{i,j-1}}{\Delta\eta_{j-1}}\right]+O(\Delta\eta)^2. \tag{E6}$$

A similar expression can be derived for $\omega_{\xi\xi}$ noting that the mesh spacing is invariant in the ξ direction, i.e. $\Delta\xi$ is constant,

$$\omega_{\xi\xi} = \frac{\omega_{i+1,j}-2\omega_{i,j}+\omega_{i-1,j}}{\Delta\xi^2}+O(\Delta\xi)^2. \tag{E7}$$

APPENDIX F

Surface Pressure Calculation Scheme

Voke and Collins (1984) have expressed the momentum equations for an incompressible, constant viscosity flow with no body force in a generalised coordinate system as

$$\partial_t u^i = -g^{ij}\partial_j P + 2u^j \omega^i_j - 2\nu J^{-1}\partial_j (J\omega^{ij}) \tag{F1}$$

where for convenience the expression for total pressure, P, has been used to simplify (F1).

$$P = \frac{p}{\rho} + \frac{u^i u_i}{2} \tag{F2}$$

with the covariant vorticity tensor defined as

$$2\omega_{ij} = \partial_i u_j - \partial_j u_i \tag{F3}$$

However in the Hybrid DVM presented here vorticity, $\tilde{\omega}$, has been defined differently,

$$\tilde{\omega} = \frac{1}{J}\left(\frac{\partial u_2}{\partial \xi^1} - \frac{\partial u_1}{\partial \xi^2}\right) \tag{F4}$$

Certain relationships between the metric tensor, g_{ij}, Jacobian, J, and the vorticity tensor, ω_{ij}, must be stated before a form of (F1) can be derived which is appropriate for the calculation of surface pressures.

$$g^{12} = g^{21} = 0,\ J = (g^{11}g^{22})^{-1/2},\ \omega^{11} = \omega^{22} = \omega^1_1 = \omega^2_2 = 0,\ \ \omega^{12} = -\omega^{21} \tag{F5}$$

$$u_1 = Ju^1,\ \ u_2 = Ju^2 \tag{F6}$$

$$\omega_{kj} = g_{ki}\omega^i_j = g_{ki}g_{jl}\omega^{il},\ \ \omega_{12} = J^2\omega^{12} \tag{F7}$$

The two definitions of vorticity are related by the expression

$$\omega_{12} = \frac{J\tilde{\omega}}{2} \tag{F8}$$

The expressions (F4)-(F8) allow the derivation of a form of the momentum equations (F1) which uses vorticity, $\tilde{\omega}$, as defined in the hybrid DVM and the contravariant form of velocity, u^i.

$$\partial_t u^i = -g^{ij}\partial_j P + 2u^j g^{ik}\omega_{kj} - 2\nu J^{-1}\partial_j (Jg^{il}g^{jk}\omega_{lk}) \tag{F9}$$

Putting i=1 and i=2 yields the following pair of equations,

$$\partial_t u^1 = -g^{11}\partial_1 P + 2u^2 g^{11}\omega_{12} - 2\nu J^{-1}\partial_2 (Jg^{11}g^{22}\omega_{12}) \tag{F10a}$$

$$\partial_t u^2 = -g^{22}\partial_2 P + 2u^1 g^{22}\omega_{21} - 2\nu J^{-1}\partial_1 (Jg^{22}g^{11}\omega_{21}) \tag{F10b}$$

Making further use of the earlier expressions and noting that

$$\dot{\xi} = u^1, \quad \dot{\eta} = u^2 \tag{F11}$$

we obtain:

$$\frac{\partial \dot{\xi}}{\partial t} = -\frac{1}{J}\frac{\partial P}{\partial \xi} + \dot{\eta}\tilde{\omega} - \frac{\nu}{J}\frac{\partial \tilde{\omega}}{\partial \eta} \tag{F12a}$$

$$\frac{\partial \dot{\eta}}{\partial t} = -\frac{1}{J}\frac{\partial P}{\partial \eta} - \dot{\xi}\tilde{\omega} + \frac{\nu}{J}\frac{\partial \tilde{\omega}}{\partial \xi} \tag{F12b}$$

These expressions can then be given in the form given by equations (4.25).

APPENDIX G

Input Files for Vortex Code

The three input files used in the DVM code are listed below together with typical input values. A description of each variable is listed on the following page. The appendix concludes with two Tables. In Table G.1 the corresponding values of γ^2 and *B/A* are given. In Table G.2 the input parameters used for the flows simulated this study are given.

sqdata1		
GAMMASQ	MY	NX
NRUN	DT	Re
XeH	FeH	STRHL
ALPHA	XeV	FeV

sqdata1		
0.3465	128	128
75000	0.0002	1000
0.2	2.4	0.154
0.0	0.0	0.0

sqdata2				
SFR	ITER	EXIN	EXOUT	UPJACK
RNU	TOR	ALAM	BETA	CUTOFF

sqdata2				
0.0	1	0.04	125	0.01
0.01	0.0	1.0	1.0	0.0002

sqdata3			
JFORCE	JUGGLE	JVORT	JLIMIT
JSTART	JFINISH	JOFTEN	JCONT

sqdata3			
1	50	1	125
75000	75000	1	0

ALAM	specifies type of vorticity boundary condition (Equation 4.19 used in all calculations for this study)
ALPHA	angle of incidence of obstacle (α)
BETA	degree of implicitness/explicitness in diffusion solver
CUTOFF	vortex cutoff strength (σ_{min})
DT	time step (Δt)
EXIN	distance of first mesh out from body surface (M_{in})
EXOUT	distance of outer mesh from body surface (M_{out})
FeH	in-line forcing frequency (f_e/f_0)
FeV	cross-flow forcing frequency (not used in this study)
GAMMASQ	controls side ratio (γ^2 see Table G.1)
ITER	number of iterations per time step in diffusion solver (not used in this study)
JCONT	output all data required for run continuation at end of simulation (1=YES, 0=NO)
JFINISH	last vortex data output at JFINISH timestep (see also JOFTEN and JSTART)
JFORCE	print force coefficents (1=yes, 0=no)
JLIMIT	output data on all vortices for which $\eta_k < \eta_{jlimit}$
JOFTEN	vortex data output given every JOFTEN timesteps (see also JSTART and JFINISH)
JSTART	first vortex data output at JSTART timestep (see also JFINISH and JOFTEN)
JUGGLE	output force coefficient data every JUGGLE timesteps
JVORT	output of vortex data (1=YES, 0=NO)
MY	number of grid points in η direction (MY)
NRUN	number of timesteps for simulation (NT)
NX	number of grid points in ξ direction (NX)
Re	Reynolds number of simulation (Re)
RNU	kinematic viscosity of fluid (ν)
SFR	controls velocity evaluation at outer boundary
STRHL	Strouhal number of flow under uniform flow conditions (St_0)
TOR	start time of run (only used if continuation of previous run)
UPJACK	lower limit on Jacobian value (J_{lim})
XeH	amplitude of in-line pulsations (x_e/d)
XeV	amplitude of cross flow pulsations (not used in this study)

B/A	γ^2
4.000	0.2184
3.000	0.2673
2.500	0.3016
2.000	0.3465
1.700	0.3809
1.620	0.3914
1.500	0.4084
1.000	0.5000
0.667	0.5916
0.617	0.6086
0.588	0.6191
0.500	0.6535
0.400	0.6984
0.333	0.7327
0.250	0.7816
0.200	0.8151
0.100	0.8945

Table G.1 Variation of $\gamma^2$with side ratio, some specific cases.

B/A	Δt	NT	M_{in}	M_{out}	σ_{min}	J_{lim}	$U_0.\Delta t.NT/A$
0.1	0.0040	150,000	0.005	125	0.0010	0.01	106.25
0.2	0.0050	120,000	0.010	125	0.0010	0.01	135.30
0.5	0.0050	65,000	0.020	130	0.0010	0.01	124.40
0.62	0.0050	55,000	0.025	130	0.0002	0.01	123.80
1.0*	0.0050	36,000	0.025	130	0.0002	0.01	125.40
2.0	0.0010	80,000	0.025	130	0.0001	0.01	122.41
3.0	0.0005	90,000	0.040	130	0.0001	0.01	118.62

Table G.2 Input parameters used in Hybrid DVM

***B/A=1.0 cylinders at an angle of attack used the same parameters**

APPENDIX H

Stream Function Outer Boundary Condition

The stream function outer boundary condition can be calculated by adding the potential flow solution to a Biot-Savart summation that includes a contribution from each individual vortex particle. All the results presented in Chapters 5 and 6 have neglected this Biot-Savart term. By neglecting the Biot-Savart contribution one is imposing a symmetry condition at the outer boundary. It has been suggested by Stansby (1998, personal communication) that the effect of imposing symmetry may be to fix the forward stagnation point. This could consequently change the nature of the vortex shedding leading to higher induced forces and/or a change in the shedding frequency. It is interesting to note that in Figure 2.11 the upstream stagnation point is clearly located away from the centre line. However there are two fundamental differences between the results of Ohya (1994) and the DVM simulations. Firstly the Reynolds number is much higher in the laboratory-based study but more importantly since Ohya's study is laboratory based the alignment of the rectangle cannot be exactly perpendicular to the flow. A slight misalignment could encourage the stagnation point to favour one side as appears to be the case in Figure 2.11.

The purpose of this Appendix is to investigate the effect of neglecting the Biot-Savart contribution and the implications with respect to the results presented in Chapters 5 and 6. A derivation of the theory used to obtain the stream function boundary condition is given first. This is followed by a direct comparison of the mean measured parameters for a range of simulations. Finally the implications of any differences are discussed.

The boundary condition for the stream function is applied in the computational ($\zeta=\xi+i\eta$) plane. This domain is periodic in the ξ-direction with a period of 2π. The periodicity must be considered since it implies infinite rows of vortices rather than a single vortex. A distribution of NV vortices given by strength Γ_k positioned at ξ_k, η_k thus becomes a distribution of NV infinite vortex rows.

Rutherford (1966, p84) has derived an expression for the stream function for an infinite row of vortices in which one vortex is placed at the origin. If the period in the ξ-direction is 2π this can be written as

$$\psi = \frac{\Gamma}{4\pi} log \frac{1}{2}\{cosh\eta - cos\xi\} \qquad \text{(H1)}$$

If each vortex in the row is displaced by ξ_k, η_k the expression becomes:

$$\psi = \frac{\Gamma_k}{4\pi} log \frac{1}{2}\left\{cosh(\eta - \eta_k) - cos(\xi - \xi_k)\right\} \tag{H2}$$

The contribution due to an infinite row of image vortices must also be considered. A major advantage of making this calculation in the computational plane is that the image vortices are simply located. For vortices of strength $-\Gamma_k$ displaced by ξ_k, $-\eta_k$ expression (H1) becomes:

$$\psi = \frac{-\Gamma_k}{4\pi} log \frac{1}{2}\left\{cosh(\eta + \eta_k) - cos(\xi - \xi_k)\right\} \tag{H3}$$

Combining expressions (H2) and (H3) and summing for all the *NV* vortices yields

$$\psi = \sum_{k=1}^{NV} \frac{\Gamma_k}{4\pi} log\left\{\frac{cosh(\eta - \eta_k) - cos(\xi - \xi_k)}{cosh(\eta + \eta_k) - cos(\xi - \xi_k)}\right\} \tag{H4}$$

In the code calculations are made in terms of mesh vorticity values, as this is less computationally expensive.

Results from the uniform flow simulations are given in Tables H.1 (a) and (b). The results indicate a maximum difference in the Strouhal number of around 3% and in the mean drag of approximately 5%. A greater difference in the rms lift of around 20% is found. However these differences are only significant at the lower values of *B/A*. Under oscillatory flow it was thus decided to perform additional runs on the lower *B/A* cases. Results from these are shown in Tables H.1 (c) and (d). The differences are less significant under pulsating flow.

Videos of the flow with and without the Biot-Savart contribution may be viewed at the following World Wide Web address: *http://vortex.mech.surrey.ac.uk/FluidsGroup/People/steggel*
The videos do not give any indication for the movement of the upstream stagnation position due to the change in the boundary condition. However it is possible that any change is too small to detect by visual interpretation.

Some overall conclusions can now be stated. The inclusion of the Biot-Savart contribution does have some effect on the mean measured parameters. However this effect is only significant when considering $C_{L(rms)}$ and for rectangles with side ratio $B/A<1.0$. Comparison can be made with Figures 5.2 and 5.4 which indicates that the calculated values still fall well within the range of numerical and experimental scatter. One should also appreciate that $C_{L(rms)}$ is a difficult quantity to determine with any confidence as has been shown in this study and in the DNS calculations of Sohankar *et al* (1996). Under pulsating flow conditions the differences appear to be less significant. On the whole one may therefore state that the general conclusions reached in Chapters 5 and 6

have not been affected by neglecting the Biot-Savart contribution. However if further simulations are to be made for rectangles with $B/A<1.0$ it would certainly be advisable to include this term.

	$B/A=0.5$		$B/A=0.62$		$B/A=1.0$	
	without	with BS	without	with BS	without	with BS
St	0.183	0.188	0.174	0.178	0.152	0.149
C_D	2.02	2.12	1.79	1.88	1.46	1.46
$C_{L(rms)}$	0.66	0.78	0.58	0.71	0.40	0.44

(a) Uniform flow, B/A=0.5, 0.62 and 1.0; Re=200.

	$B/A=2.0$		$B/A=3.0$	
	without	with BS	without	with BS
St_s	0.166	0.166	0.161	0.161
C_D	1.16	1.16	1.05	1.07
$C_{L(rms)}$	0.20	0.22	0.21	0.25

(b) Uniform flow, B/A=2.0, 3.0; Re=200.

	$f_e/f_0=1.5$		$f_e/f_0=2.3$	
	without	with BS	without	with BS
St_s	0.154	0.151	0.177	0.173
C_D	1.68	1.63	1.81	1.86
$C_{L(rms)}$	0.60	0.59	0.68	0.75

(c) Oscillatory flow, x_c/d=0.30, B/A=1.0, Re=200.

	$f_e/f_0=1.4$		$f_e/f_0=1.6$	
	without	with BS	without	with BS
St_s	0.121	0.125	0.140	0.143
C_D	2.54	2.59	2.57	2.69
$C_{L(rms)}$	1.07	1.15	0.93	1.03

(d) Oscillatory flow, x_c/d=0.30, B/A=0.62, Re=200.

Table H.1. Comparison of mean measured values for simulations with and without the Biot-Savart boundary condition.

References

Acheson, D.J. (1990) Elementary Fluid Dynamics, *Clarendon Press, Oxford.*

Al-Asmi, K. (1992) Vortex shedding in oscillatory flow, *PhD Thesis, University of Surrey.*

Al-Asmi, K., and Castro, I.P. (1992) Vortex shedding in oscillatory flow: geometrical effects, *Journal of Flow Measurement and Instrumentation*, **3**(3), 187-201.

Arfken, G. (1985) Mathematical Methods for Physicists, *Academic Press*, Third Edition.

Aris, R. (1962) Vectors, Tensors and the Basic Equations of Fluid Mechanics, *Prentice Hall, London.*

Barbi, C., Favier, D.P., and Maresca, C.A. (1986) Vortex shedding and lock-on of a circular cylinder in oscillatory flow, *Journal of Fluid Mechanics*, **170**, 527-544.

Bearman, P.W. (1984) Vortex shedding from oscillating bluff bodies, *Annual Review of Fluid Mechanics*, **16**, 195-222.

Bearman, P.W., and Trueman, D.M. (1972) An investigation of the flow around rectangular cylinders, *Aeronautical Quarterly*, 229-237.

Bieberbach (1953) Conformal Mapping, *Chelsea Publishing Company, New York.*

Borthwick, A.G.L., and Herbert, D.M. (1990) Resonant and non-resonant behaviour of a flexibly mounted cylinder in waves, *Journal of Fluids and Structures*, **4**, 495-518.

Chang, C.C., and Chern, R.L. (1991) Numerical study of flow around an impulsively started cylinder by a deterministic vortex method, *Journal of Fluid Mechanics* **233**, 243-263.

Chorin, A.J. (1973) Numerical study of slightly viscous flow, *Journal of Fluid Mechanics* **57**(4), 785-796.

Christiansen, J.P. (1973) Numerical simulation of hydromechanics by the method of point vortices, *Journal of Computational Physics*, **13**, 363-379.

Chua, K., and Quackenbush, T.R. (1993) Fast three-dimensional vortex method for unsteady wake calculations, *AIAA Journal*, **31**(10), 1957-1958.

Clarke, N.R., and Tutty, O.R. (1994) Construction and validation of a discrete vortex method for the two-dimensional Navier-Stokes equations, *submitted to Computers and Fluids.*

Clements, R.R. (1973) An inviscid model of two-dimensional vortex shedding, *Journal of Fluid Mechanics* **57**(2), 321-336.

Copeland, G.S., and Cheng B.H. (1995) Hysteretic vortex shedding from an oscillating cylinder, *in Flow Induced Vibration, ed. Bearman, Balkema, Rotterdam*, 221-230.

Couet, B., and Buneman, O. (1981) Simulation of three-dimensional incompressible flows with a vortex-in-cell method, *Journal of Computational Physics*, **39**, 305-328.

Davis, R.W., and Moore, E.F. (1982) A numerical study of vortex shedding from rectangles, *Journal of Fluid Mechanics*. **116**, 475-506.

Davis, R.W., Moore, E.F., and Purtell, L.P., (1983) A numerical-experimental study of confined flow around rectangular cylinders, *Physics of Fluids* **27**, 46-59.

Dolan, P.S., Graham, J.M.R., and Young, J.A. (1990) Computation of unsteady two-dimensional separated flow using hybrid mesh techniques, *Journal of the American Society of Mechanical Engineers, Fluids Engineering Division*, **92**, 33-40.

Doorly, D.J. and Liu, C.H. (1994) Application of a 3-D vortex particle in cell computational method to free and wall bounded shear flows, *Proc. Symposium on Boundary Layer and Free Shear Flows, ASME (FED)*, **184**, 163-172.

Franke, R., Rodi, W., and Schonung, B. (1990) Numerical calculation of laminar vortex shedding flows past cylinders, *Journal of Wind Engineering and Industrial Aerodynamics*, **35**, 237-257.

Gartshore, I.S. (1984) Some effects of upstream turbulence on the unsteady lift forces imposed on prismatic two-dimensional bodies, *Transactions of the ASME, Journal of Fluids Engineering*, **106**, 418-424.

Gerrard, J.H. (1967) Numerical computation of the magnitude and frequency of the lift on a circular cylinder. *Phil. Trans. Roy. Soc.* **261**(118), 137-162.

Goldstein, S. (1965) Modern Developments in Fluid Dynamics, *Volumes I and II, Clarendon Press, Oxford.*

Graham, J.M.R. (1988) Computation of viscous separated flow using a particle method. *Numerical methods for fluid dynamics III. Clarendon Press, Oxford,* 311-317.

Graham, J.M.R. (1994) *Private Communication.*

Graham, J.M.R. and Arkell, R.H. (1994) Effects of surface waves on vortex shedding from cylinders, *Internal Report, Department of Aeronautics, Imperial College of Science and Technology, UK.*

Griffin, O.M. and Hall, M.S. (1995) Vortex shedding lock-on in a circular cylinder wake, *in Flow Induced Vibration, ed. Bearman, Balkema, Rotterdam*, 3-14.

Griffin, O.M. and Ramberg (1976) Vortex shedding from a cylinder vibrating in line with an incident uniform flow, *Journal of Fluid Mechanics*. **75(2)**, 257-271.

Ham, N.D. (1968) Aerodynamic loading on a two-dimensional airfoil during dynamic stall. *AIAA Journal* **6**(10), 1927-1934.

Henderson, R.W., and Barkley, D. (1996) Secondary Instability in the wake of a circular cylinder, *Physics of Fluids*, **8**(6), 1683-1685.

Kiya, M. (1992) Numerical simulation of three-dimensional vortex motion, *Proceedings of The Fifth Asian Congress on Fluid Mechanics, Aug. 1992, Taejon, Korea,* 431-438.

Knisely, C.W. (1990) Strouhal numbers of rectangular cylinders at incidence: A review and new data, *Journal of Fluids and Structures*, **4**, 371-393.

Kuethe, A.M., and Chow, C.Y. (1986) Foundations of Aerodynamics, *John Wiley, Chichester.*

Laneville, A., and Yong, L.Z. (1983) Mean flow patterns around two-dimensional rectangular cylinders and their interpretation, *Journal of Wind Engineering and Industrial Aerodynamics*, **14**, 387-398.

Launder, B.E. and Kato, M. (1993) Modelling flow-induced oscillations in turbulent flow around a square cylinder, *Journal of the American Society of Mechanical Engineers, Fluids Engineering Division*, **157**, 189-199.

Laurence, D. and Mattei, J-D. (1993) Current state of computational bluff body aerodynamics, *Journal of Wind Engineering and Industrial Aerodynamics*, **49**, 23-44.

Leonard, A. (1980) (Review of) Vortex methods for flow simulation, *Journal of Computational Physics*. **37**, 289-335.

Leonard, A. (1985) Computing three-dimensional incompressible flows with vortex elements, *Annual Review of Fluid Mechanics*. **17**, 523-529.

Lewis, R. I. (1995) Vortex element methods for fluid dynamic analysis of engineering systems, *Cambridge University Press*.

Longuet-Higgins, M.S. (1981) Oscillating flow over steep sand ripples, *Journal of Fluid Mechanics*. **107**, 1-35.

Meneghini, J.R. (1994) Discrete Vortex Method incorporating viscous diffusion, *PhD thesis, Imperial College*.

Meneghini, J.R., and Bearman, P.W. (1993) Numerical simulation of high amplitude oscillatory flow about a circular cylinder using a discrete vortex method, *AIAA Shear Flow Conference, July 6-9, 1993, Orlando, AIAA paper* **93-3288**.

Minewitsch, S., Franke, R., and Rodi, W. (1994) Numerical investigation of laminar vortex-shedding flow past a square cylinder oscillating in line with the mean flow, *Journal of Fluids and Structures*, **8**, 787-802.

Minkowycz, C.J, Sparrow, E.M., Schneider, G.E., and Pletcher, R.H. (1988) Handbook of Numerical Heat Transfer, *John Wiley and Sons, Chichester*.

Morton, B.R., (1984) The generation and decay of vorticity, *Geophysics, Astrophysics and Fluid Dynamics*, **28**, 277-308.

Nagano, S., Naito, M., and Takata, H. (1982) A numerical analysis of two-dimensional flow past a rectangular prism by a discrete vortex model, *Computers and Fluids*, **10**(4), 243-259.

Nakamura, Y. (1993) Bluff body aerodynamics and turbulence, *Journal of Wind Engineering and Industrial Aerodynamics*, **49**, 65-78.

Nakamura, Y., and Ohya, Y. (1984) The effects of turbulence on the mean flow past two-dimensional rectangular cylinders, *Journal of Fluid Mechanics*, **149**, 255-273.

Nakamura, Y., Ohya, Y., and Tsuruta, H. (1991) Experiments on vortex shedding from flat plates with square leading and trailing edges, *Journal of Fluid Mechanics*, **222**, 437-447.

Nakayama, R., Nakamura, Y., Ohya, Y., and Ozono, S. (1993) A numerical study on the flow around flat plates at low Reynolds numbers, *Journal of Wind Engineering and Industrial Aerodynamics*,

Nehari, Z. (1952) Conformal Mapping, *McGraw-Hill, New York*.

Norberg, C. (1986) Interaction between freestream turbulence and vortex shedding for a single tube in cross-flow, *Journal of Wind Engineering and Industrial Aerodynamics*, **23**, 501-514.

Norberg, C. (1993) Flow around rectangular cylinders: Pressure forces and wake frequencies, *Journal of Wind Engineering and Industrial Aerodynamics*, **49**, 187-196.

Norberg, C. (1996) Private Communication.

Oertel, H. (1990) Wakes behind blunt bodies, *Annual Review of Fluid Mechanics*, **22**, 539-564.

Ogami, Y., and Akamutso, T. (1991) Viscous flow simulation using the discrete vortex model -The diffusion velocity method, *Computers and Fluids*, **19**(3/4), 433-441.

Ohya, Y. (1994) A note on the discontinuous change in wake pattern for a rectangular cylinder, *Journal of Fluids and Structures*, **8**, 325-330.

Ohya, Y., Nakamura, Y., Ozono, S., Tsuruta, H., and Nakayama, R. (1992) A numerical study of vortex shedding from flat plates with square leading and trailing edges, *Journal of Fluid Mechanics*, **236**, 445-460.

Okajima, A. (1982) Strouhal numbers of rectangular cylinders, *Journal of Fluid Mechanics*, **123**, 379-398.

Okajima, A. (1990) Numerical simulation of flow around rectangular cylinders, *Journal of Wind Engineering and Industrial Aerodynamics*, **33**, 171-180.

Okajima, A. (1995) Numerical analysis of the flow around an oscillating cylinder, *in Flow Induced Vibration, ed. Bearman, Balkema, Rotterdam*, 159-166.

Okajima, A., and Kitajima, K. (1993) Numerical study on aeroelastic instability of cylinders with a circular and rectangular cross-section, *Journal of Wind Engineering and Industrial Aerodynamics*, **46-47**, 541-550.

Okajima, A., Kitajima, K. and Ueno, H. (1993) Numerical study on wake patterns and aerodynamic forces of an oscillating cylinder with a circular and rectangular cross-section, *Journal of Wind Engineering and Industrial Aerodynamics*, **50**, 39-48.

Ongoren, A., and Rockwell, D. (1988a) Flow structure from an oscillating cylinder. Part 1. Mechanisms of phase shift and recovery in the near wake, *Journal of Fluid Mechanics* **191**, 197-223.

Ongoren, A., and Rockwell, D. (1988b) Flow structure from an oscillating cylinder. Part 2. Mode competition in the near wake, *Journal of Fluid Mechanics* **191**, 225-245.

Phillips, E.G. (1957) Functions of a complex variable, *Oliver and Boyd, Edinburgh and London.*

Roache, P. (1976) Computational Fluid Dynamics, *Hermosa Publishers, New Mexico.*

Roshko, A. (1993) Perspectives on bluff body aerodynamics, *Journal of Wind Engineering and Industrial Aerodynamics*, **49**, 79-100.

Rutherford, D.E. (1966) Fluid Dynamics, *Oliver and Boyd, Edinburgh and London.*

Sarpkaya, T. (1975) An inviscid model of two-dimensional vortex shedding for transient and asymptotically steady separated flow over an inclined plate, *Journal of Fluid Mechanics* **68**(1), 109-128.

Sarpkaya, T. (1979a) Vortex-induced oscillations, a selective review, *Transactions of the ASME, Journal of Applied Mechanics*, **46**, 241-257.

Sarpkaya, T. (1979b) Inviscid model of two-dimensional vortex shedding by a circular cylinder, *AIAA Journal*, **17**(11), 1193-1199.

Sarpkaya, T. (1988) Computational methods with vortices:- The 1988 Freeman scholar lecture, *Journal of Fluids Engineering*, **111**, 5-52.

Sarpkaya, T., (1994), "Vortex Element Methods for Flow Simulation," *Advances in Applied Mechanics*, **31**, 113-247.

Sarpkaya, T. and Schoaff (1979) Inviscid model of two-dimensional vortex shedding by a circular cylinder, *AIAA Journal*, **17(11)**, 1193-1200.

Scolan, Y.M., and Faltinsen, O.M. (1994) Numerical studies of separated flow from bodies with sharp corners by the vortex in cell method, *Journal of Fluids and Structures*, **8**, 201-230.

Smith, P.A., and Stansby P.K. (1988) Impulsively started flow around a circular cylinder by the vortex method, *Journal of Fluid Mechanics*, **194**, 45-77.

Smith, P.A., and Stansby P.K. (1991) Viscous oscillatory flows around cylindrical bodies at low Kuelegan-Carpenter numbers using the vortex method, *Journal of Fluids and Structures*, **5**, 339-361.

Sohankar, A., Norberg, C., and Davidson, L. (1996) Numerical simulation of unsteady low Reynolds number flow about rectangular cylinders at incidence, *Presented at the Third International Colloquium on Bluff Body Aerodynamics and Applications, July 1996, Virginia.*

Stansby, P.K. and Slaouti, A. (1993) Simulation of vortex shedding including blockage by the random-vortex and other methods, *International Journal for Numerical Methods in Fluids*, **17**, 1003-1013.

Steggel, N. and Rockliff, N.J. (1997) Simulation of the effects of body shape on lock-in characteristics in pulsating flow by the discrete vortex method, *Journal of Wind Engineering and Industrial Aerodynamics*, **69-71**, 317-329.

Summers, D.M., Hanson, T., and Wilson, C.B. (1985) A random vortex simulation of wind-flow over a building, *Internal Report, Dept. of Architecture, University of Edinburgh, Scotland.*

Utsunomiya, H., Nagao, F., Tojo, K., and Asano, K. (1995) Yaw angle effect on the vortex induced oscillation of a rectangular cylinder, *in Flow Induced Vibration, ed. Bearman, Balkema, Rotterdam*, 55-60.

Van Dyke, M. (1982) An Album of Fluid Motion, *The Parabolic Press, Stanford.*

Voke, P.R., and Collins M.W. (1984) Forms of the generalised Navier-Stokes equations, *Journal of Engineering Mathematics*, **18**, 219-233.

Williamson, C.H.K. (1996a) Vortex dynamics in the cylinder wake, *Annual Review of Fluid Mechanics*, **28**, 477-539.

Williamson, C.H.K. (1996b) Mode A secondary instability in wake transition, *Physics of Fluids*, 8(6), 1680-1682.

Williamson, C.H.K., and Roshko, A. (1988) Vortex formation in the wake of an oscillating cylinder, *Journal of Fluids and Structures*, **2**, 355-381.

Wolochuk, M.C., Plesniak, M.W., and Braun, J.E. (1994) The effects of turbulence and unsteadiness on the performance of vortex shedding flow meters, *Journal of the American Society of Mechanical Engineers, Fluids Engineering Division*, **183**, 1-8.

Wolochuk, M.C., Plesniak, M.W., and Braun, J.E. (1996) The effects of unsteadiness on vortex shedding from sharp-edged bluff bodies, *Transactions of the ASME, Journal of Fluids Engineering*, **118**, 18-25.

Wu, J.C., and Sankar, N.L. (1980) Aerodynamic force and moment in steady and time dependent viscous flows *AIAA paper* **80-0011**.

Xi-yun, L., Bing-gang, T., Li-xuan, Z. and Xie-yuan, Y. (1994) Numerical study on the vortex structures in the wake of an oscillating circular cylinder in uniform flow, *Journal of Hydrodynamics, Series B*, **1**, 12-22

Yeung, R.M, and Vaidhyanathan, M. (1993) Flow past oscillating cylinders, *Journal of Offshore Mechanics and Arctic Engineering, Trans. ASME*, **115**, 197-205.

Zaki, T.G., Sen, M. and Gad-el-Hak, M. (1994) Numerical and experimental investigation of flow past a freely rotatable square cylinder, *Journal of Fluids and Structures*, **8**, 555-582.

Bibliography

Anagnastopoulos, P., Iliadis, G. and Ganoulis, J. (1995) Flow and response parameters of a circular cylinder vibrating in-line with the oscillating stream, *in Flow Induced Vibration, ed. Bearman, Balkema, Rotterdam*, 167-179.

Barnard, R.H., and Philpott, D.R. (1989) Aircraft Flight, *Longman Scientific and Technical, Essex.*

Bearman, P.W., Graham, J.M.R., Lin, X.W., and Meneghini, J.R. (1995) Numerical simulation of flow-induced vibration of a circular cylinder in uniform and oscillatory flow, *in Flow Induced Vibration, ed. Bearman, Balkema, Rotterdam*, 231-240.

Bearman, P.W., and Obasaju, E.D. (1982) An experimental study of pressure fluctuations on fixed and oscillating square-section cylinders, *Journal of Fluid Mechanics*, **119**, 297-321.

Bearman, P.W., and Takamoto, M. (1988) Vortex shedding behind rings and discs, *Fluids Dynamics Research*, 214-218.

Blackburn, H.M., and Melbourne, W.H. (1992) Lift on an oscillating cylinder in smooth and turbulent flow, *Journal of Wind Engineering and Industrial Aerodynamics*, **41-44**, 79-90.

Braza, M., Chassaing, P., and Ha Minh, H. (1986) Numerical study and physical analysis of the pressure and velocity fields in the near wake of a circular cylinder, *Journal of Fluid Mechanics* **165** ,79-130.

Deng, G.B., Piquet, J. Queuety, P., and Visonneau, M. (1994) 2-D computations of unsteady flow past a square cylinder with the Baldwin-Lomax model, *Journal of Fluids and Structures*, **8**, 663-680.

Deniz, S., and Staubli, T. (1995) An oscillating rectangular profile and its vortex formations, *in Flow Induced Vibration, ed. Bearman, Balkema, Rotterdam*, 15-25.

Downie, M.J., and Graham, J.M.R. (1995) Effects of transverse vibration on the hydrodynamic damping of an oscillating bluff body, *in Flow Induced Vibration, ed. Bearman, Balkema, Rotterdam*, 213-220.

Efthymiou, M. and Narayanan, R. (1982) Current-induced forces on submarine pipelines: a discrete vortex model. *Proc. Inst. Civil Engineers* **73**(2), 109-123.

Guocan, L. (1992) Numerical study on bluff body flow structures, *Proceedings of The Fifth Asian Congress on Fluid Mechanics, Aug. 1992, Taejon, Korea*, 326-335.

Hansen E.A. (1993) A note on diffusion of vorticity in the discrete vortex method, *Institute of Hydrodyn. and Hydraulic Eng., Tech. Univ. Denmark, Progress Report no.***74**, 11-23.

Kondo, N., and Yamada, S. (1995) Third-order upwind finite element computation of the incompressible Navier-Stokes equations. Part I: Computation of flow around rectangular cylinders, *Computer Methods in Applied Mechanics and Engineering*, **127**, 87-97.

Kondo, N., and Yamada, S. (1995) Third-order upwind finite element computation of the incompressible Navier-Stokes equations. Part II: Aerodynamic characteristics of a rectangular cylinder with an angle of attack, *Computer Methods in Applied Mechanics and Engineering*, **127**, 99-113.

Kwon, K. and Choi, H. (1995) Control of laminar vortex shedding behind a circular cylinder using splitter plates, *Physics of Fluids*, **8**(2), 479-486

Lam, K.M. (1996) Phase-locked eduction of vortex shedding in flow past an inclined flat plate, *Physics of Fluids*, **8**(5), 1159-1168.

Luo, S.C. and Bearman P.W. (1990) Predictions of fluctuating lift on a transversely oscillating square section cylinder, *Journal of Fluids and Structures*, **4**, 219-228.

Luo, S.C., Yazdani, Md.G., Chew, Y.T., and Lee, T.S. (1994) Effects of incidence and afterbody shape on flow past bluff cylinders, *Journal of Wind Engineering and Industrial Aerodynamics*, **53**, 375-399.

Meneghini, J.R., and Bearman, P.W. (1995) Numerical simulation of high amplitude oscillatory flow about a circular cylinder, *Journal of Fluids and Structures,* **9**, 435-455.

Meneghini, J.R., and Bearman, P.W. (1996) An investigation of the effect on vortex shedding of a sudden transverse disturbance applied to a circular cylinder, *Presented at the Third International Colloquium on Bluff Body Aerodynamics and Applications, July 1996, Virginia.*

Moorty, S., and Olson, M.D. (1989) A numerical study of low Reynolds number fluid-structure interaction, *Journal of Fluids and Structures*, **3**, 37-60.

Murakami, S. and Mochida, A. (1995) On turbulent vortex shedding flow past 2D square cylinder predicted by CFD, *Journal of Wind Engineering and Industrial Aerodynamics*, **54/55**, 191-211.

Nakamura, Y. (1994) Galloping of a circular cylinder in the presence of a splitter plate, *Journal of Fluids and Structures*, **8**, 355-365.

Nakamura, Y. (1996) Vortex shedding from bluff bodies and a universal Strouhal number, *Journal of Fluids and Structures*, **10**, 159-171.

Naudascher, E. and Wang, Y. (1993) Flow-induced vibrations of prismatic bodies and grids of prisms, *Journal of Fluids and Structures*, **7**, 341-373.

Prasad, A., and Williamson, C.H.K. (1996) The instability of the separated shear layer from a bluff body, Physics of Fluids, 8(6), 1347-1349.

Shirayama, S., Kuwahara, K., and Mendez, R.H. (1985) A new three-dimensional vortex method, *AIAA 7th Computational Fluid Dynamics Conference*, **AIAA-85-1488**.

Stansby, P.K. (1976) The locking-on of vortex shedding due to the cross-stream vibration of circular cylinders in uniform and shear flows, *Journal of Fluid Mechanics*, **74**, 641-655.

Tamura, T., Itoh, Y., and Wada, A. (1995) Three-dimensional simulations of an oscillating rectangular cylinder, *in Flow Induced Vibration, ed. Bearman, Balkema, Rotterdam*, 181-192.

Tamura, T., Itoh, Y., Wada, A., and Kuwahara (1995) Numerical study of pressure fluctuations on a rectangular cylinder in aerodynamic oscillation, *Journal of Wind Engineering and Industrial Aerodynamics*, **54/55**, 239-250.

Tamura, T., and Kuwahara, K. (1990) Numerical study of aerodynamic behaviour of a square cylinder, *Journal of Wind Engineering and Industrial Aerodynamics*, **33**, 161-170.

Wu, J.C., Sheridan, J., Soria, J., and Welsh, M. (1994) An experimental investigation of streamwise vortices in the wake of a bluff body, *Journal of Fluids and Structures*, **8**, 621-625.